Spring 2015

Mineral and geochemical attributes of the midcontinent rift sequence; An application for deep carbon dioxide sequestration

Alsedik Mohamed Ali Abousif

Department: Geosciences and Geological and Petroleum Engineering

MINERAL AND GEOCHEMICAL ATTRIBUTES OF THE MIDCONTINENT RIFT SEQUENCE; AN APPLICATION FOR DEEP CARBON DIOXIDE SEQUESTRATION

by

ALSEDIK MOHAMED ALI ABOUSIF

A DISSERTATION

Presented to the Graduate Faculty of the

MISSOURI UNIVERSITY OF SCIENCE AND TECHNOLOGY

In Partial Fulfillment of the Requirements for the Degree

DOCTOR OF PHILOSOPHY

in

GEOLOGY AND GEOPHYSICS

2015

Approved by:

David J. Wronkiewicz, Advisor
John P. Hogan
Wan Yang
Baojun Bai
Francisca Oboh-Ikuenobe

ABSTRACT

The potential for using the Oronto Group of the Midcontinent Rift (MCR) Sequence for CO_2 sequestration has been disparaged because of low porosity-permeability characteristics, which are largely a result of extensive calcite cementation. This study investigated the potential for using the MCR as a target for CO_2 sequestration by examining reactions involving detrital host-rock minerals at high pressure-temperature conditions that could provide dissolved Ca^{2+}, Mg^{2+}, and Fe^{2+}, and then precipitating these cations as carbonate minerals. The effect of carbonic acid on cement dissolution was also evaluated with respect to enhancing porosity and permeability. The Oronto Group sediments were enriched in CaO and MgO (5-12 wt%), and dominated by volcanic-lithic fragments with traces of alkali-feldspar, plagioclase, muscovite, quartz, chlorite, illite and smectite. The overlying Bayfield Group sediments are feldspathic quartz arenites with up to 17% porosity, however, they have low abundances of CaO and MgO (<2% wt %) and generally lack an effective cap rock. Cut and polished samples were reacted with either CO_2-saturated deionized water at 90°C in Teflon vessels, or mildly acidic nitric acid solution in room-temperature core-flooding experiments to evaluate reactions under potential sequestration conditions. Rapid dissolution of calcite cement was noted in short-term tests (1.6 - 20 mg Ca/cm^2.day), while supersaturated conditions were achieved with the associated precipitation of carbonate minerals in longer-term (101.9 day) experiments following the neutralization of carbonic acid and associated pH rise. The potential of using the Oronto Group as a CO_2 sequestration target is favored by its carbonate mineralization potential, but hindered by its limited permeability, even for samples that displayed porosity enhancement following calcite cement dissolution.

ACKNOWLEDGMENTS

I would like to give a special note of thanks for my advisor Dr. David J. Wronkiewicz for his patience and guide during my study. I appreciate his guidance in writing reports, papers, and this dissertation. Also, I would like to show my appreciation for the effort of my committee members, Drs. John Hogan, Wan Yang, Baojun Bai, and Francisca Oboh-Ikuenobe, to bestow a great time of their busy schedule to review this dissertation. My great approciations I would like to send to Dr. Shadab Anwar to his suggestions and recommendation during my study period. Also, I would like to thank current and past lab colleagues, especially Dr. Varun Paul, Hanani Tajul Nahar, Robert Swain, Hang Deng, Thomas Herbst, David Davison, and Krista Rybacki. I would like to give my thanks for all institutions that supported my research including; the Department of Energy (DOE)–National Energy Technology Lab by funding this study under agreement number of DE-FE0002416, the Missouri S&T Environmental Research Center (ERC) for giving an access to the ICP-OES, and the Missouri S&T Materials Research Center (MRC), who kindly assisted me in during the SEM-EDS and XRD analysis. Special note of thanks I would like to send to Mr. Eric Bohannan (XRD specialist) and Dr. Clarissa Wisner (SEM specialist). I would like to thank Iowa Department of Natural Recourses (DNR), especially Dr. Raymond R. Anderson, and Kansas Geological Survey (KGS), especially Dr. Dave Newell, for providing us with valuable subsurface samples used in these investigations. I would like to thank Dr. Baojun Bai and his graduate student Abdulmohsin Imgam for assisting with work on the core flooding experiments. I would like to extend my appreciation to Elizabeth Roberson, a technical editor at Missouri S&T office of graduate studies, who provided a great writing editing review of this dissertation. Also, I would like to thank the Libyan Ministry of Higher Education, the University of Sebha – Libya, the Canadian Bureau of International Education (CBIE) for kindly support my study in the United States. I would like to give special note of thanks for my CBIE advisor, Amira Ismail, for her sincere advising during my critical stages of my study, and for all my colleagues and teachers at the Earth Science Department of Sebha University. Finally, unlimited notes of appreciation and thanks I would like to dispatch to my family for their prayers, wishes, and support.

TABLE OF CONTENTS

LIST OF ILLUSTRATIONS

Page

LIST OF TABLES

Page

1 INTRODUCTION

1.1 GLOBAL WARMING AND GEOLOGIC SEQUESTRATION

The emission of carbon dioxide and other anthropogenic gases within the atmosphere is potentially one of the greatest environmental concerns on Earth today. These greenhouse gases absorb a significant amount of the infrared terrestrial radiation reflected from the Earth's surface to heat the atmosphere and create what known as the greenhouse effect and global warming. Between 1970 and 2004, CO_2 emissions increased by approximately 70% (Pacala and Socolow, 2004). These emissions will increase from 7.0 GtC/y (gigga-tons carbon/year) in the year 2000 to approximately 14 GtC/y in the 2050 if emissions continue to increase as that rate recorded in 2000 (Figure 1.1(A); Pacala and Socolow, 2004).

Geologic sequestration of CO_2 involves the injection of supercritical phase CO_2 into deep underground saline aquifers, coal layers, or depleted oil and gas reservoirs for additional hydrocarbon recovery. Injection of CO_2 into deep ocean basins is another potential strategy where the high pressures and low temperatures of the deeper ocean basins would allow the injected CO_2 to convert to a negatively buoyant liquid or solid CO_2 hydrates [e.g., $CO_2.nH_2O$; Sheps et al., (2009)].

The strategy of injection into deep saline aquifers involves four main trapping mechanisms including physical trapping, residual trapping, solubility trapping, and mineralogical trapping. Due to its buoyancy, CO_2 may be trapped as an undissolved gas-phase at either the shallower stratigraphic level or the structural trap positions within a reservoir, and that known as a physical trapping. Residual trapping stores CO_2 as an undissolved gas-phase in the pore spaces due to both the surface tension between the grains and the CO_2, and due to the pressure reduction immediately after completion of the injection processes. The tail of the CO_2 plume is then trapped as bubbles that are attached to mineral grains in the reservoir. A significant portion of physical and residual trapping is converted into dissolved aqueous-phase with time. A gas solubility model of 100 m reservoir was created by Ennis-King and Paterson, (2003) with a one MtC/y injection

rate, 40°C temperature, 10MPa pressure, 10^{-13} m^2 horizontal permeability, and10^{-14} m^2 vertical permeability. This model demonstrates the dissolved aqueous-phase of CO_2 will dominate the system between 20 and 200 years after CO_2 injection. The solubility products of injected CO_2 gas and/or supercritical phase CO_2 will be $CO_{2\,(aq)}$, $H_2CO_{3\,(aq)}$, HCO_3^-, or CO_3^{2+}. These products are generally responsible for the main geochemical alteration processes associated with CO_2 sequestration under longer term scenarios when water displaced by CO_2 injection re-floods the reservoir rocks (Bachu and Bennion, 2008). These processes, including both the dissolution of the reservoir minerals and the precipitation of new carbonate mineral phases, and will be discussed in more detail in Section 1.2.

Section 1 of this study addresses a hypothetical model for CO_2 sequestration in the Midcontinent Rift (MCR), the objectives, and the methodology used in this study. Section 2 discusses the literature review of the MCR geology, advantages and challenges of CO_2 sequestration in the MCR, and the geochemistry of carbonate minerals. Section 3 discusses the petrographic characteristics of the MCR sedimentary rocks. Section 4 addresses the chemical composition of the MCR rocks, the CO_2 geochemical reactions that take place near to the injection site, and the potential CO_2 geochemical reactions related to the reduced CO_2 supply away from the injection site.

1.2 POTENTIAL FOR CO_2 SEQUESTRATION IN THE MCR

Geologic sequestration in MCR sediments involves injecting supercritical-phase CO_2 into a deep saline aquifer to prevent its return to the atmosphere. This current research project is based upon the following points:

1. Supercritical-phase of CO_2 is times less dense than any other fluids naturally found in an aquifer (0.3 – 0.4 g/cm^3; Lemmon et al., 2005; Xu et al., 2006). As a result, it will diffuse (like a balloon) from the injection point, and then spread upward with only minimal tensional adherence to the grains, which are more attracted to the aquifer brine (Kim et al., 2012; Tokunaga, 2012; Hamm et al., 2013 see Figure 1.1). Eventually, the injected CO_2 will become trapped either geochemically or physically.

2. The acidity of the aquifer water increases as the injected CO_2 dissolves into the water. Species such as dissolved carbon dioxide [$CO_{2(aq)}$], carbonic acid [$H_2CO_{3(aq)}$], bicarbonate (HCO_3^-), and carbonate (CO_3^{2-}) dominate in the aquifer water with the relative concentration of the later three species depending on the pH (Berner and Lasaga, 1983), as expressed in following equations:

$$CO_2 + H_2O \rightleftharpoons H_2CO_3 \quad (1)$$

carbonic acid (dominates at pH < 6.3)

$$H_2CO_3 \rightleftharpoons H^+ + HCO_3^- \quad (2)$$

Bicarbonate (dominates at 6.3<pH<10.3)

$$HCO^{3-} \rightleftharpoons H^+ + CO_3^{2-} \quad (3)$$

Carbonate (dominates at pH>10.3)

3. Corrosion of many MCR mineral phases may occur as the pH of the solution decreases (Berner and Lasaga, 1983; Holland, 1984; Meybeck, 1987). Calcium carbonate cement, which is commonly observed in MCR rocks, will rapidly dissolve to enhance the primary porosity and permeability as in equation 4 and 5.

$$2H^+ + CaCO_3 \rightleftharpoons Ca^{2+} + H_2O + CO_2 \quad (4)$$

$$2H^+ + CaCO_3 \rightleftharpoons Ca^{2+} + 2HCO_3^- \quad (5)$$

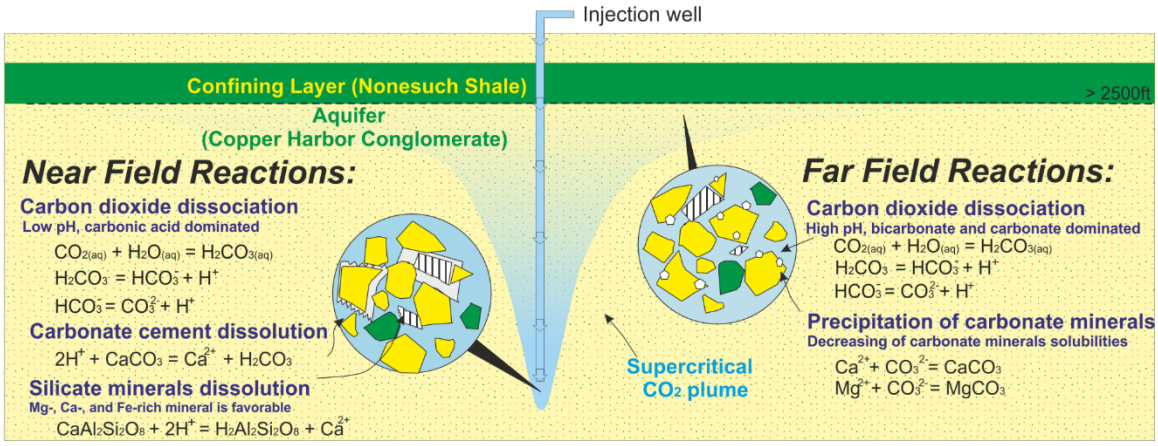

Figure 1.1 Hypothetical model of CO_2 sequestration in the MCR Oronto Group (Copper Harbor Conglomerate sealed by Nonesuch Formation shale). This shows the geochemical reactions that could exist at the injection site (near field reactions) and the disposal site (far field reactions).

4. Calcium-bearing silicates may represent an unlimited source of Ca^{2+} required to calcite precipitation for repositories containing abundant anorthitic-plagioclase, Ca-pyroxenes, or other Ca-silicate phases (Gunter et al., 1993; Bachu et al., 1994). Both Mg^{2+} and Fe^{2+} cations, also the products of the dissolution of many mafic minerals, may also be important to mineral carbon sequestration (Berner and Lasaga, 1983; Meybeck, 1987; Berner, 2003; Giammar et al., 2005; Power et al., 2013). Oxide phases containing Fe^{3+} may also be involved in reactions by providing Fe^{2+} that can be produced by reducing agents that are available in the system.

5. Many silicate minerals (e.g., feldspars) and the carbonate cements act as a base to buffer the pH when additional H^+ ions are added to the system. These minerals are likely to dominate the buffering capacity relative to the aqueous buffers that are present, as seen in equations 6, 7, 8, and 9 (Kirste et al., 2004). The alteration surfaces composed of alkali- and alkaline earth depleted hydrated feldspar will be thermodynamically unstable and will eventually alter into other phases, including dissolved silicic acid ($H_4SiO_{4\,(aq)}$) and clays such as kaolinite [$Al_2Si_2O_5(OH)_4$].

$$KAlSi_3O_8 + H^+ \rightleftharpoons HAlSi_3O_8 + K^+ \quad (6)$$
K-feldspar *hydrated feldspar*

$$CaAl_2Si_2O_8 + 2H^+ \rightleftharpoons H_2Al_2Si_2O_8 + Ca^{2+} \quad (7)$$
Anorthite *hydrated feldspar*

$$Mg_2SiO_4 + 4H^+ \rightleftharpoons H_4SiO_4 + 2Mg^{2+} \quad (8)$$
Olivine Silicic acid

$$MgSiO_3 + 2H^+ \rightleftharpoons SiO_2 + Mg^{2+} + H_2O \quad (9)$$
enstatite *quartz*

6. Far from the injection point, and/or after significantly long enough time periods have passed after CO_2 injection has ceased, the pH of the groundwater will increases as a result of neutralizing reactions with surrounding rocks, exchanging acid protons (H^+) with metallic ions (e.g., Na^+, K^+, Ca^{2+}, Mg^{2+}, Fe^{2+} etc.; Giammar et al., 2005; Knauss et al., 2005; Palandri and Kharaka, 2005; Xu et al., 2005). At such basic conditions, the equilibrium solubility of released cations will decrease and, eventually, mineral precipitation may occur in the form of carbonate mineral phases, as shown in equations 10, 11, 12, and 13:

$CO_3^{2-} + Ca^{2+} \rightleftharpoons CaCO_3$ (10)
(calcite/aragonite)

$CO_3^{2-} + Mg^{2+} \rightleftharpoons MgCO_3$ (11)
(magnesite)

$2CO_3^{2-} + Ca^{2+}\ Mg^{2+} \rightleftharpoons CaMg(CO_3)_2$ (12)
(dolomite)

$CO_3^{2-} + Fe^{2+} \rightleftharpoons FeCO_3$ (13)
(siderite)

7. Thermodynamically, these carbonate minerals are relatively stable phases and abundant throughout both the geological record on the Earth's surface and relatively shallow subsurface crust.

8. Carbonate ions may precipitate as carbonate phases once the pressure decreases at any fractured seal, much like the processes that occur in hydrothermal systems (Katz et al., 2006). Experimental work, conducted on fractured Ogachi granodiorite in Japan, found that a significant amount of Ca^{2+} was released after the supercritical-phase of CO_2 was injected at 200°C and 6 MPa (870 psi). After the temperature was reduced to 100°C, the CO_2 degasses and precipitates as a carbonate mineral phase (Ueda et al., 2005).

1.3 OBJECTIVES

The objectives of this research project are to:

1. Evaluate the MCR samples collected from both in the field and subsurface drill core samples with respect to their Ca^{2+}, Mg^{2+}, and Fe^{2+} contents, based on both their mineral and bulk chemical composition.

2. Evaluate the potential for calcium carbonate dissolution that would result following CO_2 injection and associated increases in the primary porosity-permeability of the host rock samples. Porosity may even be decreased with the formation of alteration minerals such as clays.

3. Investigate the dissolution rates and processes affecting Ca^{2+}-, Mg^{2+}-, and Fe^{2+}-bearing silicates and oxides of the MCR samples in order to quantify their contribution of dissolved ions that will complex with carbonate ions and lead to precipitation of solid

carbonate minerals. The dissolution of silicate minerals is expected to occur at a kinetically slower rate than observed with the carbonates.

4. Evaluate the potential for carbonate mineral precipitation as a result of dissolution and acid neutralization reactions following CO_2 injection and reaction with dissolved ions and repository host rocks by examining reacted solid samples for the presence of newly precipitated carbonate minerals. These reactions will also be modelled using the PHREEQ modelling code and compare modeling results to mineral reactions to experimental corrosion tests.

1.4 METHODOLOGY

1.4.1 Sample Collection. Surface samples were collected from various locations around Lake Superior, including the Keweenaw Peninsula (MI), the L'Anse area (MI;), Potato River Falls (WI), Copper Falls State Park (WI), the Bayfield Peninsula (WI), Beaver Bay Complex (MN), North Shore Volcanic Group (MN), and Duluth Complex (MN). Subsurface samples were also collected from the M. G. Eischeid #1 well, (IA) and the Texaco Poersch #1, well (KS). All samples collected from surface outcrops were trimmed in the field using a rock hammer to remove any obvious weathering rinds. Removal of all weathering affected rock material could not be guaranteed, however, especially for the more permeable sandstone samples. The majority of the surface samples were collected from eroding river valleys and generally displayed minimal to no weathering effects as rock samples from these locations tend to be physically eroded as fast as they are chemically weathered.

Copper Harbor Conglomerate (CHC; see the rift stratigraphy in Figure 1.2) samples were collected from five locations along the western shore of the Keweenawan Peninsula (MI) and designated as KEW samples (Figure 1.3). All samples were preferentially collected from sandstone- or siltstone-rich horizons located within predominantly coarser-grained conglomeratic beds. The KEW1 samples were collected from the Eagle River valley. These were collected from a stratigraphic position just above the boundary between the underlying Portage Lake Volcanics (PLV) and the CHC.

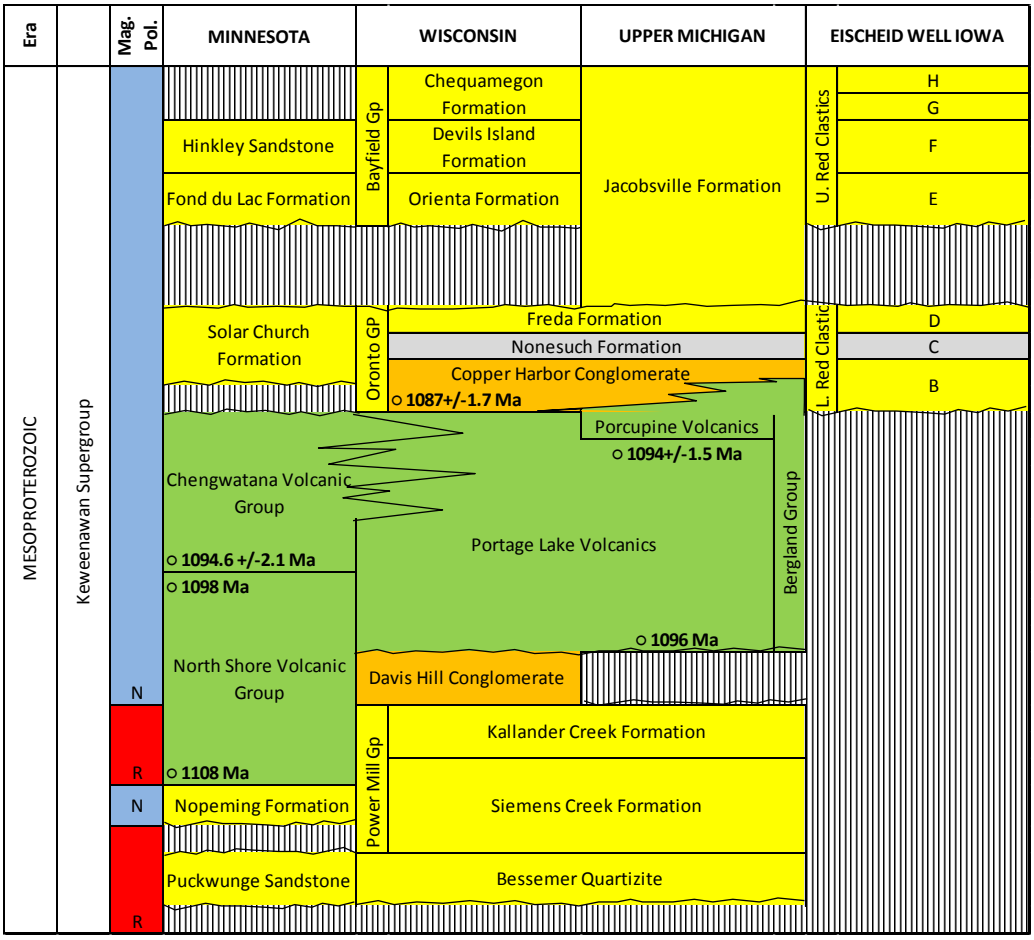

Figure 1.2 The Keweenawan Supergroup and its nomenclature in Minnesota, Wisconsin, Michigan, and Iowa. [Modified from Cannon and Nicholson (1992); Anderson (1997)].

Lithologically, the KEW1 samples are described as red colored conglomerates, conglomeritic sandstones, and sandstones. The KEW2 samples were collected near Lake Baily. These samples are composed of massive reddish sandstone with pebbly volcanic clasts and/or either cross-bedded or fissile sandstone. The KEW3 samples were collected along Michigan Highway 26, on the northeast bank of the bridge over the Silver River. These samples are composed of reddish sandstone and silty sandstones lenses located within more massive beds of conglomerate. Clay-rich layers were also recognized within these lenses. The KEW4 samples were collected along the Lake Superior shoreline, just south of the residence building located at 11,899 Highway 26. These samples were composed of reddish pebbly layers with many clast types including amygdaloidal and fine grained basalt. Calcite veins were also common at this sampling location.

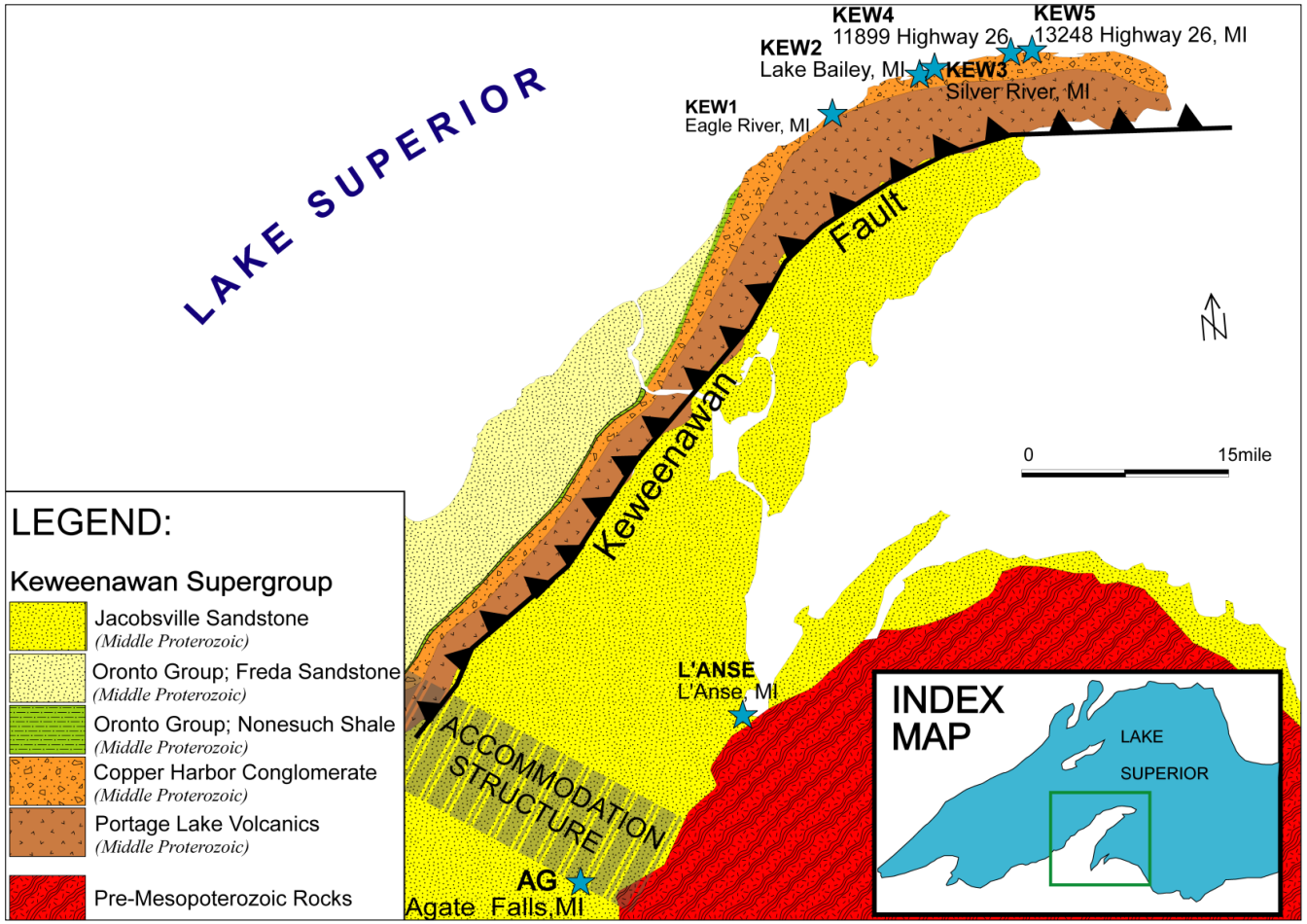

Figure 1.3 Sampling locations around the Keweenawan Peninsula, Michigan. This map showed the locations for the Oronto Group (KEW), Jacobsville Formation, around L'Anse area (L'ANSE) and Agate Falls (AG). Figure modified after USGS KML file for Google Earth prepared by (Nicholson et al., 2004).

The KEW5 samples were collected south of the residence at 13,248 on Highway 26. Lithologically, these samples were similar to the KEW4 samples.

The Jacobsville Formation samples (L'ANSE samples) were taken from a road cut along US Highway 41 between Baraga and L'Anse area (Figure 1.3). These samples were medium-coarse-grained red to buff colored sandstone with several cross-bedding structures and a distinctive white spotted coloration pattern due to iron mobilization around localized reduction zones. Another Jacobsville sandstone sample was collected from Agate Falls Park (MI; Figure 1.3). This sandstone is massive, cross-bedded, and brown-reddish to reddish-white colored and quartz-rich with minor siltstone and shale lenses. At this location, the Jacobsville Formation is exposed by incision along the Middle Branch of the Ontonagon River. The samples collected for this study were chosen from relatively unweathered exposed sections (Figure 1.4).

Samples designated with the POT prefix were collected from the Freda Formation, Nonesuch Formation, and CHC units, exposed at Potato River Falls, WI (Figure 1.5; Appendix Figure A. 1). This exposure has been tilted by tectonic forces to a nearly vertical orientation at this location. The conglomeritic-sized content is increased eastward and upstream along the Potato River, with the conglomeratic units representing the transition to the CHC. The POT1 samples were collected from a thick fissile shale/slate unit of the Nonesuch Formation. The POT2 samples were collected from the Nonesuch, from a thick sandstone-siltstone unit exposed just upstream and stratigraphically below the POT1 samples. The POT3 samples were collected just below the POT2 samples and represented more than 100 cycles of thinly bedded Nonesuch siltstone-shale units. The POT4 samples are stratigraphically below the POT3 samples and represent dominantly feldspathic sandstone, with some pebbly horizons. The samples POT4a and 4b were collected from the northern and southern portions of the river bank, respectively. The POT5 samples were collected from the south bank of the river and represented a red coarse-grained sandstone, with a few isolated pebble layers. The POT6 samples, probably, represent the transition to the CHC and are located upstream of the POT5 and are from the south bank of river. These samples are composed primarily of feldspathic sandstone with a few pebbly horizons. The POT7 was collected from CHC

located upstream at the south bank of river and are conglomeritic. The POT8 was derived from an adjacent cut bank furthest up section in the Potato River stratigraphic succession. These samples were slightly friable, red medium to coarse-grained feldspathic sandstone and are likely representative of the Freda Sandstone. The POT8 sample was collected from boulders that were washed downstream from the outcrop as deep and turbulent water conditions at the area of the outcrop along a cut bank prevented direct sampling.

Figure 1.4 Sampling collection location from a river valley incision through Jacobsville sandstone. The sampling was along the Middle Branch Ontonagon River, MI, just south of highway MI28, at Agate Falls State Park, MI.

Freda Formation sandstone samples were collected from exposed outcrops in a flowage valley along the Michigan-Wisconsin border, just inland from the Saxon Harbor entry from Lake Superior (Labeled SH in Figure 1.5). The samples were reddish-brown colored, medium-to-fine-grained, lithic to arkosic sandstone and siltstone from a vertically tilted stratigraphic horizon (Figure 1.6). They had high clay content and a low permeability. Additional Freda samples were collected from Superior Falls, WI (Labeled SF; Figure 1.5). These samples were brown-to-reddish colored siltstones and sandstones. The sequence was also titled into a vertical orientation as seen in Figure 1.7.

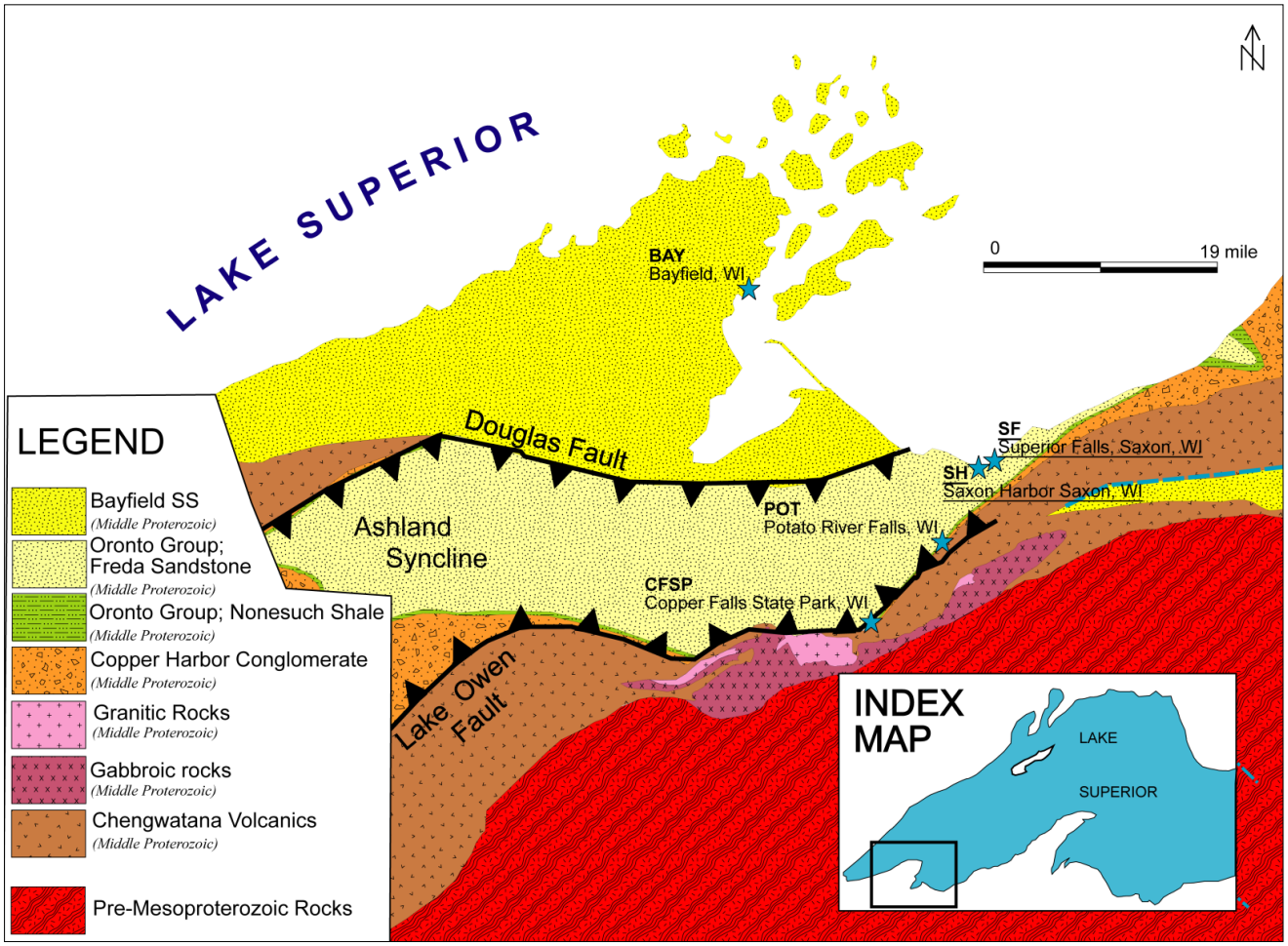

Figure 1.5 Sampling locations around the Bayfield Peninsula. The precise sampling locations around the town of Bayfield, Wisconsin are shown in Appendix Figures A.1 and A.2. Figure modified after USGS KML file for Google Earth prepared by Nicholson et al., (2004).

Figure 1.6 Sampling location of Freda sandstone (SH sample). The sample was collected from the Oronto Creek, around Saxon Bay Harbor, Michigan-Wisconsin border.

Figure 1.7 Sampling location from highly tilted red Freda sandstone (SF samples). The section located at Superior Falls, Montreal River, Michigan-Wisconsin border.

Several samples were collected from CHC and Nonesuch Formation at Copper Falls State Park and given a prefix of CFSP (Figure 1.5; Appendix Figure A. 2). The CFSP1 sample was a red fissile shale/slate collected from a tectonically tilted section of the Freda Formation. The CFSP2 sample was coarse grained gritty red sandstone. This sample was collected from a section located just stratigraphically above the CFSP1 sample and displayed low permeability. The CFSP3 was collected from the CHC at

Copper Falls State Park. This sample is red conglomerate shot through with veinlet and pods of white calcite. The CFSP3 sample was collected from boulders that were washed downstream from the outcrop exposed in the Devils Gate Waterfall. The CFSP4 sample was collected from a steeply dipping section of the CHC and displays a red colored, fine to medium-grained, well-cemented sandstone.

Samples from the Bayfield Peninsula were collected from the Bayfield Group, Chequamegon Formation (Figure 1.5), and given a prefix of BAY (Appendix Figure A. 3). The BAY1 sample was collected from the eroding shoreline along Lake Superior at Dardemple Park/Campground, north Bayfield city, WI. The BAY1 sample varied between a low permeability, buff colored, slightly friable, medium grain sandstone and a high permeability, highly friable, red colored, medium-grained sandstone. The BAY2 samples were collected from a high plateau along cliff overlooking Lake Superior shore. The sampling location was accessed from the Wild Rice Restaurant parking lot located along Old Sal Road south of city of Bayfield. The samples are a highly permeable, light-red, friable, and fine to medium-grained sandstone, with, occasionally low friable and low permeable sandstone layers. The BAY3 sample was collected from a road cut along the flanks of Mount Ashwabay, WI. This sample is as highly friable, light-red colored, medium-grained sandstone with medium to low permeability.

A thick sequence of North Shore Volcanic Group (NSVG) basalt was identified in Good Harbor Bay, MN and given a prefix of GHB. This basalt overlays a thin and discontinuous unit of brown-to-reddish colored, fine grained, volcanogenic interflow sandstone and laminated siltstone (labeled GHC; Figure 1.8 and 1.9). The outflow of water exposed in the road cut throughout these layers indicates significant permeability of the interflow sedimentary rocks relative to the underlying basalt. Samples of plagioclase-rich anorthositic rocks (BEV samples) were collected form Silver Bay, MN. These rocks are engulfed within a larger scale diabase rocks as illustrated in Figure 1.8 and 1.10.

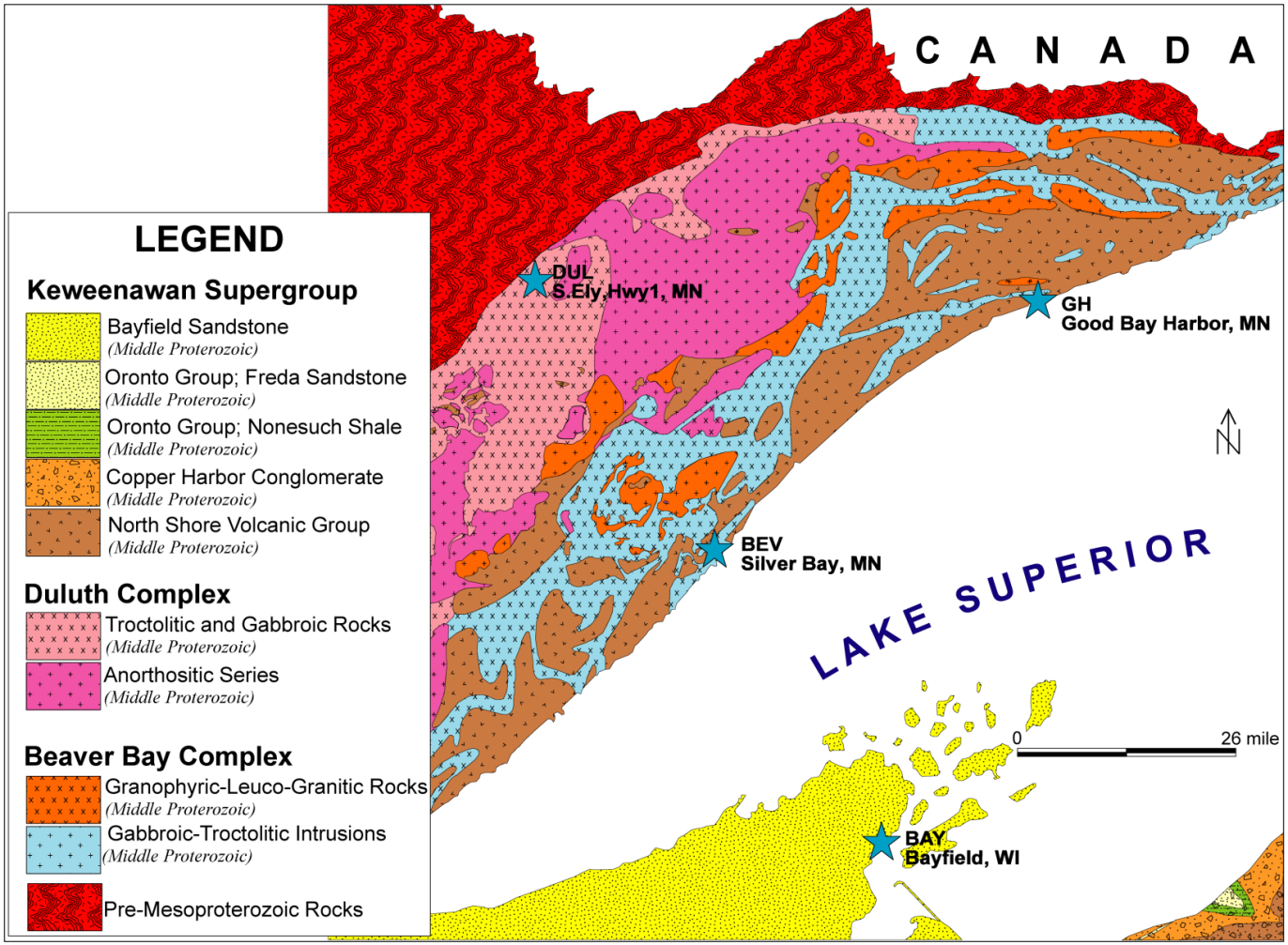

Figure 1.8 Sampling locations around the North Shore of Lake Superior and Duluth Complex. Figure modified after USGS KML file for Google prepared by Nicholson et al., (2004).

Figure 1.9 Sampling location from North Shore Volcanic Group section and interflow clastic rocks in red color. The section located on highway MN61, at the road cut of Grand Marais historical site, Good Bay Harbor, MN.

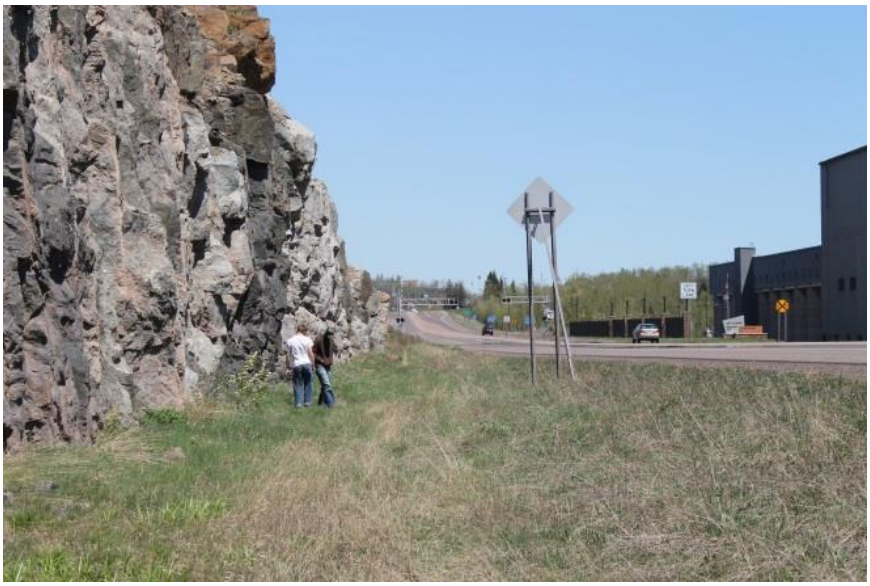

Figure 1.10 Sampling location of anorthosite mega-xenolith hosted in the Beaver Bay Complex.The section located along highway M61, just across road from North Shore Mining Company operations, Silver Bay, MN.

Subsurface samples were collected from deep drill core samples that were obtained from both the Texaco Poersch #1 well in Kansas, and the M.G. Eischeid #1 petroleum exploration well in Iowa. The Texaco Poersch #1 section contained a

significant thickness of Precambrian Midcontinent Rift clastics and igneous rocks (Berendsen et al., 1988). This well was drilled into a faulted block basement segment to a total depth of 11,300′ (Figure 1.11). The penetrated section was differentiated into the upper mafic volcanic and intrusive sections (2,846′ - 7,429′) and lower clastic-dominated arkose, sub-arkose, siltstone, and shale sequences (7,429′ - 11,300′). The clastics of the upper mafic volcanic and intrusive sections were divided into the upper mixed volcanic-sedimentary sequence (UMVSS) and the lower mixed volcanic-sedimentary sequence (LMVSS) and separated by dominated gabbroic and basaltic sequences. The underlying clastic dominated section was divided into lower sedimentary sequence (LSS), middle sedimentary sequence (MSS), and upper sedimentary sequence (USS; Figure 1.11).

The geophysical and stratigraphic interpretation of the sequences of Texaco Poersch #1 well suggest that reverse faulting, on the flanks of the central horst, juxtaposed the volcanic sequence over the clastic rocks (Woelk and Hinze, 1991). K-Ar dates from extrusive igneous intervals within the clastic dominated sequence and the overlying igneous dominated section was extremely varied relative to other MCR sequences. For the inter-stratified mafic flows, the K-Ar dates ranged between 814±31 Ma (gabbro at ~8,700′) and 895±21 Ma (basalt at ~10,660′). A single data set showed 1,021±100 Ma for the deepest basaltic rocks. All of these dates are younger than the Oronto Group, and thus represent isotopic system resetting due to post-depositional thermal-metamorphic events. It is also not easy to compare these dates to the Bayfield Group because of the lack of the absolute age dating on these sediments.

Berendsen et al., (1988) conducted detailed geochemical and geophysical investigations on the Texaco Poersch #1 well. The samples selected for testing in the present study were collected from the lower clastic dominated section and from the clastic interflows within the upper section (Figure 1.11). These rocks were alkali rich (e.g., $K_2O + Na_2O$ between 2.5 and 8.5 wt%) while the silica content ranged between 42 and 49 wt%.

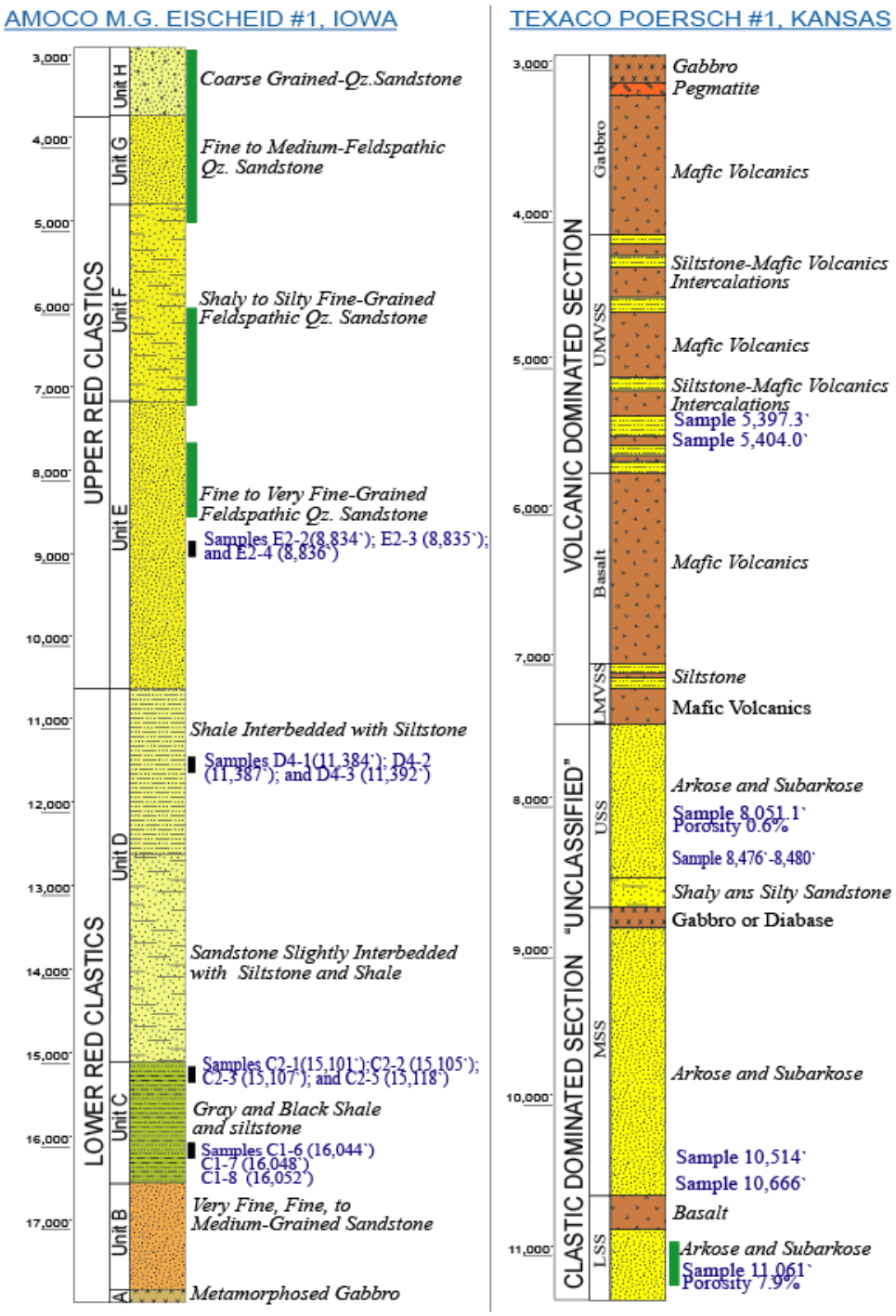

Figure 1.11 Stratigraphy of deep drilling wells penetrating MCR in Iowa and Kansas. The black stripe pattern represents locations where samples were collected for this study; the green stripe areas represent additional sampling horizons with relatively high porosity-permeability; Upper mixed volcanic-sedimentary sequence (UMVSS); Lower mixed volcanic-sedimentary sequence (LMVSS); Upper sedimentary sequence (USS), Lower sedimentary sequence (LSS).

Two samples were collected for this study from the UMVSS at depths of 5,397.3′ and 5,404′. These samples were composed of primarily oxidized red siltstone and shale. Another two samples were collected from the USS and were primarily reddish feldspathic medium-to-coarse grained sandstone (8,051′ and 8,476′-8,480′). Also, two samples were also collected from the middle sedimentary sequence (MSS; 10,514′ and 10,666′), and these samples mostly composed of feldspathic sandstone. The last sample was collected from the lower sedimentary sequence (LSS; 11061′), which is composed of feldspathic, fractured, and course-to-medium grained sandstone.

The Eischeid #1 well is located approximately 8 kilometers northwest the buried Iowa Horst, penetrating through about 14,898′ of Mesoproterozoic sequences at the northern end of the Defiance Basin. The rift clastics were grouped into the Upper Red Clastics (which correlate with the Bayfield Group and equivalent strata exposed near Lake Superior) and the Lower Red Clastics (which correlate with the Oronto Group and equivalent strata). The Lower Red Clastics were classified into Units B, C, and D. These units were subdivided into numeric subclasses like C1 and C2. The Upper Red Clastics were divided into Units E, F, G, and H. These units were also subdivided into numeric subclasses Like E1, E2, and E3. No volcanic or plutonic sections were recovered from the Eischeid #1 well section (Figure 1.11).

Three different samples were collected from the core interval that penetrated Unit E of the Eischeid #1 well (The Orienta Formation equivalent). This stratigraphic unit exhibited traces of calcite cement, a high plagioclase content, and approximately 11% porosity. The collected E2-2 sample was a laminated-to-low-angle stratified brownish red, well-cemented fine-grained sandstone. The E2-3 sample was a massive, brownish red, coarse-grained sandstone. The E2-4 sample was a mottled-color, low angle stratified brownish red, medium-grained sandstone (Figure 1.11).

Three samples were also collected from the Unit D of the Eischeid #1 well (which correlates to the Freda sandstone exposed in the Lake Superior region). The Unit D in general, exhibited indications of calcite cement and low porosity layers. Sample D4-1 was a red, with a tabular trough cross-bedding, silty to fine grained sandstone. The D4-2

sample was thick, laminated, sandstone with mudstone intercalations. The last sample (D4-3) was collected from a red, well-cemented, silty sandstone (Figure 1.11).

Five samples were collected from the Unit C2 (which correlates to the Nonesuch Formation). The Unit C is characterized by an abundance of calcite cement within a black shale and a low porosity interval. The C2-1 sample was a light gray, calcareous, laminated, very-fine grained sandstone. The C2-2 sample was a laminated, calcareous, fine-to-medium-grained sandstone. The C2-3 and 4 samples were composed of intercalated sandstone-siltstone-shale layers. The C2-5 sample was a massive, laminated, calcareous, very fine-grained sandstone (Figure 1.11).

1.4.2 Petrographic Study. One objective of this study was to investigate the mineral composition, porosity, and textural maturity of the samples that were collected from surface outcrops and drill cores. Samples from various lithologies were trimmed with a wafering saw using a water lubricant as a preparation for thin sectioning. The trimmed samples were sent to the National Petrographic Services, Inc. in Houston for staining and thin sectioning. The staining of the samples included alizarin red-S to test for calcite. Detecting the presence of potassium feldspar was also aided by staining with sodium cobalt nitrite and plagioclase feldspar by staining with barium chloride and rhodizonate. The prepared thin sections were studied using a Nikon 2000 polarized microscope to identify both the mineral composition and sedimentary textural maturity. The number of grains counted and the spacing between the points and the lines were based on the grain size of the sample. The grain modal analysis was determined based on 270 to 300 counts per thin section as a minimum statistical satisfaction of point counting (Dickinson, 1970; Dickinson, 1985). The spacing between any successive points was set to one mm to quantify the sandy grain size particles < 1 mm in diameter without repetition of counting a single grain more than once. The matrix and clay-sized particle mineralogy was investigated both petrographically and by using the X-Ray Diffraction (XRD) technique described in Section 1.4.3. The quantitative porosity analysis used a blue epoxy that was impregnated into the samples before the grinding of the thin sections. This epoxy filling was used to prevent the damage of the pore spaces and to make the pores more recognizable during the microscopic investigations.

1.4.3 X-Ray Diffraction (XRD) Analysis. This method was used to identify the matrix composition and identify any associated clay-sized minerals. Each clay-sized sample run was prepared by manual crushing (using agate mortar and pestle) to minimize potential damage to the clay's crystal structure. The mortar and pestle were cleaned using deionized water to avoid cross-contamination between the samples. Approximately 25 g of the sample was placed in a labeled beaker and mixed with 100 mL of deionized water. After approximately 15 seconds, all suspended materials were transferred to another labeled beaker. If no materials were suspended, the mixture was left to clarify, and the last step was repeated with new deionized water. A few drops of sodium hexametaphosphate (Calgon^{TM}) were added if the materials continued to settle quickly. Calgon was used only in KEW4-1, C1-6, 5,400′, 4,876′ -8,480′, 10,509′, and 10,666′ samples. If there was still no suspension, the entire procedure was repeated. When sufficient suspension occurred for at least for 10 minutes, the suspended materials were carefully pipetted from the top of the solution and placed on labeled, thermally resistant (up to 600°C) glass slides where they were left to dry overnight. This procedure produced a clay mount with the c-axes of the clay minerals preferentially aligned perpendicular to the glass slide.

The first XRD scan was an untreated (air dried) run. In the second scan, the samples were exposed overnight to an ethylene glycol atmosphere to expand and help identify smectite clays. This type of clay absorbs ethylene glycol in the interlayer position and expand so that a shifted peak occurs and is visible in the 2-theta spectral analysis. The last run was conducted after the samples were heated at 300°C for one hour. The heating process was used to identify additional clay minerals and differentiate between some overlapping peaks.

Powder X-Ray diffraction analysis was also conducted to investigate the mineral composition of the rift clastic whole rock samples. These whole rock samples were crushed using a stainless-steel mechanical rock ring shaker box for less than 30 seconds, and then sieved using either a 70 μm or 64 μm sieves to collect the powdered fraction. A small amount of clean quartz sand was crushed to clean the inside parts of the aggregate crushing parts. The aggregate crushing parts were cleaned (using tap water), dried, and

then small piece of the next sample crushed and partially disposed to coat the inside walls of the aggregate crushing parts to avoid cross-contamination.

Both clay-mounts and crushed samples were scanned using Cu-Kα radiation source with a wavelength of 1.54 Å using an X'Pert PRO^{TM} Diffractometer. The scan speed was fixed at 2.8° per minutes, and the scan range was set between 2 and 60°. The direct line of radiation to the detector (i.e. usually < 5° 2-theta) was excluded to enhance the appearance of the mineral's peaks. Computer software was used to identify the minerals based on the 2-theta degree by comparison with a library of known diffraction peaks. The semi-quantitative clay content was estimated using the methodology discussed in the Appendix A.1.

1.4.4 X-Ray Fluorescence (XRF). This analysis was used to investigate the chemical composition of the samples to identify major element oxides (SiO_2, Al_2O_3, Fe_2O_3, CaO, MgO, Na_2O, K_2O, MnO, TiO_2, and P_2O_5). These samples were crushed mechanically using the same mechanical crusher described in the previous Section. A small amount of the clean quartz sand was crushed between each sample to ensure a deep cleaning of the aggregate crushing parts. Also, to avoid any contamination between the samples, a small amount of the sample was crushed and then disposed to coat aggregate crushing parts. About 20 g of each crushed sample was sent to the Acme Analytical Laboratory in Vancouver for analysis using the 4X group lithological analyses for the major element oxides.

The accuracy of a measurement represents the closest agreement between the average measured values to the actual value (known Standard value). The accuracy can be evaluated by this equation:

$$\text{Average \% Acuracy} = \left(\frac{\text{Known Standard value} - \text{Average Value}}{\text{Average Value}}\right) * 100$$

The precision, as coefficient of variation (CV), which is related to the repeatability, is the ability to repeat the same measured value under unchanged instrument conditions, and can be calculated from this equation:

$$\%\ \text{CV Precision} = \left(\frac{\text{Standard Deviation}}{\text{Mean Value}}\right) * 100$$

The accuracy for XRF was better than 6.3% for SiO_2, Al_2O_3, Fe_2O_3, CaO, MgO, Na_2O, K_2O, MnO, and TiO_2. Additionally, the accuracy was better than 8.3% for the P_2O_5. The calculated coefficient of variation (precision) for the analyzed samples was better than 0.14 % for all checked major oxides (Appendix Table C.1).

1.4.5 High-Pressure-Temperature (HPT) Corrosion Test. This experiment mimicked reservoir mineral chemical weathering conditions, at which the dissolution processes would be accelerated by the CO_2 acidification and high-pressure-temperature conditions. The average geothermal gradient of the Eischeid #1 well was 19°C/km (Anderson, 1990). Therefore, the temperature at the top of Units E (7,020′), D (10,510′), and C (14,980′) would be expected to be approximately 41, 61, and 87°C, respectively. The kinetic rate and dissolution solubility of silicate minerals is generally increased as temperature increases (Langmuir, 1997), so a 90°C temperature was used to ensure the maximum silicate reactions in a relatively short-term experiments. These experimental temperatures would likely still be valid for any potential repository horizons that were at lower temperatures as the mineral weathering paragenesis reactions in the 90^{o}C corrosion tests are the same as those found in natural weathering profiles. Higher temperatures will also commonly accelerate mineral weathering reactions with alteration rates expected to double for every 10^{o}C rise in temperature (White, 2013).

A stainless steel Parr^{TM} 4749 General Purpose vessel with an inner 23ml-Teflon liner (Figure.1.12) was used in the HTP corrosion experiments. The cleaning and preparation procedure for these Teflon vessels is given in Appendix A2. Approximately 2-3 g of dry ice was added to preweighed Teflon-lined vessels to saturate them with CO_2 prior to testing with the rock samples. These vessels were then placed in an oven at 90°C for three days and then weighted to measure the adsorbed CO_2, and the vessels now ready for the testing.

The samples used in the experiments were sliced using deionized water lubricant Isomet Buehler™ saw to avoid contaminating the samples. The samples were trimmed into a monolith approximately 2-3 mm thick, weighed, and measured, geometrically, to determine the surface area. Several sample sets was prepared from the POT4 sample for a different test parameter settings. These tests included an evaluation of the effect of the less fluid with the sample only partially submerged in the leachant solution (mounted; MO), the higher surface area (crushed; CR), and a lower temperature (50°C) on the leachate fluid composition. The CR samples were crushed by an agate mortar and pestle and then sieved by stainless steel sieves to collect a grain size fraction between 100 and 60 mesh (0.149 to 0.250 mm). The MO sample was prepared with a rectangular dimension to ensure that the sample was only partially submerged by the leachant fluid. The 50°C samples were prepared as the regular samples preparation for the HPT testing and placed at 50°C in the oven.

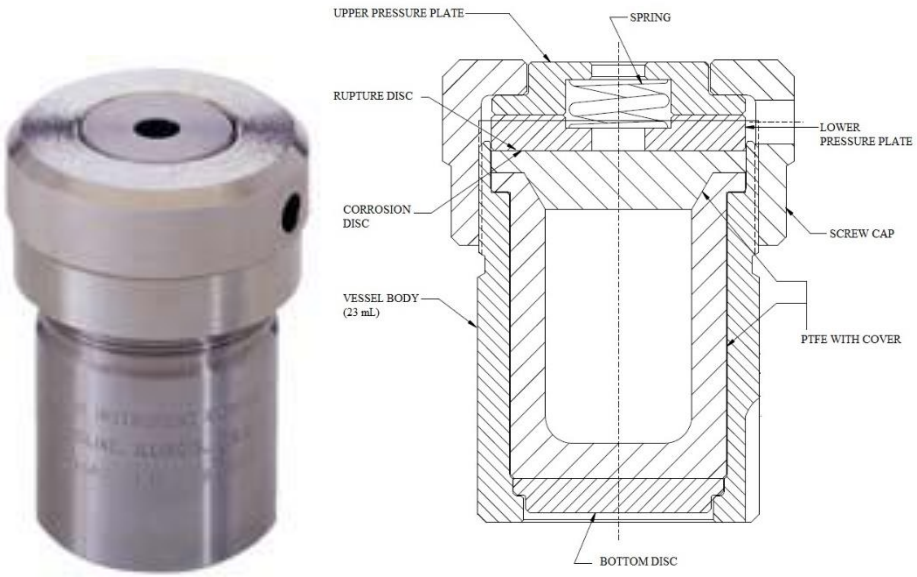

Figure.1.12 Parr™ 4749 general purpose vessel with Teflon liner.

The vessels with reactants (dry ice, DIW water, and a wafered sample) were assembled into a reaction vessel, weighed and placed in the preheated oven at 90°C. Deionized water was used in the experiments to allow the chemical composition of rocks

used in the testing to control the composition of the leachate solution by the rock-water-CO_2 interactions. The weight loss was monitored periodically, and the experiments were terminated once that loss reached one gram.

After the appropriate length of reaction time, and/or when the sample vessels had lost one gram, the vessels were cooled, opened, and then both the pH and Eh were immediately measured using an aliquot of water of approximately one ml that was transferred to a small plastic vial. The pH accuracy was within ± 0.015 and ± 0.022 for the 4.0 and 7.0 standards, respectively. The pH precision was calculated as 0.9% and 0.8%, for the 4.0 and 7.0 standards, respectively (Appendix Table D.1).

The residual fluid remaining in the Teflon vessel was then filtered by using a 10-20 ml Nalgene syringe to inject the fluid through a 0.45-μm Nalgene cellulose acetate filter and into a pre-cleaned 30-ml Nalgene bottle (cleaning procedures of new Nalgene bottle shown in Appendix A2). The filtered solution was then acidified with 3% by volume high-purity nitric acid to dissolve any possible solid residuals and to prevent any mineral precipitation. These acidified fluids were saved for Inducted Coupled Plasma–Optical Emission Spectrometry (ICP-OES) analysis.

1.4.6 Inducted Coupled Plasma–Optical Emission Spectrometry (ICP-OES) Analysis. Solutions collected from the HTP corrosion tests were diluted to collect a sufficient amount of solution for analysis by ICP-OES. The obtained analytical results were multiplied by the appropriate dilution fraction to obtain the actual concentration in ppm (mg/kg). A standard solution of 100 ppm Si, Fe, Ca, Mg, Na, K, Al, and Mn was prepared from the original 1000 ppm commercial standards, and then diluted to 100, 10, 1, and 0.1 ppm standard solutions for analysis.

The accuracy and precision of both 1 and 10 ppm standards (except the precision at 1 ppm standard for Si, Mn, and Al; and the accuracy of Ca) were better than 2.5% for all fluids that collected for the analyses with KEW1-1, KEW2-1, KEW5-1, KEW3-2, KEW4-2, POT2, POT5-1, POT6, POT8-2, POT4, CFSP4, BAY3, and L'ANSE1 samples. The accuracy of both 1 ppm standard and 10 ppm standard was ranged between 2.6% (for both Si and Na at 1 ppm standard) and 8.8% (for Fe at 1 ppm standard) for all

fluids samples collected during SF, SH, AG, DUL, GHB, and GHC sample analyses. Meanwhile, the precision was better than 1.5%. The leachate fluids that were collected from experiments with Poersch#1, KS and Eischeid #1, IA samples showed an accuracy at 1 ppm standard better than 2.9% (except Si, which was 4.7%). Meanwhile, the accuracy at 10 ppm standard ranged between 1.9% (for Si) and 7.41% (for Mg). The precision of both 1 and 10 ppm standards were better than 1.5%. All samples that collected during the core flooding experiment had an accuracy at 1ppm standard between 1.0% (for Al) and 10.5% (for Fe), and the accuracy at 10 ppm standard was between 2.7% (for Mg) and 8.1% (for Al). The precision at 1 ppm standard was between 5.7% (for Al) and 11.2% (for K). Finally, the accuracy (except Mg) was better than 4.5% for all leachate fluids that collected from T1 to T16, MO, CR, and 50°C samples. The precision was better than 1.37% at 1 ppm and 10 ppm standards (Appendix Table D.7).

1.4.7 Weathering Simulation of Minerals. Minerals representing Goldich (1938) reaction series were selected for testing using the HPT test procedure. These minerals were represented by a collection of olivine, amphibole-hornblende, pyroxene-augite, Ca-rich plagioclase, Na-rich plagioclase, orthoclase, and quartz minerals from the Missouri School of Mines Mineral Museum. The mineral samples were crushed and sieved to collect the -200 mesh fraction to increase the surface area and the reactivity rate. A leachate solution with a pH of 3.78 was prepared from a concentrated nitric acid to simulate the minimum pH that could be achieved at a maximum dissociation of CO_2 in water. Nitric acid was used rather than carbonic acid because nitric acid is not volatilized to a gaseous phase upon the periodic opening of the vessels for pH analysis. About 0.2 gram of sample was added to a 200 ml of the leachate solution for each experiment and left at room temperature in closed polyethylene vial. The pH of the leachate solution were checked periodically (for about 19 weeks) to monitor the exchange of nH^+ by any metal cations (e.g., Na^+, K^+, Ca^{2+}, Mg^{2+}, Fe^{2+} etc.) present in the mineral's chemical composition. The rapid pH increase associated with a higher cation exchange capacity indicates a potential for CO_3^{2-} ions to complex with and precipitate carbonate minerals by bonding with alkaline earth, transition metal, and/or alkali components released from the minerals.

1.4.8 Scanning Electron Microscopy (SEM). The reacted samples were mounted on 9.5 mm-specimen aluminum mount and coated for SEM microanalysis using gold/palladium (Au/Pd). The coated samples were examined with a Hitachi S570 LaB6 Scanning Electron Microscope (SEM) and/or Hitachi S4700 SEM to help characterize and identify any carbonate and other mineral phases that could have been precipitated, as well as image any dissolution features. Energy dispersive spectroscopy (EDS) was used in conjunction with the SEM to provide semi-quantitative elemental compositions of any prospective mineral phases.

1.4.9 Geochemical Modeling. The results of the experimental ICP-OES, pH, Eh, etc. analyses were used to estimate the saturation status of the chemical species in the solutions. The USGS PHREEQC^{TM} version 3 geochemical modeling software was used to estimate the saturation indices of the minerals ($SI_{mineral}$). The input data were generated using the Web-PHREEQC of aqueous geochemical modeling, which is available on this website: (http://www.ndsu.nodak.edu/webphreeq/). The physical and environmental input data includes the pH (floating and fixed options), oxidation state (Volt), temperature (°C), solution density at T and P (g/cm^3), log partial pressure of O_2 (log pO_2 in bars), and log partial pressure of CO_2 (pCO_2 in bars). The partial pressure of gases was calculated from the equation:

$$P_{\text{gas}} = \left(\frac{\text{Concentration of gas}}{\text{Total volume of gases}}\right) \times \text{pressure (bar)}$$

The pressure were estimated using Parr^{TM} 4848 reactor controller with an attached pressure gage for the same relative proportions of solid, water, and dry ice that was used in Parr^{TM}4749 general purpose reactor. The calculated pressure from the Parr^{TM} 4848 reactor controller ranged from between 69 and 71 bar. The pressures of the reactor vessels were controlled by the converted CO_2 solid to gaseous phases. The partial pressure of the O_2 was 14.7 bar assuming that the atmospheric concentration of O_2 is 21%. Giammar et al., (2005) were estimated the free CO_2 gaseous phase from this equation:

$$m_{CO_{2(free)}} = \left(V_{reactor} - \frac{m_{water}}{\rho_{water\ (P,T)}} - \frac{m_{rock}}{\rho_{rock}}\right) \times \rho_{CO_2}(P,T)$$

Where *m* is mass in gram, V is volume, and ρ is density in g/cm^3.

The volume of the reactor is 23 cm^3 and the volume of water used was 10 cm^3. The densities of the CO_2 and H_2O at 90°C were measured using the online conversion calculator: http://www.peacesoftware.de/einigewerte/einigewerte_e.html. The densities of rocks were estimated to be 2.8 g/cm^3 for the low porosity Oronto Group, and 2.0 for the higher porosities BAY sandstone samples (quartz sandstone with 25% porosity). The molal concentration of Inorganic Dissolved Carbon (DIC) was determined using the method of Duan and Sun (2003), which is available as online conversion at: http://calc.kledi.ac.cn/Pages/Solubility.aspx.

The chemical input data included the results of the ICP-OES chemical analysis of each individual sample in ppm. All input data used for the PHREEQC™ model runs is provided in the Appendix A.4. The pH of the input data was using the "floating" value which represents the charge balance of the total species provided in the chemical data input. The Eh of the solution was converted to *p*e, which is a function of Eh as in this equation:

$$Pe = \frac{F}{2.303RT} Eh$$

Where F is Faraday's constant, R is ideal gas constant, and T is temperature in °K.

1.4.10 Core Flooding Experiments and Porosity-Permeability Determinations. Core samples were prepared with an approximately one inch diameter (r) and 2 inch length (L), using a universal diamond core drilling bit with 1.1 inch inside diameter, and water-based Isomet Buehler™ saw. The total volume of the samples (V_t) was determined from this equation:

$$V_t = \pi \times r^2 \times L$$

The samples were dried at 45°C overnight and then weighed to the nearest 0.01 g to determine the dry weight (W_d). The samples were vacuum flooded with deionized water, and then weighted to determine their saturated weight (W_s). Then Φ (porosity) was estimated from this formula:

$$\emptyset = \frac{W_s - W_d}{V_t} \times 100$$

A core flooding apparatus system was prepared (see Figure 1.13) according to the methodology presented by Wellman et al., (2003). An artificial leachant solution of pH 3.7-3.8 (close to the pH of deionized water saturated with CO_2 at atmospheric pressure) was prepared by diluting a 67-70% nitric acid source with deionized water. The samples were prepared as follows: Core cutting a one inch diameter rock cylinder to between 0.55 to 1.25 inches in length. The rock sample was then glued into an Acrylic tube wall hosting the sample using a viscous, insoluble epoxy with a rubber ring inserted between the sample and acrylic tube to prevent any leakage, and to ensure that all flow will be through the sample pores and/or fractures. The fluid pump and the tubing were washed with deionized water to reduce the contamination from NaCl brine, which often adheres to the vessel walls from previous runs. The core holder could tolerate a maximum pressure of 500 psi, thus, the samples were chosen for testing that had either 1) a fair amount of porosity and/or a large percentage of calcite cement (e.g., KEW3-1 with 8.9% porosity; 10.0% calcite cement); 2) fair porosity and low calcite cement (Poersch#1, 11,061.5′, well sample with 7.8% porosity); or 3) high porosity and low calcite cement (BAY2 with 22.1% porosity and 0% calcite cement). Some low porosity samples were also tested, but these tests had to be terminated early because they exceeded the 500 psi-limit of the testing apparatus.

The initial permeability of the core flooded samples was compared with the final to determine whether or not flooding with acidified fluids had any effect on the sample reservoir properties. The initial and final permeability was estimated by comparing the onset backpressure (immediately after the pressure stabilization) and the final backpressure at the end of the test cycle. A steady flow backpressure through the sample indicated the pore opening was not affected by the fluid acidification or the pore openings

have stabilized following initial dissolution. Meanwhile, the non-steady flow represented either a pressure decrease resulting from the widening of the pore openings (i.e. porosity and permeability increases) or a pressure decrease through the destruction of the pore space by authigenic clay precipitation or particle blockage of restricted pores.

Solution blank samples were collected from the syringe pump (wash sample) as a background check so that any potential contamination from previous runs could be identified (the core flooding apparatus has many experimental users, some whom test samples with NaCl brine fluids). Periodic samples of the effluent fluid were collected during the experiments for pH, alkalinity, and ICP-OES chemical analysis. The final sample was collected from the core holder apparatus, just above the sample, at the end of the testing, to reveal the actual chemical composition of the leachant fluid prior to its passing through the core sample (influent).

1.4.11 CO_2 Generated During the Calcite Dissolution. Eight experiments using an average of 0.1021±0.0031 grams of calcite were conducted by completely digested calcite grains in a 5% HCl in a closed system to measure the volume of CO_2 gas produced at atmospheric pressure. The experiment apparatus composed of conical flask, graded cylinder, rubber tubes, and rubber bung (Figure 1.14). At the pre-test setting the calcite was completely attached to the rubber bung, the rubber tubing opened, and the water level in both right and lift graded cylinders are equal. At the onset of the experiment the rubber tubing were connected carefully and the calcite grain was dropped into the 5% HCl. The volume of the CO_2 generated during the dissolution of the calcite grain was measured from the water volume difference (DV) in both the right and the left graded cylinders, and then compared to the stoichiometrical calculations.

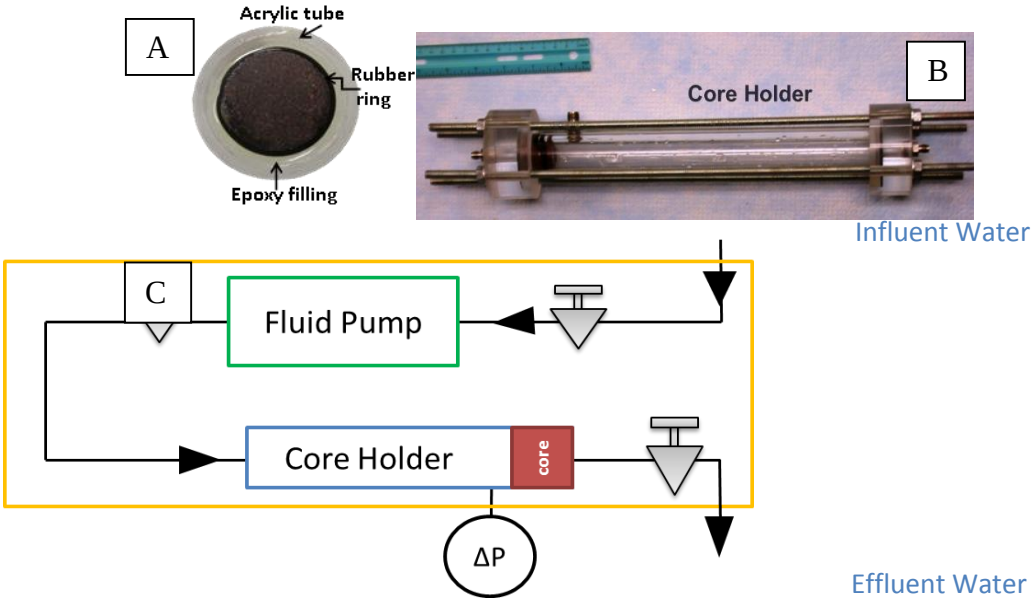

Figure 1.13 Photograph and schematic diagram for the core flooding experiment test apparatus. The diameter of the central dark-colored rock core in figure A is 1.1 inches (2.8 cm). The ruler in the top left of figure B is 6" long (15 cm).

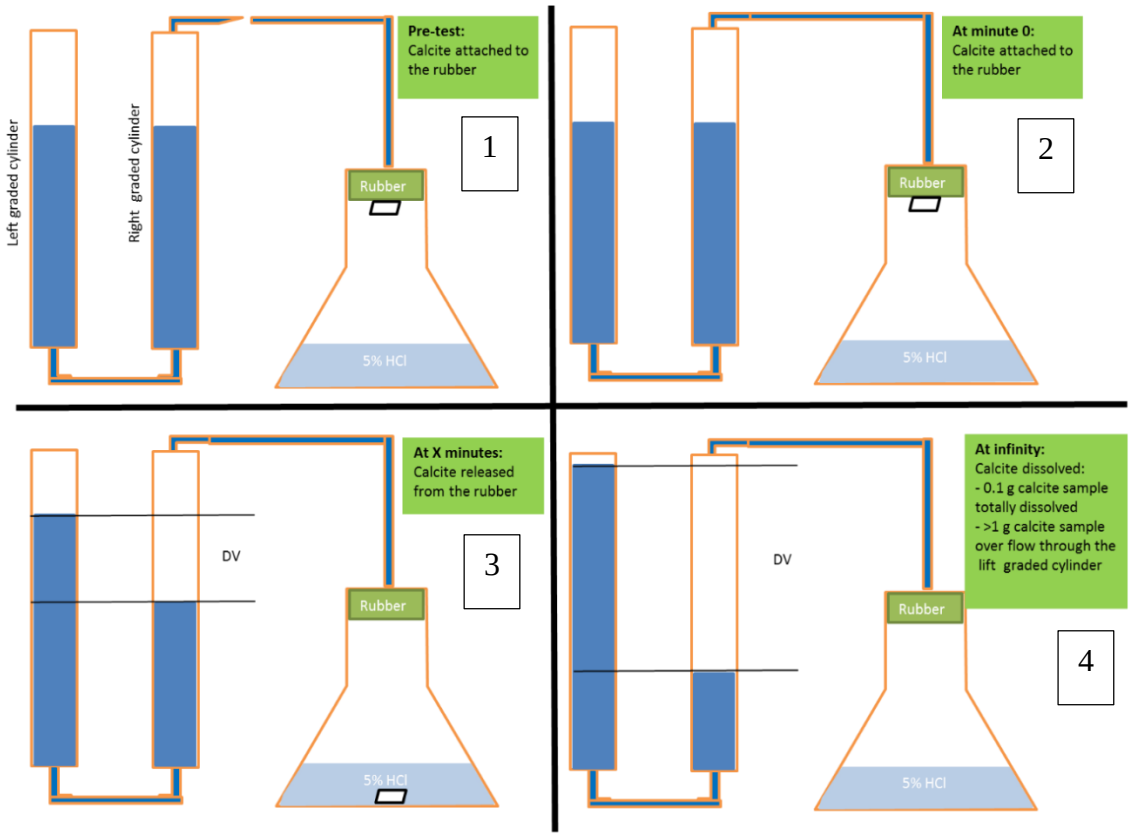

Figure 1.14 Schematic diagram for test apparatus used to calculate the CO_2 generated by the dissolution of calcite grain.

2 LITERATURE REVIEW

2.1 GEOLOGY OF THE MIDCONTINENT RIFT

The Midcontinent Rift (MCR) system in central North America is a Mesoproterozoic (1,115-1,050 Ma) volcanic and sedimentary rock sequence that has formed within a series of rifted basins (Woollard, 1943; Thiel, 1956; King and Zietz, 1971; Behrend et al., 1988; Miller, 2007). Collectively, the intrusive, volcanic, and sedimentary successions associated with the MCR are referred to as the Keweenawan Supergroup. Surface exposures of the rift sequence rocks are commonly encountered in the region around western Lake Superior. Although the configuration of the MCR is largely concealed under Phanerozoic sedimentary successions away from the Lake Superior region, its position can be easily traced in the subsurface through both Bouguer gravity and aeromagnetic surveys, as illustrated in Figure 2.1. The MCR originally developed as a triple junction rift system (Ojakangas et al., 2001). The southwestern MCR arm reaches a minimum of 1,300 km from the center of Lake Superior to Kansas. The southeastern arm stretches from Michigan to Ohio, approximately 700 km, and its geophysical signature terminates against the Grenville orogenic front. The Lake Nipigon dike and sill province, north of Lake Superior, is considered to be the third failed arm.

2.1.1 Tectonic Development of MCR. The development of MCR began as a result of extensional stresses (Green, 1983; Cannon and Hinze, 1992; Paces and Miller, 1993; Cannon, 1994). The initial extension phase began as a triple junction at Lake Superior associated with mantle plume and crustal thinning. The first period of sedimentation following the initiation of rifting and basinal subsidence is represented by the Nopeming Formation in Minnesota and other stratigraphically equivalent units around Lake Superior (Green, 1982b). The Nopeming Formation is mature quartz-rich sandstone with basal pebbly horizons deposited in a braided river environment (Ojakangas and Morey, 1982). Later, a thick, reversed and normal polarity, series of tholeiitic volcanic flows filled the central axis along the rift to form a huge lava plateau that was incised and interlayered with minor clastic infill (Green, 1982b). When this volcanic activity ceased, well-developed grabens were established as a result of the volcanic rock load and the

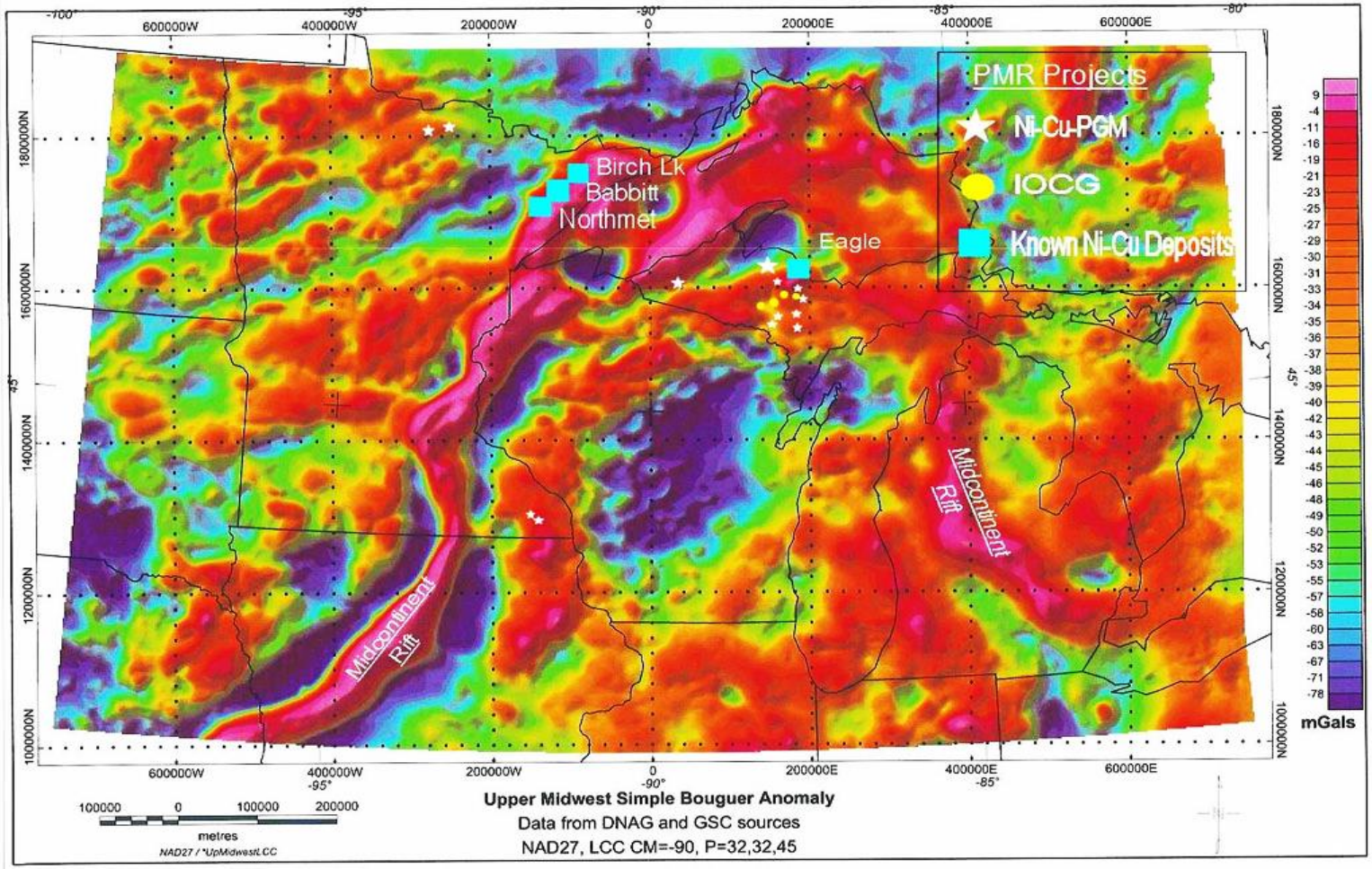

Figure 2.1 Bouguer gravity anomaly map of north-central United States shows the location of the MCR. That location can be traced from its higher anomaly of volcanic rocks and lower anomaly of the sedimentary rocks in Minnesota, Wisconsin, and northern Iowa (Stein et al., 2011).

thermal subsidence followed the hot spot abatement. Subsequently, a fining upward prograding wedge of the Copper Harbor Conglomerate was deposited, and this was in turn followed by the deposition of broad lacustrine siltstone-shale deposits known as the Nonesuch Formation. The facies of the Nonesuch Formation coarsened upward due to the reduction of the subsidence rate. Finally, extensive fluvial deposits of the Freda Formation spread over the previous units (Anderson, 1990).

Compression stresses began when the Freda Formation was being deposited due to the initiation of the Grenville orogenic event along the eastern seaboard of the paleo-North American Continent (Cannon, 1994). The central grabens of the various segments of the MCR were converted into present day horsts, and the vast majority of the Oronto Group was eroded wherever it was exposed at the top of these horst structures. Reworked fluvial deposits of the Orienta Formation sandstone and its stratigraphic equivalents were deposited at the horst flanks with a higher maturity level than that of the older Oronto clastics (Anderson, 1990). The uppermost units (Devil Island and Chequamegon Formations) were deposited as reworked sediments derived from eroded remnants of previous formations. Extensive reworking has produced chemically mature sediments up to the point where quartz arenite is apparent in many of these units, covering even the central horsts (Ojakangas and Morey, 1982).

2.1.2 Structural Elements of the Rift. The basement of the MCR is comprised from five Pre-Keewenawan terranes. The Archean Greenstone-Granite Orogenic Terrane (3.0 – 2.7 Ga) and Minnesota Gneiss-Migmatite Terrane [>3.6 Ga; Hoffman (1989)] located to the north and separated by the Great Lake Tectonic Zone (GLTZ). The Penokean Volcanic Belt Proterozoic Terrane (1.86–1.8 Ga) separated from Minnesota Terrane by Penokean Suture Zone (PSZ) to the north and from the Central Plains Orogenic Belt (1.8-1.7 Ga) to the south and west by Fayette Structural Zone (FSZ), and Central Plains Suture Zone (CPSZ), respectively. The Mazatzal Orogenic Belt (1.65-1.62 Ga) bounded by Mazatzal Suture Zone (MSZ) and Central Missouri Tectonic Zone (CMTZ) as illustrated in Figure 2.2

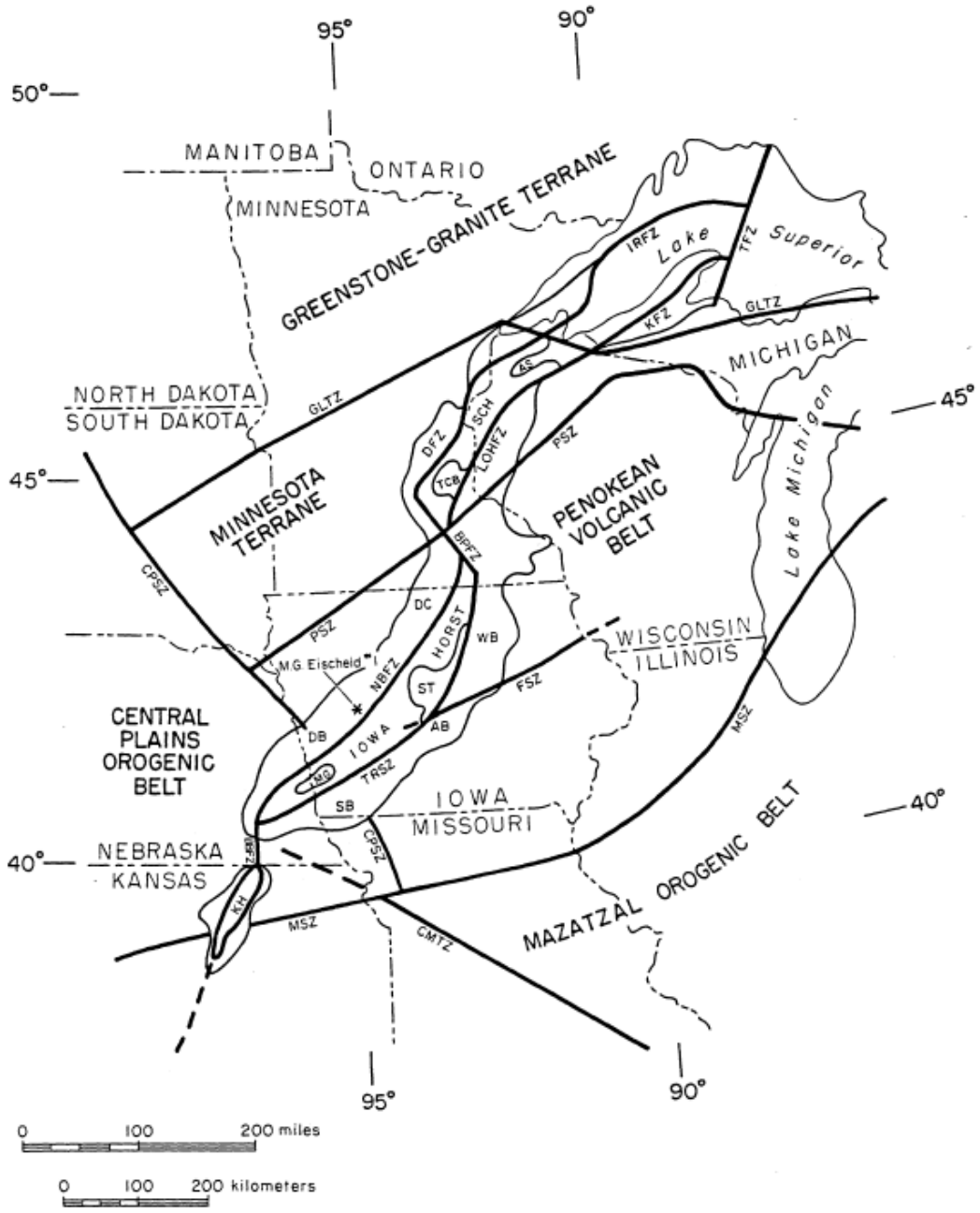

Figure 2.2 The main structural elements of the western arm of MCR. Legend: Thiel Fault Zone (TFZ), Isle Royale Fault Zone (IRFZ), Keweenaw Fault Zone (KFZ), Douglas Fault Zone (DFZ), Lake Owen-Hastings Fault Zone (LOHFZ), Belle Plaine Fault Zone (BPFZ), Northern Boundary Fault Zone (NBFZ), Thurman-Redfield Structural Zone (TRSZ), Big Blue Fault Zone (BBFZ), St. Croix Horst (SCH), Kansas Horst (KH), Defiance Basin (DB), Duncan Basin (DC), Shenandoah Basin (SB), Ankeny Basin (AB), Wellsburg Basin (WB), Twin City Basin (TCB), Ashland Syncline (AS), Stratford Basin (ST), Mineola Graben (MG), Great Lake Tectonic Zone (GLTZ), Penokean Suture Zone (PSZ), Fayette Structural Zone (FSZ), Mazatzal Suture Zone (MSZ), Central Missouri Tectonic Zone (CMTZ), Central Plains Suture Zone (CPSZ) (Anderson, 1990).

The known extent of the western arm of MCR is composed of four segments that separated by accommodation structures, as illustrated in Figure 2.2 (Anderson, 1990; Dickas and Mudrey, 1997). Dickas and Mudrey (1997) have segregated the continuum of the western and eastern arms into five zones: the Kansas, Iowa, Superior, Mackinaw, and Maumee Zones, based upon four accommodation structures that are visible as offsets in the geophysical trends of the MCR.

The Lake Superior Zone is composed of a central horst that bounded by the Keweenawan Fault Zone (KFZ) to the south, the Isle Royale Fault Zone (IRFZ) to the northeast, the Thiel Fault Zone (TFZ) to the east, and the Belle Plaine Fault Zone (BPFZ) to the south. The Superior Zone was further subdivided into four segments (the Manitou, Ontonagon, Brule, and Chicago units) separated by second order accommodation structures. The seismic cross section of Lake Superior units shows a thickening of the each one of the second order units in opposite direction to the next unit (Dickas and Mudrey, 1997). The Minnesota part of Lake Superior Zone is characterized by a central horst, known as St Croix Horst (SCH), which is bounded by the Douglas Fault Zone (DFZ) to the northeast, the Lake Owen-Hastings Fault Zone (LOHFZ) to the southeast. The Keweenawan sediments are flanking St. Croix horst. These sediments are preserved in both the Ashland syncline and the Twin City basin (Anderson, 1990).

The Iowa Zone is composed of the Iowa Horst, which is bounded by the Northern Boundary Fault Zone (NBFZ) to the north, the Thurman-Redfield Structural Zone (TRSZ) to the southeast, the Belle Plaine Fault Zone (BPFZ) to the north, and the Big Blue Fault Zone (BBFZ) in Nebraska (Anderson, 1990). The clastic infill of Iowa Zone is preserved in seven sedimentary basins that flank and overly the central horsts. The sedimentary basins include the Wellsburg basin (WB), Ankeny basin (AB), and Shenandoah basin (SB) to the south of the central horst, the Duncan basin (DC) and Defiance basin (DB) to the north of central horsts, and the Mineola Graben (MG) and Stratford basin (SB) on the central horst.

The Kansas Zone is the smallest segment of the MCR western arm. It is flanked, primarily, by clastic infill, and bounded by reverse faults (Anderson, 1990; Dickas and

Mudrey, 1997). Based on the geophysical seismic, magnetic, and gravitational surveys of the MCR sector in Kansas, the rift created a significant thrust fault that caused the older volcanic sequences to overly the younger sedimentary sequences (Behrend et al., 1988; Woelk and Hinze, 1991). Interpretations of the seismic and the gravitational profiles revealed a reverse fault that bounds the central horst with an angle between 15° and 75°. The younger extensional sediments were overlain by the older volcanic rocks, and the younger compressional sediments were overlain by older extensional sediments (Anderson, 1990). The juxtaposition of the normally impermeable-natured early-rift stage extensional rocks on top of the relatively permeable late stage sedimentary rocks could provide a possible sedimentary-structural trap for any physical sequestration of carbon dioxide.

The Eastern arm is represented by Mackinaw and Maumee Zones. Both of the eastern arm zones are not as well characterized as the western arm of the MCR. Neither of these zones were investigated in the present study.

2.1.3 Rift Stratigraphy. The overall Mesoproterozoic volcanic-sedimentary succession of MCR is known as Keweenawan Supergroup, however, the overall MCR stratigraphic nomenclature varies from one state to another as indicated in Figure 1.2. The pre-Keweenawan volcanism is represented by the Sibley Group (1,340 Ma) Bessemer, Powder Mill, Nopeming, and Puckwunge clastics (Green, 1982b; Ojakangas and Morey, 1982). The rift volcanic rocks are typically composed of normally polarized volcanic rocks, including Portage Lake volcanics, Chengwatana volcanics, and the North Shore Volcanic Group (Miller, 2007; Ojakangas and Morey, 1982). These volcanics unconformably overlie the Powder Mill Group and its equivalent stratigraphic units. The post-volcanic groups are clastic dominated sedimentary rock comprised of an extensional phase group (the Oronto Group). This group is unconformably overlain by the Bayfield Group and its stratigraphic equivalents, which were deposited during a compressive tectonic phase associated with the Grenville Orogeny.

2.1.3.1 Volcanic and intrusive rift sequence. These units are, primarily, comprised of both reversed and normal polarity volcanic rocks exposed around the

present-day Lake Superior shoreline. The volcanism in MCR developed in four stages during late Mesoproterozoic Stenian period (Miller, 2007), as the following:

1) The early magmatic stage (1,115 – 1,107 Ma) is reversed polarized and composed of mafic to ultra-mafic olivine-rich igneous rocks directly sourced from a mantle plume (Miller, 2007). A Significant crustal contamination has affected the initial composition of the magma especially during the early magmatic stage.
2) The latent magmatic stage (1,107-1,102 Ma) is normal to reversed polarized, with felsic volcanism associated with slight vertical subsidence (Miller, 2007). The vertical subsidence allowed the high-energy sedimentary facies like Power Mill Group and Bessemer Quartzite, MI and WI to accumulate within the rift on pre-volcanic basement rocks. The Davis Hill Conglomerate is another stratigraphic unit that underlies the Portage Lake Volcanics in WI (Ojakangas and Morey, 1982). The likely stratigraphic equivalents to these clastics are Puckwunge and Nopeming Formations in MI.
3) The main magmatic stage (1,102 – 1,092 Ma) is a normal polarized magma event with a dominantly bimodal composition. This eruption began with tholeiitic basalt and felsic compositions, which were followed by olivine picritic basalt and lesser tholeiitic basalt, with locally abundant episodes of felsic volcanism (Miller, 2007). The main volcanic sequences erupted during the main magmatic stage represented by Berglund Group (i.e. Portage and Porcupine Volcanics; WI and MI), Chengwatana Volcanics (MN), and the North Shore Volcanic Group (MN).
4) The late magmatic stage (1,094 – 1,086 Ma) is period of normal polarized, felsic volcanism that developed when the rate of extension decreased. This sequence may be locally associated with interstratified alluvial, fluvial, and lacustrine deposits of the Oronto Group (e.g., “The Traps”; Miller, 2007).

2.1.3.2 Oronto Group and stratigraphic equivalents. Both Craddock (1972) and White (1972) have described the Oronto Group in west central Wisconsin as being comprised of three formations deposited in stratigraphic succession: the Copper Harbor Conglomerate, the Nonesuch Formation, and the Freda Formation sandstone (see Figure 1.2). The Lower Red Clastic Group (Units B, C, and D; in Iowa) and the Solar Church Formations (in Minnesota) are the stratigraphic equivalents of the Oronto Group. This

group was deposited as a result of the rift's thermal subsidence directly following the main magmatic stage. Ojakangas and Morey (1982) noted that the paleocurrent direction was toward the central grabens during the extensional phase of the rift development. The oldest unit (the Copper Harbor Conglomerate) is a fining upward sequence of immature conglomerate, lithofeldspathic sandstone, and siltstone. This formation is approximately 2,130 m (7,000 ft) thick in its most developed sections (Daniels, 1982). Its lower portion is interpreted to be alluvial fan deposits, whereas the uppermost portion, which is a coarse-grained sandstone, is interpreted to be a meandering stream deposit (Elmore, 1984).

The Nonesuch Formation is a 75-210 m (250-700 ft) gray-to-black organic-rich shale and shaly siltstone. Elmore et al., (1989) and Suszek (1997) described the depositional environment of this formation, based on their bacterial and algal contents as a restricted lacustrine deposit. Pratt et al., (1991), based on its similarity to organic molecules in marine fossils, suggested that the Nonesuch Formation has an estuarine origin. The Freda sandstone is the upper-most unit in the Oronto Group. This unit has approximately 3,500 m (1,150 ft) of cyclic sandstone, siltstone, and mudstone deposited in a braided river system (Daniels, 1982).

In the Iowa sector, the Lower Red Clastic Group (equivalent to the Oronto Group) is designated the units of B, C, and D (Witzke, 1990). The primary difference between the Unit B and the Copper Harbor Conglomerate is the dominace of the sandy quartzose facies in Unit B compared to a conglomertic dominated Copper Harbor Conglomerate (Daniels, 1982; Ludvigson et al., 1990). Lithologically and sedimentologically, Units C and D in the Iowa sector are similar to the Nonesuch and Freda Formations, respectivly (Anderson, 1990; Witzke, 1990). The Unit C is characterized by the abundant siltstone and shale. Also, the vein-filling calcite, pore-filling cement calcite, and structural deformation is abundant in the Unit C. The Unit D is a sandstone dominated fining upward facies.

2.1.3.3 Bayfield Group and stratigraphic equivalents. The Bayfield Group sandstones are exposed exclusively in the Bayfield Peninsula area of Wisconsin. These

unconformably overlie the Oronto Group and are stratigraphically equivalent to the Jacobsville Formation in Michigan and the Fond du Lac-Hinkley Formation in Minnesota, (Figure 1.2; Ojakangas and Morey, 1982). The Bayfield Group is divided into three units: the Orienta, the Devils Island, and the Chequamegon Formations. In contrast to the Oronto Group, the Bayfield Group is associated with the Grenville-aged compressional phase that followed initial rift development. The paleocurrent directions indicate movement of sediment primarily, away from the central horst. The oldest Bayfield unit is the Orienta sandstone, which constitutes 575 m (1,880 ft) of red-lithofeldspathic sandstone-siltstone-shale facies. The fining upward nature of the succession is evidence of its fluvial origin (Anderson, 1990; Ojakangas et al., 2001). The Orienta sandstone is conformably overlain by the Devils Island sandstone, which is the thinnest stratigraphic unit (~90 m). Lithologically, the Devils Island sandstone is a buff colored facies formed primarily when the less mature facies from the Orienta sandstone and the older Oronto Group were reworked by eolian and lacustrine processes (Tryhorn and Ojakangas, 1972). The Chequamegon sandstone, the youngest unit, lies conformably on the underlying Devils Island sandstone. Sandstones in the Chequamegon Formation can be described as a mature, porous, and permeable quartz-arenites with a total thickness of approximately 150 m (Ojakangas, 1986).

Witzke (1990) assigned, informally, Unit E, Unit F, and Unit G for the Upper Red Clastics (Bayfield Equevalent) of M.G. Eischeied #1 well in Iowa, and the Unit H was added later by Anderson (1990). The Unit H is a light redish-brown very course-grained sandstone with some micaceous shaley to sandy siltstone (Anderson, 1990). Unit G is red-brown fine to medium-grained sandstone intercallated with minor shale and siltstone. Unit F cycles between very fine to fine grained gray sandstone and red and brownish siltstone and shale. Unit E is sandstone-dominated unit with minor lithic fragments. The Upper and Lower Red Clastic sequence displays a significant difference in stratigraphic correlation when compared to the Bayfield and Oronto Groups (Ojakangas and Morey, 1982; Ojakangas, 1986; Ludvigson et al., 1990; Ojakangas et al., 2001). The mineral and textural maturation of the Upper Red Clastic Group is less than that for the Lower Red

Clastic Group. That is not the case for the Oronto Group and Bayfield Group, where is the upper most Bayfield Group, is more mature compared with the Oronto Group.

2.1.3.4 Overlying Phanerozoic sequence. The Phanerozoic Sequence unconformably overlies the Keweenawan Supergroup, and much of the Phanerozoic cover has been completely eroded away in most portions of the Lake Superior region during more recent erosional cycles (Anderson, 1990; Anderson, 1992; Anderson, 1997). About 914 m (~ 3,000 ft) of Phanerozoic sediments are preserved in the penetrated section of the Eischied #1 well, in Iowa. The Cambrian sequence constitutes approximately 196 m (640 ft) of, primarily, glauconitic arenaceous to argillaceous facies sandstone, similar to that found in the Mt. Simon-Lamotte Formation rocks and some carbonate intervals (i.e. the Bonneterre Formation). The Ordovician succession consists of approximately 230 m (760 ft) of carbonate-dominated facies, with slight contributions from marine shale. The Devonian Sequence unconformably overlies the Ordovician strata with approximately 130 m (430 ft) of open marine carbonate transgressive-regressive cycles. Both the Mississippian and the Pennsylvanian Sequences are, primarily, dominated by marine carbonate to shale. They also contain some non-marine coal, sandstone, and shale of Cherokee Formation. The Dakota Formation (Cretaceous) unconformably overlies the Cherokee Formation with, primarily, quartz arenite sandstone. The lower parts of Cherokee Formation represent an important productive aquifer. The Quaternary deposits are represented by 70 m (235 ft) of glacial till units.

2.1.4 Rift Economic Mineralization. Copper mineralization in the MCR (i.e. in Copper County in the Upper Michigan peninsula) represents one of the largest native copper districts in the world. The early mining oparations started in 1845 and peaked between 1945 and 1968 with more than 5 billion kg of pure copper being produced (Crane, 1929; White, 1968; Weege and Pollack, 1971). About 58.5% of the copper deposits occurred in the vessicular and brecciated Portage Lake basaltic flow tops. The interflow conglomeritc facies and the veins in the fractured basalts hosted the remaining 39.5% and 2% of native copper, respectively. Other regions such as the White Pines district recorded mostly copper sulfide mineralization as the copper bearing fluids interacted with sulfide-rich sediments of the Nonesuch Formation. The structural

development of the rift is a critical factor controlling the timing and location of the mineral precipitation. The compressional stresses, associated with the Grenville Orogeny, allowed or forced the hydrothermal fluids to rise through the the activated faults. Bornhorst et al., (1988) and Cannon et al., (1993) determined the ages of copper mineralization to 1,060±20 Ma, which is contemperaneous with post-Freada Formation stages. Also, the tilting of the volcanic rocks occurred before the metamorphism (low temperature-pressure burial metamorphism to zeolite and pumpellite metamorphic facies) and associated with the copper mineralization (Livnat, 1983). Copper deposition was associated with a significant hydrothermal alteration of the volvanic lava flows (i.e. K-feldspar, epidote, lamountite, calcite, quartz, and chlorite) and within the conglomerate facies [i.e. K-feldspar, epidote, quartz, and calcite; (Bornhorst, 1997; Bornhorst et al., 1988)]. Formation of extensive calcite vein and pore filling deposits represent an ancient analog process that can potentially be repeated as a mechanism to sequester anthropogenic CO_2 in these deposits as mineral phases.

2.2 ADVANTAGEOUS FEATURES OF THE MCR FOR CO_2 SEQUESTRATION

The aquifer attributes that make geologic formations attractive targets for mineral sequestration were summarized by (Bachu, 2000, 2002). These attributes were applied to the MCR rocks, and the best attributes are represented by the following:

1. The disposal depth will need to exceed 760 m (2,500 ft; Thorleifson, 2008). The Bayfield clastics were distributed as wedge-like basins at the eastern and western flanks of the St. Croix Horst in Minnesota and Wisconsin, with a 6 km-thickness maximum. The underlying Oronto Group fills in the St Croix Horst with more than one km of sediment in the Ashland Syncline and Twin City Basin. On the eastern and western flanks of the St. Croix Horst, the Oronto Group exceeds 6 km in depth. In the drilled well of the Defiance Basin the top of the Bayfield Group is more than 914 m (3,000 ft). The injected CO_2 should be kept in its supercritical phase at these depths (Buchanan and McCauley, 1987; Doughty and Pruess, 2004). The density of supercritical CO_2 phase is between 0.32 kg/m^3 and 0.27 kg/m^3, so the space taken by supercritical CO_2 is much less compared with both gaseous phase CO_2 and liquid phases. Also, the diffusion rate of supercritical

CO_2, especially through the tiny pore spaces, is faster than both gaseous and liquid phases. Finally, that depth of sequestration may reduce the risk of contaminating drinking water aquifers that occur at shallower depths.

2. The Copper Harbor Conglomerate is stratigraphically overlain by an effective geologic seal represented by about 250 m (820 ft) of Nonesuch Formation siltstones and shales.

3. The faulted margins of the basins could create structural traps. Moreover, in some portions of the rift sequence, the Bayfield Group and its subsurface stratigraphic equivalents are overlain by volcanic sequences and the Oronto Group sediments due to the thrust nature of the rift segment faults (e.g., Kansas well; Berendsen et al., 1988). This stratigraphic juxtaposition represents a highly attractive target for anthropogenic carbon sequestration.

4. Most of these units, particularly the Oronto Group, contain an abundance of silicate, oxide and carbonate minerals that are enriched with Ca^{2+}, Mg^{2+}, Fe^{2+} and other cations that could play an important role in long-term mineral sequestration.

5. The proximal distribution of stationary coal-fired power plants and the existing of pipe line infrastructure will allow for a reduced cost of CO_2 transport associated with sequestration in the MCR. (Thorleifson, 2008; Figure 2.3). The average distance to transport liquid-phase CO_2 through the pipeline without CO_2 recompression stations is about 300 km, and a maximum distance is 1,600 km to ensure a beneficial economic sequestration.

6. The Bayfield Group and its stratigraphic equivalent units are the most permeable units (Thorleifson, 2008). The majority of this sequence is unconformably overlain by permeable Cambrian sandstones and carbonate rock.

7. The exploration activities associated with mineral and petroleum resources within the MCR sedimentary rocks are minimal and thus there is a low drilling density intruding the sequence (Thorleifson, 2008).

2.3 CHALLENGES FOR CO_2 SEQUESTRATION IN MCR

Thorleifson et al., (2008) introduced a comprehensive report about the sequestration potential for the MCR in Minnesota. These authors report that the MCR

clastics were suitable for deep CO_2 sequestration due to their great sequestration depth, availability of an effective cap sequence seal, availability of the faulted traps, abundance of Ca^{2+}-, Mg^{2+}-, and Fe^{2+}-rich minerals, and the suitable distribution of the pipelines net relative to the major power plants. But there were also many challenges for CO_2 sequestration discussed in the report, including:

1. The generally impermeable nature of the lower part of the rift clastics, namely Oronto Group and its equivalent stratigraphic units, could hinder CO_2 injection and storage volume. The geophysical investigations determined that the seismic velocity (Vp) of the clastics deeper than one km was more than 12,000 ft/sec (3.6 km/sec) suggesting a low-overall permeability for the sequence. Thorleifson et al., (2008) noted, however, that there was a general lack of direct measurement data for porosity and permeability in the Minnesota MCR strata as well as for MCR sequences encountered in other states. Porosity estimates of the MCR clastics in all drilled pore holes are summarized in Table 2.1. The main porosity reduction was reported to result from the precipitation of an authigenic, fine grain matrix, clays, iron oxides, and calcite between the detrital grains. However, studies of the Kansas section drill cored have revealed local zones of higher porosity (up to 15% porosity in a 22' thick stratigraphic succession; Berendsen et al., 1987).

2. The complexity associated with the tectonic history of the MCR clastics is assumed to be a disadvantage due to leakage concerns through the fault plane(s). These structures can, however, also produce structural traps along fault planes and domes as they often do in hydrocarbon occurrences.

3. The most porous and permeable aquifers (i.e. the Bayfield Group) are characterized by low Ca^{2+}, Mg^{2+}, and Fe^{2+} contents that reduce the potential to induce carbonate mineralization (present study).

4. Finally, although the Bayfield Group and its equivalent stratigraphic units have a wide lateral extent, the Bayfield Group is overlain by the Phanerozoic calcareous, arenaceous, or argillaceous deposits (i.e. as seen in Section 2.1.3.4). These deposits will have variable effectiveness as seal rocks, but generally will be poor seals as evidenced by widespread formation of the basal Mt. Simon Formation sandstone.

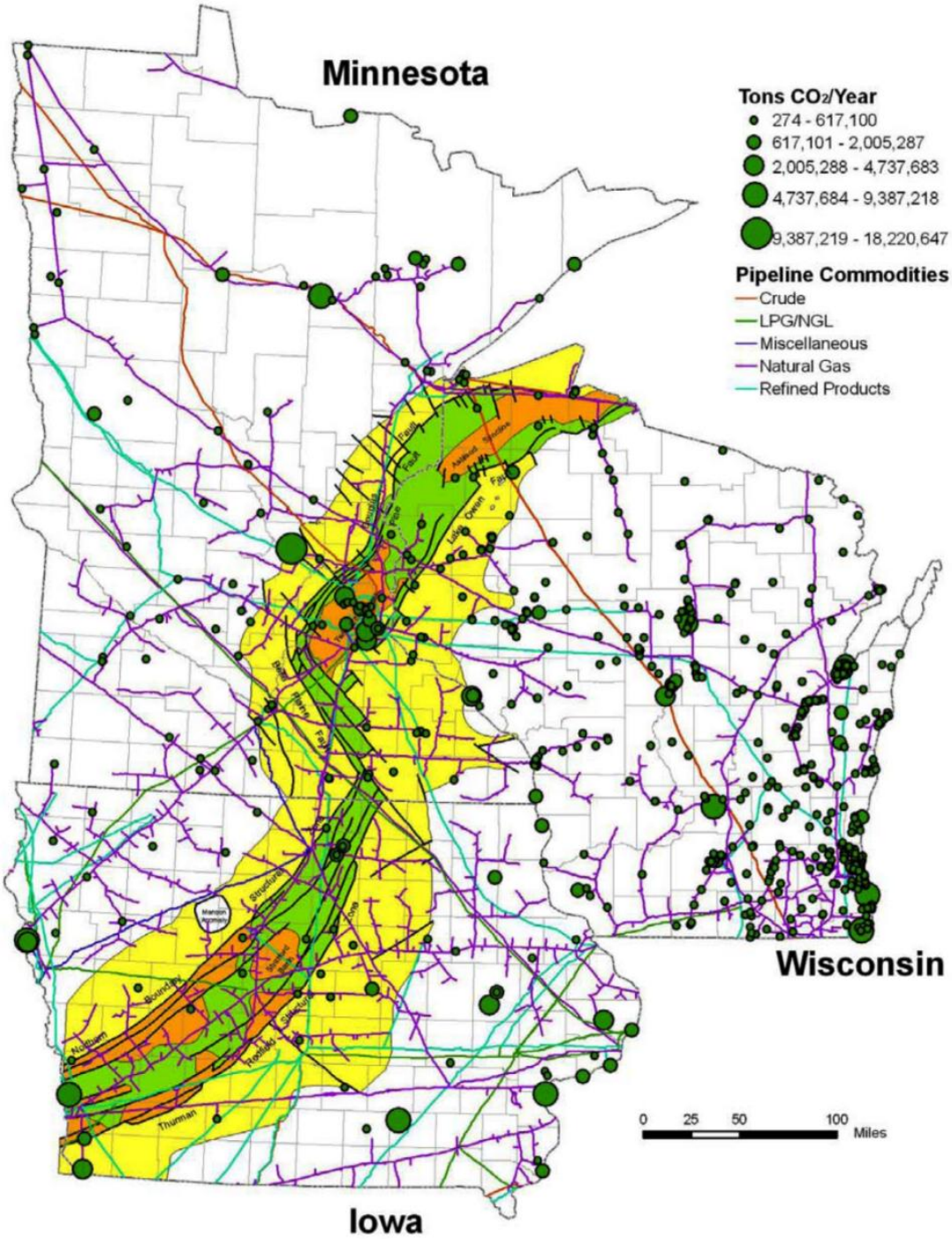

Figure 2.3 Stationary power plants, pipeline distribution, and the extent of MCR sediments in IA, MN, and WI. The yellow color represents the presence of the Bayfield Group at the top of the sequence, whereas the orange color represents the Oronto Group at the top. The stratigraphy in the immediate vicinity of the Lake Superior region is exposed at the surface, whereas stratigraphic units approximately 50 or more miles southwest from Duluth, Minnesota are buried beneath Phanerozoic and/or younger sediments (Thorleifson, 2008).

2.4 GEOCHEMISTRY OF CARBONATE MINERAL PRECIPITATION

Many factors can play an important factor for carbonate mineral equilibria, including pH, temperature, pressure, mineralization inhibitors (e.g., phosphate, organic matter, and sulfate), and alkalinity (Walter, 1986; Morse and Mackenzie, 1990; Morse, 2003). The most important factors in carbonate equilibria are the ionic activity of the respective mineral constituents, solution pH, and pCO_2. The equilibrium of carbonate minerals is defined by the stoichiometric solubility product (equilibrium constant; K_{sp}). The saturation index of the carbonate minerals can be expressed as:

$$\mathrm{SI}_{mineral} = \log\left[\frac{m_{Me^{2+}} \times m_{CO_3^{2-}}}{K_{sp}}\right]$$

($SI_{mineral}$) is Saturation Index, (Me^{2+}) is any two-plus valance state cation like Ca^{2+}, (K_{sp}) is the equilibrium constant solubility product, and (*m)* is molal concentration in mole/kg. If SI = 0, the solution will be in equilibrium with the respective solid mineral phase; if SI < 0, the solution will be undersaturated; and if SI > 0, the solution will be supersaturated and will eventually precipitate carbonate minerals (Morse, 2003; Morse and Mackenzie, 1990).

The relative amounts of dissolved inorganic carbon species (H_2CO_3, HCO_3^-, and CO_3^{2-}) concentrations vary as a function of pH of the solution. For instance, at low pH (> 6.4), the carbonic acid is the dominate specie, and the carbonate minerals are difficult to form due to high solubilities. At intermediate pH (between 6.4 and 10.3), bicarbonate ion is the dominant specie, and dissolution/precipitation may occur. When the pH is high, > 10.3, the carbonate ion is the dominant specie with a high probability of carbonate precipitation (Figure 2.4). The overall cumulative abundance of all carbonate species will also generally increase with solution pH in open systems.

Table 2.1 Summary of measured porosity (P) and permeability (K) within deep drilling boreholes from the MCR clastics. Data is segregated into method used for collection including laboratory flooding tests, downhole geophysics, and thin-section point counting. Depths for measurement intervals are noted. Compiled by Thorleifson (2008).

Borehole	St. Amour # 1-29 Test and Hickey Creek	Terra-Patrick #7-22	M.G. Eischeid #1	Ray McCallum A1	Rhinehart Farms A1	Texaco Poersch #1
Location	Michigan, Upper Peninsula	NW Wisconsin	West-Central Iowa	Southwest Iowa	Southwest Iowa	Northeast Kansas
Porosity-Permeability by Laboratory Flood Test			8835-15,106′ 27 samples P = 1.9% avg., range 0.3-3.8% 26 samples K ≈10^{-3} m^2 avg.	3014′ P = 8.87% K = 10^{-3}	3069-3080′ 4 samples P = 9.1% avg., range 6.3-11.6% K = 10^{-2} m^2 avg. range 10^{-2} to 10^{-4} m^2	7.9% (this study)
Permeability Measurement by Downhole Geophysics		2500-3000′ P = 7-10% 3000-4500′ P ≈0-10% >4500′ P = 3% avg.	>11,450′ P = 2.3% avg., range 1-6%			~4500-11,296′ P = <2% exception at 11,055′ where 22′ thick interval with P ≤ 15%
Permeability by Thin Section Point Count	2500 to > 4500′ P = 0.6% avg., range 0-3.3%		2500-3000′ P = 6% 3000-4500′ P = 1-2.5% 4500-15,000′ P = 0-1%			

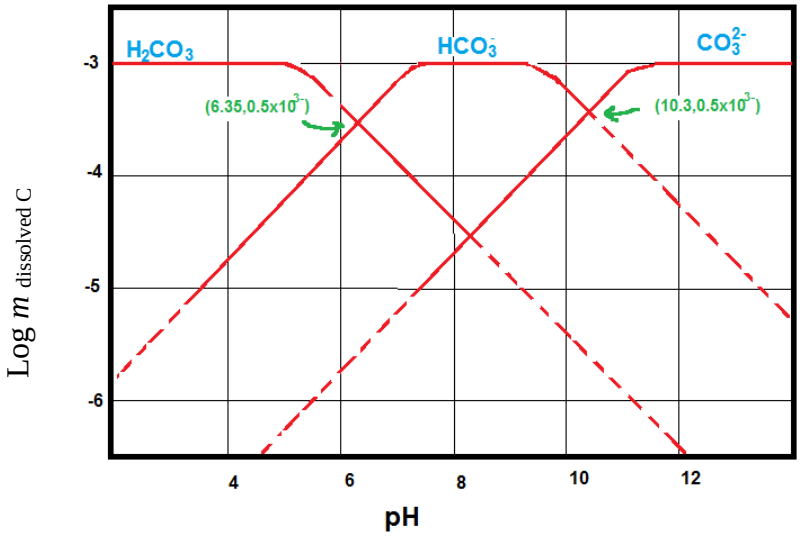

Figure 2.4 The molal concentration of the common carbonate species as a function of pH change of the solution in a closed system.

Carbonate minerals are generally divided into either the calcite group (a six-fold coordinated structure in the hexagonal crystal system) or aragonite group (a nine-fold coordinate structure in the orthorhombic crystal system (Railsback, 2011). Large radii cations (e.g., Sr^{2+}, Pb^{2+}, and Ba^{2+}) fit easily into the nine-fold structure (around the oxygen in the carbonate anion), while low radii cations (i.e. Mg^{2+}, Co^{2+}, Zn^{2+}, Fe^{2+}, Mn^{2+}, and Cd^{2+}) preferentially fill the six-fold structure. Only Ca^{2+} can is found in appreciable quantities as end-member minerals in both the six-fold (calcite) and nine-fold structures (aragonite). The most soluble carbonate minerals are recognized at the end members of each group (Figure 2.5) and thus are also less favored, thermodynamically.

In general, Ca^{2+} and Mg^{2+} are the most common cations found during carbonate mineralization due to their abundance in the Earth's crust and the relatively insoluble nature of the minerals that contain them. Therefore, these cations are the most important cation in any geochemical investigation regarding mineral sequestration. Calcium carbonate is commonly represented by the calcite and aragonite polymorphs. Vaterite and hydrated calcium carbonate (i.e. monohydrocalcite and ikaite) are less common. The

hydrated calcium carbonate minerals are the most soluble, followed by vaterite, aragonite, and then calcite.

The fourth most common component identified in sea water (1.3% of total sea salts) is Mg^{2+} (Pytkowicz, 1965; Berner, 1975). This component, however, is rarely precipitated directly from sea water as pure Mg-carbonate (magnesite; $MgCO_3$) or dolomite [$Ca,Mg(CO_3)_2$] due to the high hydration energy of Mg^{2+} with water molecules. The higher attraction of Mg^{2+} to the water molecules is a result of the higher ionic potential (ionic charge/ionic radii) of Mg^{2+}.

The substitution of Ca^{2+} by Mg^{2+} in calcite is common. Therefore, calcite is grouped into low Mg-calcite (Mg< 4 mole %), high Mg-calcite (Mg >11 mole %), plus disordered and ordered dolomite [Mg =50 mole %; (Boggild, 1930)]. The solubility of high Mg-calcite is greater than that of low Mg-calcite as illustrated in Figure 2.5 and Table 2.2 (Morse and Mackenzie, 1990). Dolomite is occasionally found precipitating in modern hypersaline lagoons and sabkhas (Bush, 1973; Machel and Mountjoy, 1986), but more commonly occurs during Mg-metasomatism of limestone. The solubility of Mg-bearing calcite increases proportionally with the Mg-content. The solubility of dolomite increases as the crystallinity of dolomite decreases.

Potassium and sodium are each likely to be less important in most geologic mineral sequestration processes because their respective potential carbonate mineral phases are more soluble in natural systems. Dawsonite [$(NaAlCO_3(OH)_2$] precipitation was predicted to occur in computer simulations of sequestration environments (Ferrante et al., 1976; Zerai et al., 2006; Bénézeth et al., 2007). However, it is rarely recognized in natural systems or even the lab syntheses from NaCl, $NaHCO_3$, and Al minerals (Kaszuba et al., 2005). Dawsonite exists naturally as pore filing cement in Shepwa basin, Yemen (Warden, 2006), extreme alkaline-sodium-rich Eocene Green River Formation, CO, WY, UT (Smith and Milton, 1966), and in weathered nepheline syenite of alluvial deposits, Tanzania (Hey, 1963). Potassium-calcium carbonate minerals exist as the rare and unstable dimorphs of butschliite and fairchildite [$(K_2Ca(CO_3)_3$], and these minerals are found in wood ash of fir and hemlock trees (Olanders and Steenari, 1995).

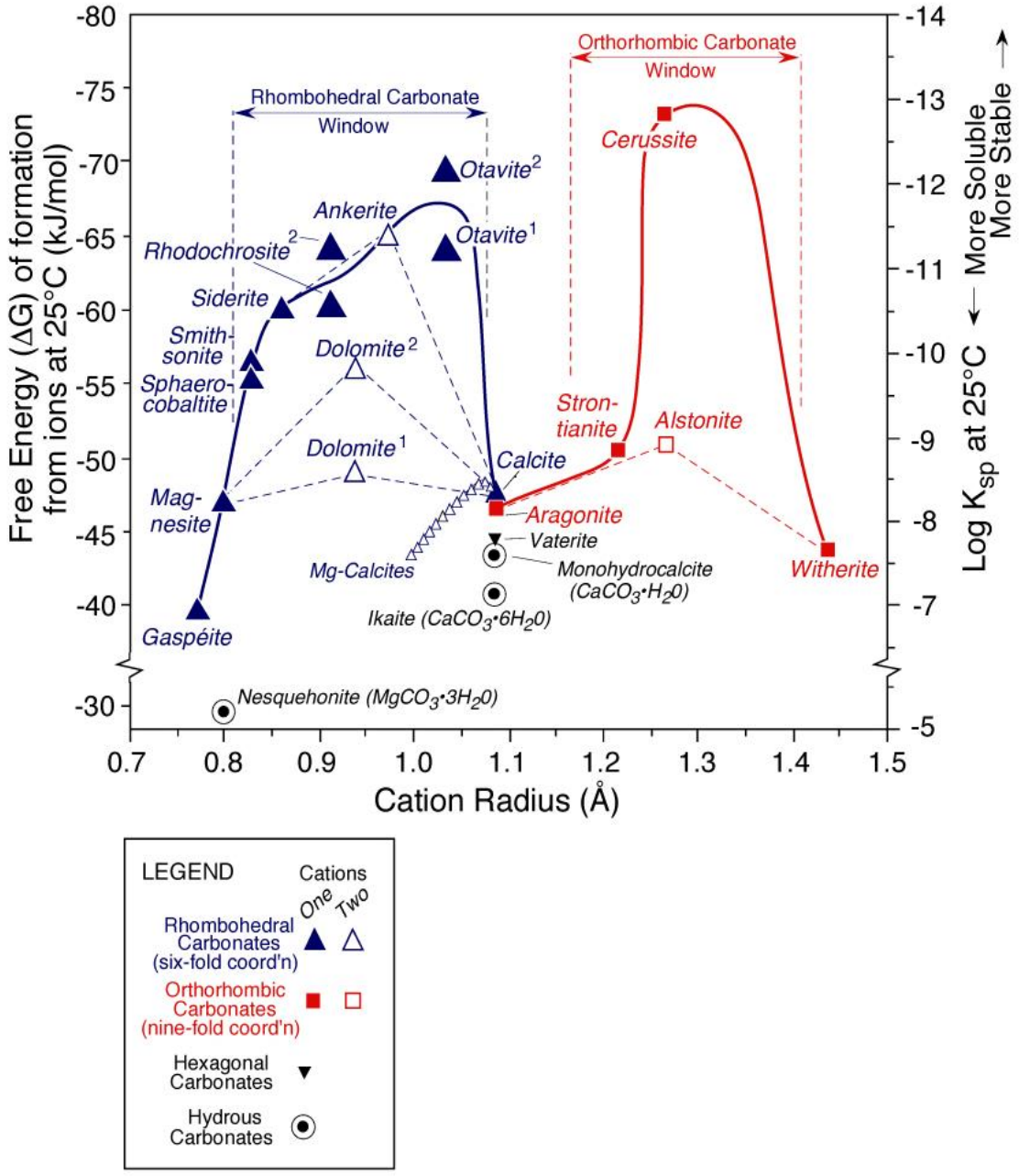

Figure 2.5 Summary of carbonate minerals based on their type, solubility, and free energy of formation. After Railsback, (1999; 2011).

Table 2.2 Summary of calcium and magnesium carbonate minerals with their corresponding solubility products (K_{sp}) and occurrence. After Railsback, (2011).

Mineral	K_{sp} (25°C)	Sedimentary Occurrence
Ikaite ($CaCO_3.6H_2O$)	7.94×10^{-8}	Rare. Cold-water marine tufas.
Monohydrocalcite ($CaCO_3.6H_2O$)	3.16×10^{-8} to 2.5×10^{-8}	Rare. One cave; low-temperature deposits; lakes
Vaterite ($CaCO_3$)	1.25×10^{-8}	Rare. Biomineralization
Aragonite ($CaCO_3$)	5.01×10^{-9}	Common. Marine and terrestrial sediments
Low Mg Calcite ($Mg_{0.04}Ca_{0.96}CO_3$)	3.16×10^{-9}	Some biomineralization; dominate in ancient limestone
Medium Mg Calcite ($Mg_{0.04-0.12}Ca_{0.96-0.88}CO_3$)	3.16×10^{-9} to 5.01×10^{-9}	Marine sediments via biomineralization and precipitation
High Mg Calcite ($Mg_{0.12-0.25}Ca_{0.88-0.75}CO_3$)	5.01×10^{-9} to 3.16×10^{-8}	Marine sediments via biomineralization and precipitation
Disordered Dolomite ($Mg_{0.5}Ca_{0.5}CO_3$)	$\sim6.30\times10^{-9}$	
Ordered Dolomite ($Mg_{0.5}Ca_{0.5}CO_3$)	$\sim2.51\times10^{-9}$	Ancient limestone and dolomite
Magnesite ($MgCO_3$)	$\sim6.3\times10^{-9}$	Lake sediments (as an alteration of hydromagnesite
Barringtonite [$MgCO_3.2H_2O$]		
Nesquehonite ($MgCO_3.3H_2O$)	$\sim1.00\times10^{-5}$	Diagenesis product in lake sediments
Lansfordite ($MgCO_3.5H_2O$)		
Artinite ($Mg_2(CO_3)(OH)_2.3H_2O$)		
Hydromagnesite ($Mg_5(CO_3)_4(OH)_2.4H_2O$)		Ephemeral Lake; Speleothems
Dypingite ($Mg_5(CO_3)_4(OH)_2.6H_2O$)		

The sulfate ion (SO_4^{2-}) is reported to be an inhibitor of both calcite and aragonite precipitation, because Ca^{2+} ions will be consumed to form gypsum ($CaSO_4.2H_2O$; Walter, 1986). Magnesium is a potential inhibitor for calcite formation by adsorption of Mg-hydrated sphere complexes with high dehydration energies on the surface of calcite that inhibit further Ca adsorption (Berner, 1975). Phosphate (PO_4^{3-}) may also influence both calcite and aragonite formation by adsorption on Ca-ions at their surfaces, but PO_4^{3-} mainly is consumed in photosynthesis and metabolism of living organisms, and commonly is found in apatite ($Ca_5(PO_4)_3(OH,Cl,F)$. The Fe^{2+} ion is another inhibitor for

calcite by competition to create siderite ($FeCO_3$), which is another potential phase for mineral sequestration, but iron is commonly is encountered as Fe^{3+} in subsurface oxidized settings as various ferric-oxide, -hydroxide, and mixed oxide-hydroxide phases (Meyer, 1984). Many studies revealed that the chance of mineral sequestration of CO_2 as siderite was increased by Fe_2O_3 reduction, which in turn was caused by the presence of H_2S (Palandri and Kharaka, 2005; Murphy et al., 2011). The sulfide ion will be oxidized spontaneously to sulfate by transferring electrons to the ferric oxide ion, which in turn will be reduced as in the following equations:

$$S^{2-} - 8\ e^- \rightleftharpoons S^{6+}$$
$$8\ Fe^{3+} + 8\ e^- \rightleftharpoons 8\ Fe^{2+}$$
$$H_2S + 6\ H_2O + 4\ Fe_2O_3 + 14\ CO_2 \rightleftharpoons 8\ Fe^{2+} + 14\ HCO_3^- + SO_4^{2-}$$

An effective mineral sequestration process is dependent, primarily, on the dissolution of Ca-, Mg-, and Fe silicate or oxides and/or the presence of significant quantities of these ions in groundwater brines. The rate of dissolution for Ca-, Mg-, and Fe silicate or oxides can be accelerated by increasing the surface area of the host rocks, temperature, and acidification [e.g., organic and carbonic acids accelerate the reaction (Martell et al., 1997; Golubev and Pokrovsky, 2006; Huijgen et al., 2006)]. The most efficient cation source for any carbonate mineralization process is forsterite (5.86 tons to sequester one ton of carbon), followed by serpentine (7.69 tons to sequester one ton of carbon), basaltic glass (8.76 tons to sequester one ton of carbon), wollastonite (9.68 tons to sequester one ton of carbon), and then anorthite [23.1 tons to sequester one ton of carbon (Oelkers et al., 2008)].

In the Earth's oceans, calcite and aragonite are distributed between 40°N and 40°S latitudes, and restricted to < 4 km depth (calcite compensation depth), where these carbonate minerals dissociate to a dissolved compounds. There is inverse relationship between the dissolved CO_2 content and the carbonate mineralization, so, the degasing of $CO_{2(aq)}$ from the water is one of important factors that promotes carbonate mineralization (Ryan, 2014). The degasing or removal of $CO_{2(aq)}$ could be a result of pressure decrease, temperature increase, and/or biologic activity. The solubility product of the carbonate minerals as a function of pressure as the following:

$$K_{cc} = \frac{Me^{2+} \times CO_3^{2-}}{pCO_2}$$

Where: (Kcc) is a solubility product of the carbonate mineral, (pCO_2) partial pressure of CO_2; (Me^{2+}) is any two-plus valance state cation like Ca^{2+}.

The high pressure-temperature conditions applied on carbonate minerals may cause carbonate mineral to lose CO_2 (500°C minimum), and then converted to a calc-silicate minerals (Morse and Mackenzie, 1990). The equilibrium curve between calcite and aragonite indicates that calcite is dominant at high temperature and aragonite at higher pressure settings (Figure 2.6). Also, the aragonite-calcite equilibrium line showed a strong positive relationship between temperature and pressure with slight decrease in the slope at high temperature-pressure setting where the higher stable calcite phases will dominate (Radha and Navrotsky, 2013). Calcite is expected to be the equilibrium stable phase under CO_2 sequestration conditions.

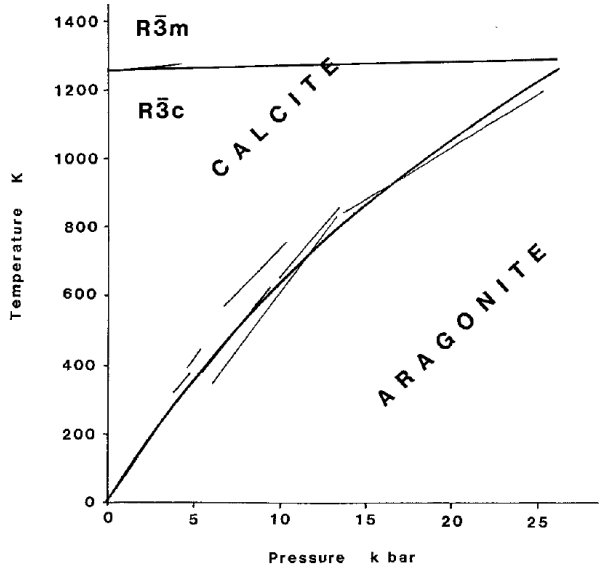

Figure 2.6 Summary of calcite-aragonite temperature-pressure phase equilibrium. R3c and R3m space groups are different calcite phase's transition at 1,240°K. Data compiled by (Radha and Navrotsky, 2013).

3 PETROGRAPHIC AND X-RAY DIFFRACTION ANALYSIS OF THE MIDCONTINENT RIFT ROCKS

Thin-sectioned samples from both Midcontinent Rift clastics around Lake Superior region and deep drilling wells in Iowa and Kansas were studied using a Nikon 2000 polarized microscope. The petrographic investigations were performed to identify the mineral composition, fabric, porosity, grain form, roundness, contact, surface texture, matrix, cementation, and diagenetic features.

The intergranular primary porosity was significantly reduced by carbonate cementation during the evolution of the MCR basin. So, the term *original porosity* is used to describe the syn-depositional and fractured porosity (i.e. including pore space that was present in the rock samples plus pore space and fractures filled now with calcite cement). The term *residual porosity* is used to describe the petrographically identified porosity left over after all the cementation event(s). The term *dissolution porosity* used to describe the porosity created after the H_2CO_3 or HNO_3 acid attack on the calcite cement in corrosion experiments performed as a part of this study.

3.1 ORONTO GROUP AND STRATIGRAPHIC EQUIVALENTS

3.1.1 Copper Harbor Conglomerate and its equivalent stratigraphic units.

All Copper Harbor Conglomerate samples represent the finer grained sand-dominated lenses and have been selectively sampled to avoid larger pebble to boulder-sized clasts. These analyses are thus representative of only the finer grained portions of this sedimentary sequence.

3.1.1.1 Eagle River Falls (KEW1-1 and KEW1-3 samples). The KEW1-1 sample, collected from the Copper Harbor Conglomerate, has a Quartz-Feldspar-Lithic (Q-F-L) ratio of $Q_{10}F_{13}L_{77}$ (Figure 3.1, Figure 3.2, and Table 3.1). Consequently, based on Folk et al., (1970) classification of sandstone, this sample was classified as a lithic-arenite. The plagioclase to K-feldspar ratio was about 1.5:1 and 2.4:1 for KEW1-1 and

KEW1-3, respectively. The total matrix content of KEW1-1 was about 8.5%, and semiquantitative XRD analysis showed that chlorite phyllosilicate mineral [$(Mg,Fe)_3(Si,Al)_4O_{10}$-$(OH)_2$.$(Mg,Fe)_3(OH)_6$] dominated this clay-sized matrix material (~76%) with minor components of illite [$K_{1.5\text{-}1.0}Al_4(Si_{6.5\text{-}7.0},Al_{1.5\text{-}1.0}O_{20})(OH)_4$; (~19%)], and smectite (~5%). The non-clay minerals in the matrix-sized materials were represented by quartz (SiO_2), K-feldspar, and calcite (Figure 3.3 and Table 3.2).

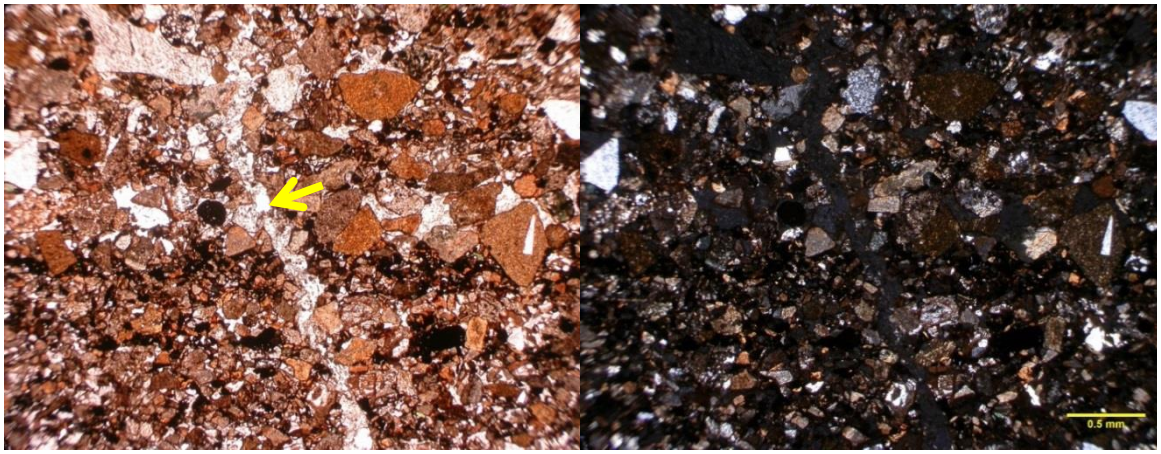

Figure 3.1. Thin section of CHC sample (KEW1-1).The figure is showing poorly sorted nature and fracture vein-filled by calcite "arrow". Plane-polarized light (left) and cross-polarized light (right).

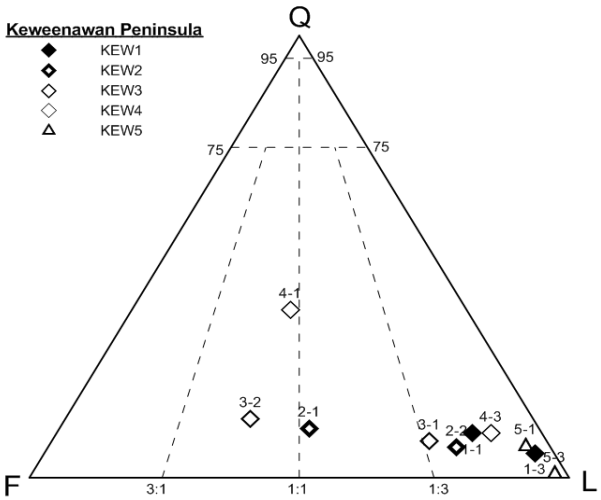

Figure 3.2. Triangular plot of quartz, feldspar, and lithic fragments based on point counting of 300 points per thin section for samples collected from Keweenawan Peninsula, MI.

Table 3.1. Percentage of mineral components of surface outcrop samples from Oronto Group. Analysis is based upon 300-270 counts per thin section sample. Qz is quartz, Plag is plagioclase feldspar, K-spr is K-feldspar, L is lithic fragment, OQ is opaque mineral oxides, M is mica, HM is heavy minerals, Ep is epidote, Uk is unknown, SM is silty matrix, CM is clayey matrix, IO is iron oxide cement, CCe is carbonate cement, and P is residual porosity. CHC is Copper Harbor Conglomerate. * reflects porosities where samples displayed evidence of grain dislodgement "plucking". CHC is Copper Harbor Conglomerate.

Sample ID	UNIT	Qz	Plag	K-spr	L	OQ	M	HM	Ep	Uk	SM	CM	IO	CCe	P	Total
KEW1-1	CHC	6.0	4.6	3.0	45.7	4.0	0.3	0.3	0.3	0.0	8.3	0.3	10.3	15.9	1.0	100.0
KEW1-3	CHC	3.7	1.7	0.7	60.9	0.0	0.3	0.0	0.0	0.3	0.0	0.0	0.7	16.7	15.0*	100.0
KEW2-1	CHC	7.0	10.6	15.0	28.8	1.7	0.0	0.3	0.3	1.3	5.6	0.3	8.3	14.6	5.3	100.0
KEW2-2	CHC	5.0	6.7	6.0	55.3	0.7	0.0	0.0	0.3	0.3	5.0	1.0	8.3	8.7	2.7	100.0
KEW3-1	CHC	5.0	6.1	7.1	42.5	3.9	0.0	0.0	0.4	1.1	6.4	1.8	6.4	10.4	8.9	100.0
KEW3-2	CHC	5.7	11.4	11.1	14.8	7.0	0.0	0.3	0.3	3.0	17.4	7.0	6.7	11.1	4.0	100.0
KEW4-1	CHC	23.8	12.8	7.7	18.5	2.3	0.0	0.0	0.0	0.7	11.7	4.7	6.7	8.1	3.0	100.0
KEW4-3	CHC	5.4	2.7	2.3	43.0	4.7	0.0	0.0	0.0	0.3	2.0	1.3	4.7	23.5	10.1*	100.0
KEW5-1	CHC	5.3	2.3	1.0	65.7	0.7	0.0	0.3	0.3	0.0	3.7	1.0	2.3	14.7	2.7	100.0
KEW5-3	CHC	0.7	1.1	0.7	79.4	0.4	0.0	0.0	0.4	0.0	2.2	1.8	4.8	6.6	1.8	100.0
POT4	Nonesuch	21.1	11.6	8.8	24.0	3.4	1.0	0.0	2.4	0.0	9.0	3.4	12.6	0.3	2.4	100.0
POT5	Nonesuch	28.2	13.0	14.3	32.0	0.7	0.3	0.0	2.4	0.0	0.0	5.7	0.0	0.0	3.4	100.0
POT6	CHC	25.3	18.0	7.8	36.5	4.0	0.4	0.0	2.6	1.1	0.0	1.3	2.2	0.0	0.8	100.0
POT8-1	Freda	28.9	5.3	22.7	32.9	6.8	0.0	0.0	3.4	0.0	0.0	0.0	0.0	0.0	0.0	100.0
POT8-2	Freda	28.4	9.6	17.2	36.1	4.7	0.0	0.0	2.8	0.0	0.0	0.0	0.0	0.0	1.2	100.0
Average		**13.3**	**7.8**	**8.4**	**41.1**	**3.0**	**0.2**	**0.1**	**1.1**	**0.5**	**4.8**	**2.0**	**4.9**	**8.7**	**2.9**	

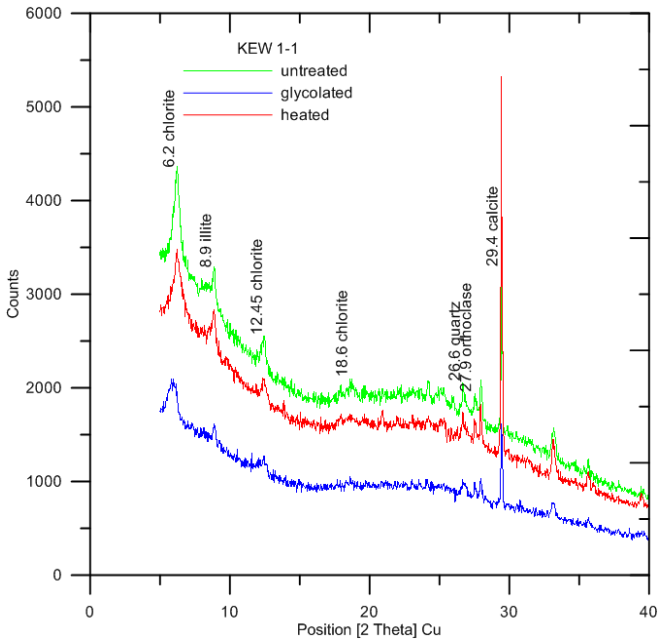

Figure 3.3. X-Ray diffraction spectra of Eagle River Falls KEW1-1 sample. This is showing the peaks for chlorite and illite, as well as quartz, orthoclase, and calcite in the clay-size matrix fraction of the sediments.

The KEW1-3 sample was also collected from Copper Harbor Conglomerate from a primarily, conglomeritic sandstone composition. The compositional Q-F-L ratio of the sample was $Q_{5.5}F_{3.5}L_{91}$ (Figure 3.2 and Figure 3.4; Table 3.1). The other grain components were represented by muscovite [$KAl_2(Si_3Al)O_{10}(OH,F)_2$], epidote [$Ca_2(Al,Fe^{3+})_3Si_3O_{12}(OH)$], and unidentified heavy minerals. The matrix and clay size fraction was dominated by chlorite and some traces of quartz, K-feldspar, and calcite (Table 3.2; Appendix Figure B.1).

A. Post-depositional alteration of Eagle River samples: These processes are including diagenesis, early metamorphism, and hydrothermal alteration. Calcite cementation and compaction were the main post-depositional alteration features recognized in Eagle River samples. The cement was dominated by calcite, which was precipitated as pore-filling and vein-filling minerals (Figure 3.1 and Figure 3.4). Opaque minerals oxides were also present as pore-filling cement and sometimes occurred as a meniscus around the grains. Grain compaction of the sample KEW1-1 resulted in the

formation of concave-convex and line contacts, while the contacts for the KEW1-3 sample varied between float grains and concave-convex contacts (Table 3.3). All of these features tend to decrease the porosity-permeability of the sandstones.

Table 3.2. A summary of the minerals identified by the XRD analysis of the clastics collected from the MCR.

Stratigraphic Unit	Sample ID	Phyllosilicate Minerals					Non-clay Minerals					
		Kaolinite	Chlorite	Smectite	Illite	Zinwaldite	Calcite	Orthoclase	Laumontite	Albite	Dolomite	Quartz
BAYFIELD GP.	BAY2b	x						x				x
	BAY1	x						x				x
	BAY3	x						x				x
Jacobsville Fm	L'ANSE1	x			x			x				x
E Unit	E2-2	x			x					x		x
	E2-3	x			x					x		x
	E2-4	x			x					x		x
Copper Harbor Conglomerate	KEW1-1		x		x		x	x				x
	KEW4-1		x		x		x	x				x
	KEW4-3		x				x	x				x
	KEW1-3		x				x	x				x
	KEW2-1		x				x	x	x			x
	KEW2-2		x				x	x	x			x
	KEW3-2		x				x	x				x
	KEW5-1		x				x	x				x
	KEW5-2		x				x	x				x
Nonesuch Formtion	C2-2		x		x		x			x		x
	C2-3		x		x					x		x
	C2-4		x		x					x		x
	C2-5		x		x		x	x	x			x
Freda Formation	D4-1		x		x		x	x		x		x
	D4-2		x		x		x	x		x		x
	D4-3		x		x		x	x		x		x
	POT8-1		x	x	x		x	x	x			x
	CFSP2		x	x	x				x			x
Texaco Poersch #1 "Unclassified"	5396`		x									x
	5400`		x				x			x		x
	8052.5`		x			x	x			x		x
	8476-8480`		x			x	x			x		x
	10509`		x			x	x			x		x
	10666`		x							x		
	11061.5`		x							x	x	

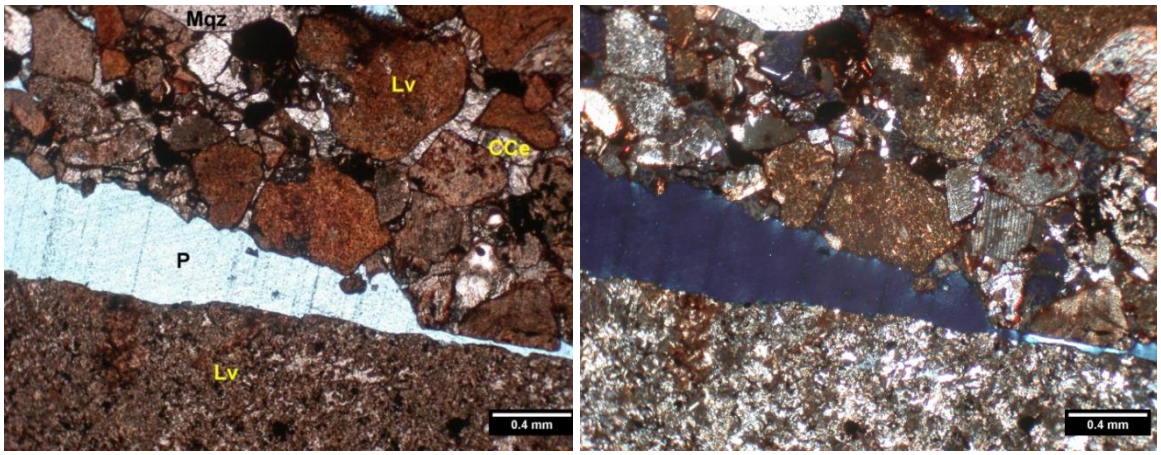

Figure 3.4. Thin section of CHC sample (KEW1-3). The microphotographe is showing poorly sorted conglomeritic sandstone, lithic volcanic "Lv", mono-quartz "Mqz", calcite cement "CCe", and plagioclase "Plag". The large open pore "P" is likely not a primary porosity feature, but rather was produced from "plucking" of grains during the thin section preparation. Plane-polarized light (left) and cross-polarized light (right).

B. Fabric and maturity of Eagle River samples: The grain size of KEW1-1 sample was fine to very fine-grained (Appendix Figure B.22), poorly sorted lithic-arenite, while KEW1-3 was lithic-rudite. The matrix fraction of the KEW1-1 sample constitutes approximately 8.5% of total sample volume. The grains of KEW1-1 sample were dominantly equant, while KEW1-3 grains were elongate. The grain shapes of both samples were sub-angular to sub-rounded grains as seen in Table 3.3. Therefore, this texture could be considered sub-mature.

C. Porosity of Eagle River samples: The residual porosity of Eagle River Falls KEW1-1 sample sandstone was 1%. There were two factors or concerns about correlating the KEW1-3 thin section porosity determinations to the actual porosities of similar units that may be found at sufficient depth for carbon sequestration. The pebbly KEW1-3 sample showed about 15% residual porosity and displayed evidence of grain dislodgement "plucking" or sample fracturing that occurred during the cutting and/or polishing of the thin section samples. In general, this evidence could be noted where the open space pores were simply too large to not have been filled in by sedimentation and compaction processes (see label "P" in Figure 3.4).

Table 3.3 Percentage of grain forms, roundness, contact and surface texture of surface outcrop samples from Oronto Group samples. Analysis is based upon 300 counts per thin section sample. Elg is elongated, Eq is equant, VA is very angular, A is angular, SA is sub-angular, SR is sub-rounded, R is rounded, WR is well rounded, F is fractured contact, S is sutured contact, CC is concave-convex contact, L is line contact, P is point contact, Fl is floated grain, C is corroded surface, Fr is fractured surface, and Po is polished surface.

	Grain form			Roundness						Grain contact						Surface texture		
	Elg - Eq	Elg	Eq	VA	A	SA	SR	R	WR	F	S	CC	L	P	Fl	C	Fr	Po
KEW1-1	6.8	43.2	50.0	0.0	14.6	46.4	31.8	7.3	0.0	1.0	0.5	48.5	27.8	15.5	6.7	35.4	12.5	52.1
KEW1-3	13	50.5	36.5	0.0	10.1	40.7	46.2	2.5	0.5	0.0	13.5	41.5	17.0	3.5	24.5	12.1	4.0	83.9
KEW2-1	4.0	47.5	48.5	0.0	33.5	30.5	27.0	9.0	0.0	2.0	9.6	49.5	22.2	11.6	5.1	35.0	13.5	51.5
KEW2-2	1.8	77.0	21.2	1.3	12.6	22.4	61.0	1.8	0.9	3.6	2.7	25.1	10.3	5.8	52.5	22.9	5.4	71.7
KEW3-1	4.8	39.6	55.6	0.0	27.8	34.8	26.7	10.7	0.0	2.1	9.1	35.3	27.3	19.8	6.4	45.7	7.0	47.3
KEW3-2	0.0	43.6	56.4	0.0	46.6	21.5	18.4	13.5	0.0	4.9	6.7	32.5	32.5	20.9	2.5	49.7	6.7	43.6
KEW4-1	2.0	33.3	64.6	0.0	35.0	22.3	27.9	14.7	0.0	0.5	0.0	36.9	26.3	32.3	4.0	46.0	6.1	48.0
KEW4-3	0.0	46.6	53.4	0.0	31.0	25.3	24.1	19.5	0.0	1.1	1.1	18.9	12.6	35.4	30.9	48.0	0.6	51.4
KEW5-1	2.2	42.3	55.5	0.0	31.0	30.1	33.2	5.8	0.0	2.6	2.6	49.3	25.1	16.3	4.1	15.9	0.0	84.1
KEW5-3	0.4	10.7	88.9	0.0	11.1	7.1	7.1	74.7	0.0	0.0	1.8	4.0	8.4	8.9	76.9	15.1	1.3	83.6
POT4	7.7	30.9	61.4	3.2	16.8	36.1	33.4	10.5	0.0	1.3	2.7	46.8	19.3	20.6	9.3	22.4	19.1	58.5
POT5	3.8	36.9	59.3	0.6	15.1	42.5	28.2	13.6	0.0	0.0	0.3	57.6	29.0	8.6	4.5	31.2	24.2	44.6
POT6	1.5	41.7	56.8	0.0	9.8	21.6	40.6	28.0	0.0	1.6	1.0	48.0	44.9	6.5	5.0	30.8	20.3	48.9
POT8-1	6.1	27.9	66.0	0.0	6.5	24.3	30.2	38.4	0.6	0.0	1.4	53.0	31.2	12.1	2.3	27.9	16.9	55.2
POT8-2	1.6	31.2	57.2	0.0	12.3	22.3	29.8	35.6	0.0	0.0	2.4	57.7	28.0	11.1	0.8	26.8	20.4	52.8

The second caveat in interpreting the origin of the pore space relates to the present group of samples that all being collected from surface outcrops. Surface samples are by nature subjected to modern chemical weathering phenomena and thus may had some alteration of their mineral grain structures. Typically, chemical weathering dissolves mineral grains and thus potentially may increase the amount of pore space. In some areas, however, the deposition or precipitation of relatively insoluble weathering residue material (e.g., iron oxides) may also fill in pore space. However, all Copper Harbor Conglomerate samples were collected from actively eroding river valleys and lake shore locations, environments that will tend to mechanically abrade away chemically weathered material thus minimizing this effect.

3.1.1.2 Baily Creek Falls (KEW2 -1 and KEW2-2 samples). The proportional composition of the major sandstone components were $Q_{11}F_{42.5}L_{46.5}$ for Copper Harbor Conglomerate KEW2-1 sample and $Q_{07}F_{17.5}L_{76}$ for KEW2-2 sample (Figure 3.2, Figure 3.5, and Figure 3.6). Therefore, the KEW2-1 was classified as feldspathic–lithic-arenite and KEW2-2 was classified as lithic-arenite. The plagioclase to K-feldspar ratio was 1:1.4 and 1:1 for KEW2-1 and KEW2-2 samples, respectively. The minor mineral components were epidote, iron oxide(s), and heavy minerals (Table 3.1). The XRD analysis illustrated chlorite as the major clay component and some traces of laumontite [$Ca\ (AlSi_2O_6)_2{,}_4H_2O$; a zeolite mineral], quartz, K-feldspar, and calcite (Table 3.2; Appendix Figures B.2 and B. 3).

A. Post-depositional alteration of Baily Creek falls' samples: The authigenic carbonate and iron oxide pore-filling materials were the dominant cementation agents. A high percentage of concave-convex contacts showed the effect of compaction on these grains (Table 3.3). Also, the fractured quartz grains could reflect the high tectonic stresses that were applied on these rocks during their geologic history.

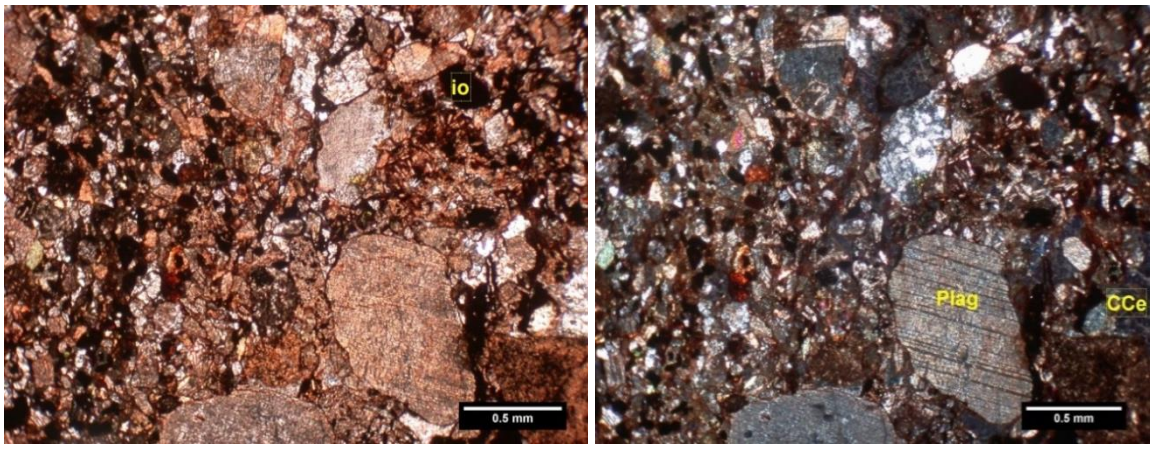

Figure 3.5. Photomicrograph of CHC KEW2-1 sample. The figure is showing poorly sorted grains, plagioclase "Plag" iron oxide "io", and calcite cement "CCe". Plane polarized light image (left) and cross-polarized image (right).

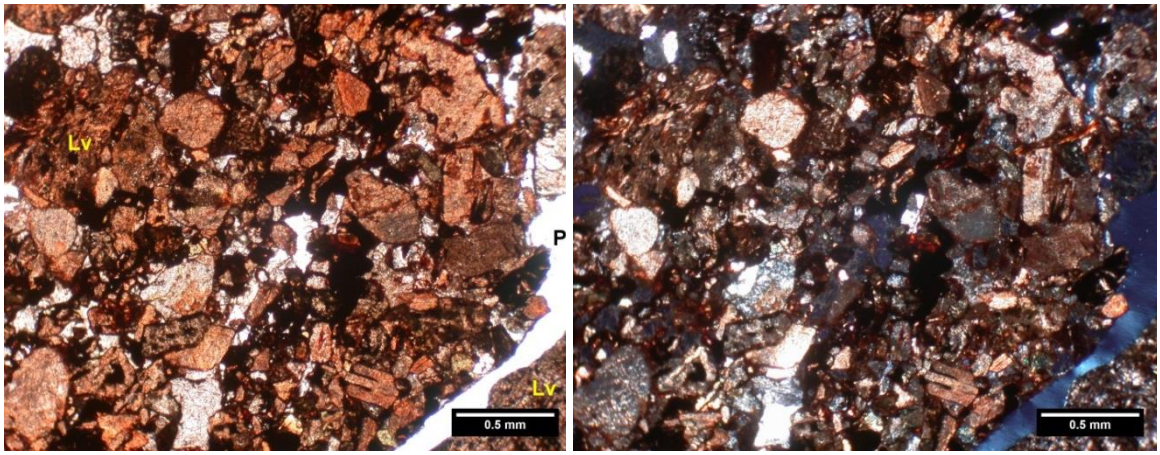

Figure 3.6. Photomicrograph of CHC KEW2-2 sample. The figure is showing poorly sorted grains and lithic volcanic "Lv". The fracture pore space (P) likely resulted during the thin section preparation. Plane polarized light image (left) and cross-polarized image (right).

B. Fabric and maturity of Baily Creek falls' samples: The grain size measurements indicate that the KEW2-1 sample was a very fine to medium-grained-feldspathic-lithic-arenite (Appendix Figure B.23) and KEW2-1 was a lithic-rudite. The silty matrix constitutes approximately 5.0 to 5.6% of the total grain counting volume. The

grain forms were elongate to equant, and the roundness of the grains was angular to sub-angular for KEW2-2 and sub-rounded to sub-angular for KEW1-2 sample as illustrated in Table 3.3. Both of the samples were poorly sorted. Therefore, the KEW2 samples were immature to sub-mature texturally. The original porosity was extensively filled by the calcite cement. The residual porosity ranged between 2.7% and 5.3% for KEW2-2 and KEW2-1 samples, respectively (Table 3.1).

3.1.1.3 Esrey Park (KEW3-1 and KEW3-2 samples). The major grain component of the KEW3-1 sample was represented by $Q_{08}F_{22}L_{70}$, so this sample was designated as lithic-arenite, while the proportional composition of the KEW3-2 sample was $Q_{13}F_{53}L_{34}$ and that classified it as lithic-feldsarenite (Figure 3.2, Figure 3.7, and Figure 3.8). The plagioclase to K-feldspar ratio was 1:1.2 for KEW2-1 sample and 1:1 for KEW3-2 sample. The minor mineral components were represented by iron oxides, heavy minerals (KEW3-2 only), and epidote (Table 3.1). The semiquantitative XRD analysis showed chlorite phyllosilicate mineral and traces of quartz, K-feldspar, and calcite in the major components of the clay-sized matrix material (Table 3.2; Appendix Figures B.4).

A. Post-depositional alteration of Esrey park's samples: The original porosity of the sample was almost completely filled by carbonate cement with contributions of iron oxides as well as another unidentified cement material (Figure 3.7 and Figure 3.8). The contact between the grains were, primarily, convex-concave and line contacts, and this could reflect the compaction pressures affecting these rocks. Additionally, the surface texture of the grains was dominated by corroded feldspar and polished lithic grains, which reflected varied degrees of grain alteration. The KEW3-1 sample had relatively high residual porosity (8.9%) while the KEW3-2 sample had approximately 4.0% residual porosity. The KEW3-1 sample also displayed fractured porosity with fracture width of 0.2 mm, roughly.

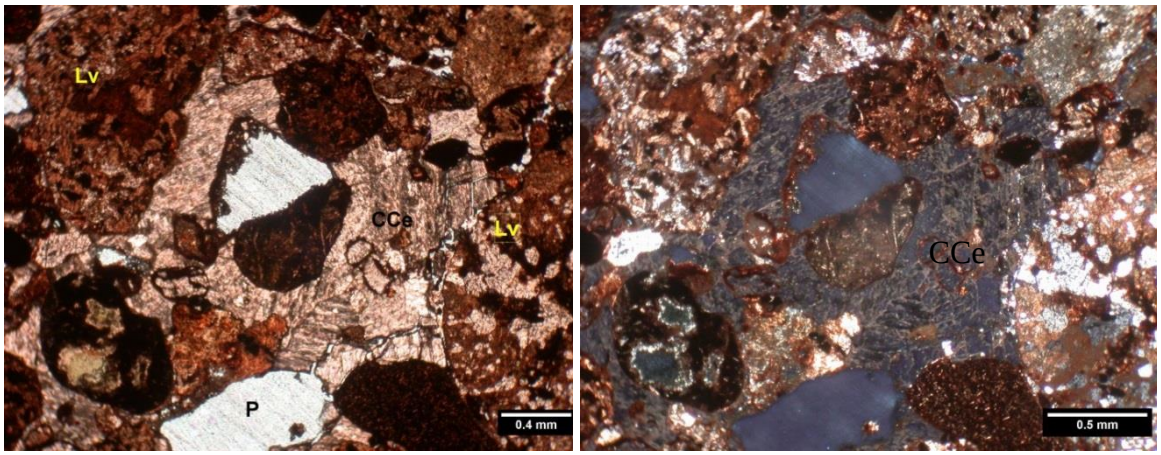

Figure 3.7. Photomicrograph of CHC KEW3-1 sample. This figure is showing poorly sorted grains, lithic volcanic "Lv", calcite cements "CCe", and residual porosity "P". Plane polarized light image (left) and cross-polarized image (right).

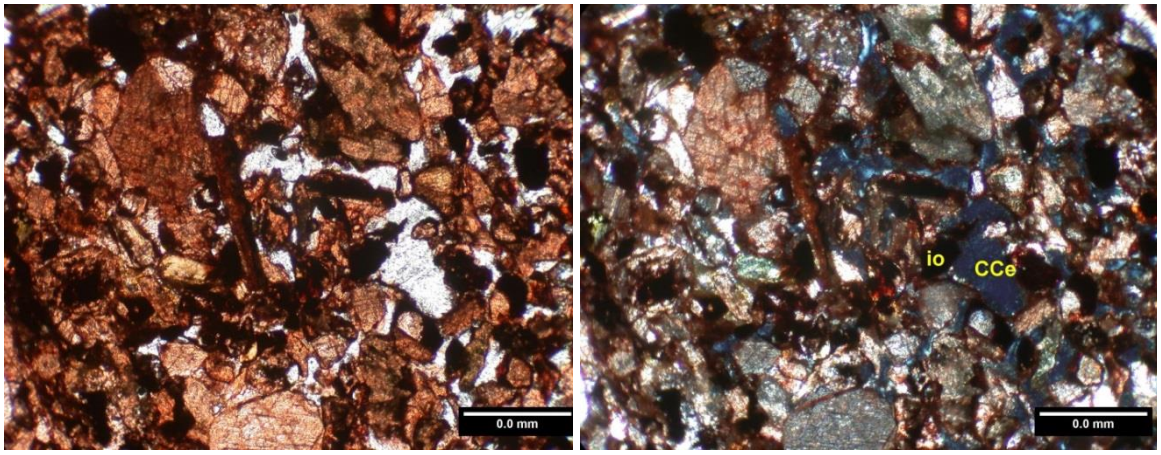

Figure 3.8. Photomicrograph of CHC KEW3-2 sample. This photomicrograph is showing poorly sorted grains, iron oxide "io", and calcite cement "CCe". Plane polarized light image (left) and cross-polarized image (right), the scale bar is 0.025 mm.

B. Fabric and maturity Esrey park's samples: KEW3-1 was a very fine to fine-grained-lithic-arenite (Appendix Figure B.24), and KEW3-2 was a lithic-feldsarenite. The grain shapes for the KEW3-1 sample were sub-angular to angular equant grains; while the KEW3-1 sample was composed of angular to sub-angular equant grains (Table 3.3). Based on the sorting, matrix, and the roundness, KEW3-1 had a sub-mature texture; while KEW3-2 was immature texturally.

3.1.1.4 Dan Point (KEW4-1 and KEW4-3 samples). Copper Harbor Conglomerate sandstone samples from Dan Point varied in their composition from $Q_{38}F_{32.5}L_{29.5}$ in KEW4-1 sample to $Q_{10}F_{9.5}L_{80.5}$ in KEW4-3 sample (Figure 3.2, Figure 3.9, and Figure 3.10). Therefore, KEW4-1 was classified based on Folk et al., (1970) as a lithic-feldsarenite and KEW4-3 as lithic-arenite. The plagioclase to K-feldspar ratio was 1.7:1 and 1.2:1 for KEW4-1 and KEW4-3 samples, respectively. The matrix mineralogy was also dominated by chlorite (~70%) with lesser amounts of illite (23%), and smectite (~7%). The other non-phyllosilicate components are quartz, K-feldspar, and calcite (Figure 3.11; Table 3.2; Appendix Figures B.5).

A. Post-depositional alteration of Dan Point's samples: Carbonate cement was dominant in Dan Point's samples, especially with the KEW4-3 sample. Precipitation of calcite is present as pore-filling and vein-filling features (Figure 3.9). Also, iron oxide cement was present as pore-filling and meniscus around the grains. The grain compaction of KEW4-1 was concave-convex and point contact; while KEW4-3 had relatively less features of high compaction (Table 3.3). Corroded feldspar grains also were recognized in these investigated samples.

B. Fabric and maturity of Dan Point's samples: The mineralogy and grain size analysis of the KEW4-1 sample resulted in it being classified as a feldspathic-arenite (Figure 3.2; Appendix Figure B.25). Meanwhile, the KEW4-3 sample was classified as medium to course grained-lithic-arenite. Both samples had equant angular to sub-rounded grains as illustrated in Table 3.3. Therefore, the KEW4-1 was texturally immature and the KEW4-3 was sub-mature. The residual porosity of the KEW4-1 was 3%, while the KEW4-3 reached 10% (Table 3.1).

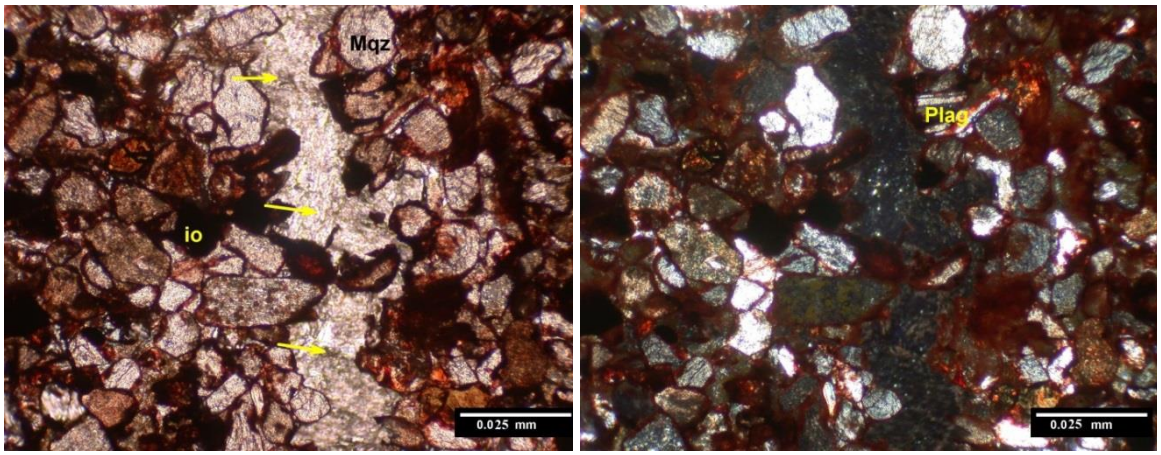

Figure 3.9. Thin section of the CHC KEW4-1 sample. The thin section is showing poorly sorted grains, and vein-filled calcite “arrow”, iron oxide “io”, monocrystalline-quartz “Mqz”, and plagioclase “Plag”. Plane polarized light image (left) and cross-polarized image (right).

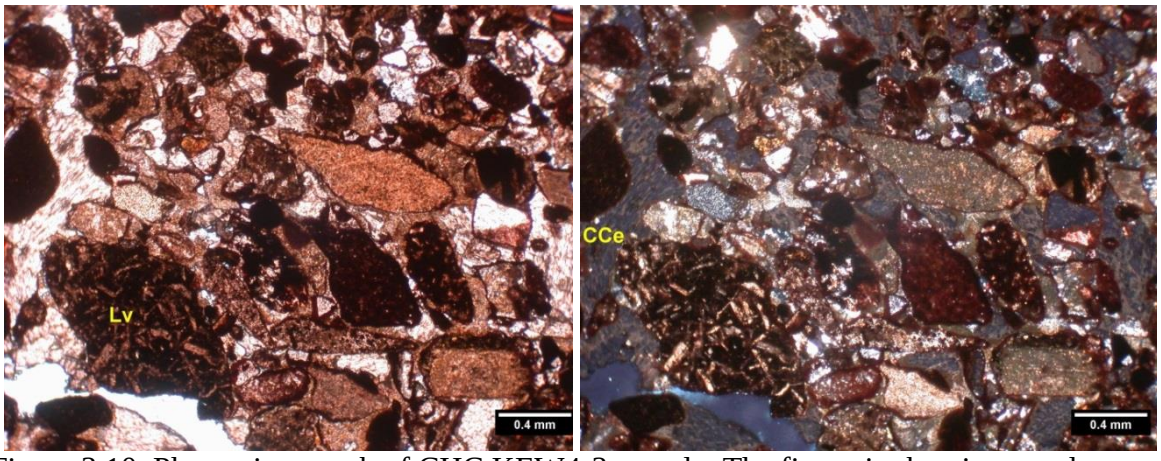

Figure 3.10. Photomicrograph of CHC KEW4-3 sample. The figure is showing poorly sorted grains, lithic volcanic “Lv”, and calcite cement “CCe”. Plane polarized light image (left) and cross-polarized image (right).

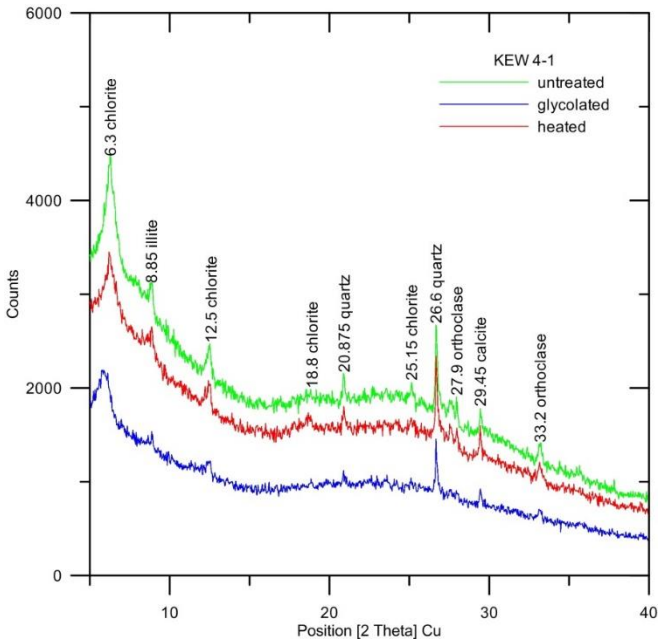

Figure 3.11. X-Ray diffraction spectra of KEW4-1 collected from Dan Point sample from Copper Harbor Conglomerate.The spectra is showing the peaks of chlorite and illite, as well as quartz, orthoclase, and calcite in the matrix of clay-sized fraction.

3.1.1.5 Hobard State Park (KEW 5-1 and 5-3 samples). The proportional compositions of the KEW5-1 and the KEW5-3 samples were $Q_{07}F_{4.5}L_{88.5}$ and $Q_{01}F_{02}L_{97}$, respectively (Figure 3.2, Figure 3.12, and Figure 3.13). So, these samples could be described as lithic-arenites. The plagioclase to K-feldspar ratios was 2.3:1 and 1.6:1 for KEW 5-1 and KEW5-3 samples, respectively (Table 3.1). The minor components were represented by epidote and heavy minerals. The matrix and clay sized components were characterized by presence of chlorite, quartz, calcite, and K-feldspar (Table 3.2; Appendix Figures B6 and B.7). The lithic volcanic components, which displayed variable types of volcanic textures (e.g., porphyritic, trachytic, and granophyric textures), were dominated by K-feldspar and quartz phenocrysts.

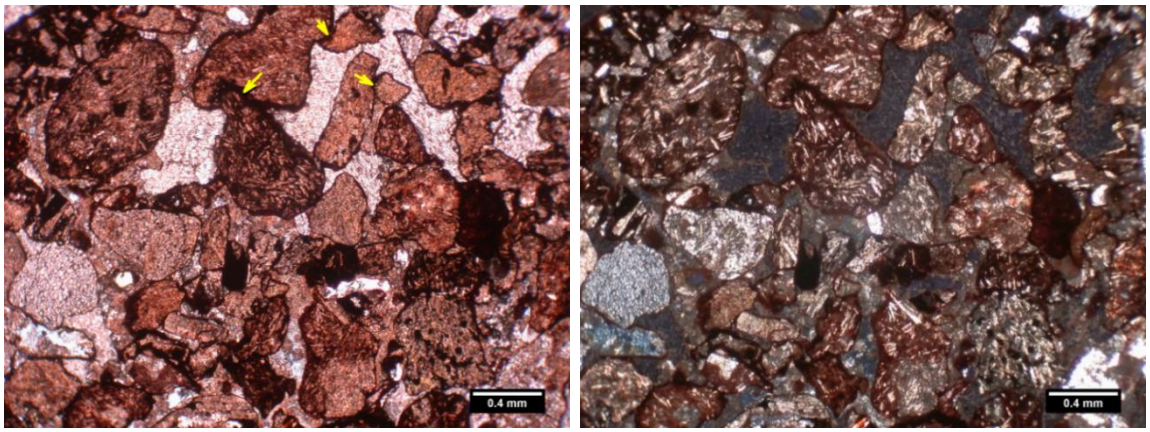

Figure 3.12. Thin section of CHC KEW5-1 sample. This thin section is showing poorly sorted, concave-convex contact between the lithic volcanic grains “arrow”. Plane polarized light image (left) and cross-polarized image (right).

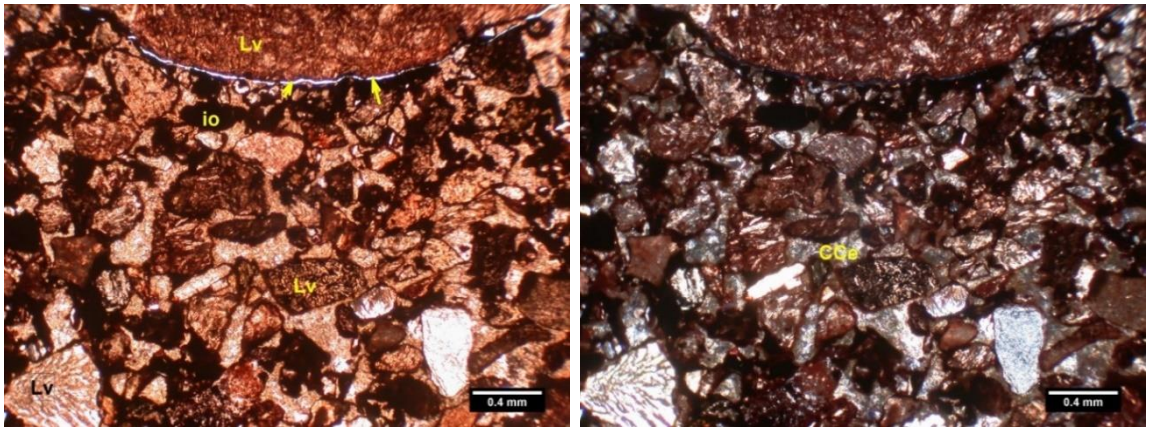

Figure 3.13. Photomicrograph of CHC KEW5-3 sample. This photomicrograph is showing poorly sorted grains, lithic volcanic “Lv”, calcite cement “CCe”, iron oxide, and micro-fracture “arrow”. Plane polarized light image (left) and cross-polarized image (right).

A. Post-depositional alteration of Hobard State park’s samples: The grain compaction of the KEW5-1 had remarkable concave-convex contact boundaries, which reflect high compaction stress on these grains. In contrast the KEW5-3 sample was dominated by floating and point contact grains (Table 3.3). Cement is dominated by carbonate cementation with lesser iron oxide cement.

B. Fabric and maturity of Hobard State park's samples: The KEW5-1 sample was classified as a medium-grained-lithic-arenite (Appendix Figure B.26), and the KEW5-3 sample was a lithic-rudite. The samples exhibited a wide range of grain shapes between angular and sub-angular, with dominantly equant grain forms (Table 3.3). The KEW5-3 sample displayed equant, rounded, pebble grains and sub-angular to sub-rounded sandy grains. Based on the matrix content, sorting, and roundness, both Hobard State Park samples were texturally immature. The intergranular original porosity of these samples was, primarily, occupied by calcite and iron oxide pore-filling cement and the samples had low residual porosity (between 1.8% and 2.7%).

3.1.1.6 Potato River Falls (POT6). The proportional ratio of Quartz-Feldspar-Lithic fragments of the POT6 samples was $Q_{28.9}F_{29.5}L_{41.7}$ as illustrated in Table 3.1 and Figure 3.14. The feldspar ratio was 2.3 to 1 for plagioclase and K-feldspar, respectively. The other minor components were opaque mineral oxides (4.0%), mica (0.4%) and epidote (2.6%). This sample was classified as feldspathic-lithic arenite. The matrix and the clay mineralogy showed chlorite as a major component and illite, quartz, and calcite as minor constituents (Table 3.2).

A. Fabric and maturity of POT 6: The modal analysis of POT6 sample showed abundant equant grains (56.8%). The grain shapes ranged between sub-rounded to rounded in the sample. Therefore, this sample was more rounded and more matured, when compared with the samples collected from the Keweenawan Peninsula.

B. Post-depositional alteration of POT6: About 48% of the total counted grains had concave-convex grain type contacts, and about 44.9% of the grains counted had line contacts. In addition, alteration of feldspar minerals constitutes common diagenetic features in the sample, and a significant amount of quartz grains had fractured surfaces. The estimated residual porosity from the petrography for this sample was very low (About 0.8% of total counting).

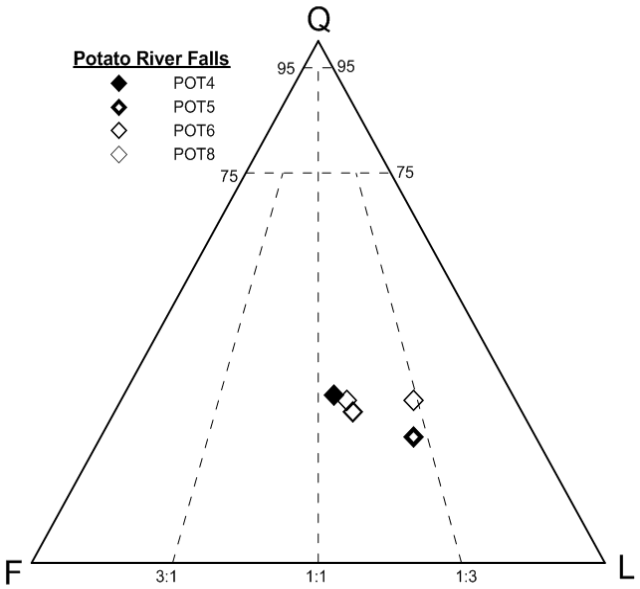

Figure 3.14. Proportional composition of quartz-feldspar-lithic fragments for the Potato River Falls (POT) samples.

3.1.2 Nonesuch Formation and its equivalent stratigraphic units. Nonesuch Formation samples that investigated in this study represented by the Potato River POT4 and POT5 samples, and the Unit C samples collected from the Eischeid #1 well.

3.1.2.1 Potato River Falls (POT4 and POT5). The POT4 sample was considered a feldspathic-lithic arenite as $Q_{32.2}F_{31.1}L_{36.6}$. (Figure 3.14, Figure 3.15, and Table 3.1). The plagioclase to K-feldspar ratio was 1.3 to 1. The other components were opaque mineral oxides (3.4%), mica (1.0%), and epidote (2.4%). Iron oxide was the main cement material (12.6%) and the carbonate cements constituted only 0.3% of the total counted grains. The silty and clayey matrixes constituted 9.0% and 3.4% of the total counts, respectively. The proportional composition of the POT5 sample was $Q_{24.1}F_{21.2}L_{54.6}$. Therefore, the sample was classified as a feldspathic-lithic arenite (Figure 3.14 and Figure 3.16). The plagioclase to K-feldspar ratio was 1 to 1.1. The other minor components were opaque mineral oxides (0.7%), mica (0.3%), and epidote (2.4%). The cement was predominantly iron oxide with lesser amounts of calcite (Table 3.1).

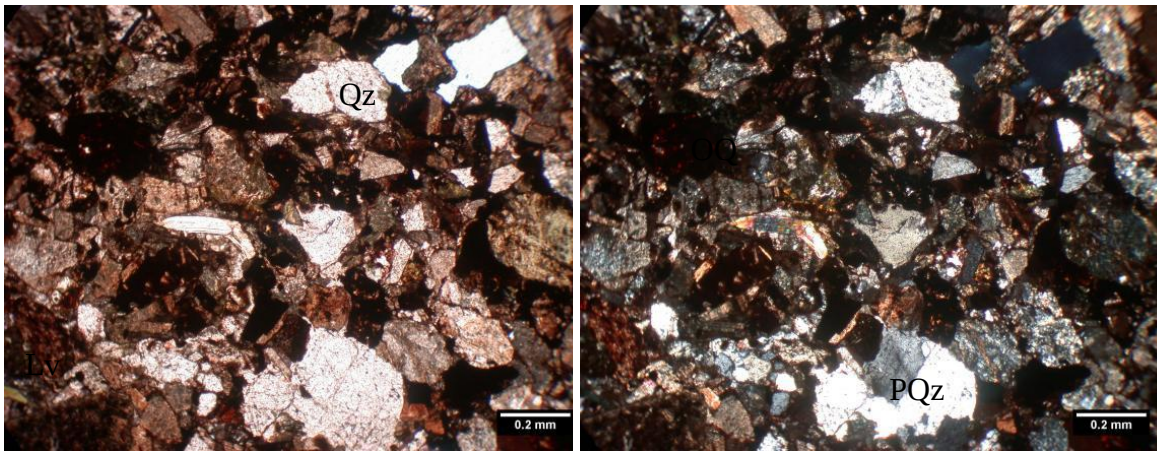

Figure 3.15. Thin section of Nonesuch Formation (POT4). The thin section is showing monocrystalline-quartz grains (MQ), K-feldspar (K-spr), volcanic lithic fragments (Lv), and opaque mineral oxides (OQ). Plane polarized light image (left) and cross-polarized image (right).

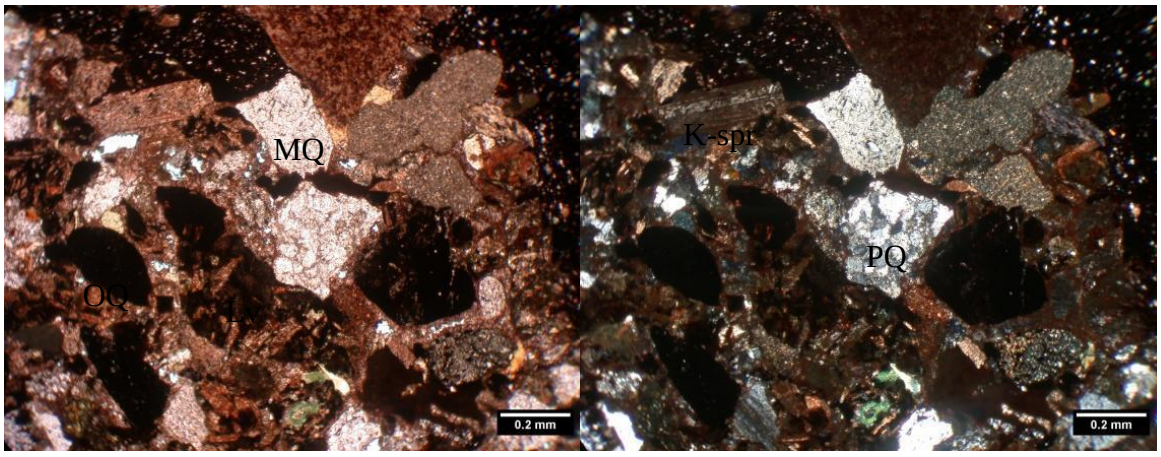

Figure 3.16. Thin section of Nonesuch (POT5). This thin section is showing monocrystalline-quartz grains (MQ), polycrystalline-quartz (PQ), volcanic lithic fragments (Lv), sedimentary lithic fragments (Ls), K-feldspar (K-spr), and opaque mineral oxides (OQ). Plane polarized light image (left) and cross-polarized image (right).

A. Post-depositional alteration of POT4 and POT5 samples: Feldspar and lithic volcanic grains showed moderate to extensive alteration. The degree of compaction, which was estimated from the grain contact features, could be described as moderately packing of the grains, because the vast majority of the grains displayed concave to convex to line contacts. Also, the quartz grains were obviously fractured. The residual

porosity counts represent about 2.4% and 3.4% for the POT4 and the POT5 samples, respectively, as seen in Table 3.1

B. Fabric and maturity of POT4 and POT5 samples: The size range for POT4 clastic grains was between very course to fine grained sandstone, and the grain average was, approximately, 0.45 mm (Appendix Figure B.27). The POT5 sample was course-grained to conglomeritic sandstone. The grain forms of the samples were predominantly equant, and their shapes ranged between sub-angular to sub-rounded. Based on the clay content, grain sorting, and the grain shape, the textural maturity of the POT4 sample could be described as a texturally immature. However, the POT5 sample had a total matrix content of only 5.7%. Consequently, this single sample was classified as a texturally sub-mature to mature as displayed by its clay content, roundness, and grain sorting features.

3.1.2.2 Amoco M. G. Eischeid #1 Well, Unit C, Iowa. The Unit C of the Lower Red Clastics in the Amoco M. G. Eischeid #1 well is interpreted to be an equivalent unit to the Nonesuch Formation of Oronto Group exposed near Lake Superior. This unit was investigated by Anderson (1990) and was classified as a lithic feldspathic arenite to feldspathic arenite (Figure 3.17, Figure 3.18, and Table 3.4). The main diagenetic feature recognized in Unit C was the abundance of calcite cement as noted in Table 3.4 (15 to 33%). Based on the 250 point counts by Anderson (1990) the C2 samples were classified as feldsarenite to lithic feldsarenite. The grains were mainly composed of monocrystalline quartz, plutonic lithic fragments, K-feldspar, mica, and epidote. The average matrix composition from the clay size materials of Unit C was about 49% chlorite, 9% I/S (illite/smectite layers), and 41% illite. The XRD spectra also showed peaks of albite and calcite (Figure 3.19; and Appendix Figures B.8 - B.13).

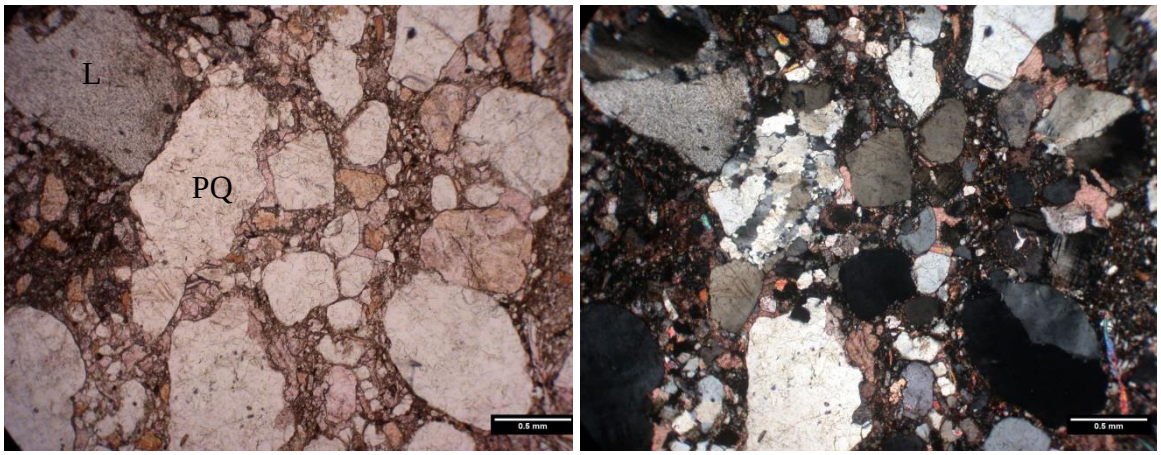

Figure 3.17. Thin section of Unit C2 (15107`). The figure is showing monocrystalline-quartz grains (MQ), polycrystalline-quartz (PQ), and lithic fragments (L). Plane polarized light image (left) and cross-polarized image (right).

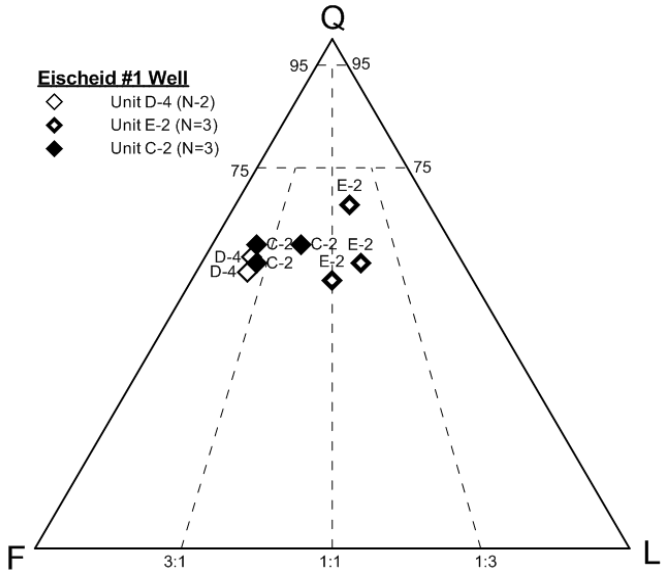

Figure 3.18. Proportional triangular plot of total quartz (Q), total feldspar (F), and total lithic fragment content of the Amoco M.G. Eischeid #1 well samples, Iowa. Data source is Anderson, (1990).

Table 3.4. The results of the petrographic investigations based on 250 point counts from the Amoco M. G. Eischeid #1 samples, Iowa. The data is from Anderson, 1990. Qz is quartz, K-spr is K-feldspar, Plag is plagioclase, L is lithic fragment, HM is heavy minerals, M is matrix, IO is iron oxide cement, CC is carbonate cement, and Ab. C is albite cement.

Unit	Depth (ft)	Qz	K-spr	Plag	L	HM.	Mtrx.	Ab. C	CC	IO
E2	8,834.3	50	10	6	25	0	0	2	1	4
E2	8,835.6	52	16	7	23	1	0	1	0	0
E2	8,836.5	56	4	7	16	5	0	4	trace	7
D4	11,387.5	36	5	17	5	6	4	0	1	26
D4	11.392.6	38	12	14	6	11	1	0	6	12
C2	15,101.9	40	3	14	10	trace	0	0	33	0
C2	15,107.6	42	13	13	7	3	3	0	17	0
C2	15,109.0	40	12	10	5	14	3	0	15	0

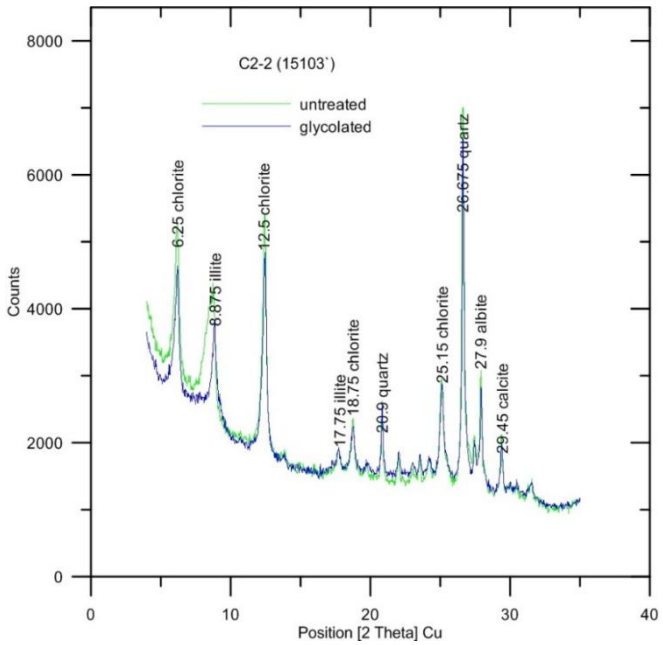

Figure 3.19. X-Ray diffraction spectra of the Unit C (C2-2 sample). The spectra is showing the peaks for chlorite and illite, as well as quartz and albite in the clay-sized matrix fraction.

3.1.3 Freda Formation and its Stratigraphic Equivalents.

The Freda Formation sandstone samples collected from the Potato River Falls location (POT8

samples) and the D Unit samples from the Amoco M. G. Eischeid #1 well are represented in this section.

3.1.3.1 Potato River Falls location (POT8-1 and POT8-2). The proportional mineral compositions of the POT8-1 and POT8-2 samples were $Q_{31.1}F_{17.7}L_{51.1}$ and $Q_{31.1}F_{29.4}L_{39.5}$, respectively, as illustrated in Table 3.1. Therefore these samples are classified as feldspathic-lithic arenite (Figure 3.14 and Figure 3.20). The plagioclase to K-feldspar ratios were1:4.3 and 1:1.8 for both samples, respectively. The clay-sized fraction contained abundant chlorite (~43%), smectite (~42%), and traces of illite and laumontite (Figure 3.21).

B. Post-depositional alteration of POT8 samples: The compaction rates on the samples were significant with 53.0% and 57.7% of the total grains having concave-convex contacts and 28.0% to 31.2% with line contacts for the POT8-1 and POT8-2 samples, respectively. The vast majority of the investigated grains had an unaltered surface, and a significant amount of the feldspathic grains were altered (Table 3.3).

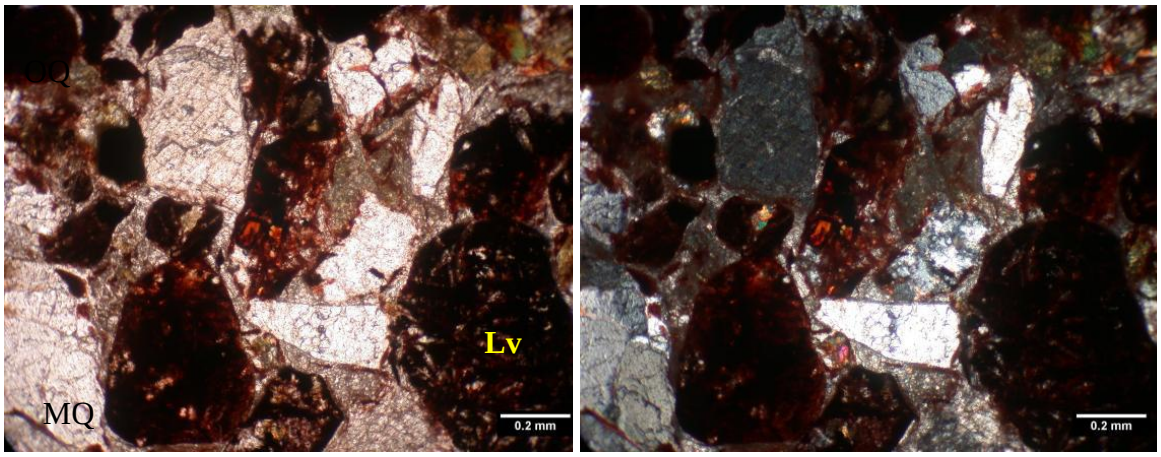

Figure 3.20. Thin section of CHC (POT8-1). The thin section is showing monocrystalline-quartz grains (MQ), volcanic lithic fragments (Lv), and opaque mineral oxides (OQ). Plane polarized light image (left) and cross-polarized image (right).

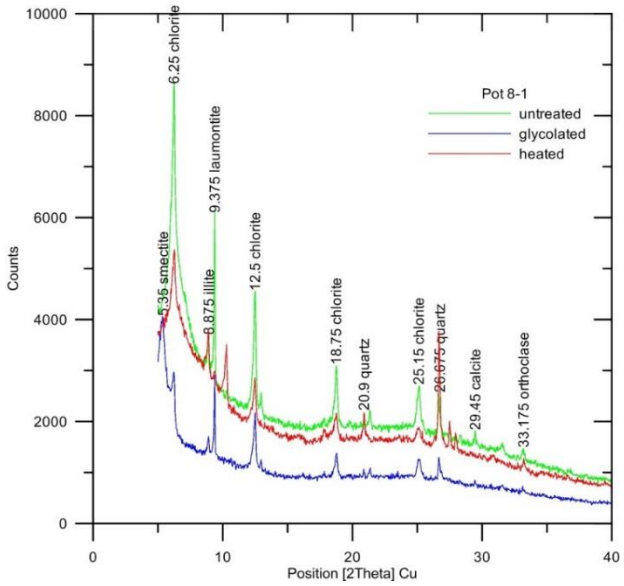

Figure 3.21. X-Ray diffraction spectra of the Freda Formation sample POT8. The spectra is showing peaks for chlorite, smectite, and illite, as well as quartz, orthoclase, laumontite, and calcite in the clay-sized matrix fraction.

B. Fabric and maturity of POT8 samples: The grain shapes ranged between rounded to sub-rounded in all POT8 samples, and the grain form ranged between equant and elongated (Table 3.3). The grain size distribution of the clastic materials ranged between 0.4 and 1.1 mm, therefore, the sample was a medium to course-grained sandstone (Appendix Figure B.28). Based on the roundness and the matrix content, the samples were considered more mature when compared to the POT4, POT5, and POT6 samples (Sections 3.1.1.6 and 3.1.2.1). The residual porosity estimated from the petrographic investigations was between 0.0% and 1.2 for POT8-1 and POT8-2, respectively.

3.1.3.2 Amoco M. G. Eischeid #1 Well, Unit D, Iowa. The point counts results for the two thin sections samples from Unit D of Amoco M. G. Eischeid #1 well suggest a classification as feldsarenite ($Q_{36\ to 38}F_{22\ to\ 26}L_{5\ to\ 6}$). The samples represent a very fine-grained sandstone. The major mineral components are represented by quartz, plagioclase, K-feldspar, heavy minerals, and less lithic fragments compared with the Unit E sediments (Figure 3.18, Figure 3.22, and Table 3.4). Iron oxide cement dominated in Unit D compared with calcite cement in Unit C or albite in Unit E (Anderson, 1990). The

chlorite content was very low in the clay-sized matrix fraction compared with the Unit C2 (ave. 8 ±5%), while the main clay-phyllosilicate mineral type was illite (ave. 63 ±5%). The I/S content was also higher than that in the Unit C2 samples, with an average of about 27 ±5%. The non-clay minerals, represented in the XRD spectra, were quartz, albite, K-feldspar, and calcite (Figure 3.23; Table 3.2; Appendix Figures B.14 and B.15).

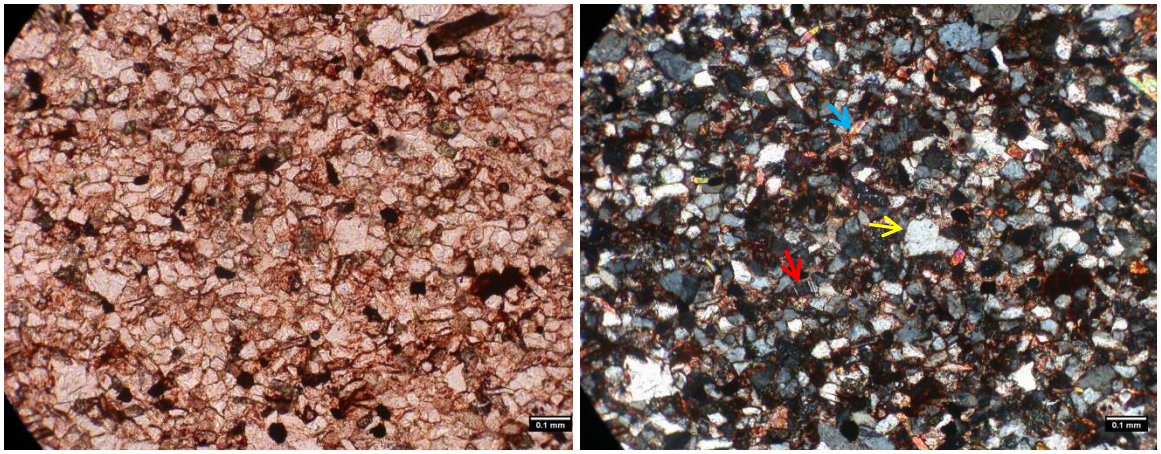

Figure 3.22. Thin section of Unit D (D4). The figure is showing monocrystalline-quartz grains (yellow arrow), plagioclase (red arrow), and muscovite (blue arrow). Plane polarized light image (left) and cross-polarized image (right).

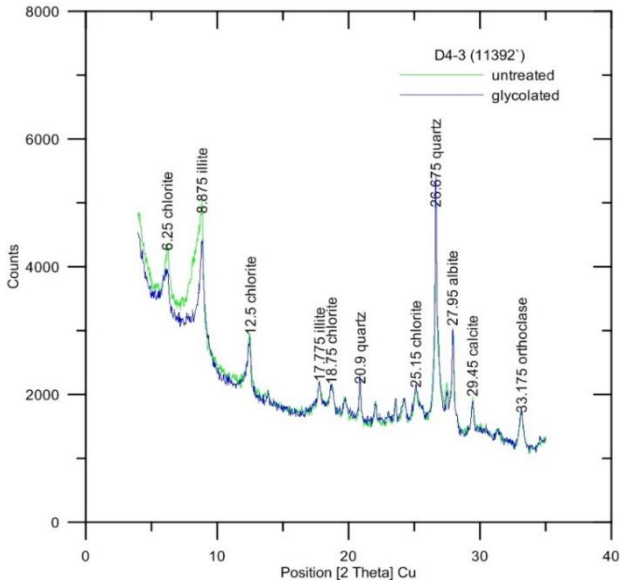

Figure 3.23. X-Ray diffraction spectra of the Unit D (D4-3 sample). This spectra is showing the peaks for chlorite and illite, as well as quartz, orthoclase, albite, and calcite in the clay-sized matrix fraction.

3.2 BAYFIELD SANDSTONE AND STRATIGRAPHIC EQUIVALENTS

3.2.1 Chequamegon Formation. The Chequamegon Formation is the youngest stratigraphic unit of the Bayfield Group, and stratigraphically equivalent to the H and G Units in the Amoco M. G. Eischeid #1 Well and also the Jacobsville sandstone.

3.2.1.1 Dardemple Park (BAY1 sample). The proportional triangular plot for the Bayfield Formation sample BAY1 plotted within the subfeldsarenite field with a mineralogical composition of $Q_{82.5}F_{11}L_{6.5}$ (Figure 3.24, Figure 3.25, and Table 3.5). Mica and microcline were the additional minor mineral components. The matrix, which was analyzed by XRD, showed a significant accumulation of kaolinite plus non-clay minerals (i.e. quartz and K-feldspar; Table 3.2; Appendix Figures B. 16).

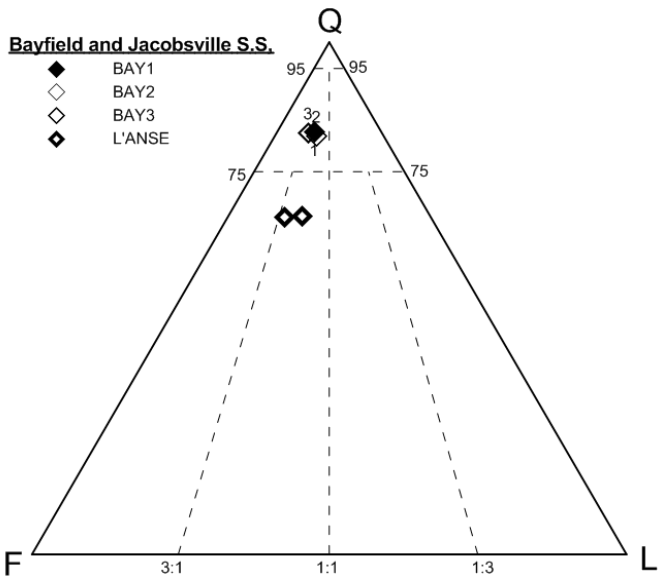

Figure 3.24. Triangular plot of quartz, feldspar, and lithic fragments based on point counting of 300 points per thin section of thin section samples collected from the Bayfield Peninsula, WI.

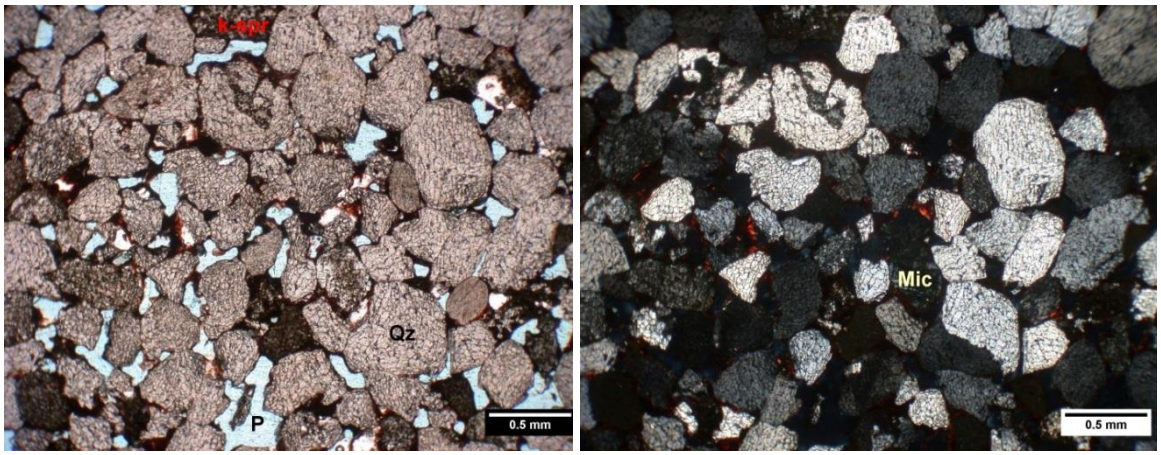

Figure 3.25 Thin section of Bayfield Formation BAY1 sample. The figure is showing well sorted, monocrystalline-quartz "Qz", porosity "P", and microcline "Mic". Plane polarized light image (left) and cross-polarized image (right).

A. Post-depositional alteration: The alteration of feldspar grains was the most recognizable diagenetic feature in BAY1 sample. Precipitation of authigenic kaolinite clay within the primary intergranular pore space likely occurred as consequence of feldspar alteration. The vast majority of the grains were slightly compacted with dominantly line contacts (Table 3.6). The quartz grains were heavily fractured and that could reflect the effect of tectonic stresses applied on this sandstone during its geologic history.

B. Fabric and maturity: This sandstone was medium to course grained sandstone (Appendix Figures B.29) with a very low matrix content. The grain shape varied between sub-rounded to rounded and were primarily equant grain forms (Table 3.6). This sample was well sorted with a very low matrix content, so it is super-mature texturally. Point counting on BAY1 thin section showed that the type of porosity was intergranular and constituted approximately 19.7% of total sample volume.

Table 3.5. Percentage of mineral components from surface outcrop samples of the stratigraphically equivalent Bayfield Group and Jacobsville Formation. Analysis is based upon 300 counts per thin section sample. Qz is quartz, Plag is plagioclase feldspar, K-spr is K-feldspar, L is lithic fragment, OQ is opaque mineral oxides, M is mica, HM is heavy minerals, Ep. is epidote, Uk is unknown, SM is silty matrix, CM is clayey matrix, IO is iron oxide cement, CC is carbonate cement, and P is porosity.

Sample ID	UNIT	Qz	Plag	K-spr	L	OQ	M	HM	Ep.	Uk.	SM	CM	IO	CC	P	Total
BAY1	Bayfield	61.5	7.0	1.3	4.7	0.0	0.0	0.0	0.0	0.0	0.7	0.3	4.7	0.0	19.7	100
BAY2	Bayfield	64.5	7.7	0.3	5.0	0.0	0.3	0.0	0.0	0.0	3.0	4.3	0.0	0.0	14.7	100
BAY3	Bayfield	50.8	0.3	7.3	3.3	0.0	0.0	0.1	0.0	0.0	2.7	1.3	1.0	0.0	32.2	100
L'ANSE1	Jacobsville	50	8.6	10.1	7.3	2.8	0	0	0	0	1.6	4.5	2.4	1.7	11	100
L'ANSE2	Jacobsville	51.2	5.5	11.2	9.6	3	0	0	0	0	2.3	4.7	3.5	0.8	8.2	100

Table 3.6. Percentage of grain forms, roundness, contact and surface texture from surface outcrop samples of the stratigraphically equivalent Bayfield Group and Jacobsville Formation. Analysis is based upon 300 counts per thin section sample. Elg. is elongated, Eq. is equant, VA is very angular, A is angular, SA is sub-angular, R is rounded, WR is well rounded, F is fractured contact, S is sutured contact, CC. is concave-convex contact, L is line contact, P is point contact, Fl. is floated grain, C is corroded surface, Fr. is fractured surface, and Po is polished surface.

	Grain form			Roundness						Grain contact						Surface texture		
Sample ID	Elg. - Eq.	Elg.	Eq.	VA	A	SA	SA	R	WR	F	S	CC.	L.	P	Fl.	C	Fr.	Po.
BAY1	8.1	19.3	72.6	0.4	8.1	22.0	39.5	18.8	11.2	8.1	1.8	26.5	53.4	9.8	0.4	14.9	81.9	3.2
BAY2	5.6	31.0	63.4	0.5	8.4	19.5	33.0	25.6	13.0	3.7	2.8	43.9	39.3	5.6	4.7	16.4	79.9	3.7
BAY3	6.9	24.5	68.6	0.0	3.7	15.4	34.6	22.9	23.4	2.1	4.8	48.9	32.4	9.6	2.2	14.9	83.0	2.1
L'ANSE1	15	13.8	71.2	0.8	7.7	12.6	27.1	36.6	15.2	1.1	3.6	39.8	34.3	14.7	6.5	24.3	71.7	4
L'ANSE2	15.4	15.1	69.5	1.2	7.5	13.9	28	35.8	13.6	2	3.2	43.3	36.9	10.1	4.5	25.8	72.3	1.9

3.2.1.2 Old Sal Road (BAY2 sample). This Bayfield Formation sample (BAY2) was similar to the BAY1 sample in its major components ($Q_{82}F_{11}L_{7}$) as illustrated in Figure 3.24 and Figure 3.26. The lithic fragments were comprised of 75% sedimentary-lithic and 25% lithic volcanics. The point counting of the sample revealed some mica and traces of microcline (Table 3.5). Kaolinite was the main recognizable clay matrix material (~99%), and the non-phyllosilicate minerals were represented by quartz and K-feldspar in the XRD diffraction (Figure 3.27; Table 3.2).

A. Post-depositional alteration of BAY2: Fractured quartz was abundant in this sample. The main diagenetic feature recognized was feldspar alteration as seen in Figure 3.26 under an "F" label. The feldspar grains displayed greenish gray to green spots on the cleavage surfaces of the crystals. Also, some alteration products (e.g., kaolinite) were recognized in the intergranular porosity (Table 3.5).

B. Fabric and maturity of BAY2: This sample displayed a medium-grained quartz-sandstone distribution. The grains were sub-rounded to rounded with equant dimension (Table 3.6). The sample was very well sorted with limited occurrence of matrix (approximately 10%). These features make the BAY2 sample a texturally mature sandstone. The intergranular porosity was determined from the point counting and comprised about 14.5% of the total sample volume with no evidence of calcite pore filling.

3.2.1.3 Mount Ashway (BAY3 sample). This Bayfield Formation sample has approximately the same composition of the BAY1 and BAY2 samples with a composition of $Q_{82}F_{12.5}L_{5.5}$ (Figure 3.24 and Figure 3.28). About 80% of the total lithic grains were lithic sedimentary fragments and the remaining 20% were lithic volcanics. The minor components were represented by microcline, mica, and heavy minerals. The matrix fraction was about 4% of the total counting, and predominantly composed of kaolinite and non-clay minerals like quartz and K-feldspar (Table 3.2).

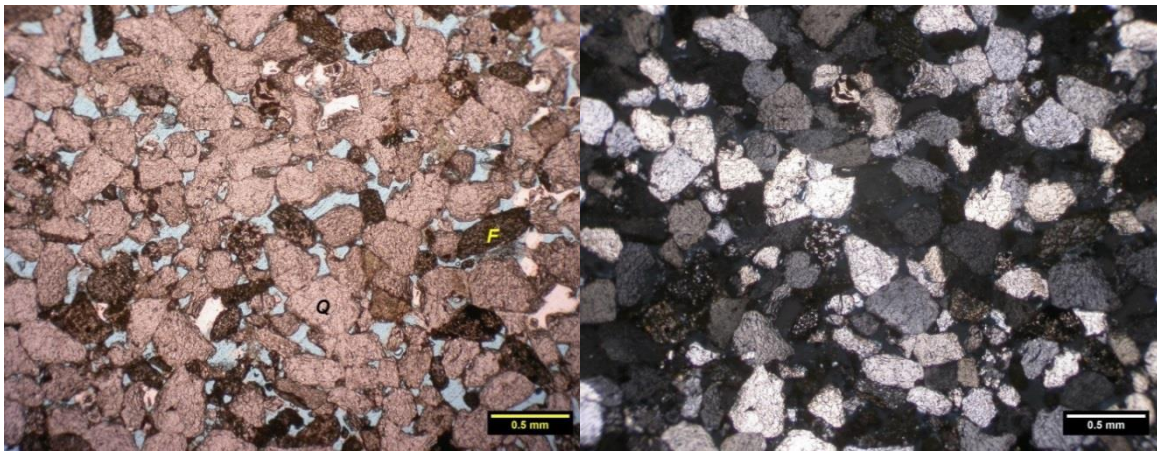

Figure 3.26. Thin section of Bayfield Formation (BAY2 sample). The thin section is showing well-sorted monocrystalline-quartz "Q" and feldspar "F". Plane polarized light image (left) and cross-polarized image (right).

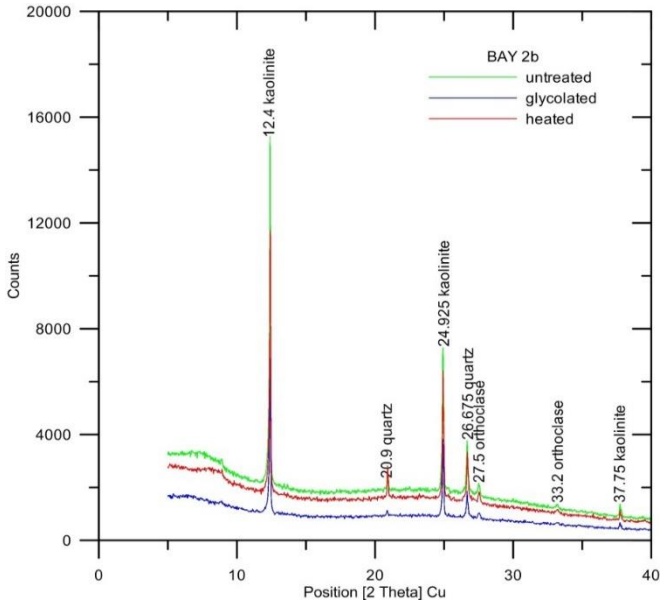

Figure 3.27. X-Ray diffraction spectra of the Old Sal Road sample (BAY2; Bayfield Formation). The spectra is showing the peaks of kaolinite, as well as quartz and orthoclase in the clay-sized matrix fraction.

A. Post-depositional alteration of BAY3: The alteration of feldspar formed a clear diagenetic feature in BAY3 sample. The grain contact (i.e. concave-convex to line

contact) indicated the compaction processes that affected the grains during their geological history.

B. Fabric and maturity of BAY3: This sample (BAY3) is a fine to medium-grained quartz arenite. The grain shape and form were, primarily, equant, and sub-rounded to rounded (Table 3.6). With only about 4% matrix material the textural maturity of the sample can be classified as mature. The point counting showed about 32.2% porosity of the total count, however, the high number is likely a result of plucking of the loose and friable grains during thin section polishing. The direct measurement of the primary porosity by water flooding of a core sample was 17.5%.

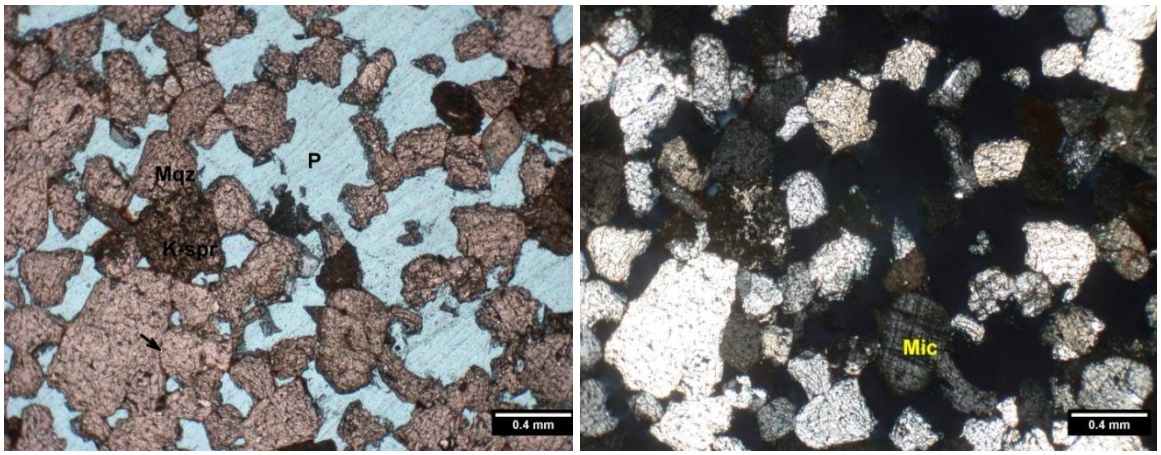

Figure 3.28. Thin section of Bayfield sandstone sample (BAY3). The figure is showing poor sorting, high porosity "P" (though some of this is due to grain plucking during sample polishing, monocrystalline-quartz "Mqz", altered K-feldspar "Kspr", and microcline "Mic". Plane polarized light image (left) and cross-polarized image (right).

3.2.2 Jacobsville Sandstone, L'Anse Area (L'ANSE). The proportional triangular plot of L'ANSE1 was $Q_{65.6}F_{24.6}L_{9.6}$ and L'ANSE2 was $Q_{66.1}F_{21.5}L_{12.4}$. So, these samples fall in the lithic-feldspathic arenite field with a shift towards a quartz-rich composition (Figure 3.24 and Figure 3.29). Quartz constituted about 50% of the total grain counts. The plagioclase to K-feldspar feldspar ratio was 1:18. The other minor components were represented by opaque mineral oxides. From the XRD analysis, the clayey matrix composition was represented by 87% kaolinite, with traces of illite (~5%)

and chlorite (~7%), and the non-clay minerals were represented by quartz and orthoclase (Figure 3.30; Table 3.2)

A. Fabric and maturity: The L'Anse area samples were a medium to coarse grained sandstone. The grain size range of 0.3 to 0.8 mm was the most abundant fraction of the total counts (Appendix Figure B.30). L'ANSE sample grains were equant in their grain forms and rounded to sub-rounded in their grain shape. The clay matrix material formed a very small portion of the total counted grains. Therefore, this sample was classified as a supermature sandstone.

B. Post-depositional alteration: Feldspar alteration was common in these samples. As the result of this alteration, kaolinite clay dominated the matrix and the clay-sized material. The quartz grains also demonstrated significant evidence of compaction and fracturing. Precipitation of authigenic clays as pore-lining coatings toward the center of the pores was the main recognized feature that affected the primary porosity and permeability (see Pl labeled on Figure 3.29). The porosity fraction was about 11% and 8.2% of the total point counts for L'NASE1 and L"NASE2, respectively.

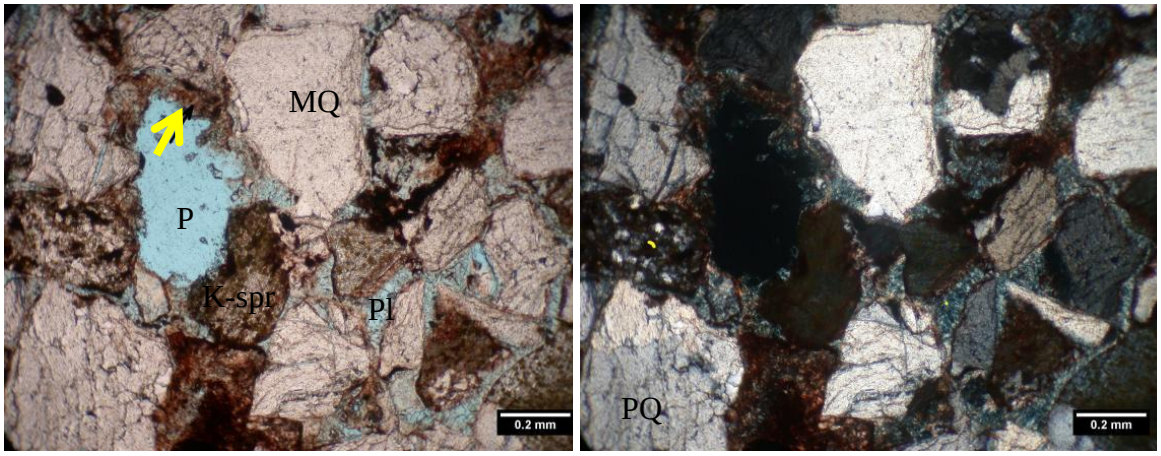

Figure 3.29. Thin section of Jacobsville Formation sample (L'ANSE 1). The photomicrograph is showing monocrystalline-quartz grains (MQ), polycrystalline-quartz (PQ), K-feldspar (K-spr), diagenetic clay (arrow), authigenic pore lining clay (Pl), and porosity (P). Plane polarized light image (left) and cross-polarized image (right).

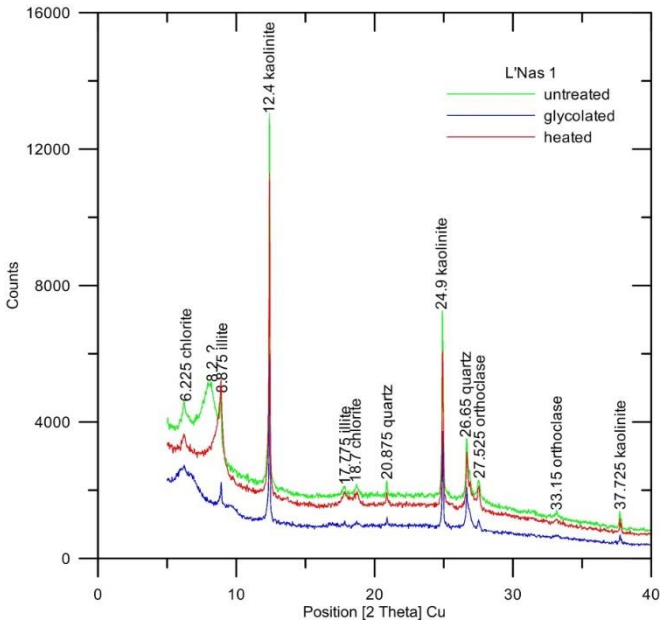

Figure 3.30 X-Ray diffraction spectra of the Jacobsville Formation L'ANSE 1 sample. The spectra is showing the peaks of chlorite, kaolinite, and illite, as well as quartz and orthoclase in the matrix of clay-sized fraction.

3.2.3 Amoco M. G. Eischeid #1 Well, Unit E, Iowa. The Unit E of the Eischeid #1 well is stratigraphically equivalent to the Orienta sandstone of the Bayfield Group. This unit was a lithic feldsarenite to feldspathic lithic arenite, and displayed moderately sorted fine to medium-grained sand grains (Anderson, 1990). The proportional composition of the main grains constituents was Q_{52} $F_{16}L_{25}$, Q_{51} $F_{23}L_{23,}$ and $Q_{56}F_{11}L_{16,}$ for the three samples from Unit E2 (represented from shallowest to the deepest Unit E2 samples). The grain components are represented by monocrystalline quartz, lithic fragments, K-feldspar, plagioclase, and heavy minerals (Figure 3.18 and Figure 3.31). Albite and iron oxide cements were the main diagenetic feature recognized in the Unit E, and traces of calcite cement were also recognized (Anderson, 1990). Samples were dominated by the presence of quartz and illite, with minor albite detected in the XRD analysis of the matrix fraction. The peaks for chlorite from this core were substantially more subdued than they were for the C1, C2, and D4 samples. This reflected a lower abundant of this mineral in the Upper Red Clastic sequence. The illite peak at the 8.8° two-theta position displayed shoulder-broadening to lower angle positions, suggesting the presence of smectite and/or mixed layer I/S clays. A substantial increase in the 5.2 degree

two-theta position for glycolated samples also indicates the presence of expandable smectite clay (Figure 3.32; Table 3.2; Appendix Figures B17, B.18). Smectite is often used as a drilling mud. It is thus possible that this mineral is present as a contaminant phase introduced during drilling rather than something that was present in the original sedimentary rock, however, pure smectite, rather than mixed layer illite-smectite is most commonly used as a drilling mud.

The main diagenetic feature in the Unit E was the development of pore-filling cement. The cement was dominated by the formation of iron oxide, albite, and calcite. The primary porosity of the samples was mainly intergranular, where the cement only had a limited influence on the porosity as compared with the Lower Red Clastics of the M. G. Eischeid #1 well segments (Anderson, 1990).

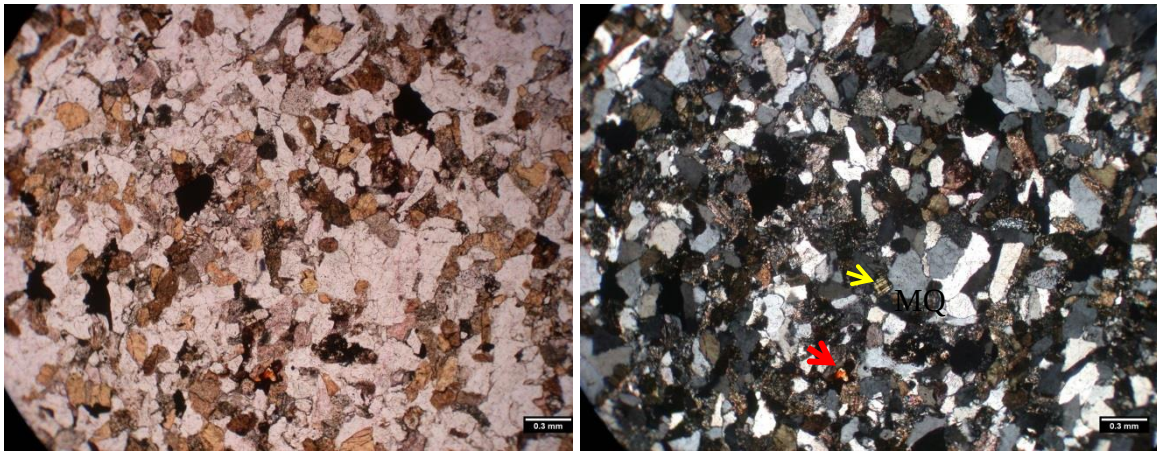

Figure 3.31. Thin section of Unit E (E2-4 sample). This thin section is showing monocrystalline-quartz grains (MQ), heavy mineral (red arrow), and K-feldspar (yellow arrow). Plane polarized light image (left) and cross-polarized image (right).

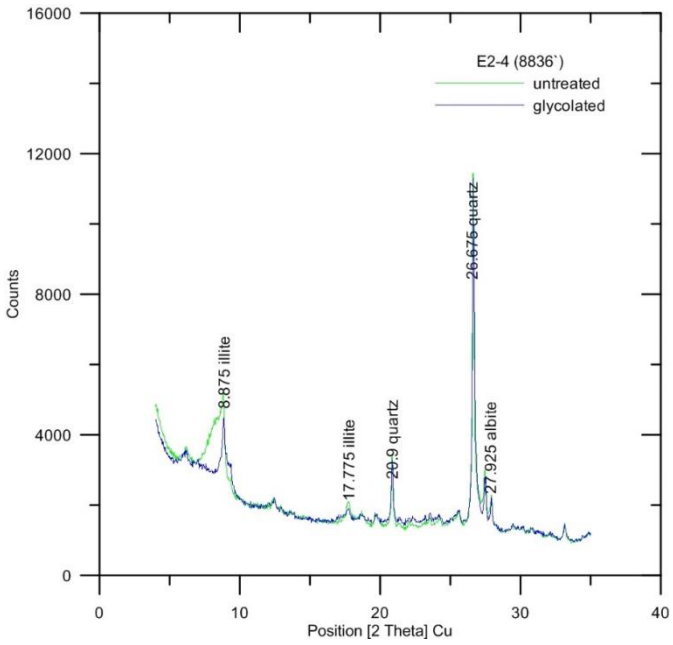

Figure 3.32. X-Ray diffraction spectra of the Unit E (E2-4) sample. This spectra is showing the peaks for illite, as well as smectite, quartz and albite in the clay-sized matrix fraction.

3.3 TEXACO POERSCH #1 WELL

Several samples were collected from an unnamed stratigraphic unit within the clastic-dominated portion of the Texaco Poersch #1 well, in Kansas as drill cutting fragments of sandstone. The lithological description of the samples was described by Berendsen et al., (1988). The petrographic investigations showed a significant amount of plagioclase feldspar in the arkosic to subarkosic samples. Microcline (K-feldspar) and individual quartz grains were also found, but were less abundant. Some grains of volcanic lithic fragments were also recognized. The Lower Sedimentary Sequence (LSS; 11,050' – 11,090') was characterized by a significant decrease in the grain size [fine to very fine-grained arkose reported in Berendsen et al., (1988) report] as compared with the upper part of the LSS, which is pebbly to course to medium-grained arkose. The grain shapes of these arkosic components were mainly angular to subangular in shape. Individual fractured quartz grains were recognized, and these likely reflected a significant amount of stress applied on the grains following burial and/or tectonism (Berendsen et al., 1988).

The XRD analysis of the clay-sized matrix fraction showed significant peaks for different types of clay and non-clay minerals. The Upper Mixed Sedimentary-Volcanic Sequence (UMVSS; see Figure 1.11) samples (5,396` and 5,400`) had, primarily, a similar matrix and clay mineralogy. Peaks for Ni-Mg-rich chlorite (probably nimite [$(Ni,Mg,Fe)_5Al(Si_3Al)O_{10}(OH)_8$]) were recognized at 6°, 12°, 18°, and 24° 2-theta positions. Phlogopite, $KMg_3AlSi_3O_{10}(F,OH)_2$, which represents the Mg-end member of biotite solid solution series, was also recognized by a peak at the 8.8° 2-theta position. Also, a significant concentration of Mg (270 ppm maximum) was detected in the UMVSS letchate solution after the high pressure temperature testing (see Section 4.2.1.3). Non-phyllosilicate minerals were represented by peaks for dolomite at the 31° 2-theta position and albite at the 27° 2-theta position (Figure 3.33; Table 3.2; Appendix Figures B.19).

The Upper Sedimentary Sequence (labeled as USS in Figure 1.11) and the Middle Sedimentary Sequence (MSS as in Figure 1.11) samples (i.e. 8052.5`, 8476'-8480`, and 10,514`) had a similar mineral composition and clay content, with nimite present in both. The presence of lithium-rich illite [probably zinnwaldite, $KLiFe(AlSi_3)O_{10}(OH,F)_2$] was suggested by XRD spectra analysis peaks at 8.8° 2-theta position and second sharp peak at ~26°. The other non-clay minerals were represented by quartz, albite, and calcite (Figure 3.34; Table 3.2; Appendix Figures B.20 and B.21). The MSS sample (10,666`) had unique and strong chlorite peaks at 6, 12, 18, and 24 degrees 2-theta. The non-phyllosilicate minerals were represented by albite and dolomite (Figure 3.35; Table 3.2). The Lower Sedimentary Sequence (label as LSS in Figure 1.11) sample (11,061`) displayed only very small peaks for chlorite. Albite and dolomite peaks dominated the mineral component of non-clay matrix material (Figure 3.36 and Table 3.2).

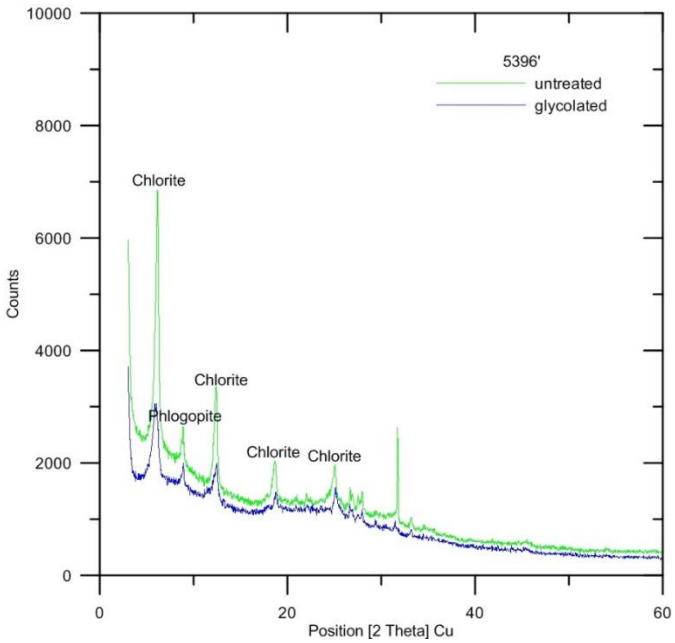

Figure 3.33. X-Ray diffraction pattern of 5,396` sample. This spectra is showing the peaks for chlorite and phlogopite, as well as albite and dolomite in the matrix of clay-sized fraction.

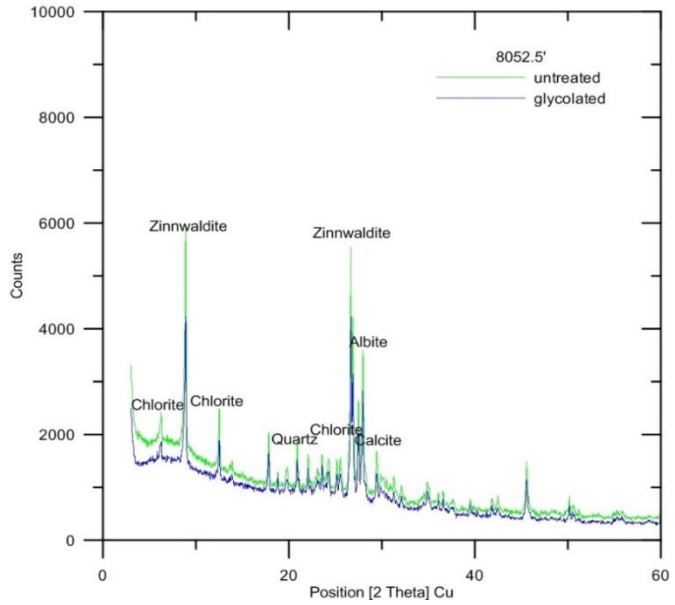

Figure 3.34. X-Ray diffraction pattern of 8,052.5` core sample. This spectra is showing the peaks for chlorite and zinnwaldite, as well as quartz, albite and calcite in the clay-sized matrix fraction.

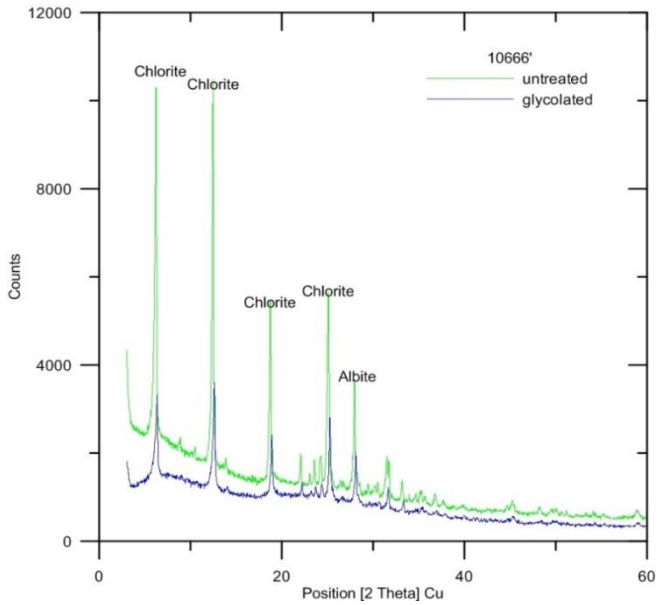

Figure 3.35. X-Ray diffraction pattern of 10,666` core sample. This spectra is showing the peaks for chlorite as well as albite and dolomite in the clay-sized matrix fraction.

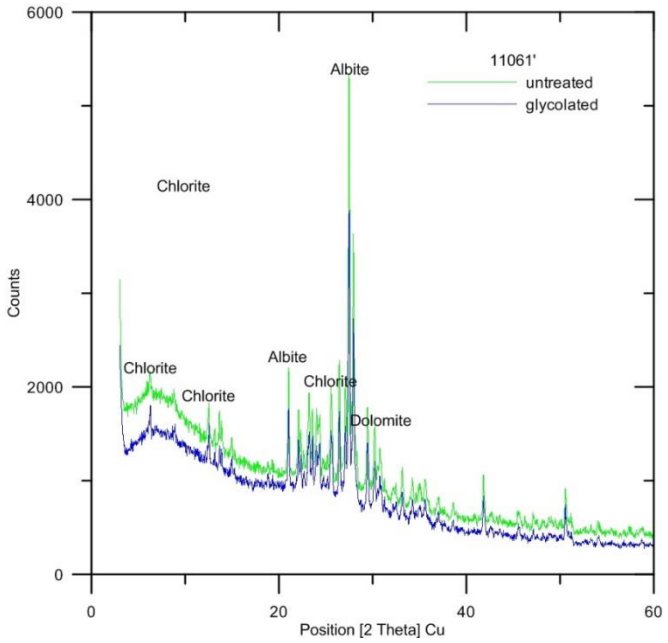

Figure 3.36. X-Ray diffraction pattern of 11,061` core sample. This spectra is showing peaks for chlorite as well as albite and dolomite in the clay-sized matrix fraction.

3.4 THE MCR IGNEOUS VOLCANIC ROCKS

The Keweenawan-age volcanics represent one of the largest igneous provinces in the world and has been investigated extensively around the Lake Superior region. Tholeiitic basalts are the major volcanic rock type with lesser volumes of picrite and rhyolite. Plutonic rocks range in its composition between the ultramafic peridotitic compositions to a felsic granitic compositions. The vast majority of the plutonic rocks display plagioclase-rich gabbro and troctolite compositions (Green, 1982a; Klewin, 1987; Klewin and Berg, 1991; Klewin and Shirey, 1992). The petrographic investigations of the Duluth Complex rocks displayed a troctolitic and peridotitic composition composed of 45% olivine (plus secondary oxides and serpentinite), 40% clinopyroxene and secondary chlorite, 8% plagioclase, 3% hornblende, and minor sericite and traces of Fe-Ti oxides (Southwick et al., 1988; Weiblen and Morey, 1980).

4 GEOCHEMICAL ATTRIBUTES OF MCR SEQUENCES

4.1 BULK CHEMICAL COMPOSITION OF KEWEENAWAN SUPERGROUP ROCKS

The chemical compositions of the major oxides of the MCR samples (SiO_2, Al_2O_3, Fe_2O_3, CaO, MgO, Na_2O, K_2O, MnO, TiO_2, and P_2O_5) were investigated by the XRF chemical analysis. The accuracy was better than 6.3% for all major oxides except for the P_2O_5, which was better than 8.3%. Also, the precision was better than 0.14% for all the investigated oxides (Appendix Table C.1). The bulk chemical composition will be discussed in the following sections, while the chemical analyses for individual samples are presented in Appendix Table C.2 to C.8.

4.1.1 Oronto Group and Equivalent Stratigraphic Units. A chemical analysis of 44 samples taken from the Oronto Group and its laterally equivalent units revealed the presence of a high concentration of both alkaline earth metal oxides (CaO and MgO) and iron oxide as compared to the overlying Bayfield Group and its laterally equivalent units. The SiO_2 content represents the highest oxide concentration (between 50 and 60 wt%). In general, the alkaline earth and alkaline metals, reported as oxides, averaged between 1.0 and 10 wt% of the Oronto Group sediments (see Figure 4.1). Alumina is also abundant with an average of about 12 wt%. Aluminum, alkaline earth metals, and alkali metal oxides represent the main constituents of the feldspars, which were recognized during petrographic examination of the samples. The carbonate cement recognized in the petrographic investigations represents another source for Ca. Further discussion of the Oronto Group sediments from different sampling areas is discussed in the following sections.

4.1.1.1 Copper Harbor Conglomerate (Keweenawan Peninsula). Petrographic investigations of the Keweenawan Peninsula samples revealed an abundance of volcanic rock lithic fragments. The average of the major elements represented in these samples, reported as oxide percent, was approximately 54 wt% SiO_2, 10 wt% alkaline earth metals

(CaO + MgO), 11 wt% Al_2O_3, 9 wt% Fe_2O_3, and 6 wt% alkali metals [Na_2O and K_2O; Figure 4.2(A)]. A detailed chemical analysis of the individual Keweenawan Peninsula samples is given in Appendix Table C.2. The high CaO content could be sourced from plagioclase and/or carbonate cement. An abundance of carbonate cement was detected during petrographic investigations of these samples (Sections 3.1.1.1 to 3.1.1.5). The high Loss on Ignition values (LOI, weight loss upon ashing samples at 1,100 ^oC) for these samples also provides supporting evidence for the presence of carbonate minerals as CO_2 will be volatized during heating of the samples. Additional sources of Ca, Mg, and Fe could be from chlorite, mafic minerals, and opaque mineral oxides.

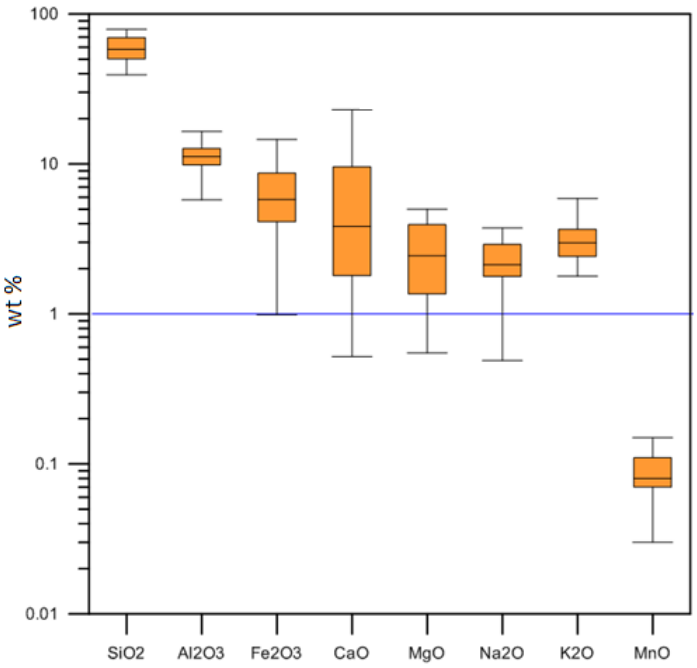

Figure 4.1. Box-Whisker diagram showing the average and standard deviations of the chemical composition of 44 samples of the clastic samples collected from the Oronto Group and its equivalent stratigraphic units. The represented samples were collected from the Keweenawan Peninsula, MI, Potato River Falls, WI, Copper Falls State Park, WI, Superior Falls WI, Saxon Harbor Bay, WI, and the Eischeid #1 Well, IA locations.

4.1.1.2 Copper Harbor Conglomerate (Potato River Falls and Copper Falls State Park samples). The average chemical composition of the alkaline earth metal oxides from CHC samples collected at the Potato River Falls and Copper Falls State Park

locations was approximately 7 wt%. The amount of Na_2O and K_2O was approximately 5 wt%. The iron and aluminum oxides were 13 wt% and 12 wt%, respectively [see Figure 4.2 (B) and Appendix Table C.3]. SiO_2 was the most abundant component in the sediments at 56%.

4.1.1.3 Nonesuch Formation (Potato River Falls samples). The samples collected from the Nonesuch Formation at the Potato River Falls location have an average chemical composition of 8 wt% alkaline earth metals [Figure 4.2 (C) and Appendix Table C.3]. The alkali metal oxides average of 4 wt%, while Al_2O_3 and Fe_2O_3 average of 14 and 13 wt%, respectively. Silica constitutes the major oxide component with an average of about 53 wt%.

4.1.1.4 Unit C (Amoco M. G. Eischeid #1 Well, Iowa samples). The average chemical composition of the Amoco M. G. Eischeid #1 well samples collected from Unit C exhibited an enrichment of the alkaline earth metal oxides [approximately 12 wt% CaO + MgO; Figure 4.2(D)]. The overall chemical composition of these sediments was similar to that of the samples collected from the Keweenawan Peninsula, Copper Falls State Park, and Potato River Falls locations. The detailed chemical composition of the Amoco M. G. Eischeid #1 well samples are given in Appendix Table C.4.

4.1.1.5 Freda Formation (Potato River Falls and Copper Falls State Park samples). Freda sandstone samples were collected from the Potato River Falls (POT8), Copper Falls State Park (CFSP1, 2, and 3), Saxon Harbor (SH), and Superior Falls locations (SF1, 2, 3, and 4). This sample contained approximately 5 wt% sequestration-important metal oxides [i.e. CaO and MgO; Figure 4.2 (E)]. The alkali metal oxides were about 4 wt%, alumina 11 wt%, and iron oxides 6 wt% The SiO_2 constitutes an average of 56 wt% (Appendix Table C3).

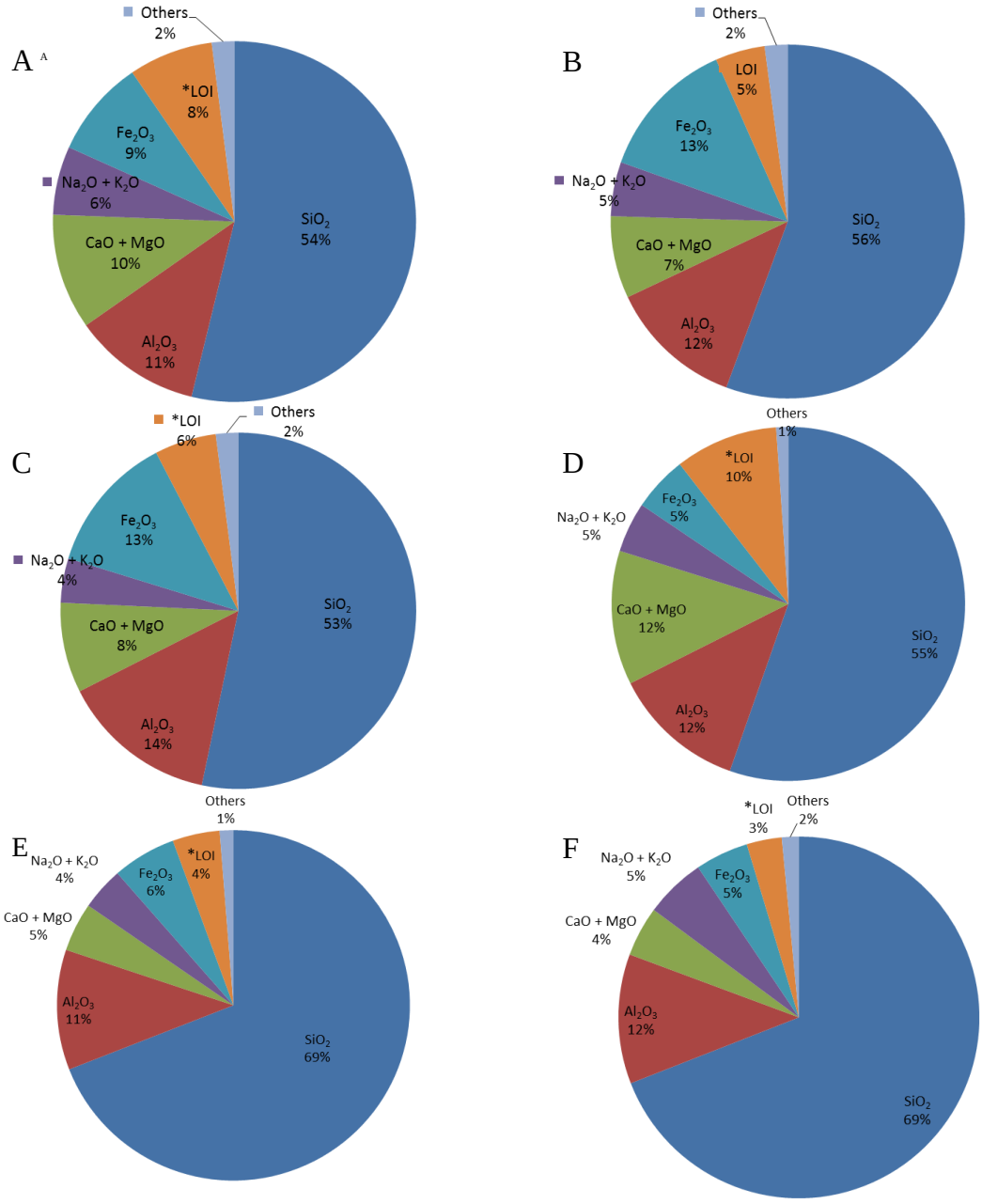

Figure 4.2. Average major oxide composition of Oronto Group samples and its stratigraphically equivalent units. A) CHC from the Keweenawan Peninsula, B) CHC at Potato River Falls and Copper Falls State Park, C) Nonesuch Formation at Potato River Falls, D) Unit C of Eischeid #1 Well, E) Freda Formation at Potato River Falls, Copper Falls State, Saxon Harbor Bay, and Superior Falls, F) Unit D of Eischeid #1 Well. "Others" includes TiO2, P_2O_5, and Ba. LOI represents Loss on Ignition.

4.1.1.6 Unit D (Amoco M. G. Eischeid #1 Well, Iowa Samples). Unit D of the Eischeid #1 well exhibited a significant amount of the alkaline earth metal oxides and alkali metal oxides, 4 and 5 wt%, respectively [Figure 4.2 (F)]. The alumina was 12 wt% and the iron oxide was about 5 wt%. The SiO_2 constituted about 69 wt %, which is the highest average reported in the Oronto Group for the major element oxides (Appendix Table C4).

4.1.2 Bayfield Group and Equivalents. The chemical composition of ten samples collected from the Bayfield and its stratigraphic equivalents (i.e. Jacobsville of L'Anse and Agate Falls area; Unit E of Eischeid #1 well) exhibited relatively low alkaline earth metal oxide contents (between 0.1 and 1.0 wt% CaO + MgO as illustrated in Figure 4.3). Silica represents the highest chemical component in the investigated sample at about 90 wt%. The high silica contents reflect the quartz to feldspar ratios noted during the petrographic analysis of these sedimentary units (Table 3.5). Potassium, aluminum, and iron oxides display a range of chemical compositions from between 0.1 and 1.0 wt%, which could be represent the presence of alkali-feldspar, kaolinite, and the iron oxide cement that was noted during petrographic investigations of the samples.

4.1.2.1 Bayfield Group samples. Results gathered from the major element XRF analysis conducted on the whole rock analysis of BAY1, BAY2, BAY3, and samples displayed high SiO_2 concentrations (92.5 ±5 wt%) and relatively low concentrations for all other oxides [Figure 4.4 (A); Appendix Table C.5]. The alkali metals were, generally, low (~ 3 wt% as oxides), and the alkaline earth metals was almost < 1.0 wt%. The alumina content was relatively high (5 wt%) and related, primarily, to the presence of clay minerals, particularly kaolinite clays (Section 3.2). The high silica content was a result of the quartz-dominated mature sedimentary sequences recognized in the Bayfield Group, petrographically (Table 3.5).

4.1.2.2 Jacobsville sandstone samples. The Jacobsville sandstone samples represented by samples were collected from the Agate Falls (AF) and L'Anse (L'ANSE) in WI. The average of silica content (81.7 ±7 wt %), alumina, alkali metal oxides, and iron oxides were close to those percentages recognized in the Bayfield Group samples [Figure 4.4 (B)]. The average alkaline earth metal oxides were about 1.0 wt%, which approximately derived from the higher Mg content where it compared to the Ca content as shown in the Appendix Table C.5.

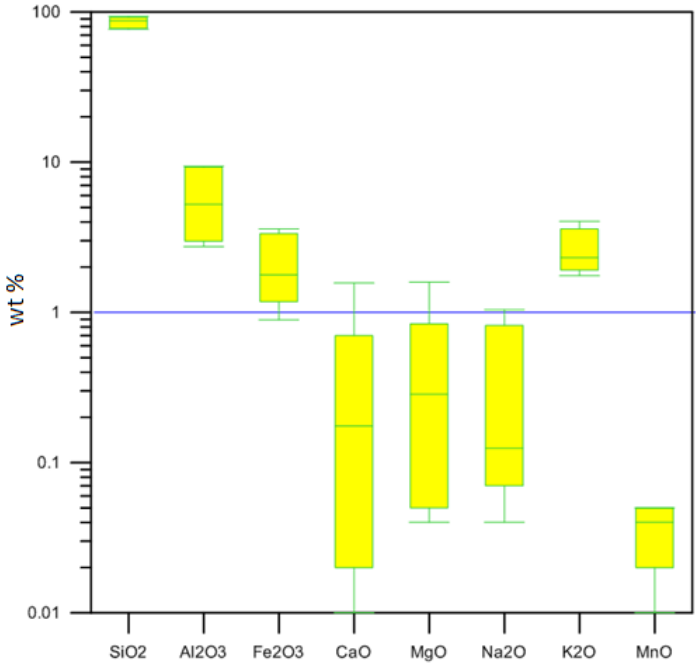

Figure 4.3. Box-Whisker diagram showing the total chemical composition of Bayfield Group and its stratigraphic equivalents. The represented samples were collected from the Bayfield Peninsula, Jacobsville of L'Anse and Agate Falls area, and Unit E of Eischeid #1 well.

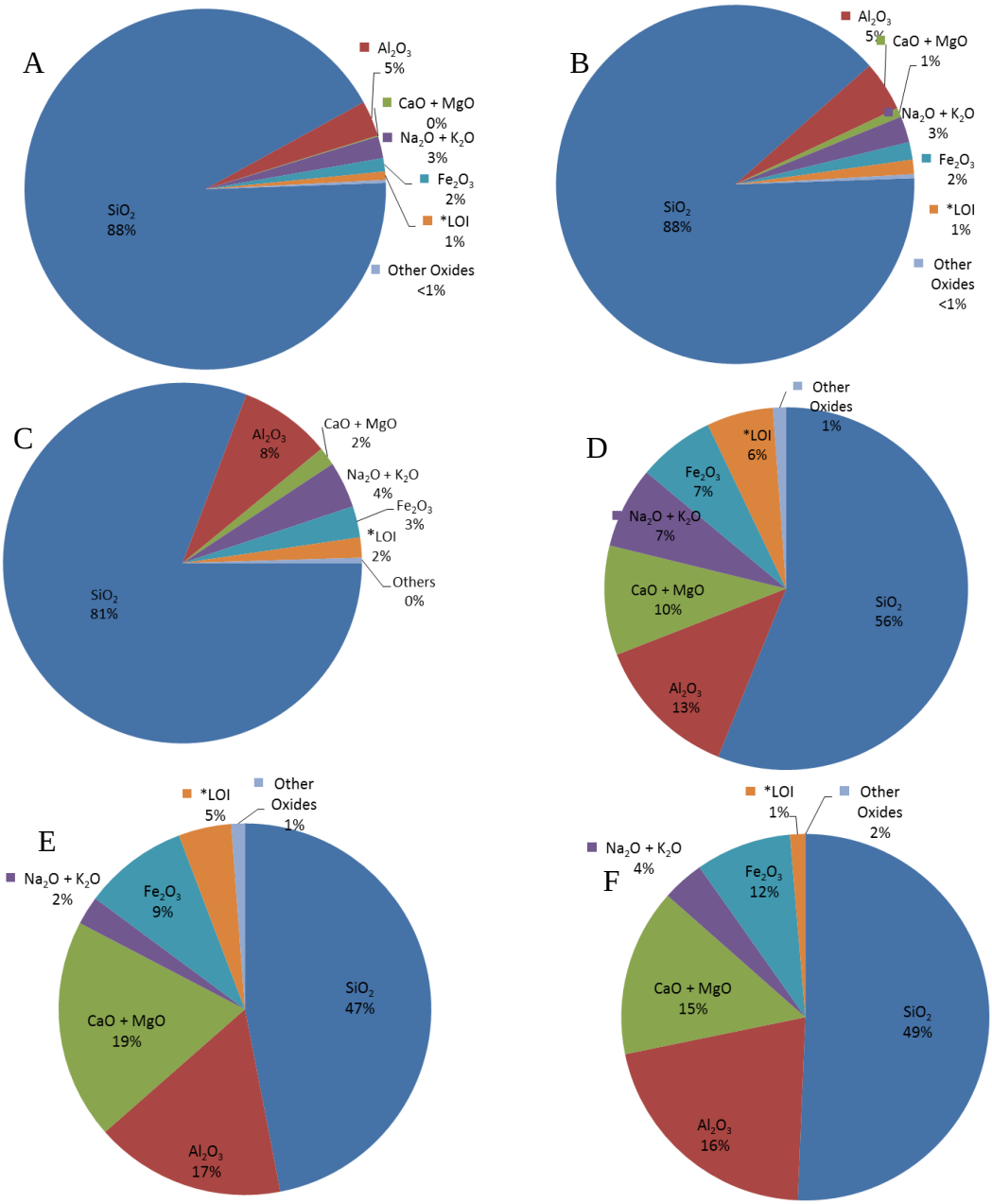

Figure 4.4. Average major oxide element composition of Bayfield Group and its stratigraphic equivalents. (A) Bayfield Group, (B) Jacobsville sandstone, (C), Unit E of Eischeid #1 Well, (D), Texaco Poersch #1 Well, (E), the North Shore Volcanic Group (NSVG) including compositions from Brannon (1984), and (F) Beaver Bay Complex including data from Miller and Chandler (1997). "Others" includes TiO2, P2O5, and Ba. LOI represents Loss on Ignition).

4.1.2.3 Unit E (Amoco M. G. Eischeid #1 Well, Iowa samples). The SiO_2 content in the Unit E was found to be significantly enriched when compared to the other oxides. The alkali metal oxide content was approximately 4 wt% and the alkaline earth metal content was approximately 2 wt% [See Figure 4.4 (C) and Appendix Table C.4]. The chemical determinations correlate with the petrographic characteristics of the Upper Red Clastics, which indicated the presence of a texturally mature sandstone. Because of the existence of calcite cement, identified petrographically in the Unit E2 (8,834 ft samples), the CaO has a significant concentration between 0.7 wt% and 1.57 wt% (Appendix Table C.4). Conversely, the Bayfield and Jacobsville samples displayed a maximum of 0.03 and 0.33 wt% CaO, respectively, and did not display any evidence for carbonate cement in the thin sections (Appendix Table C.5).

4.1.3 Texaco Poersch #1 Well, Kansas. In the results of the XRF analysis of the samples collected from the Texaco Poersch #1 well, the concentration of both Ca and Mg oxides were significantly enriched for most of the samples that had a relatively low Si oxide content (Appendix Table C.6). Higher Na_2O and K_2O concentrations indicated the presence of feldspathic, igneous lithic fragments, and/or clay enriched components. Although the various horizons of the Texaco Poersch #1 well were not correlated stratigraphically to the other MCR sequences, the average chemical composition of the penetrated sections of Poersch #1 Well in Kansas was close to that identified in the Oronto Group sediments from the Lake Superior region [i.e. compare Figures 4.2 to the Figure 4.4 (D)], suggesting that the two units may be time correlative and/or sourced from similar provenience materials. Chemical analyses of the Texaco Poersch #1 volcanic-dominated sequence revealed an enrichment of Ca, Mg, and Fe oxides, which reflects the mafic nature of these rocks and a good potential of these rocks for mineral sequestration of anthropogenic carbon (Berendsen et al., 1988; Appendix Table C.7).

4.1.4 MCR Igneous Rocks. The North Shore Volcanic Group (NSVG) was dominated by tholeiitic basalts along with subordinate, but locally abundant components of felsic volcanism. Brannon (1984) found that tholeiitic basalt samples taken from Good Bay Harbor, MN, exhibited a significant enrichment in their alkaline earth elements (~19 wt%; CaO + MgO) and had relatively low alkali element concentrations [Figure 4.4 (E)].

The NSVG was also characterized by the presence of thin interflow sedimentary rocks that also contained high alkaline earth element contents (11.49 wt% CaO + MgO). Additional components included SiO_2 (52.2 wt%), Al_2O_3 (17.0 wt%), K_2O and Na_2O (3.0 wt%), and Fe_2O_3 (4.18 wt %; Appendix Table C.8). The average chemical composition of Silver Bay anorthosite (this study), Lax Ely gabbro (this study), Lax Lake gabbro (Miller and Chandler, 1997), Blesner Lake gabbro (Miller and Chandler, 1997), Victor Head diabase (Miller and Chandler, 1997), Beaver River diabase (Miller and Chandler, 1997), Silver Bay gabbro (Miller and Chandler, 1997), and upper Manitou gabbro (Miller and Chandler, 1997) exhibited an enrichment of alkaline earth metal oxides (15 wt% average CaO + MgO). The mafic nature of the Beaver Bay Complex is reflected in its relatively low in SiO_2 content [Figure 4.4 (F); Appendix Table C.8]. However, the plutonic felsic rocks, which are a minor component of the complex, are comprised of approximately 73 wt % SiO_2, 0.7 wt % of alkaline earth elements, and 5.8 wt % alkali elements (Miller and Chandler, 1997).

4.2 HIGH PRESSURE-TEMPERATURE (HPT) SIMULATED NEAR-FIELD GEOCHEMICAL REACTIONS

The geochemical conditions at the injection points (*near field*) in the aquifer are represented by high $CO_{2\,(supercritical)}$ and $CO_{2\,(aq)}$, which causes the local acidification of groundwater by the formation of carbonic acid. This acidification is responsible for changing the equilibrium conditions of the aquifer environment (e.g., dissolution of aquifer cement and detrital grains), and exchanging acid protons for the mineral alkali and alkaline earth metals. Selected samples from the MCR rocks were sliced and reacted with deionized water and dry ice at high pressure-temperature conditions to mimic this corrosion environment. The reactants were placed at 90°C in Teflon-vessels until the whole reactor lost one gram from its original weight. Some samples were also treated at different experimental conditions to monitor the effect of larger surface area, less fluid, and lower temperature as explained in Section 1.4.5.

4.2.1 Leachate Solutions Composition. The reaction vessels were left to cool to room temperature, and then, aliquots of each sample were collected and checked for pH, Eh, and the major elements composition as in the following sections.

4.2.1.1 Oronto Group and stratigraphically equivalent units. HPT testing on the samples collected from the Oronto Group and its equivalent stratigraphic units revealed a general trend of weight loss, which was measured after corrosion testing was completed and the samples were dried at room temperature. Weight losses averaged 0.45% (ranged between 0.02% and 1.21%), and that representing a balance of the dissolution that occurred during the testing of the samples, hydration, and secondary mineral phase formation. Two exceptions to this trend were recognized in the CSFP4 and the C2-3 samples, which displayed a slight increase in weight by 0.12% and 0.01%, respectively, from their original weights (Table 4.1). This gain could be due to precipitation of a carbonate solid phase like calcite or formation of secondary hydrated minerals.

The recorded pH taken from the blank samples (containing deionized water and dry ice only) ranged between 3.8 and 4.0. These values represent the minimum pH obtained without the acid buffering effect of the rock samples. The pH range of the leachate solutions after HTP corrosion testing with rock samples present varied between 5.0 and 6.43 (Table 4.1). These increased pH values relative to the blank samples reflected an extensive neutralization of the carbonic acid bearing solutions due to reactions with the host rock minerals. In general, the Eh of the leachate solutions ranged between +31 and +91 mV, so Eh values reflected oxidizing conditions of the leachate fluids.

The ion concentrations released to solution showed variable release amounts from each individual sample (Table 4.2). The element release amount is dependent on the duration of the testing, the surface area of the sample, the corrosion rate and/or solubility of any original minerals in the rock samples, solution pH, Eh for redox for sensitive elements, temperature, and pressure. Also, the precipitation of new mineral phase will decrease the elemental concentrations of any elements that were initially released into

solution (e.g., Fe^{2+} released from pyroxene and precipitated as Fe_2O_3 in oxidizing conditions).

A. Silicon release: Overall, the silicon concentration in the leachate solution collected from the CHC samples varied between 26 ppm in the KEW1-1 and 141 ppm in the CFSP4 (Table 4.2). The leachate fluids collected from the Nonesuch Formation had SiO_2 contents that ranged between 70 and 121 ppm, detected in POT2 sample and POT4 sample, respectively. The Freda sandstone samples released between 28 and 164 ppm of silica as showed in Table 4.2. This silicon may be derived from the corrosion of quartz. However, Si is most likely derived from the hydrolysis of feldspars or other silicate minerals as quartz is known to be relatively inert in the presence of acidic solutions (Garrels and Mackenzie, 1967; Dove and Crerar, 1990; Bennett, 1991; Dove, 1999).

Table 4.1. HTP corrosion test solution data for Oronto Group samples and equivalents stratigraphic units. The data is following reactions in a $CO_2 + H_2O$ system at 90°C. All KEW, and CFSP prefixes denote Copper Harbor Conglomerate, as well as sample POT8; POT2, POT4, and POT5 are Nonesuch Formation samples; SF and SH are Freda sandstone samples; C2 is Unit C; and D4 is Unit D from the Eischeid Well in Kansas.

Sample ID	Location	Surface area (cm^2)	% weight loss/gain	pH final	Eh (mV)	Time (days)
KEW1-1	Keweenaw P., MI	5.6	-0.48%	6.08	+50	6.0
KEW4-2	Keweenaw P., MI	4.8	-0.20%	5.87	+67	87.8
KEW5-1	Keweenaw P., MI	5.6	-0.45%	5.00	+31	102
POT8-2	Potato R. F., WI	4.8	-0.08%	5.80	+78	25.0
CFSP4	Copper F. P., WI	5.0	+0.12%	5.78	+68	48.8
POT2	Potato R. F., WI	5	-0.80%	6.43	+33	43.0
POT4	Potato R. F., WI	4.3	-0.03%	6.22	+67	25.0
POT5-1	Potato R. F., WI	6.0	-0.65%	6.42	+72	34.0
SF1-1	Superior F., WI	8.5	-0.08%	5.78	+68	59.9
SF3-1	Superior F., WI	12.1	-0.12%	5.86	+65	59.9
SH1	Saxon H., WI	11.8	0.02%	5.38	+91	59.9
SF1-2	Superior F., WI	10.1	-0.02%	6.16	+47	59.9
SF3-2	Superior F., WI	12.4	-0.06%	5.82	+67	59.9
SH2	Saxon H., WI	11.7	-0.00%	5.38	+93	59.9
C2-1	Eischeid #1, IA	6.3	-1.21%	6.24	+45.7	26.5
C2-2	Eischeid #1, IA	6.2	-0.87%	5.77	+58.2	43.0
C2-3	Eischeid #1, IA	7.0	+0.01%	5.65	+80.8	26.5
C2-5	Eischeid #1, IA	4.5	-0.46%	5.71	+84.0	14.0
D4-1	Eischeid #1, IA	7.2	-0.79%	5.85	+53	43.0
D4-2	Eischeid #1, IA	3.8	-0.94%	6.00	+66.5	18.0

The concentration of silicon was converted to the molal concentration, and normalized to the surface area of the sample, reaction duration, and expressed in mol/cm^2.day. The initial concentration of SiO_2, obtained from the XRF analysis of the CHC solid samples, was relatively high (54 wt% - 56 wt%) when compared to other elements. However, the normalized release rate of the Si from the CHC was low (between 4.62×10^{-6} and 2.67×10^{-5} mol/cm^2.day; Appendix Table D.9). Also, the Nonesuch Formation release rate of silicon was low and ranged between 5.96×10^{-6} and 4.01×10^{-5} mol/cm^2.day. The Si release from the Freda sandstone was between 1.55×10^{-7} and 4.87×10^{-5} mol/cm^2.day, which was also low when compared to other elements such as Ca (e.g., Figures 4.5 to 4.7). Based on the Goldich stability of minerals, silicon dissolution rate is most likely controlled by the dissolution of mafic silicate minerals (e.g., Ca-feldspars and pyroxenes). As a result, the rate of silicate mineral hydrolysis can be implied from the rate of Si release and/or the Ca, Na, K, and Mg release rates.

B. Calcium release: The CHC samples released the highest amount of Ca at a maximum concentration of about 915 ppm (KEW5-1). The lowest recorded Ca concentration from the CHC samples was from the CFSP4 sample at about 282 ppm. The Ca release detected from the Nonesuch and the Unit C samples ranged between 44.6 ppm in C2-3 to 58 ppm in the POT2 sample. The Freda sandstone leachate fluid samples had a Ca release concentrations between 451 and 486 ppm (Table 4.2). Calcium is important for geologic sequestration because of its ability to react with carbonate to produce calcite, aragonite, vaterite, or other mixed composition of alkali and alkaline earth carbonate minerals. Generally the Oronto Group samples released the highest amount of Ca into the solution as a result of the presence of abundant calcite cement and vein infilling (Section 3.1). Dissolution of carbonate minerals of course would not result net increase of carbonate mineralization.

Samples from the CHC had a very high normalized Ca release rates. For example, the release rate was approximately 5.21×10^{-4} mol/cm^2.day for the KEW1-1 (Figure 4.5) and 4.71×10^{-5} mol/cm^2.day for the KEW4-2 samples (Appendix Table D.9). The molal release rate of Ca was 10-times greater than the rate for either the Mg or the Si, especially for the samples that contained a high percentage of calcite cement (e.g., 10% for KEW1-

1). The Nonesuch Formation and Unit C samples displayed release rates ranging between 6.0×10^{-6} and 6.97×10^{-5} mol/cm^2.day. The Freda sandstone sample displayed high release rates of calcium that ranged between 3.39×10^{-7} and 1.77×10^{-4} mol/cm^2.day. An exception was noted with the Superior Falls (SF) and Saxon Harbor (SH) samples, which had a release rates below 1.27×10^{-6} mol/cm^2.day. The main cause for the higher release rate of the Ca is due to the rapid dissolution of calcite cement upon exposure to the acidified leachant solution. A high dissolution rate of calcite cement indicates secondary porosity could be created or enhanced by CO_2 acidification in a carbon sequestration system.

Table 4.2 Chemical composition of leachate solutions of Oronto Group and its equivalent stratigraphic units. The samples were collected after opening the HPT vessels for the Keweenawan Supergroup samples (KEW), Potato River Falls (POT), Copper Falls State Park (CFSP), Superior Falls (SF), Saxon Harbor (SH), Unit C (C2), and Unit D (D4). Values are in ppm (mg/L). Accuracy is shown in Appendix Tables D2, D3, and D5; Molal concentration data is shown in Appendix Table D.8.

Unit	Sample ID	Si	Al	Fe	Ca	Mg	K	Na	Mn
CHC	KEW1-1	26.0	< 0.1	< 0.1	702	39.0	17.0	4.3	7.8
	KEW4-2	64.0	< 0.1	< 0.1	796	166	23.0	4.8	3.2
	KEW5-1	74.0	< 0.1	< 0.1	915	134	22.0	12.0	3.1
	POT5-1	51.0	< 0.1	< 0.1	600	120	19.0	7.7	0.1
	CFSP4	141	< 0.1	< 0.1	282	109	51.0	1.0	10
Nonesuch and Unit C	POT2	70.0	< 0.1	< 0.1	459	128	32.0	4.4	0.1
	POT4	121	< 0.1	< 0.1	230	81.0	15.0	2.9	17
	C2-1	28.3	< 0.1	0.1	267	35.3	16.3	15.9	0.1
	C2-2	44.6	< 0.1	0.1	376	8.8	5.5	5.5	1.2
	C2-3	44.6	< 0.3	0.8	44.6	27.8	9.3	14.1	1.5
	C2-5	10.8	< 0.1	0.1	176	13.8	8.5	13.7	0.8
Freda and Unit D	POT8-2	164	< 0.1	< 0.1	230	16.0	29.0	5.4	2.1
	SF1-1	41.2	< 0.1	< 0.1	223	36.7	9.0	18.4	2.0
	SF1-2	37.3	< 0.1	< 0.1	159	29.7	8.2	16	0.6
	SF3-1	41.2	< 0.1	< 0.1	287	37.6	6.8	15.9	1.7
	SF3-2	27.9	< 0.1	< 0.1	167	20.3	5.9	12.9	0.3
	SH-1	36.7	< 0.1	< 0.1	67.0	32.2	9.5	13.2	1.7
	SH-2	37.0	< 0.1	< 0.1	58.0	29.0	8.4	12.2	2.2
	D4-1	68.1	< 0.1	0.1	451	14.8	12.0	12.3	4.0
	D4-2	36.3	< 0.1	0.1	486	7.0	7.6	5.6	3.5

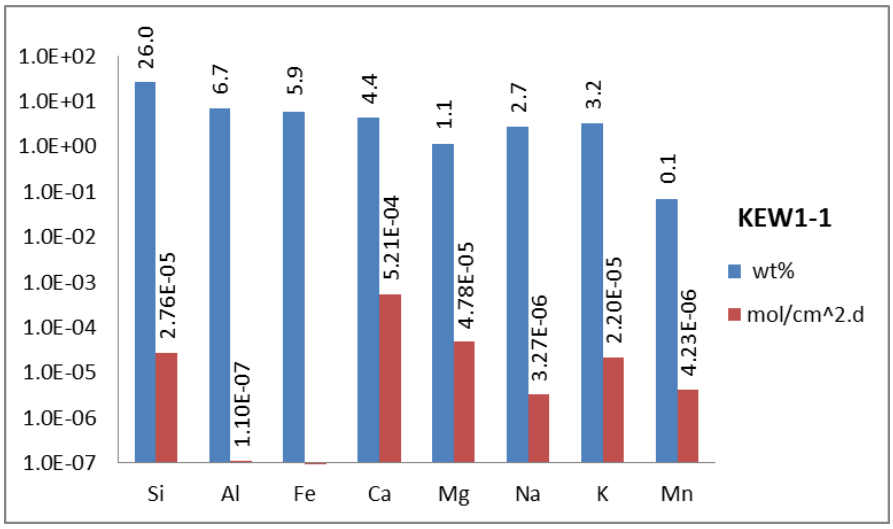

Figure 4.5 Comparison between the normalized dissolution release rate (red bars, in mole/m^2.sec) and the concentration of elements in wt% in the unreacted solid KEW1-1 sample (CHC).The chart is showing that the fastest release rate results from Ca. Dissolution testing was conducted at 90°C in a $H_2O + CO_2$ solution for 6 days.

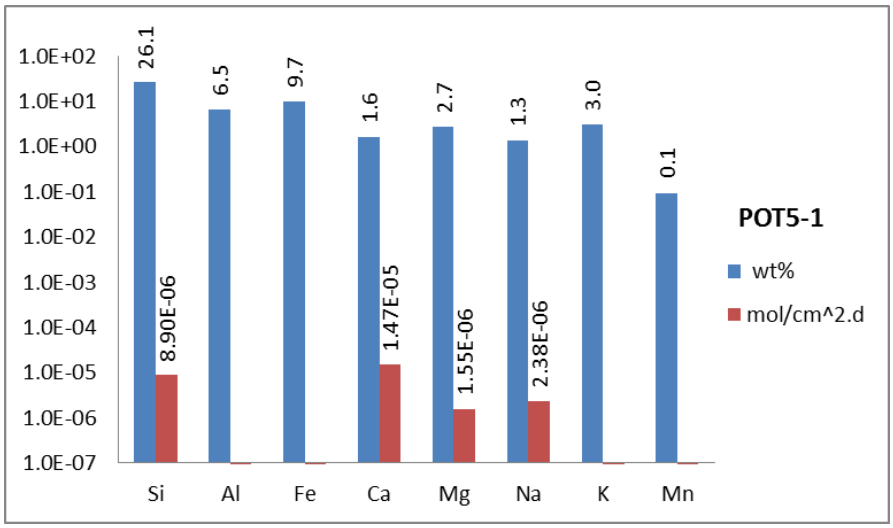

Figure 4.6 Comparison between the normalized dissolution release rate (mole/m^2.sec) and the initial concentration of elements in wt% of unreacted POT5-1 sample (Nonesuch Formation). This chart is showed that the fastest release rate belongs to Ca. Dissolution testing was conducted at 90°C in a $H_2O + CO_2$ solution for 34 days.

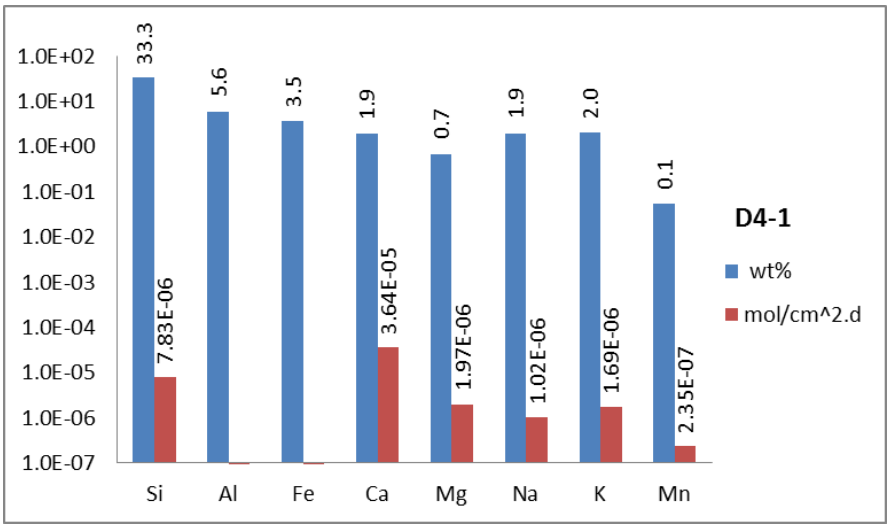

Figure 4.7 Comparison between the normalized dissolution release rate (mole/m^2.sec) and the initial concentration of elements in wt% of the unreacted D4-1 sample (Unit D). That chart is showing that the fastest release rate belongs to Ca. Dissolution testing was conducted at 90^{o}C in a H_2O + CO_2 solution for 59 days.

C. Magnesium release: Solid rock samples with the highest concentration of Mg commonly produced a higher Mg leachate concentrations. The concentration of Mg in CHC leachate solutions ranged between 39 and 166 ppm. Meanwhile, the Mg concentration released from the Nonesuch Formation samples ranged between 8.8 and 128 ppm, also, the Freda Formation samples released between 7 and 37 ppm (Table 4.2). Isolated calcite cement samples were collected from the KEW1 and the KEW4 samples and completely digested in a 5% nitric acid solution and then analyzed to investigate the Ca/Mg ratio in the calcite. The average mole fraction of Ca and Mg in the cement samples was dominated by low Mg-calcite (i.e. Ca was 99.46 mole% and Mg was 0.54 mole %). Thus, any significant release of Mg during HPT experimentation is more likely to be derived from the hydrolysis of Mg-bearing silicate minerals rather than calcite dissolution.

The release rates of Mg from samples collected from the CHC and stratigraphically equivalent units were between 1.69×10^{-7} and 4.78×10^{-5} mol/cm^2.day. In the Nonesuch Formation and the Unit C samples the release rates of Mg were between 8.42×10^{-7} and 9.17×10^{-6} mol/cm^2.day. Freda sandstone and Unit D samples released Mg at a rate between 1.3×10^{-7} and 5.49×10^{-6} mol/cm^2.day (Appendix Table D.9).

D. Potassium and sodium release: Little correlation exists between the amount of K and Na in the rock samples versus the amount released into the solution (Figures 4.5 to 4.7). Potassium and sodium are often released from feldspars, clay minerals, and other phyllosilicate minerals *via* H^+ ions exchange processes with or other alkali and alkaline earth elements present in solution. Although these ions may not directly complex with the CO_3^{2-} ions to precipitate as carbonate mineral phases (as discussed in Section 2.4), their release into the solution would contribute to the acid buffering capacity of the fluid-rock system due to the exchange of H^+ for K^+ and/or Na^+. Potassium, sodium, and calcium are often found in zeolite minerals within the MCR volcanic rock sequence as well.

The CHC samples released Na into the solution between 1 and 12 ppm, while K was released between 17 and 51 ppm. The Nonesuch and Unit C samples released between 4.4 to 15.9 ppm Na, while the amount of K released was between 5.5 to 16.3 ppm. The Freda sandstone and the Unit D samples released between 5.4 to 18.4 ppm Na and 5.9 to 29 ppm K, respectively (Table 4.2). The release rate of Na for the CHC samples was between 2.9×10^{-7} and 5.35×10^{-6} mol/cm^2.day; while K was between 2.13×10^{-8} and 2.2×10^{-5} mol/cm^2.day. Nonesuch Formation and Unit C release rates for Na were between 5.28×10^{-7} and 5.56×10^{-6} mol/cm^2.day, while K was between 2.02×10^{-8} and 6.88×10^{-6} mol/cm^2.day. The Freda Formation and Unit D samples had a release rates of Na ranging between 5.3×10^{-8} and 2.1×10^{-6} mol/cm^2.day. Meanwhile, K release ranged from was 4.3×10^{-8} and 1.05×10^{-5} mol/cm^2.day (Appendix Table D.9).

E. Aluminum, manganese, and iron release: In general, the cations of Al, Mn, and Fe represented the smallest fraction of elements released into the leachate solution for samples collected from the Oronto Group. The reason is related to the stability of their mineral species under these experimental conditions (i.e. pH, Eh, temperature, and pressure) or the formation of stable alteration phases that that contain these components (Table 4.1 and 4.2).

4.2.1.2 Bayfield Group and stratigraphically equivalent units. The weight loss of the tested samples collected from the Bayfield Formation and its stratigraphically equivalent units reflected a slight decrease in weight (weight loss between 0.08% in E2-4 sample and 1.24% in the E2-2 sample) after testing was complete (Table 4.3). The pH increased from approximately 4.0 to a maximum of 5.9 due to the cation exchange reactions that consumed the H^+ ions. The Eh of the leachate solution exhibited oxidizing condition (+14 to +127.5 mV).

A. Silicon release: The amount of silicon released from the Bayfield, Jacobsville, and Unit E samples was between 18.6 ppm in the E2-3 sample and 64 ppm in the L'ANSE sample (Table 4.4). The release rate of silica from the Bayfield Group and its stratigraphically equivalent units was between 1.18×10^{-6} and 2.46×10^{-5} mol/cm^2.day (Appendix Table D.11).

B. Calcium release: The Ca concentration of the Bayfield sample leachate solutions was relatively low (4 ppm) when compared to those for both the Jacobsville (between 9.4 to 27.5 ppm) and the Unit E samples (between 26.5 to 496.9 ppm; Table 4.4). The calcite cement, which was identified only in limited amounts in the petrographic study of the Jacobsville sandstone and Unit E samples, was the most likely the source of the Ca in the solution.

The Bayfield samples exhibited lower Ca release rates than the Oronto Group and its stratigraphically equivalent units. Only ~1% calcite was revealed in the petrographic study of the Unit E samples from the Eischeid #1 well core, which is stratigraphically equivalent to the Bayfield. The calcium release rate was 3.19×10^{-6} mol/cm^2.day for the BAY3 sample, between 7.31×10^{-7} and 1.75×10^{-6} mol/cm^2.day for the Jacobsville samples, and between 6.56×10^{-6} and 5.37×10^{-5} mol/cm^2.day for the Unit E2 of the Eischeid #1 well samples (Figure 4.8 and Appendix Table D.11).

Table 4.3 Sampling and HTP test data for Bayfield and its stratigraphic equivalents.Legend; Bayfield sample (BAY), L'Anse (L'ANSE), Eischied #1 well (E), and Agate Falls (AG) samples following reaction in a CO_2 + H_2O system at 90°C. BAY is Bayfield Group; L'ANSE and AF are Jacobsville sandstone; andE2 is Unit E.

Sample ID & depth	Location	Surface area (cm^2)	% weight loss/gain	pH final	Eh (mV)	Time (days)
BAY 3	Bayfield, WI	6.6	-0.38%	5.39	+86	19.8
L'ANSE1	L'Anse, MI	10.0	-0.09%	4.78	+14	37.8
AG-1	Agate Falls, MI	11.6	-0.12%	5.06	+109	59.9
AG-2	Agate Falls, MI	12.6	-0.17%	5.59	+79	59.9
E2-2 (8,834′)	Eischeid #1, IA	4.5	-1.24%	5.90	+53	50.0
E2-3 (8,835′)	Eischeid #1, IA	4.5	+0.10%	4.96	+127	6.0
E2-4 (8,836′)	Eischeid #1, IA	4.7	-0.08%	5.06	+104	50.0

Table 4.4 Chemical composition of leachate solutions of Bayfield and stratigraphically equivalent units.The samples were collected after opening the HPT vessels for Bayfield sample (BAY), L'Anse (L'ANSE), Eischeid #1 well (E), and Agate Falls (AG). Values are in ppm (mg/L). Accuracy is shown in Appendix Tables D2, D3, and D4; Molal concentration is shown in Appendix Table D.10.

Unit	Sample ID	Si	Al	Fe	Ca	Mg	K	Na	Mn
Bayfield	BAY3	30.0	132	17.0	4.0	18.0	10.0	3.7	10.0
Jacobsville	L'ANSE1	64.0	<0.1	27.0	9.4	28.0	7.3	1.0	1.0
	AG-1	30.4	1.8	1.8	27.5	11.4	24.4	1.6	2.1
	AG-2	25.0	0.1	0.1	22.5	9.7	21.2	1.4	1.3
Unit E	E2-2 (8,834′)	50.5	<0.1	<0.1	496	3.7	4.8	4.4	0.6
	E2-3 (8,835′)	18.6	<0.1	0.3	26.5	1.4	4.5	4.5	1.1
	E2-4 (8,836′)	48.6	0.2	<0.1	63.3	3.2	7.7	7.8	2.3

C. Magnesium release: The Mg release from the Jacobsville Formation samples had a maximum release of 28 ppm in L'ANSE1 sample. Sample E2-2 reached a maximum concentration (3.7 ppm) among the group of E2 samples. The Bayfield sample had a released concentration of 18 ppm Mg. The Mg release rate was lower than that of Ca and ranged between 5.29×10^{-7} and 2.14×10^{-6} mol/cm^2.day (Figure 4.8; Appendix Table D.11). The Ca/Si ratio was significantly high in the E2-4 sample, which reflects an important source of both Si and Ca like Ca-plagioclase.

D. Potassium and sodium release: These elements were released in small quantities into the leachate solutions. Potassium was released at a 24.4 ppm maximum concentration and Na was 7.8 ppm maximum (Table 4.4). The maximum release rates of K and Na were 7.28×10^{-6} and 4.28×10^{-6} mol/cm^2.day, respectively, and these rates were much lower that the release rates for Si and Ca (Appendix Table D.11).

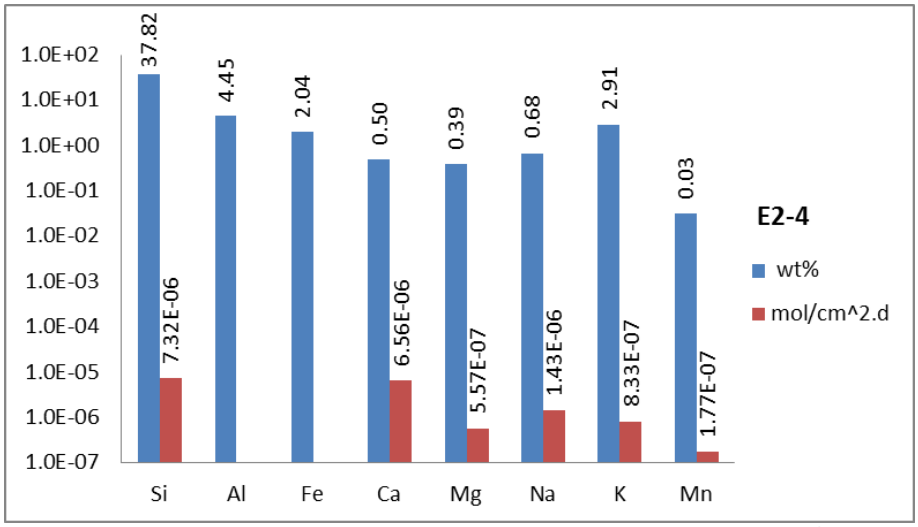

Figure 4.8 Comparison between the normalized dissolution rate (mole/m^2.sec) and the initial concentration of elements in wt% of E2-4 sample (Unit E of Eischeid #1 well, IA). This chart is showing the fastest release rates for Ca and Si. Dissolution testing was conducted at 90^{o}C in a $H_2O + CO_2$ solution for 50 days.

E. Aluminum, manganese, and iron release: The overall iron release was generally very low due to the low solubility that commonly exhibited by Fe^{3+} bearing mineral compounds. The BAY3 and L'ANSE1 samples, however, released a significant amount of Fe at 17 and 27 ppm concentrations, respectively, while all other samples were <1.8 ppm in general. The aluminum was highly insoluble under our experimental setting as evidenced by the very low Al release data collected (Table 4.4).

4.2.1.3 Texaco Poersch #1 Well, Kansas. Fourteen samples from the Texaco Poersch #1 well in Kansas were reacted in the HTP testing apparatus. The pH values, taken immediately after testing, were variable and dependent on the extent of H^+ exchange with the rock-forming minerals. All of the samples displayed a rise in pH from

a 3.8 starting leachant value to final values of between 5.73 and 6.12. All of the samples tested also exhibited some weight loss during testing, indicating that corrosion had occurred. The samples displayed a range of weight loss between 0.22% and 1.26% (Table 4.5). No clear stratigraphic correlation exists between the Texaco Poersch #1 well in Kansas and either the Eischeid well in Iowa or the surface outcrops of MCR rocks in the Lake Superior region. Therefore, the Texaco Poersch #1 leachate solutions cannot be directly correlated as an equivalent unit to the Oronto or Bayfield Groups.

A. Silicon release: The amount of silica released during the HPT testing of the Texaco Poersch #1 well sample was between 45.8 and 48.9 ppm in the uppermost mixed clastic-volcanic sequence (5,397.3′ - 5,404′). The lowermost clastic-dominated sequence (8,051′ - 11,061′) had a silica release into solution that varied from 76.4 ppm in the 8,051.1′A sample to 9.2 ppm in the 11,061′A sample (Table 4.6). The uppermost volcanic-dominated sequences displayed slightly higher Si release rates (i.e. 8.33×10^{-6} mol/cm^2.day in 5,404′A sample and 4.7×10^{-7} mol/cm^2.day in 5,397.3′A sample) relative to the lowermost mixed clastic-dominated sequences (i.e. 2.2×10^{-6} mol/cm^2.day in 8,051.1′B sample and 2.3×10^{-7} mol/cm^2.day in 10,514′B sample; Appendix Table D.13).

Table 4.5 HTP test data for Texaco Poersch #1 well samples (Kansas) following reaction in a $CO_2 + H_2O$ system at 90°C.

Sample ID	Location	Surface area (cm^2)	% weight loss/gain	pH final	Eh (mV)	Time days
5,397.3′ A	Poersch #1 Well, KS	9.9	-0.42%	5.94	+47.6	43.0
5,404′ A	Poersch #1 Well, KS	9.5	-0.22%	5.73	+82.0	22.0
8,051.1′ A	Poersch #1 Well, KS	7.8	-1.26%	5.79	+59.3	95.0
8,476′-8,480′ A	Poersch #1 Well, KS	8.9	-1.20%	6.03	+64.9	18.0
10,514′ A	Poersch #1 Well, KS	7.8	-0.92%	5.87	+75.0	14.0
10,666′ A	Poersch #1 Well, KS	10.8	-0.97%	5.84	+76.3	22.0
11,061′ A	Poersch #1 Well, KS	7.0	-0.96%	5.85	+74.8	3.0
5,397.3′ B	Poersch #1 Well, KS	10.0	-0.28%	6.12	+51.7	26.5
5,404′ B	Poersch #1 Well, KS	9.6	-0.17%	-	-	36.0
8,051.1′ B	Poersch #1 Well, KS	7.1	-0.73%	5.78	+75.4	3.0
8,476′-8,480′ B	Poersch #1 Well, KS	8.6	-1.17%	5.81	+72.7	6.0
10,514′ B	Poersch #1 Well, KS	9.3	-1.19%	5.8	+59.0	95.0
10,666′ B	Poersch #1 Well, KS	9.6	-0.74%	5.9	+72.0	14.0
11,061′ B	Poersch #1 Well, KS	7.1	-1.26%	5.77	+60.9	71.0

Table 4.6 Chemical composition of leachate solutions collected after opening the high-pressure vessels for Texaco Poersch #1 well samples, Kansas. Values are in ppm (mg/L). The accuracy range is between 0.91 ppm and 1.12 ppm for a 1 ppm concentration standard (Accuracy data is shown in Appendix Table D2; Molal concentration is shown in Appendix Table D.12). UMVSS is upper mixed volcanic-sedimentary sequence; USS is upper sedimentary sequence; MSS is middle sedimentary sequence; and LSS is lower sedimentary sequence.

Unit	Sample ID	Si	Al	Fe	Ca	Mg	K	Na	Mn
UMVSS	5,397.3′ A	48.6	<0.1	<0.1	54.2	240	19.6	99.9	0.1
	5,397.3′ B	45.8	<0.1	<0.1	158	120	13.1	63.6	3.4
	5,404′ A	48.9	0.2	<0.1	110	48.6	16.6	41.9	1.9
USS	8,051.1′ A	76.4	<0.1	<0.1	513	2.4	4.7	7.1	3.0
	8,051.1′ B	11.8	<0.1	<0.1	342	1.6	2.8	2.5	2.3
	8,476-8,470′ A	37.4	<0.1	<0.1	502	4.9	2.8	4.9	4.1
	8,476-8,480′ B	20.9	<0.1	<0.1	518	4.8	2.0	3.5	3.5
MSS	10,514′ A	16.4	<0.1	<0.1	419	1.1	1.8	3.0	3.6
	10,514′ B	51.3	<0.1	<0.1	497	1.5	2.6	7.4	4.5
	10,666′ A	21.5	<0.1	<0.1	242	25.9	3.7	15.1	5.7
	10,666′ B	25.4	<0.1	<0.1	360	32.6	3.5	15.1	8.6
LSS	11,061′ A	9.2	<0.1	0.3	363	1.2	2.3	4.3	1.4
	11,061′ B	39.5	<0.1	<0.1	566	1.1	3.5	7.8	1.5

B. Calcium and magnesium release: Both Ca and Mg release concentrations varied with the initial sample weight percentage for each element. The calcium release range was between 54.4 ppm in 5,397.3′ sample and 566.4 ppm in the 11,061′B sample. Magnesium release, however, was more than 120 ppm in the 5397.3′A and B samples and less than 48.6 ppm in the rest of the samples (Table 4.6). Both calcite and dolomite peaks were identified in the XRD analysis (as discussed in Section 3.3). The XRD spectra also displayed well-developed peaks for the mica phlogopite in all of the upper volcanic-dominated sequence, thus the Mg-rich mica (phlogopite) represents a potential source of Mg in the 5,397.3′ samples, which was released to a concentration of 240.4 ppm maximum. In the Texaco Poersch #1 samples, the release rate of Ca was generally found to be high (e.g., 100-fold or more than K, Na, Mg, and 25-fold more than Si in the 11,061′ sample; Figure 4.9; Appendix Table D.13). A significant amount of Ca and Mg could also be enhanced by the presence of dolomite cement in the lower arkosic-dominated sequence of the Texaco Poersch #1 well. The arkosic nature of the lower clastic-dominated sequence could be responsible for the release rate of the alkali metals.

C. Potassium and sodium release: The K and Na released from the uppermost mixed clastic-volcanic section were significantly higher than the release from the lowermost clastic dominated sequence (Table 4.6). The concentration of K was 4.7 ppm maximum in the lowermost clastic dominated sequence and 13.1 ppm or more in the uppermost mixed clastic-volcanic sequence, while the Na release was less than 15.1 ppm maximum in the lowermost clastic dominated sequence and 41.9 ppm or more in the uppermost mixed clastic-volcanic sequence. Overall Na release rates were between 4.22×10^{-8} and 8.72×10^{-6} mol/cm^2.day, while, K release rate ranged between 8.71×10^{-9} and 2.03×10^{-6} mol/cm^2.day (Appendix Table D.13).

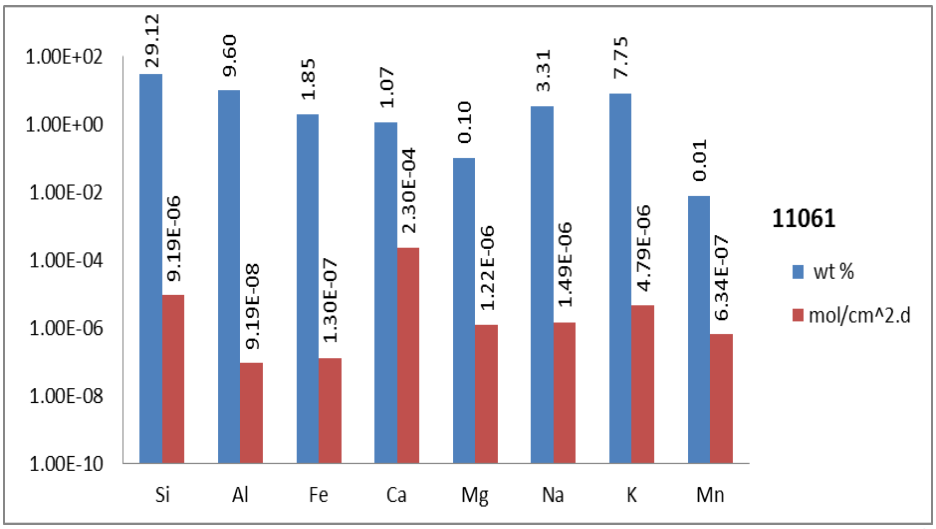

Figure 4.9 Comparison between the normalized dissolution release rate (mole/m^2.sec) and the initial concentration of elements in wt% of 11,061′ sample of Texaco Poersch #1 well, core #13.This sample is showing that the fastest release rate belongs to the Ca. Dissolution testing was conducted at 90^{o}C in a $H_2O + CO_2$ solution for 71 days.

D. Aluminum and iron release: Both Al and Fe concentrations were very low with a maximum of 0.3 ppm of iron in the 11,061′A sample and 0.2 ppm of aluminum in the 5,404′A sample (Table 4.6). The low concentrations of these elements are likely related to the relatively insoluble nature of iron and aluminum bearing alteration phases.

4.2.1.4 MCR Igneous Rocks. Only a limited number of igneous rock samples were tested using the HPT apparatus. These rocks representing common sources for the clastic rocks in the MCR sequence. Igneous rocks included the Beaver Bay (BEV) anorthositic sequence, the Duluth Complex (DUL) gabbro and the North Shore Volcanic Group (NSVG) basalts. These samples exhibited significant alteration during high temperature-pressure corrosion testing; especially the basaltic rocks (weight loss between 1.18% and 3.78%). The clastic interflow sediment GHC-1 and GHC-2 samples revealed a significant weight gain (0.42%) and a weight loss (-0.07 %), respectively. The pH of the aqueous solutions contacting the tested samples increased significantly from the initial pH of approximately 3.8 to between 5.0 and 6.1 in the NSVG basaltic samples. The Eh in the Beaver Bay (BEV) anorthositic sample experiment was higher than that in both the North Shore Volcanic Group (NSVG) samples and the Duluth Complex (DUL) samples (Table 4.7). Measured Eh values were +124.4 and +103.6 mV for BEV1 and BEV2, respectively. Meanwhile the maximum Eh for the NSVG and DUL samples was +64.7 mV.

Table 4.7 Sampling and HTP test data for MCR igneous rocks samples. The data is following reaction in a CO_2 + H_2O system at 90°C. BEV is Beaver Bay Complex; DUL is Duluth Complex; GHB is Good Harbor Bay basalt (North Shore Volcanic Group); GHC is Good Harbor Bay clastic interflow sediment.

Sample ID	Location	Surface area (cm^2)	% weight loss/gain	pH Final	Eh (mV)	Time (Days)
BEV1	Silver Bay, MN	-	-	5.0	+124.4	10.0
BEV2	Silver Bay, MN	5.0	-	-	+103.6	43.0
DUL-1	Hwy 1, Ely, MN	5.7	-0.15%	5.92	+60.9	59.9
DUL-2	Hwy 1, Ely, MN	5.6	-0.21%	5.84	+64.7	59.9
GHB-1	Good Harbor Bay, MN	17.0	-3.78%	6.12	+48.7	59.9
GHB-2	Good Harbor Bay, MN	17.1	-1.18%	5.87	+64.0	59.9
GHC-1	Good Harbor Bay, MN	9.4	+0.42%	5.93	+60.4	59.9
GHC-2	Good Harbor Bay, MN	8.8	-0.07%	6.22	+44.1	59.9

A. Silicon release: The silicon released from the corrosion test samples exceeded 120 ppm for the clastic interflow GHC-1 (sedimentary clastic bed sandwiched between

flow basalts). The other samples were, primarily, below 90 ppm (Table 4.8). The silicon concentration in the leachate solution reflects the amount of silicate mineral' dissolution that could occur during the testing period. The rate of Si release was varied between 1.09×10^{-6} mol/cm^2.day maximum and 1.78×10^{-7} mol/cm^2.day minimum as illustrated in the Appendix Table D.15.

B. Magnesium, calcium, and iron release: The presence of the mafic silicate minerals could represent a possible source of Ca, Mg, and Fe into the leachate solutions. Both the DUL and BEV gabbroic samples were characterized by a small release of Ca into the solution (<39.4 ppm) when compared to the NSVG samples (>123.6 ppm). Due to the mafic nature (i.e. Mg-Fe-rich) of theses volcanic units, the Mg concentration was relatively high in all samples (66.7 ppm minimum) except for the BEV samples, which had a maximum release of 16 ppm Mg. Iron was also released in high concentrations, especially from the basaltic GHB samples, but eventually precipitated as iron oxides or hydroxides on the surfaces of the Teflon vessels (see Section 4.2.2.2).

The release rate of Ca and Mg was between 3.29×10^{-7} and 2.68×10^{-6} mol/cm^2.day (Figure 4.10; Appendix Table D.15), which is considered relatively high and is a likely result of the mafic nature of these rocks. A significant portion of the MCR clastics were derived from the volcanic dominated rocks such as NSVG (Hamblin, 1965; Hamblin and Horner, 1961; Elmore, 1984). Therefore, those mafic-dominated sequences represent a good indicator of the potential of mineral sequestration in MCR clastics by the rapid dissolution of the mafic minerals (e.g., pyroxene, amphibole, and olivine) as a result of CO_2 exposure to produce Fe, Ca and Mg required to CO_2 sequestration.

C. Sodium and potassium release: The alkali metal concentration was between 0.5 and 4.7 ppm for K and between 3.8 and 24.0 ppm for Na. These amounts of released alkali metals reflect the lower concentration of alkali metal elements in the mafic igneous rocks in general. The rate of the alkali metal release was less than 4.15×10^{-8} mol/cm^2.day for K and less than 1.77×10^{-7} mol/cm^2.day for Na (Appendix Table D.15).

D. Aluminum and manganese release: The aluminum concentration was below the instrument's detection limit of 0.1 ppm for all samples (Table 4.8). Manganese was

released in small amount in the DUL, GHC, and GHB samples, and was below the detection limit for the BEV samples (Table 4.8). The release rate of Mn in the DUL, GHC, and GHB samples was generally slow and below 7.19×10^{-9} mol/cm^2.day (Appendix Table D.15).

Table 4.8 Chemical composition of leachate solutions collected after opening the vessels contained MCR igneous rocks samples. Values are in ppm (mg/L). The accuracy range is between 0.8 ppm and 1.08 ppm for a 1 ppm concentration standard. Accuracy is shown in Appendix Table D4; Molal concentration in Appendix Table D.14. BBC is beaver Bay Complex; NSVG-IC is North Shore Volcanic Group –Clastic Interflow.

Unit	ppm	Si	Al	Fe	Ca	Mg	K	Na	Mn
Beaver Bay C.	BEV1	27.1	<0.1	0.4	17.3	7.0	1.9	3.8	<0.1
	BEV2	54.0	<0.1	<0.1	31.4	16.0	2.2	5.9	<0.1
Duluth C.	DUL-1	90.2	< 0.1	< 0.1	39.4	192	3.9	7.2	0.4
	DUL-2	74.8	< 0.1	< 0.1	38.2	134	4.7	6.7	0.4
NSVG	GHB-1	52.6	< 0.1	< 0.1	224	183	1.4	24	1.8
	GHB-2	44.2	< 0.1	< 0.1	123	101	1.1	19.6	0.5
	GHC-1	124	< 0.1	< 0.1	288	66.7	0.7	19.5	1.2
	GHC-2	125	< 0.1	< 0.1	278	67.0	0.5	14.4	1.8

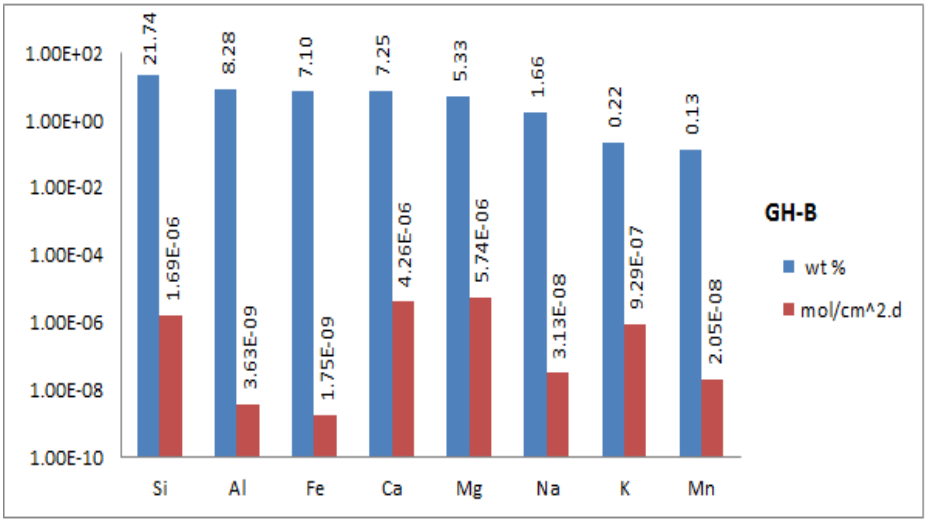

Figure 4.10 Comparison between the dissolution rate (mole/m^2.sec) and the initial concentration of elements in wt% of GH-B sample. The sample is from basaltic flow from the NSVG, Good Bay Harbor, MN and showed that the fastest release rate belongs to the Ca. Dissolution testing was conducted at 90^{o}C in a H_2O + CO_2 solution for 59 days.

The chemical composition of the underground waters represented by 66 wells that penetrated the Mt. Simon and Hinckley Aquifers (Lively et al., 1992) indicates the average of Ca concentration was 71.1 ppm with maximum value of 526 ppm. The Mg concentration average was 27 ppm and the maximum value was 240 ppm. Sodium was 66.4 in average and 1870 ppm as maximum value. All other major oxides were present in < 10 ppm concentrations. The total dissolved solids were 7,471 ppm maximum, which made the water type as brackish water type. These maximum values were reached for the MCR sample during this high-pressure-temperature testing. There is no corresponding aquifer composition data available for a chemical composition of the water samples for stratigraphic units of the Oronto Group (Thorleifson, 2008).

4.2.2 Factors Controlling the Dissolution of the Minerals. The amount of elemental release into the solution is dependent on several factors, including the mineral composition of the detrital grains, the surface area, time, pressure, temperature, and the fluid composition. Twenty one samples were prepared from a single POT4 sample to test the relative influence of these factors in the high-pressure corrosion experiments. The POT4 sample was collected from the Potato River Falls area in northern Wisconsin. Sixteen duplicates were wafered, cleaned, and dried for corrosion tests as a variable of time. Another section of the sample was crushed in an agate mortar and pestle and then sieved to collect the 100 mesh (0.149 mm) to 60 mesh (0.250 mm) size fraction using stainless steel sieves. These samples were used to investigate the effect of larger surface area on the dissolution rate. Three samples were tested at 50°C to investigate the effect of variable temperature. A sample was partially submerged in the fluid reactants to attempt to simulate a partially hydrated surface representing alteration around a CO_2 gas pocket. Based on the XRF results, the POT4 sample used in this corrosion test had relatively high Mg (MgO = 4.23 wt%) and Ca concentrations (CaO = 4.06 wt%). The other major oxides included SiO_2 = 54.0 wt%, Al_2O_3 = 12.68 wt%, Fe_2O_3 = 13.77 wt%, Na_2O = 2.04 wt%, K_2O = 1.39 wt%, and MnO = 0.16 wt% (Appendix Table C3). The petrographic modal analysis of 300 point counts for the POT4 sample indicates a Q-F-L ratio of $Q_{31.4}F_{31.6}L_{36.0}$ (Section 3.1.2.1). The plagioclase to K-feldspar ratio was 1.32: 1. Accessory minerals included unidentified opaque mineral oxides (3.4%), mica (1.0%), and epidote (2.4%). The cement in this sample was represented by iron oxide (12.6%)

and carbonate 0.3%. The matrix was comprised of 9.0% silty material and 3.4% clayey matrix material.

4.2.2.1 Reaction time and corresponding change in fluid composition. All of the samples used in the HPT test of the POT4 displayed increased pH values from the 3.8 value that represents the maximum saturation with CO_2 (blank samples) with time, which reflects the acid (H^+) buffering capacity of the investigated samples (Figure 4.11).

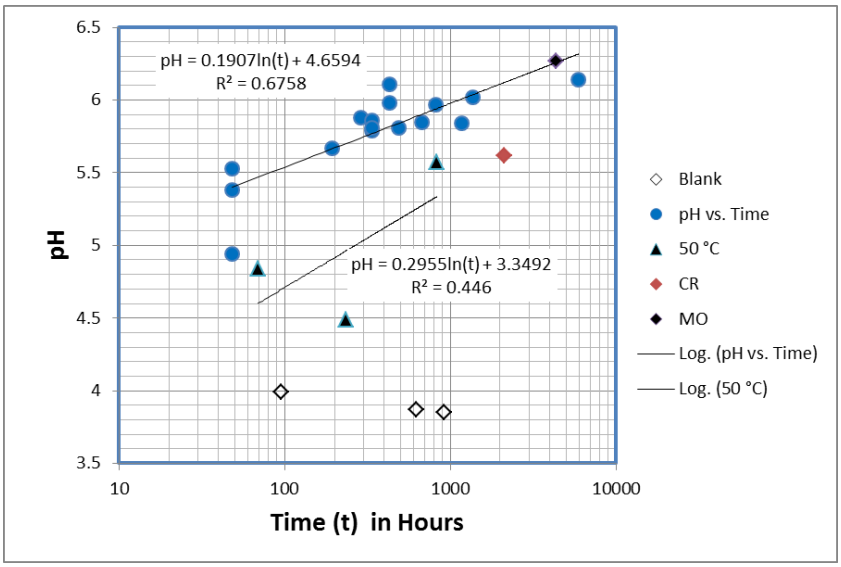

Figure 4.11 pH variation with time, surface area (crushed; CR), low temperature (50 °C), and fluid volume (mounted; MO) for the Nonesuch Formation POT4 sample.

The pH of the fluids collected from the crushed sample experiments was about 5.7 after 2112 hours, which was slightly less than the pH for the regular 90°C samples at 6.0, at the same time period. The pH of the mounted sample (MO) was 6.2, which is slightly higher than the regular trend of the 90°C samples. The slope of the trend line on the 50°C samples showed a pH increasing at a rate more rapidly than that for the 90°C samples (0.29 pH units/hour and 0.19 pH units/hour for the 50°C and 90°C samples, respectively). However, the number of data of the 50°C samples and the scattering of these data reducing the importance of that comparison. Eh-pH diagram in Figure 4.12 illustrates that most of the solutions contacting the reacting POT4 samples have a composition where hematite (Fe_2O_3) should be precipitating. Therefore, any ferrous iron (Fe^{2+}) that may be

released from dissolving samples should be immediately converted to the ferric iron (Fe^{3+}) and most will precipitate as hematite or other ferric-iron hydroxide phases once the iron concentration reaches the saturation level to any respective ferric iron mineral phases. The required energy to oxidize the ferrous to ferric iron is +0.77 volts, and CO_2 (C^{4+}) could act as an electron acceptor, in the absence of oxygen in subsurface reduced acidic conditions, by converting to either carbon monoxide (CO; C^{2+}; -0.106 volt) or carbonaceous acid (H_2CO_2; C^{2+}; -0.114 volt).

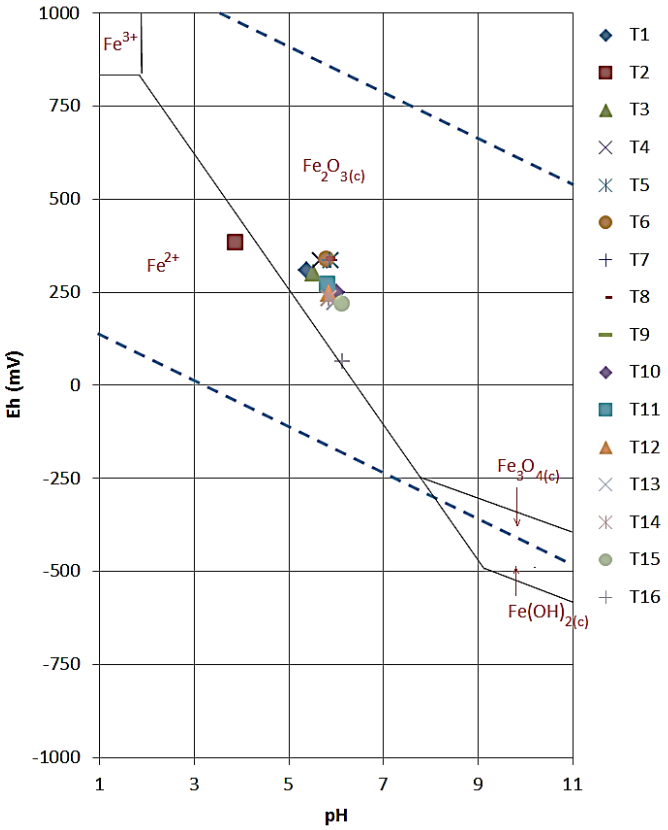

Figure 4.12 Eh-pH characteristics of the leachate fluids collected after testing POT4 sample relative to the solubility of hematite. The equilibrium lines for hematite represented by an iron solution activity of 5.56×10^{-5}ppb. The hematitic rust on the walls of the Teflon vessels (Figure 4.13) reflects the oxidation conditions and saturated conditions for hematite during testing. The testing was at 90°C and 65-70 bars.

The iron concentration of final leachate solution was, normally, below the detection limit of the instrument (<0.1 ppm). However, a significant staining on the

inside walls of the Teflon vessels was recognized. The colors of the rust were ranged between yellowish brown and pale brown, which is a characteristic of the precipitation of the ferric-iron oxides or hydroxide phases during the reactions under an oxidized setting. Figure 4.13 showed the comparison between the blank samples Teflon liner and a Teflon liner that contained the GHB (Good Harbor Basalt) sample during testing. The GHB sample released a significant amount of Fe^{2+}, and then converted to Fe^{3+} phases. In this experiment conditions (6.5>pH>4), the minimum Fe^{3+} concentration that could be present as dissolved phase is 5.6×10^{-5} ppb.

Figure 4.13 A Teflon liner with only CO_2 and H_2O (to the left) and a Teflon liner containing GH-B sample (to the right). The figure is showing a precipitation of Fe^{2+} mineral phases on the inside walls of the Teflon liner. Spots along the rim are fragments of metal from the stainless steel sample liners.

4.2.2.2 Sample solid surface area to solution volume. Both surface area and the morphology of the mineral surface affect the rate of dissolution. A smaller grain particle is, primarily, characterized by either more atoms or ions at positive kinks, steps, or alone on a terrace, thus making the smaller grains more soluble than larger grains (Berner and Morse, 1974; Railsback, 2011). The cleavage in the minerals (surface roughness) increases the number of positive kinks, steps, and ion that are isolated and alone. The plagioclase feldspar detected in the POT4 sample from Nonesuch Formation (illustrated

in Figure 4.14 and Appendix Figures D.1 and D.2 displayed a distinctive dissolution pit features that were identified at the corners of the cleavage planes and edges along the cleavage planes.

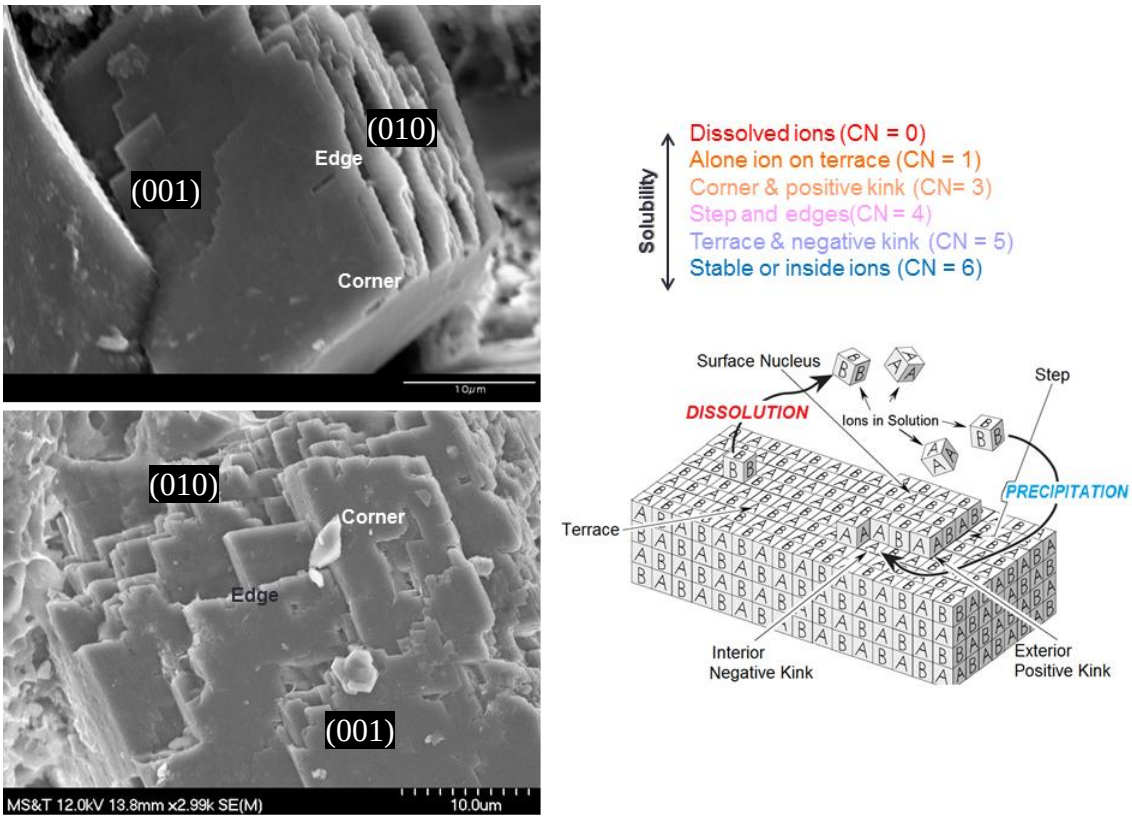

Figure 4.14 SEM photomicrograph of POT4 sample. The photomicrograph showed selective dissolution of plagioclase feldspar crystals along the most vulnerable sites for dissolution. (Right) schematic diagram showing the equilibrium between the dissolution at precipitation and their relation with the surface area, modified from Railsback (2011).

The dissolution process affecting calcite cement in the MCR samples is characterized by preferential dissolution along the cleavage planes, which could enhance the residual porosity for any samples containing calcite cement. SEM images of the KEW1-1 sample revealed significant dissolution along such calcite cleavage features (Figures 4.15 and 4.16; Appendix Figures D.3). Also, a significant dissolution of calcite occurred along the boundary between the calcite cement and clastic grains, where the calcite crystallized in a smaller size crystals compared with the pore center where longer

crystal segments occurred. Again, the smaller crystal size appears to produce a more rapid solubility potential. The crystals on the pore boundary may also be more impure compared to the central portion of the pore infilling and this may also result in an increase in solubility.

The increased surface area of the crushed Nonesuch POT4 sample helped to increase the Si, Mg, and K release rates relative to the wafered samples. The only exception was for Ca and K, which are, generally, lower than the concentrations of 90°C samples' average trend. Further discussion of surface area and corresponding change in the elemental concentration for all samples will be addressed in Section 4.2.2.4.

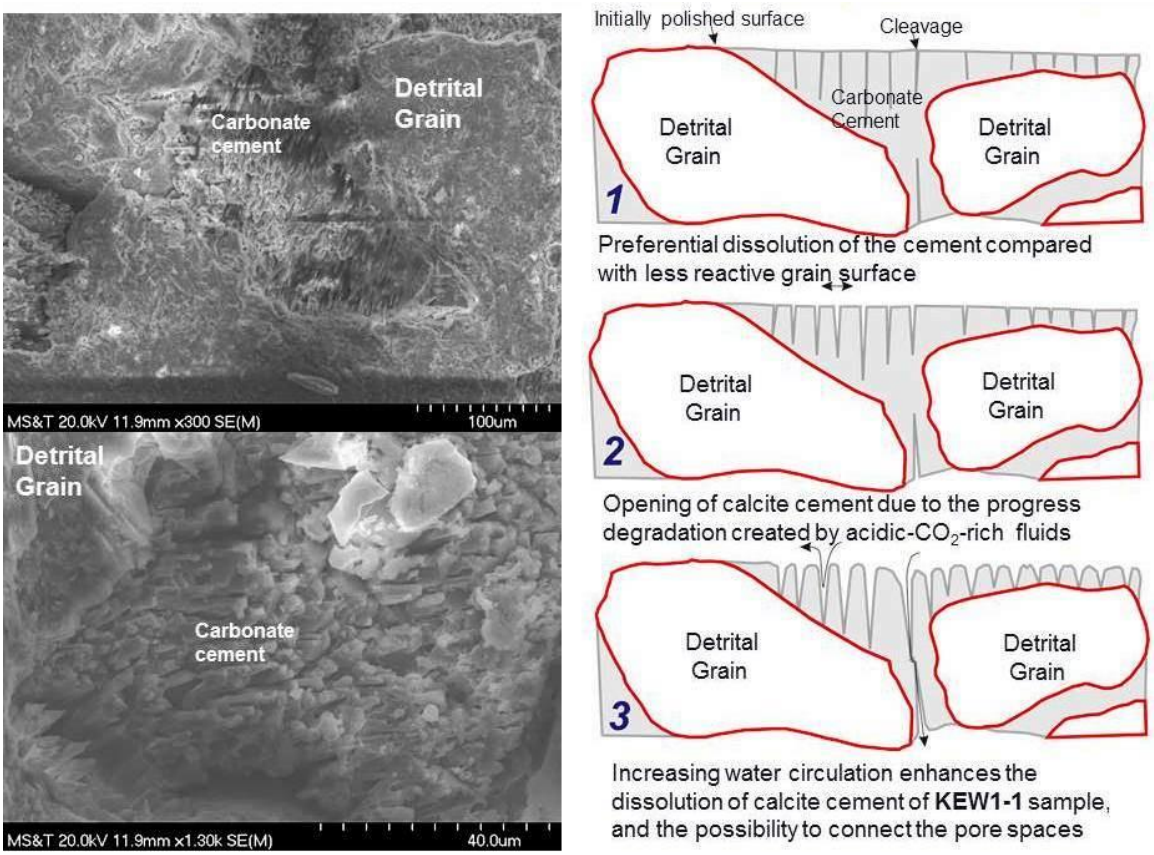

Figure 4.15 SEM photomicrograph of KEW1-1 sample from Copper Harbor Conglomerate. The sample has reacted for 143 hours at 90°C in a deionized water + CO_2 environment. The dissolution of calcite cement is enhanced along the parallel cleavage plane surfaces. The increase in the surface area created by more acid fluids passed through the cleavages will further accelerate penetration of fluid into the rock and additional dissolution of previously unexposed surfaces.

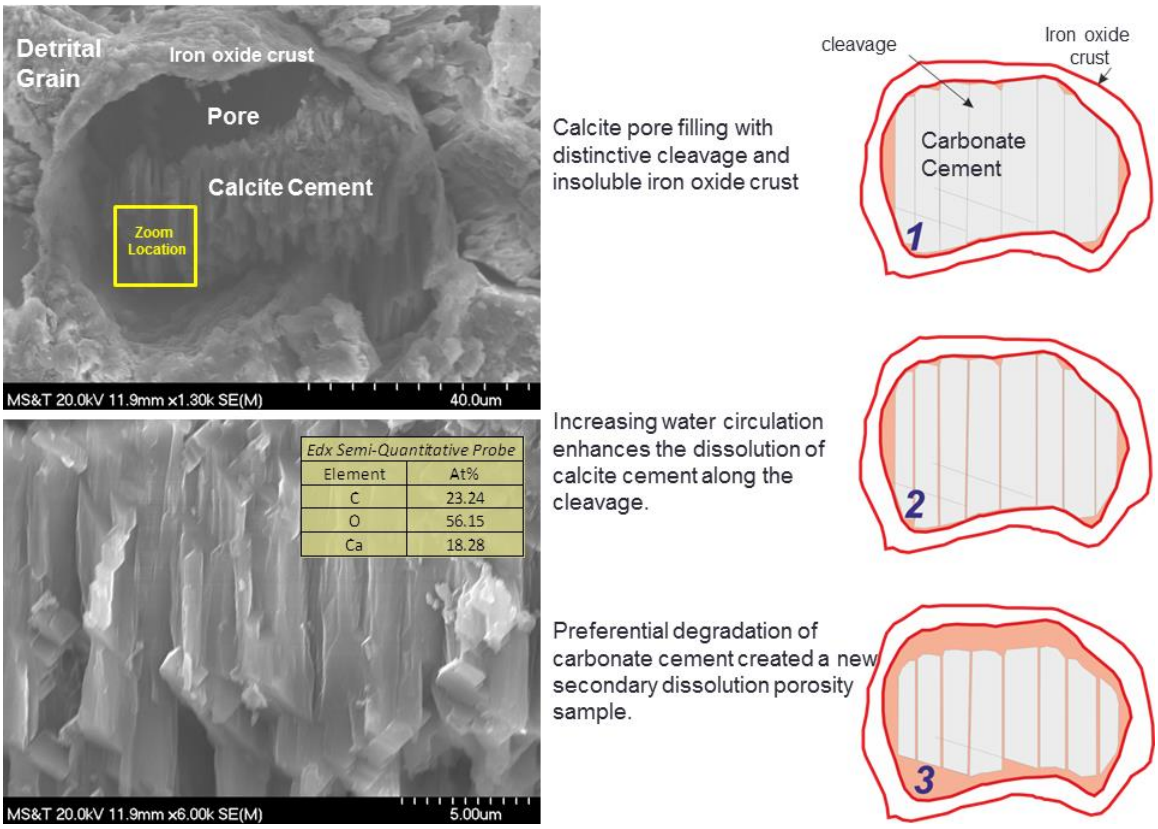

Figure 4.16 SEM photomicrograph of KEW1-1 sample. Dissolution of carbonate cement had occurred preferentially along calcite cleavage planes and the top and bottom pore boundaries where the cement was in contact with detrital grains and/or detrital grains covered with iron oxides.

4.2.2.3 Temperature. Overall, the solubility and kinetic dissolution rates of silicate minerals increase as the temperature is increased. Temperature relevant changes in feldspar solubility, which is increasing with temperature in the following manner [i.e. Log K$sp_{(anorthosite)}$ is between -23.75 to -21.25 at 0°C, and between -19 to -19.25 at 90°C; Log K$sp_{(albite)}$ is between -20 to -23.5 at 0°C, and between -16 and -17 at 90°C; and Log K$sp_{(K\text{-feldspar})}$ is between -24 to -26 at 0°C and between -19 and 19.5 at 90°C; (Berman, 1988; Shock and Helgeson, 1988; Shock et al., 1989; Rsson and Nsson, 1999; Arnorsson and Stefansson, 1999). Quartz and its polymorphs also become more soluble as temperature increases [Figure 4.17(A)]. Opposite to the trend for silicates, aragonite and calcite solubility, exhibits a progressive decrease in solubility from 0 to 100°C, as illustrated in Figure 4.17 (B). Witherite and strontianite show slight increase of solubility

with temperature before decreasing above temperature of approximately 50ºC (Langmuir, 1997; Plumber and Busenberg, 1982).

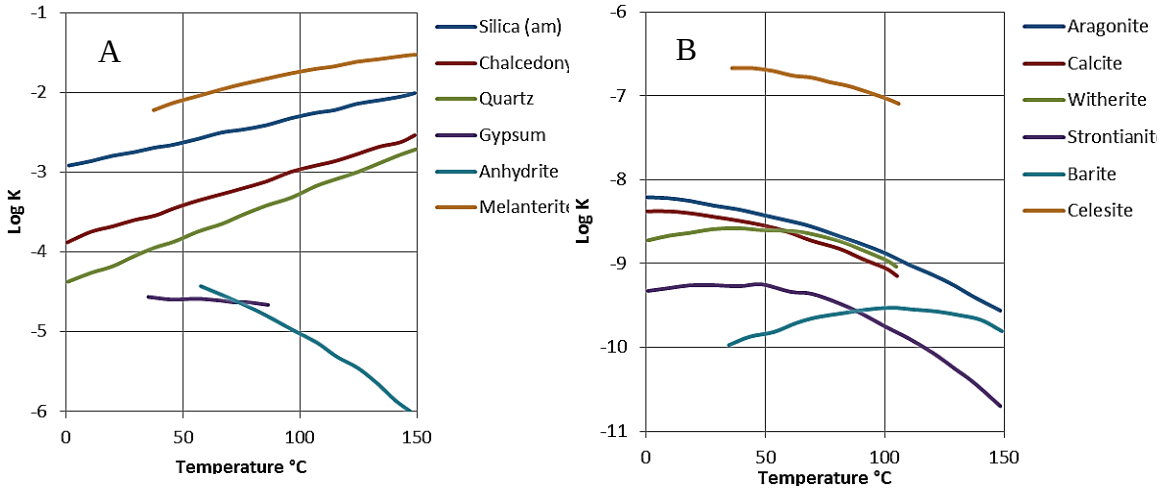

Figure 4.17 The relationship between solubility product K_{sp} of minerals and temperature. (A) SiO_2 species and calcium carbonate; (B) Some of carbonate minerals [Modified from Langmuir (1997)].

The average geothermal gradient in the Iowa sector of the MCR was approximately 19°/km (Anderson, 1990). Therefore, if the thermal profile of the MCR clastics was linear with depth, the maximum solubility of silicate minerals at approximately 90°C would be achieved at a depth of 4.7 km (15,090′).

Three samples of POT4 were tested at 50°C. The average concentration of Ca, Mg, Si, and K released from the samples reacted at 50°C was lower than that of the 90°C samples. The samples that reacted at 50°C displayed a strong positive relationship between the amount of Si and Ca released into the leachate solution and time (Figures 4.18 and 4.19). However, Mg released from the 50°C samples showed a slower dissolution rate as compared with the 90°C average trend line for Mg. Sodium and potassium did not display a strong relationship between the amounts of the released cations with time.

4.2.2.4 Reaction time and corresponding change in the elemental concentration. The overall pH logarithmic time trend line for the 90ºC samples is displayed in Figure 4.11. This figure reveals a moderately high correlation between the pH and the reaction time (R^2=0.67). A moderately high positive correlation also exists between the released silicon concentration and time at 90°C (R^2=0.63; Figure 4.18). However, the silicon concentration, which likely reflects the hydrolysis of silicate minerals, is low (<60 ppm) when compared to Ca concentration, for example, which was more than 70 ppm Ca.

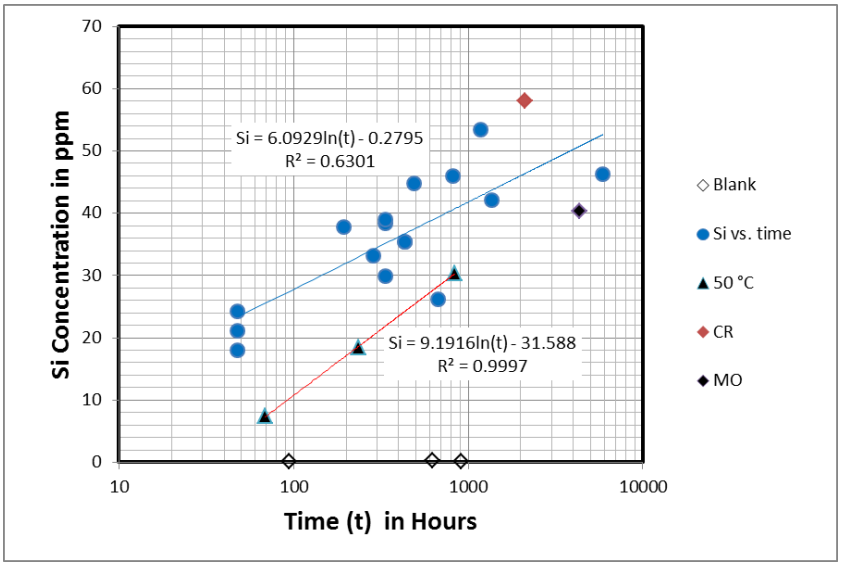

Figure 4.18 Silicon concentration variation with time, surface area (crushed; CR), lower temperature (50 °C), and fluids volume (mounted; MO) for the Nonesuch Formation POT4 sample. Details in Appendix Table D16.

The Ca concentration released at 90°C is weakly correlated to the reaction time (R^2=0.19; Figure 4.19), while the Mg concentration displays a strong positive relationship with reaction time (R^2=0.77; Figure 4.20). The early rapid release and high concentrations for Ca likely reflects the rapid dissolution of the calcite cement in the acidified leachant solution produced by adding CO_2 to the reaction vessels. The calcite cement comprises 0.3% percent of the POT4 sample by volume. Magnesium, being sourced largely from silicate minerals would, alternatively, be expected to display slower,

and steadier release rates. The 90°C temperature represents the point at which the lowest solubility would be expected for the carbonate minerals that could achieved during the HPT experiment as seen in Figure 19(B).

The release of Na, K, and some Ca is believed to result from the hydrolysis of feldspars, pyroxenes, and other silicate minerals through an ion exchange with H^+ ions in the solution. The release of Na and K displays only moderate to weak correlation between the concentration and the reaction time (potassium R^2=0.35 and sodium R^2=0.52; Figures 4.21 and 4.22, respectively).

The correlation between the Mn concentrations and time is very weak (R^2=0.002). Alternatively, Mn vs. time for the 50 °C sample showed a very strong relationship (R^2 =0.99; Figure 4.23), which could reflect a steadier and stable release rate at lower temperature. The measured concentrations of both Fe and Al in the collected solutions were near the instrument's detection limit, which is 0.1 ppm.

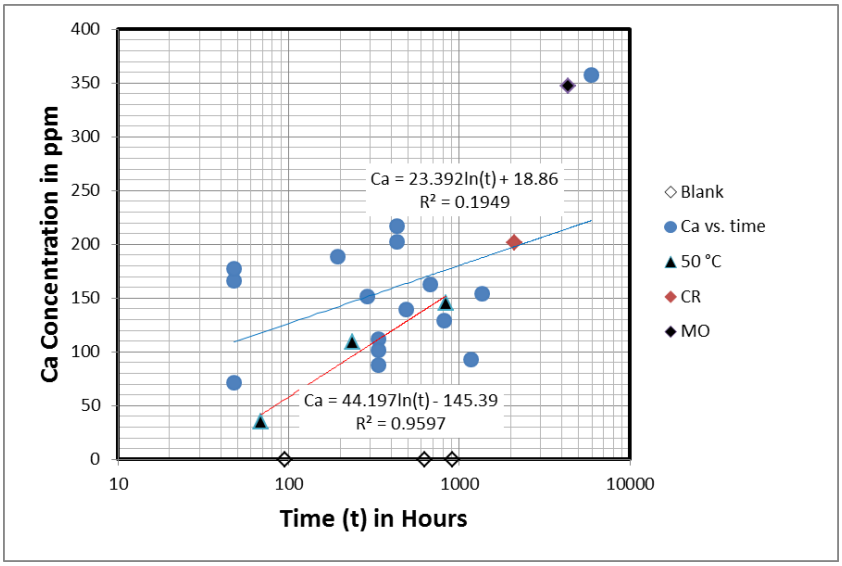

Figure 4.19 Calcium concentration variation with time, surface area (crushed; CR), lower temperature (50 °C), and fluids volume (mounted; MO) of the Nonesuch Formation POT4 sample. Details in Appendix Table D.16.

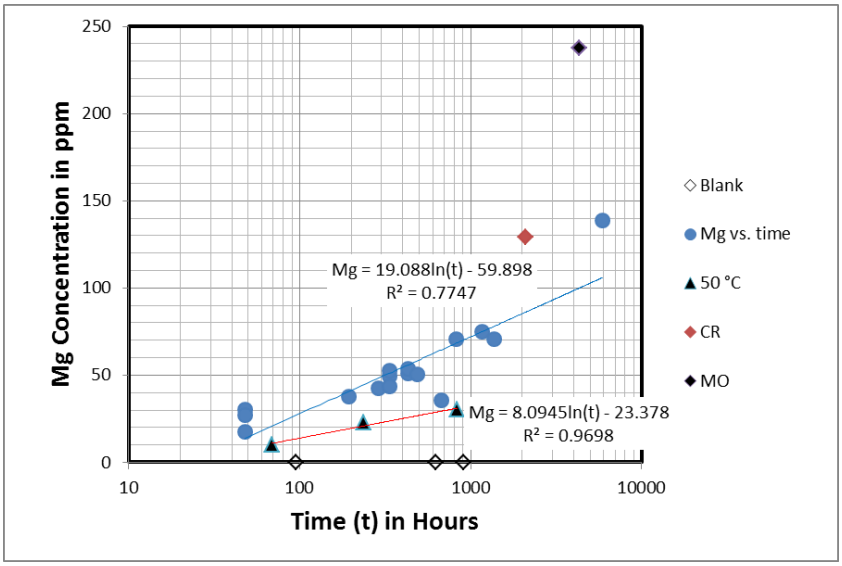

Figure 4.20 Magnesium concentration variation with time, surface area (crushed; CR), lower temperature (50 °C), and fluid volume (mounted; MO) of POT4 sample. Details in Appendix Table D.16.

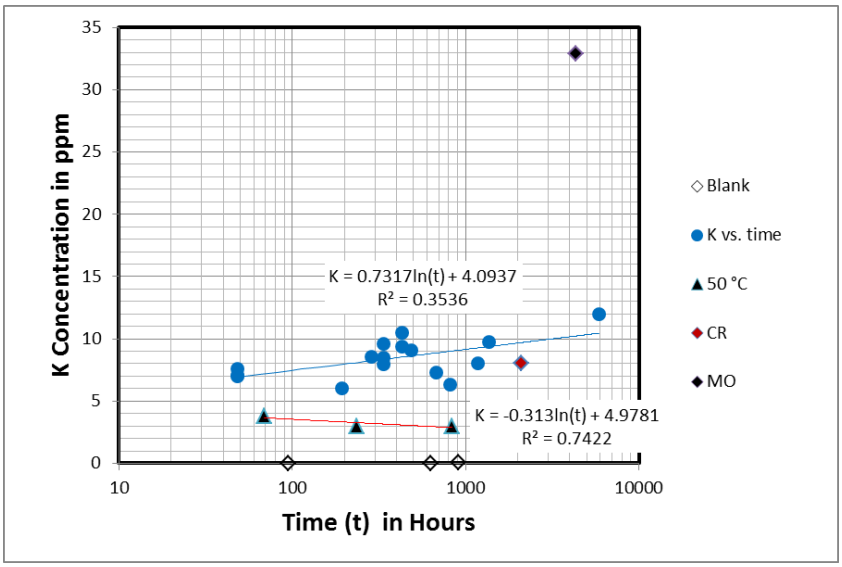

Figure 4.21 Potassium concentration variation with time, surface area (crushed; CR), low temperature (50 °C), and fluid volume (mounted; MO) of POT4 sample. Details in Appendix Table D.16.

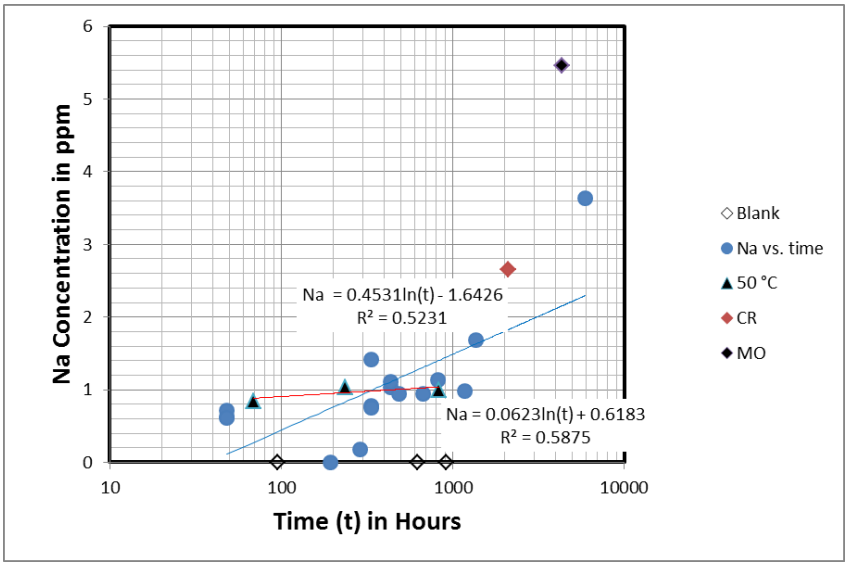

Figure 4.22 Sodium concentration variation with time, surface area (crushed; CR), low temperature (50 °C), and fluid volume (mounted; MO) of the Nonesuch Formation POT4 sample. Details in Appendix Table D.16.

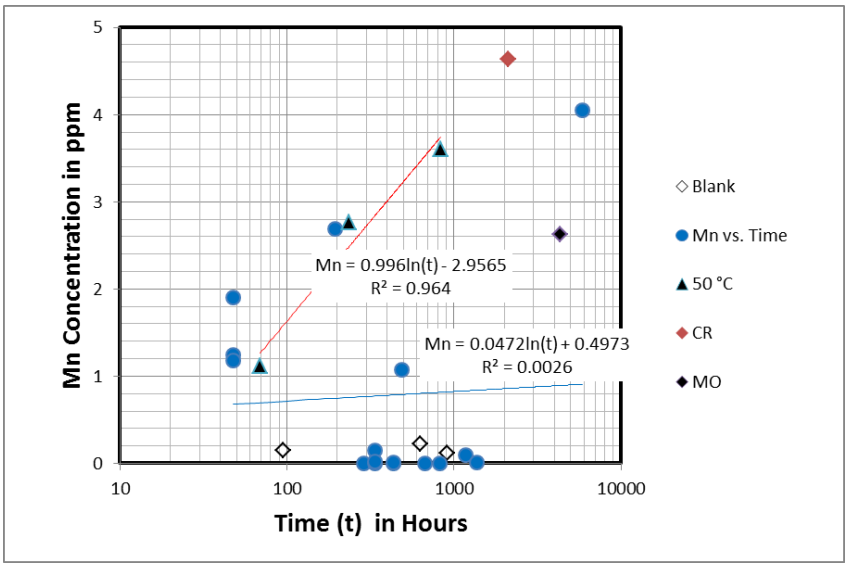

Figure 4.23 Mn concentration variation with time, surface area (crushed; CR), low temperature (50 °C), and fluid volume (mounted; MO) of the Nonesuch Formation POT4 sample. Details in Appendix Table D.16.

4.2.2.5 Relative rates of mineral weathering and associated elemental release. The mineral composition of the sediments and the relative durability of the minerals is a major factor controlling the release rate of the various ions into solution, with dissolved components often being release from multiple mineral phases. To test the relative release rates of elements from individual mineral phases, we reacted individual minerals in a leachant solution prepared to a pH of 3.78 using nitric acid as a surrogate for carbonic acid. This leachant solution pH simulated the mildly acidic nature of deionized water exposed to a 100% CO_2 atmosphere at atmospheric pressure. The use of nitric acid allowed the test vessels to be opened and closed for the pH measurements without the loss of CO_2 from the system and associated pH changes. The experiments were conducted at room temperature and pressure. Reaction rates of the minerals were evaluated by monitoring the pH of the solution, with minerals reacting the fastest driving the solution pH up more rapidly and to higher final values than the less reactive mineral phases.

Calcite exhibited the most rapid increase in the pH, reaching a value of 8.78 in only two days. Rapid calcite dissolution may enhance the porosity of rock samples like the MCR sediments where the pores are often occluded with calcite cement. Most of the silicate mineral reaction rates followed the predicted Goldich (1938) stability trend. For example, the olivine peaked at pH of 8.46 in one week, and the Ca-rich feldspar peaked at 5.53 in 105 days. Overall olivine showed the fastest reaction rate among the selected minerals, and then followed by amphibole, pyroxene, K-feldspar, Ca-plagioclase, Na-Plagioclase, and finally quartz. The quartz sample exhibited no apparent change in the pH of during testing indicating no detectible reaction with the acidified leachant fluid (Figure 4.24).

Hematite, which commonly occurred as cement material in MCR clastics, was only slightly reactive. For instance, the pH of the hematite sample increased from 3.78 to 4.20 in 14 days. Therefore, the dissolution of both quartz and hematite will not appreciably enhance porosity as a result of carbonic acid acidification as it does with calcite. However, the solubility of hematite would increase as a of result any reduction condition to provide more Fe^{2+} required to $FeCO_3$ formation. Epidote is commonly

occurred in the MCR rock samples, and the acceleration weathering of the sample exhibited a fairly rapid pH rise to 6.3 in just 4 days, and then continued to slow rise to reach 6.8 after 63 days. Both Ca and Fe^{2+} are common products of epidote alteration, which potentially would sequester CO_2 as calcite or siderite.

Lasaga (1994) compiled a quantitative summary of the expected life time in years of a 1 mm grain-sized mineral at pH of 5 and temperature of 25°C (Figure 4.25). Ca-pyroxene (Wollastonite; $CaSiO_3$), and Mg-olivine (forsterite; Mg_2SiO_4) were predicted to be the fastest reacting silicate minerals. Meanwhile, quartz was predicted to be almost inert, geochemically. The fastest reaction rates would reflect rapid cation exchange (e.g., $2H^+ \leftrightarrow Mg^{2+}$ and $H^+ \leftrightarrow Na^+$) and greater minerals buffering capacity for acids. Buffering capacity and/or the release of alkaline earth elements incorporated into carbonate phases may also promote carbonate mineralization. Therefore, the mafic minerals, rock fragments, and basaltic flows (containing reactive Ca^{2+}, Mg^{2+}, and Fe^{2+} mineral phases) represent higher potential for any mineral sequestration processes in the MCR.

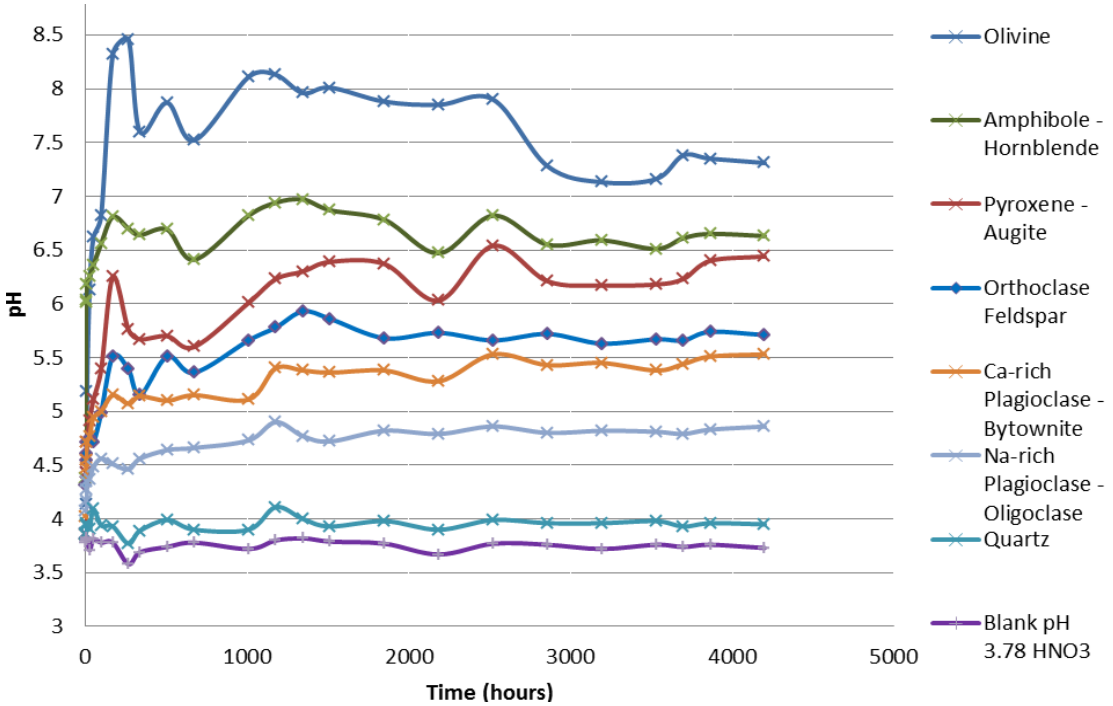

Figure 4.24 Mineral weathering rates reflected with pH buffering with time for individual mineral samples.

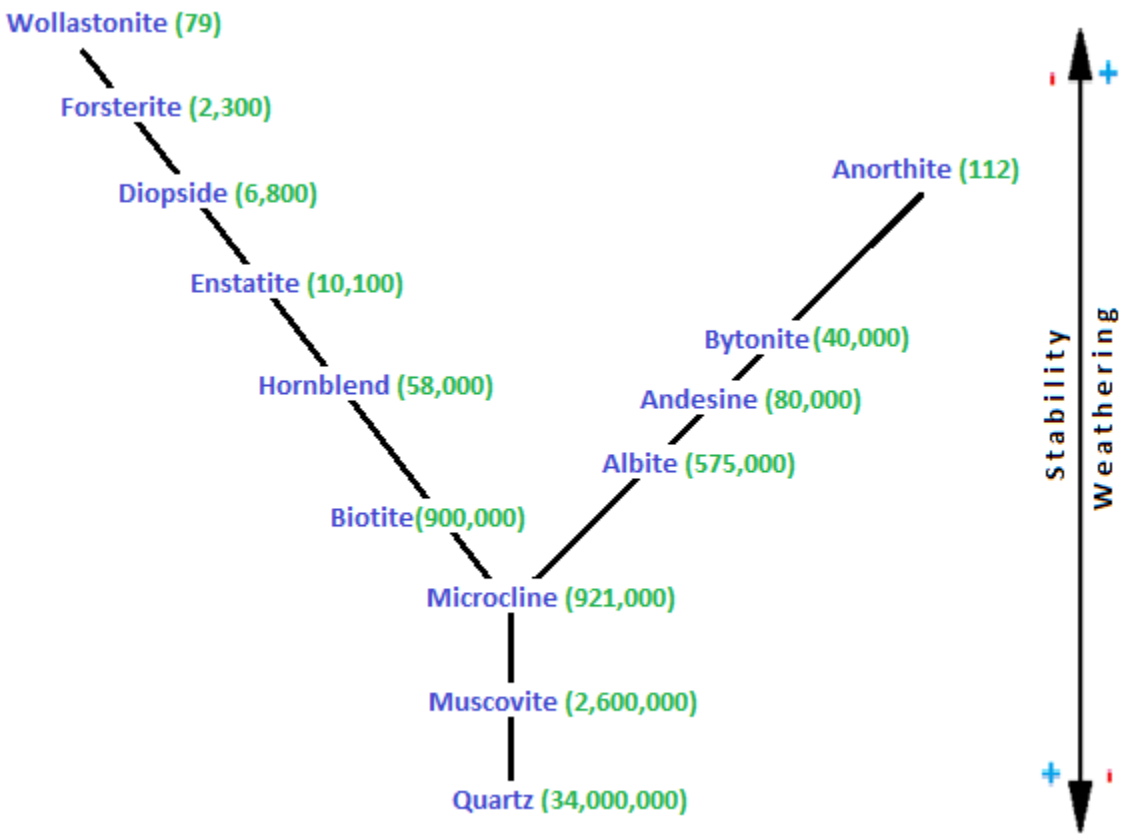

Figure 4.25 The calculated life time (in years) and relative weathering stability of a one mm grain-sized mineral. Data on mineral dissolution rates from (Lasaga, 1994).

4.2.3 Core Flooding Experiments. Core flooding experiments were conducted to show the effect of the CO_2- rich fluids on the aquifer properties, and specifically permeability. Eight samples have been reacted in the core flooding experiments ranging from the high porosity-permeability Bayfield (BAY2) sample, the moderate porosity and calcite cemented CHC (KEW3-1) sample, the non-calcite Freda (POT8-2) sample, the moderate porosity-permeability 11,061.5′ (and Texaco Poersch #1) sample (Table 4.9). The core flooding experiments exposed a core rock sample to a pressurized container filled with nitric acid acidified water (pH=3.8) at ambient room temperature. The relative permeability changes of the rock was evaluated by measuring pressure changes as it undergoes chemical reactions with the leachant fluid.

Table 4.9 Samples used in the core flooding experiments. The symbol "P" represents the porosity determined by petrographic analysis, "CCe" represents volume percent calcite cement also determined by petrographic analysis. Thickness of rock sample testes in core flooding experiment is given in centimeters.

		Percent Calcite Cement Content	
		Low	High
Initial Porosity	Low/Moderate	POT8-2: (P=1.2%; CCe =0.0%) 1.27 cm.	KEW1-1: (P=1.0%; CCe =15.9 %) 1.65 cm. KEW3-2: (P=4.0%; CCe =11.1%) 2.29 cm. KEW3-1 Sample:(P=8.9%; CCe =10.4%) 1.65 cm.
	High	BAY2: (P=32.2%; CCe =0.0%) 3.18 cm. Texaco Poersch #1 - 11,061.1′ (P=7.9%; CCe= minor reaction with HCl, dolomite detected by XRD analysis) 1.91 cm.	

A. Low calcite cement - high porosity sample: The Bayfield BAY2 sample represents a mature quartz arenite composition with a high initial porosity (14.7%) and permeability and no detected calcite cement. The diameter of the sample was 2.5 cm and the length of the sample was 3.18 cm. The measured initial permeability was > 340 mD, though impregnation of the sandstone pores along the outer edge of the sample core caused some blockage that was accounted for by estimating a smaller disk diameter in the permeability calculation. The experiment with the BAY2 sample was started with an initial flow of 0.25 ml/min, with additional tests at 0.50, 0.75, and 1.0 ml/min. The flow rate of the leachant fluid did not appreciably change during any of the tests indicating that the sample did not react very much to change permeability during the testing interval. A steady-state fluid pressure was achieved in approximately two minutes and backpressure remained very low throughout the 15 minute testing interval (Figure 4.26). The continuous steady-state high flow rate is a characteristic of a good aquifer rock for injection with CO_2.

The initial and final pH of the influent and effluent fluids was 3.7 and 3.8, respectively. The low buffering capacity of sample reflects the inert nature of its quartz-

dominated mineralogy. This feature was also reflected in the low concentrations of dissolved constituents in the leachate fluids (Table 4.10). Sodium was the only element present in the solutions and this was likely occurring as a trace contaminant derived from previous experiments conducted with the vessel apparatus using Na-brine fluids. Sodium tends to adsorb to plastic test vessel components and thus is difficult to remove completely without extensive pre-test rinse cycles.

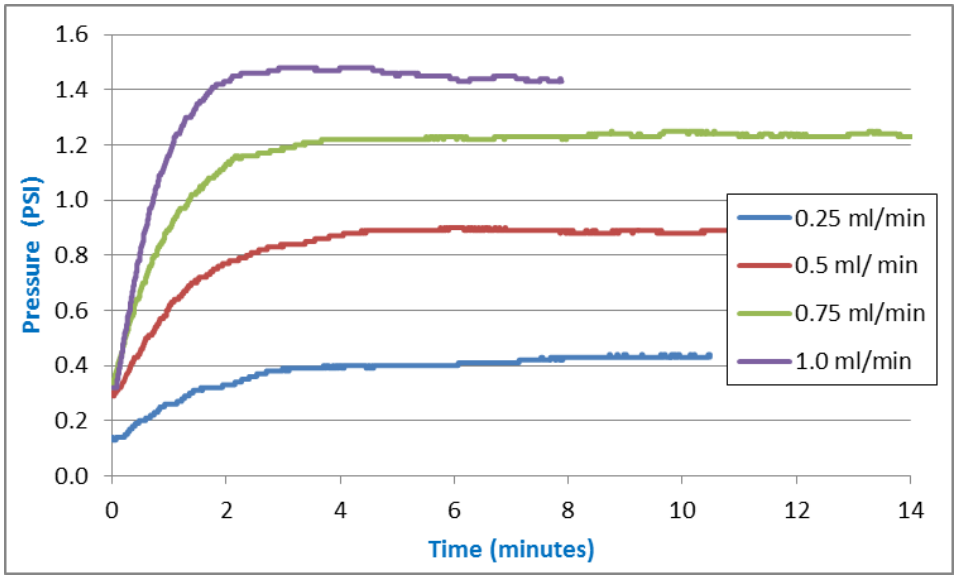

Figure 4.26 Steady flow (dp/dt = 0) for sample BAY2 in the core flooding experiment. The breakthrough was after 10 minutes of flooding. The rapid attainment of steady-state flow after the initial incubation period indicates that no detectible change in the rock permeability had occurred during testing.

Table 4.10 Chemical composition of the core flooding experiment influent and effluent fluids (in ppm) for the BAY2 sample. The initially high Na concentration was created by contamination from previous brine runs with the experimental apparatus.

	Time (min.)	Ca	Mg	K	Na	Mn	Fe	Si	Al
Blank		<0.1	<0.1	<0.1	<0.1	<0.1	<0.1	<0.1	<0.1
Influent-*in*	30	<0.1	<0.1	<0.1	0.2	<0.1	<0.1	<0.1	<0.1
Effluent	~ 10	0.9	<0.1	<0.1	23.1	<0.1	<0.1	<0.1	0.8
	~15	<0.1	<0.1	<0.1	7.1	<0.1	<0.1	<0.1	0.5
	30	<0.1	<0.1	<0.1	2.1	<0.1	<0.1	<0.1	0.5

B. Low calcite cement - low/moderate porosity samples: The POT8-2 sample was a feldspathic lithic arenite collected from the Freda Formation at the Potato River Falls location. This sample displayed a low initial petrographic porosity (1.2%) and no observable calcite cement during thin section analysis. The flow rate used in this experiment was one ml/min. The pressure curve reflected a gradual increase of back pressure over time (transient flow; dp/dt>0). Therefore the permeability of the aquifer decreased over time from 0.190 mD after 5 minutes to 0.175 mD after about 30 minutes of testing. The experiment was terminated once a significant leakage developed in the sample due to the formation of a fracture, as indicated by the sharp decrease in pressure at the end of the experiment (Figure 4.27).

The pH of the effluent fluids of the POT8-2 sample rapidly increased from 3.8 to 6.4 during the first 13 minutes and then was constant after that. The effluent water showed a Si concentration between 0.26 ppm and 0.5 ppm. Calcium was approximately 3.0 ppm in the fluid samples except for a pulse of Ca release at 6 minutes, which was at 26 ppm (Table 4.11). The potassium concentration was approximately one ppm in the effluent samples except the sample collected after about 6 minutes (3.5 ppm) while the sodium concentration ranged between 2.8 ppm and 5.1 ppm, and again the sample collected after 6 minutes had high Na pulse (13.2 ppm). This POT8-2 sample was characterized by the presence of smectite clay (42% of the total clays), chlorite (43%) and traces of illite and zeolite as illustrated in Figure 3.21. All these mineral components could represent possible sources of the cations released into the effluent water. The pulse release at 6 minutes suggests the rapid attack and removal of a mineral component(s) in the sample. Solutions were filtered upon collection, so this pulse is not the result of the release of particulate material into solution. The 6 minute pulse also coincided with the attainment of a steady backpressure, thus indicating breakthrough along a blocked pore had likely occurred.

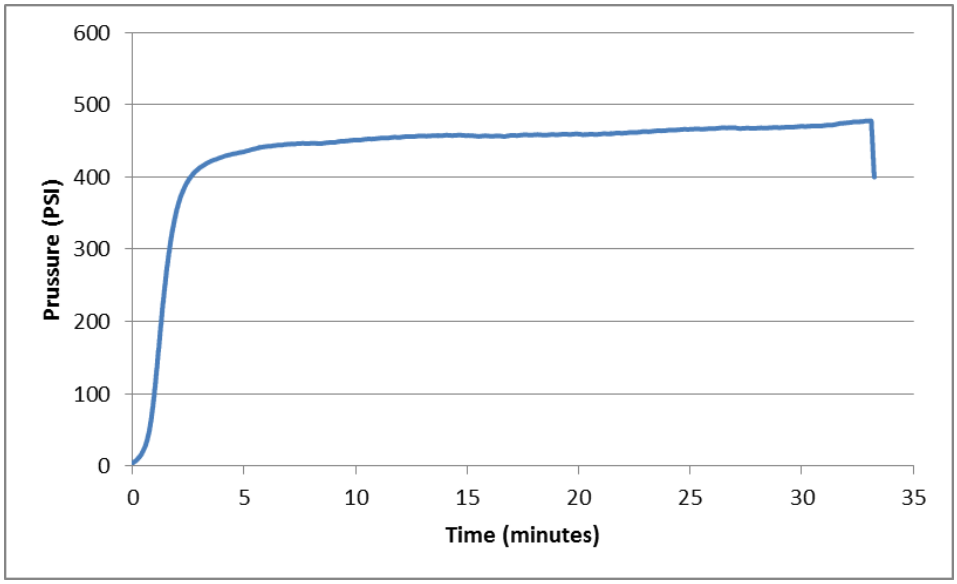

Figure 4.27 The pressure curve recognized in POT8-2 flooding experiments. The curve is indicating initial breakthrough in only 3-4 minutes and approximately transient flow until the sudden decrease in pressure at the 34th minute.

The Texaco Poersch #1 well sample from 11,061.5′ depth contained abundant feldspar, only a minor amount of calcite cement, and moderate porosity (~7.9 %; measured using lab flood test). Additionally, peaks for dolomite, chlorite, and albite were identified during the XRD examination of the segregated clay-sized particle matrix fraction of this sample (Figure 3.36).

Table 4.11 Chemical composition of the in core flooding experiment influent and effluent fluids (in ppm) of POT8-2 sample. A high initial Na and K concentration was, probably, created by contamination from previous brine runs inside the pump.

	Time (min.)	pH	Si	Fe	Ca	Mg	K	Na	Mn	Al
Blank			<0.1	<0.1	<0.1	<0.1	<0.1	<0.1	<0.1	<0.1
Influent-*in*	~35	3.8	<0.1	<0.1	<0.1	<0.1	0.44	0.38	<0.1	<0.1
Effluent	~6	5.7	0.50	<0.1	25.5	0.51	3.45	13.2	<0.1	<0.1
	~13	6.4	0.36	<0.1	3.48	<0.1	1.22	5.10	<0.1	<0.1
	~19	6.3	0.32	<0.1	3.09	<0.1	1.02	3.93	<0.1	<0.1
	~24		0.30	<0.1	3.06	<0.1	0.95	3.42	<0.1	<0.1
	~29	6.4	0.28	<0.1	3.06	<0.1	0.89	3.03	<0.1	<0.1
	~34		0.26	<0.1	3.15	<0.1	0.92	2.84	<0.1	<0.1

Three stages of fluid break-through were recognized during the core flooding test for Texaco Poersch #1 well sample (Figure 4.28). The first stage occurred between 1 and 8 minutes where a pressure increase was occurring. The second stage occurred between 8 and 45 minutes and was characterized by a steady flow (dp/dt=0; 1.011 mD average permeability). The third stage was followed by an abrupt decrease in pressure, likely resulting from the activation of a fracture or the final dissolution and breakthrough of mineral cements that were blocking the pores in the sample. The fracture hypothesis is favored due to the very rapid decrease in pressure observed during the final stage of testing. The last stage (from 45 to ~105 minutes) was characterized by a transient flow, in which the pressure increased very gradually over time (dp/dt>0) and the permeability correspondingly decreased over time from 1.28 to 1.11 mD. This final stage may reflect blockage of pores due to dislodging of particles and subsequent clogging of restrictive pore throats. Expansion of clay particles may also produce a similar core-flooding test result; however, no expansive clays were detected in the XRD analysis of this sample.

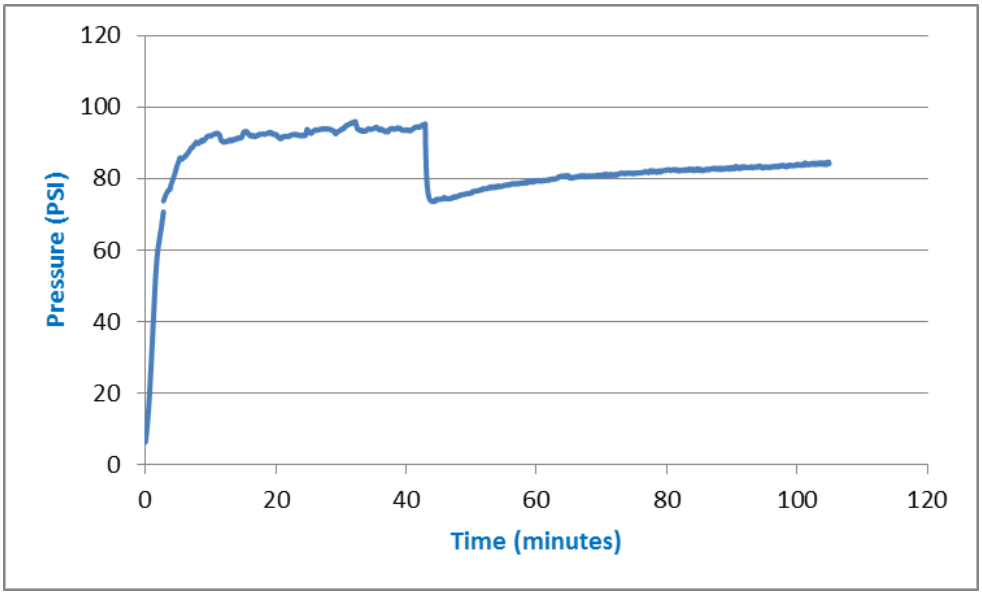

Figure 4.28 The pressure curve recognized in 11,061.5′, Texaco Poersch #1, core#13 flooding experiments. The curve is indicating initial breakthrough in only 8 minutes, steady flow until 45 minutes, then an abrupt pressure drop, and final transient flow until ~110 minutes.

The solution pH of the Texaco Poersch #1 well sample increased from a starting 3.8 to 5.5 after 100 minutes of testing. The chemical composition of the effluent fluid displayed an increase in the following components over the first 100 minutes of testing: alkalinity (from 3 to 20 mg/L) and Ca (from <0.1 to 5 ppm). Increases in Si, Fe, and K also are noted but were very subdued (Table 4.12). The increase in alkalinity, pH and Ca content could be created by both the dissolution of carbonate minerals while the Ca and pH changes could also result from the hydrolysis of plagioclase. Silicon release was very low however, indicating that the rate of feldspar hydrolysis was likely too slow to be a major contributing factor.

Table 4.12 The chemical composition of the 11,061.5′ sample's influent and effluent water (in ppm). The high Na content indicates contamination from the pump and/or tubing apparatus.

	Time (min.)	Ca	Mg	K	Na	Mn	Fe	Si	Al
Blank		<0.1	<0.1	<0.1	<0.1	<0.1	<0.1	<0.1	<0.1
Influent-*in*	120	<0.1	<0.1	<0.1	3.9	<0.1	<0.1	<0.1	<0.1
Effluent	60	4.9	<0.1	<0.1	8.3	<0.1	<0.1	0.1	<0.1
	80	4.9	<0.1	<0.1	4.2	<0.1	<0.1	0.1	<0.1
	100	5.0	<0.1	<0.1	4.0	<0.1	<0.1	0.1	<0.1
	120	3.6	<0.1	0.5	7.5	<0.1	0.4	0.1	<0.1

C. High calcite cement – low to moderate porosity samples: The Copper Harbor Conglomerate (KEW3-1) sample exhibited a significant amount of calcite cement (10.4%) and relatively high petrographic porosity (8.9%). Permeability rose ~ 30%, from approximately 0.92 mD to 1.20 mD in 180 minutes of core flood testing (dp/dt <0) suggesting a progressive increase in porosity and permeability upon exposure to the acidified leachant fluid (Figure 4.29).

The chemical composition of the effluent fluid of the KEW3-1 sample displayed an increase in the following components over the three hour test interval: alkalinity (from

~3 to ~9 mg/L), pH (from 3.7 to ~ 5.7), Ca (from <0.1 to 7.5 ppm), K (from <0.1 to 0.9 ppm), and Si (from <0.1 to 0.3 ppm; total solution volume was ~325 ml; Table 4.13). The increase in alkalinity, pH and Ca concentration all reflect the dissolution of calcite cement, whereas the more subdued increase in K and Si concentrations reflect the contribution from silicate minerals, likely K-feldspar. The total weight of the sample also decreased by 11% during testing, suggesting that most of the calcite contained in the 1.65 cm long segment of core had been dissolved during the two hours of testing as the weight loss was approximately the same mass of the calcite calculated to be in the sample before corrosion testing was initiated. These experimental results demonstrate that a repository containing calcite cement with some primary interconnected porosity will experience rapid pore widening and permeability-porosity increases following injection of CO_2. The reactions of this sample removed most of the calcite (10.4 volume percent) in a 1.65 cm thick sample in two hours.

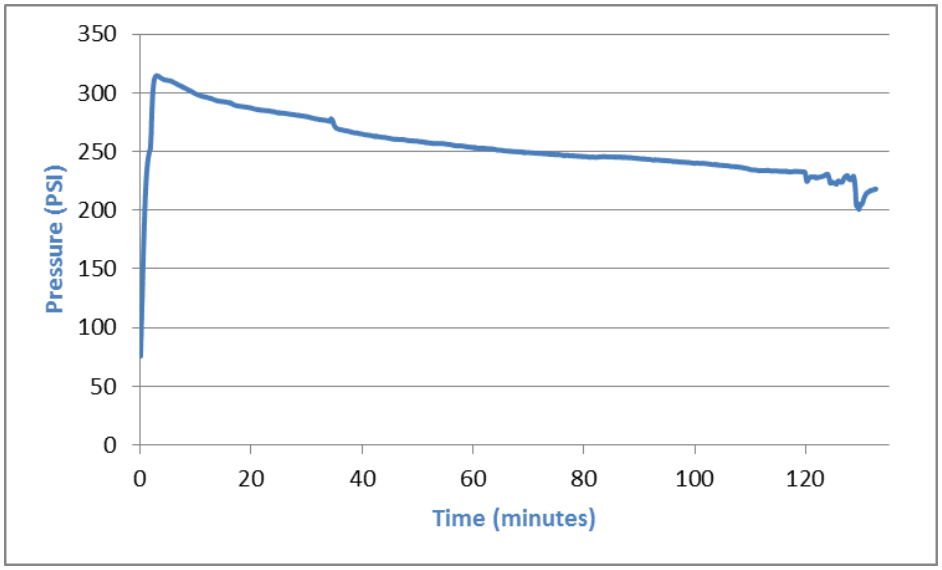

Figure 4.29 Transient flow (dp/dt <0) recognized in KEW3-1 sample core flooding experiments. The curve is indicating that the initial breakthrough occurring in only several minutes and gradual enhancement in the sample's porosity and permeability (reflected by a gradual long-term decrease in backpressure) associated with dissolution of calcite cement during the two hour core flooding run.

Table 4.13 Chemical composition of the influent and effluent water, in ppm, for the KEW3-1 sample core flooding experiments. A significant part of dissolved material is Ca, derived from the dissolved calcite from the rock sample. High initial Na concentration is due to the contamination inside the pump from previous experiments.

	Time (min.)	Ca	Mg	K	Na	Mn	Fe	Si	Al
Blank		<0.1	<0.1	<0.1	<0.1	<0.1	<0.1	<0.1	<0.1
Influent-in	120	<0.1	<0.1	<0.1	<0.1	<0.1	<0.1	<0.1	<0.1
Effluent	30	3.9	<0.1	0.9	3.4	<0.1	<0.1	0.3	<0.1
	60	5.4	<0.1	0.8	1.4	<0.1	<0.1	0.3	<0.1
	120	6.1	<0.1	0.5	0.5	<0.1	<0.1	0.2	<0.1

The CHC sample KEW3-2 sample contained a significant amount of calcite cement (11.1%) and moderate petrographic porosity (4.0%). The sample is a lithic feldsarenite composition. The flow rate on the core flooding experiment with this sample was started with one ml/min and then increased to be two ml/min after approximately 3 minutes of the testing. In contrast with KEW3-1 sample, the pressure curve showed a transient flow with positive pressure gradient ($dp/dt>0$; Figure 4.30). The permeability was decreased from 2.004 mD at the onset of the pressure stabilization after 5 minutes) to 1.790 mD after 53 minutes of testing. The increasing pressure gradient behavior over time for the KEW3-2 sample (Figure 4.30) was unexpected and did not correlate with the increasing of pH and dissolved Ca + Mg content that were observed, both features being suggestive of an increase in porosity-permeability following calcite dissolution.
A lowering of the backpressure was expected, opposite to the observed pattern. A possible explanation for this trend would invoke the blockage of restricted pore throats by migrating particles within the sample. Mineral particles (e.g., clays) could have been liberated and entrained in the fluid flow from zones where calcite was dissolving, and then became trapped in the narrow pore throat passages where grain boundaries come closest together. Sample KEW3-2 contained the highest proportion of silt and clay material (17.4 and 7.0 volume %, respectively; Table 3.1) for all the CHC samples thus there is thus a significant potential in this sample for particle migration.

The pH of the effluent water for the KEW3-2 sample increased from the starting leachant value of 3.8 to a value of 6.2 after about 40 minutes of testing (Table 4.14). Dissolution of the calcite cement was likely the cause of the rapid increase in the pH and released Ca, followed by a decline as the easily accessible calcite in the pores was progressively dissolved away. This indicates channelized flow paths were developing in the rock sample where the calcite was dissolving the most rapidly. Magnesium was only detected in the 20 minute sample with the highest Ca release, reflecting the fact that the calcite contains only 0.54 mole % Mg and thus would only occur in detectible concentrations when large amounts of calcite were being dissolved. The concentration of Si was at a maximum of 2.8 ppm at 40 minutes, but did not display any consistent trend with time. Sodium concentrations were high and reflected contamination from previous pump tests with brines.

Sample KEW1-1 was selected as a low petrographic porosity (1.0%) and high calcite cement (15.9%) specimen for the core flood test. This sample was exposed to the maximum pressure limit of 500 psi without any fluids being extruded after about two to three minutes of testing. The experiment was terminated immediately after three minutes to avoid over pressurization and damage to the core flooding equipment.

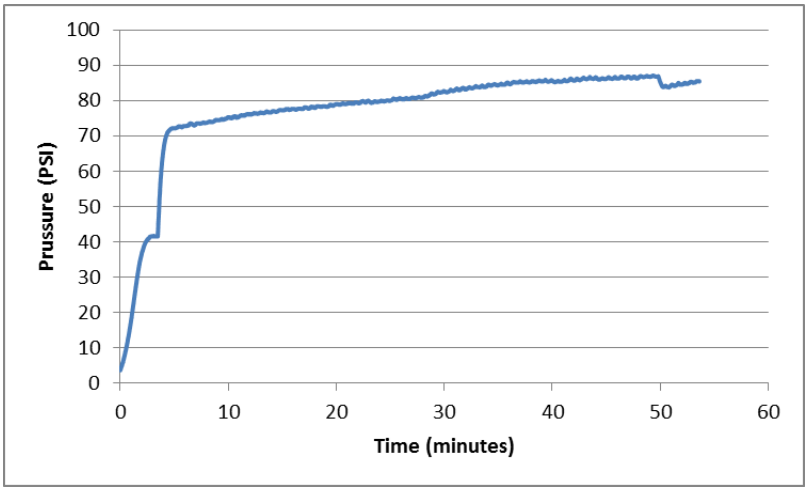

Figure 4.30 Transient flow (dp/dt>0) recognized in KEW3-2 sample core flooding experiments. The first flow rate at 1 cc/min for the first 5 minutes, then 2 cc/min between 5 and 53 minutes.

Table 4.14 Chemical composition of the influent and effluent water, in ppm, for the KEW3-2 sample core flooding experiments. A significant part of dissolved material is Ca, derived from calcite present in the rock sample. High initial Na concentration is due to the contamination inside the pump from previous runs.

	Time min.	pH	Si	Fe	Ca	Mg	K	Na	Mn	Al
Blank			<0.1	<0.1	<0.1	<0.1	<0.1	<0.1	<0.1	<0.1
Influent-*in*	53		<0.1	<0.1	<0.1	<0.1	14	3.6	<0.1	<0.1
	10		0.5	<0.1	56.4	1.1	2.8	101	<0.1	<0.1
	20	5.7	0.3	<0.1	11.0	<0.1	1.2	47.1	<0.1	<0.1
	30	5.6	0.3	<0.1	4.4	<0.1	0.7	22.9	<0.1	<0.1
	40	6.2	2.8	<0.1	2.2	<0.1	0.4	9.0	<0.1	<0.1
	50		<0.1	<0.1	2.5	<0.1	0.4	6.2	<0.1	<0.1

4.2.4 Flow Paths for Fluids in Reacted Samples. Porosity variations and different dissolution rates within and between minerals may have a large impact on permeability at spatially small scales. Porosity-permeability factors are often heterogeneous, and may become more-so as corrosive fluids migrate along preferential regions of a sample dissolution and expand these regions to create a channelized flow zone within specific regions of the rock sample (Wellman et al., 2003).

A three mm thick cylindrical core section of the KEW1-1 sample was sliced, polished, and then reacted in the static 90°C HPT testing environment with $H_2O + CO_2$ for 43 days. Upon completion of the corrosion test, the sample was impregnated with blue stained epoxy to preserve porosity features, and then cut along its cylinder c-axis. Detailed high resolution microscopic point counting was conducted on the reacted sample using a microfilm projector. The sample displayed a highly heterogeneous post-testing porosity, with alternating high- and low porosity zones occurring as porous and calcite-cemented course-grained lamina [e.g., zone A; Figure 4.31(B)] with less porous-Fe oxide cemented-fine grained lamina (e.g., zone B). The sample lost approximately 1.8% of its original weight during testing. The Ca concentration in the leachate fluid at the end of the corrosion testing was 496 ppm and Mg was 114 ppm. The final pH of the collected fluids was 6.2, indicating a significant acid-neutralization following dissolution within the sample as the initial pH in the CO_2-rich atmosphere of the tests was approximately 3.8.

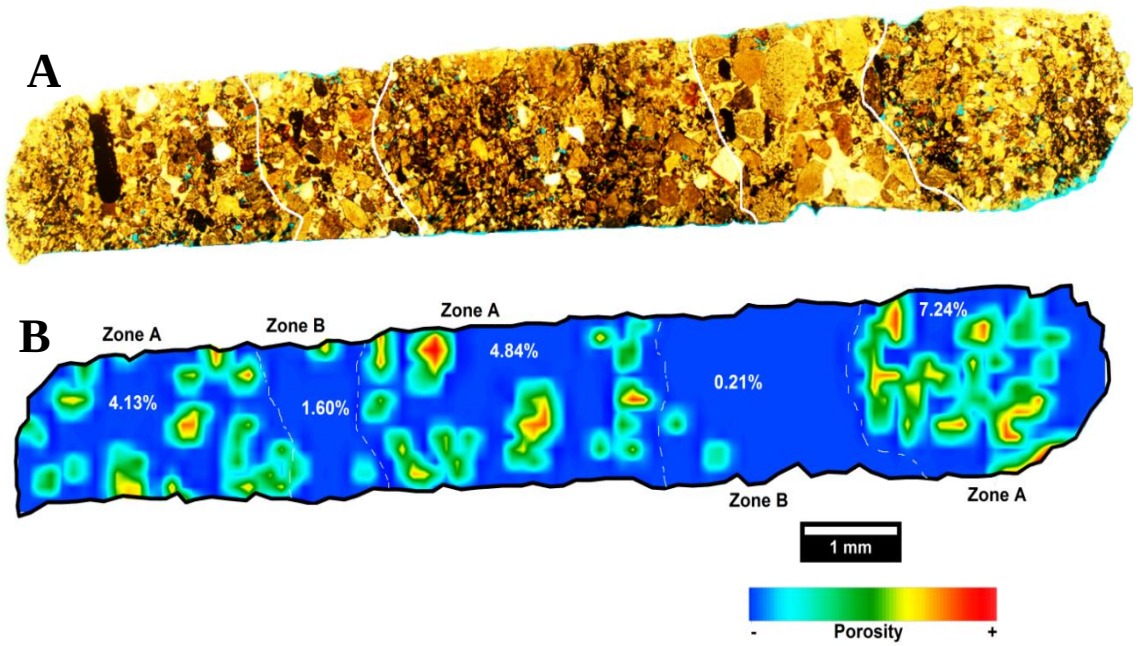

Figure 4.31 Plan polarized optical image of the KEW1-1 sample section after exposure to 90°C environment with CO_2 and H_2O for 43 days. (A) showing the laminations and the porosity distribution. Color enhancement image is showing the zonation of the porosity and the average porosity of each zone (B). The connected warm colors (red – green) represent the most favorable flow path through the sample.

4.3 FAR-FIELD GEOCHEMICAL REACTIONS AND REACTIONS INDUCING CARBONATE MINERAL PRECIPITATION

4.3.1 SEM/EDS Microanalysis. A primary goal for long-term geologic sequestration of CO_2 is the immobilization of injected CO_2 in a subsurface repository as carbonate mineral phases. The incorporation of CO_2 into solid minerals represents an immobilized from of the sequestered carbon that will remain in place for geologic time scales. One of the main experimental goals of this study sought to produce carbonate minerals through the geochemical reactions between MCR rock samples and a H_2O + CO_2 reaction environment. The most effective way to ensure that MCR sedimentary and volcanic rocks can produce carbonate minerals is to examine the reacted sample surfaces using a combination of SEM-EDS microanalysis, solution analysis, and geochemical modelling. SEM-EDS analysis of the CHC samples KEW1-1 and KEW 5-1 revealed the presence of numerous 4 to 6 µm diameter calcium carbonate crystals that were rhombohedral and had a Ca-C-O composition in ratio of approximately 1:1:3, both features which are characteristic of calcite (Figures 4.32; Appendix Figures D4 to D8). The crystals were euhedral and there were no signs of dissolution pits occurring on their surfaces, suggesting that these were newly formed crystals. Any calcite present as an original constituent of the rock, and present during test initiation, would likely show the formation of dissolution pits as a result of the acidified carbonic acid-rich solution contacting the samples at the initiation of the experiments. In longer term reactions, the reactions between the rock samples and the aqueous fluid would neutralize the acids and allow carbonate minerals to form.

The two samples that displayed the formation of carbonate minerals, KEW1-1 and KEW 5-1, were reacted for a total of 143 and 2,446 hours, respectively, (6 and 102 days). The precipitation of the calcite minerals in such a short time period confirms that carbonate mineralization will likely be initiated in very short time periods in a potential MCR GCS site when acid neutralization is achieved. The MCR rocks that were tested in these experiments contain an abundance of carbonate minerals that quickly dissolved by the carbonic acid solution in the test vessels to neutralize the solution pH and release Ca^{2+} ions into solution, both factors which will induce carbonate mineral formation. The final bulk solution pH for the KEW1-1 sample was 6.1 and the Ca concentration was 702 ppm.

For the KEW5-1, sample the final pH was 5.0 and the Ca concentration was 915 ppm. We expect that the solution in the microenvironments in the pore spaces may achieve even higher pH values and Ca contents than the bulk solution that was measured. Since both experimental solutions were still mildly acidic when the tests were terminated, we would also expect that continued carbonate mineralization would occur in longer term tests as the solutions were further neutralized through reactions with the rock minerals. These tests thus simulate longer-term and/or more distal reactions where the buffering capacity of the groundwater system and associated rocks have neutralized acids formed in association with CO_2 injection.

In addition to calcite forming as a precipitated alteration phase, sample POT4 also had developed rounded alteration precipitates as in Figure 4.32 (F) with a SEM-EDS chemical composition of (in mole %) of 10% Na, 10% Al, 26% Si, and 52% O, with trace Fe and Mg (Appendix Figure D.9). The relatively small size of the crystals hindered an accurate chemical determination as the EDS response signal likely included an analysis from the surrounding and/or underlying substrate in the sample. The composition and occurrence of this phase on altering basaltic rock fragments is consistent, however, with the presence of the zeolite group mineral analcime ($NaAlSi_2O_6.H_2O$). Analcime commonly displays a trapezohedron morphology, but may also exhibit platy, cubic, and rounded forms.

4.3.2 CO_2 Generated During the Calcite Dissolution. During the dissolution of calcium carbonate minerals, a significant amount of CO_2 may be produced according to the equation: $CaCO_3 + 2H^+ = Ca^{2+} + CO_2 + H_2O$. To test for this gas generation, we reacted eight samples averaging 0.1021±0.0031 grams of calcite in a testing apparatus designed to capture the CO_2 gas generated during calcite dissolution. The calcite samples produced an average of 2.24 ±0.14 ml of gas phase CO_2 following complete dissolution of calcite (after ~2 minutes of submersion in a 5% HCl solution). The stoichiometric calculations of that reaction showed that amount of calcium carbonate (0.1021 g) should produce 0.0449 grams of carbon dioxide (calculated stoischimetrically fron http://www.webqc.org/balance.php), which is about 22.7 ml. That emplied some of CO_2 generated trapped as DIC into the acidic water.

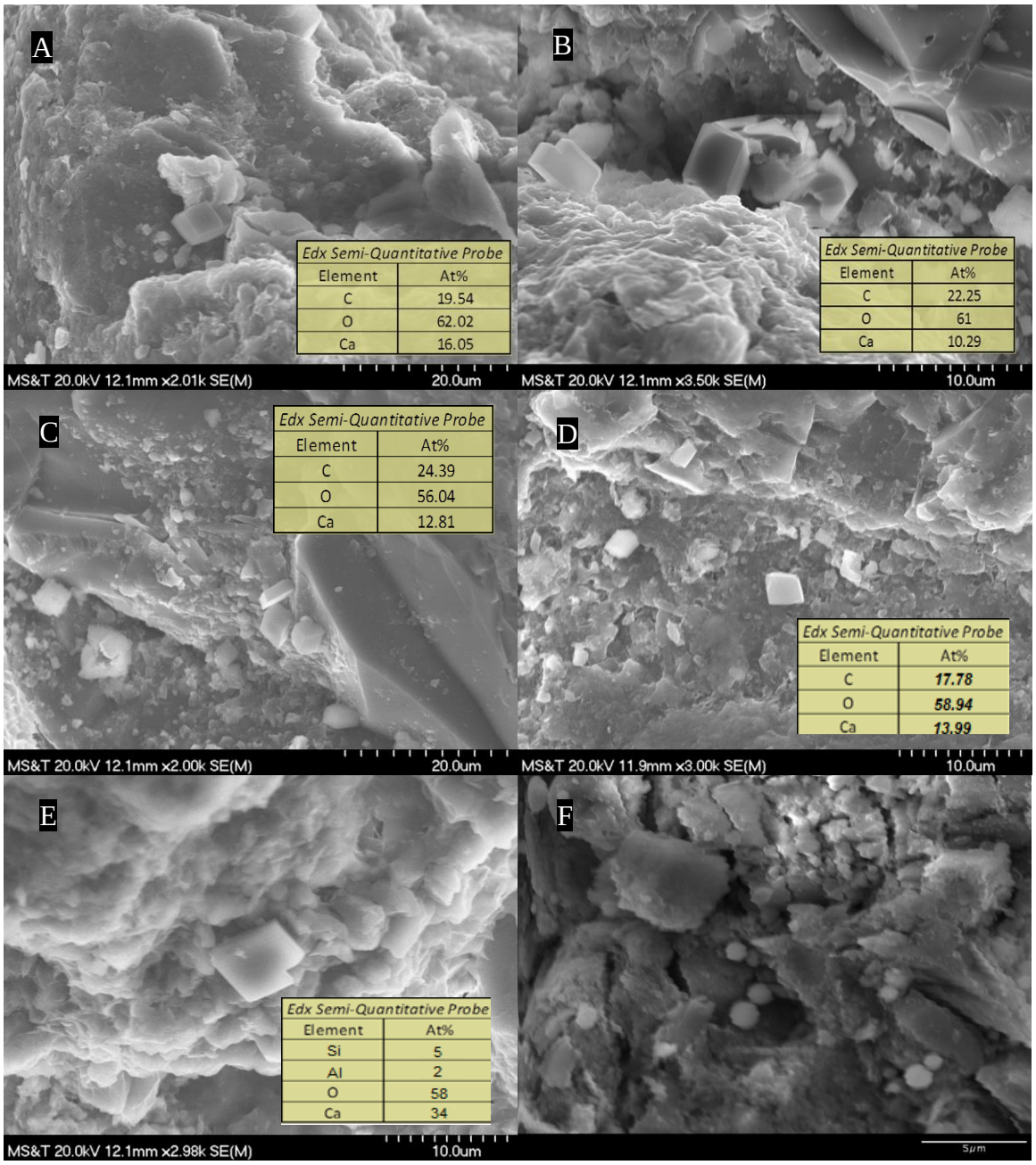

Figure 4.32 Midcontinent Rift sediment samples displaying precipitated alteration minerals following reaction in a CO_2 + DIW environment at 90ºC. Calcite crystal identified from EDS microanalysis and rhombohedral morphology from CHC sample KEW5-1 reacted for 2446 hours (101.9 days). B) Calcite crystal on sample KEW5-1. C) Calcite crystal on sample KEW5-1. D) Calcite crystal on CHC sample KEW1-1 sample reacted for 143 hours (6 days). E) Calcite crystal based on the atomic percentage obtained from the EDS microanalysis. F) Rounded mineral formed on an altered surface of POT4 sample.The rounded phase is tentatively identified as analcime based on its morphological characteristics and chemical composition.

4.3.3 Geochemical Modeling of Carbonate Minerals Precipitation. Modeling of the leachate solution results provide an estimation of the mineral phases that could form during the HPT testing and were not recognized under the SEM-EDS microanalysis. The physical, environmental, and chemical input data for the model were provided in the Appendix A.4. These data were used to generate mineral saturation model of the leachate solutions using the USGS PHREEQC^{TM} aqueous geochemical modeling. The saturation index [$SI_{mineral} = \log (m_{me}^{2+} \times m_{CO3}^{2-})/Ksp$] of the mineral represents maximum solubility point at which the leachate solution could precipitate the mineral (if SI>0) or that leachate solution is undersaturated with respect of that mineral (if SI<0; see Section 2.4). The assumptions of the model are based from these points: (1) The pH and Eh of the leachate solutions were collected, immediately, after the opening of the vessels to ensure minimum CO_2 degassing. So, the pH and Eh represented the closest value to the actual values during the HPT testing. (2) The generated model calculates the phases that could be exist in equilibrium based on both fixed pH and a calculated pH from the charge balance. (3) The model calculated from the fixed pH showed a negative SI for minerals in all samples investigated, although significant precipitations of these minerals were detected by the SEM, so a floated pH model was considered.

The samples from the Keweenawan Peninsula (KEW) were calculated to be supersaturated with respect of carbonate minerals based on the USGS PHREEQC^{TM} modelling results (i.e. aragonite, calcite, dolomite, and rhodochrosite; Figure 4.33; Table 4.15; and Appendix Table D.17). Talc, quartz, and chalcedony were also calculated to be saturated in the KEW4-2, and KEW5-1 tests. The manganese oxides had a positive saturation indices for hausmannite (Mn_3O_4) and pyrochroite ($Mn(OH)_2$) minerals in the Keweenawan samples. Potato River samples (except POT8-2) were determined to be supersaturated with respect to aragonite, calcite, and dolomite. The Unit C2 samples were commonly calculated to be undersaturated with respect to carbonate minerals except for sample C2-1 (supersaturated for calcite only) and C2-2 (supersaturated for aragonite and calcite). Quartz and Mn oxides were determined to be supersaturated for the C2-2 and C2-3 samples, and Fe oxides and hydroxides minerals were supersaturated in all of the Unit C2 samples. Unit D4 samples were determined to be supersaturated with respect of

aragonite, calcite, and rhodochrosite. Also, the Mn and Fe oxides had positive saturation indices as in the Unit C2 samples.

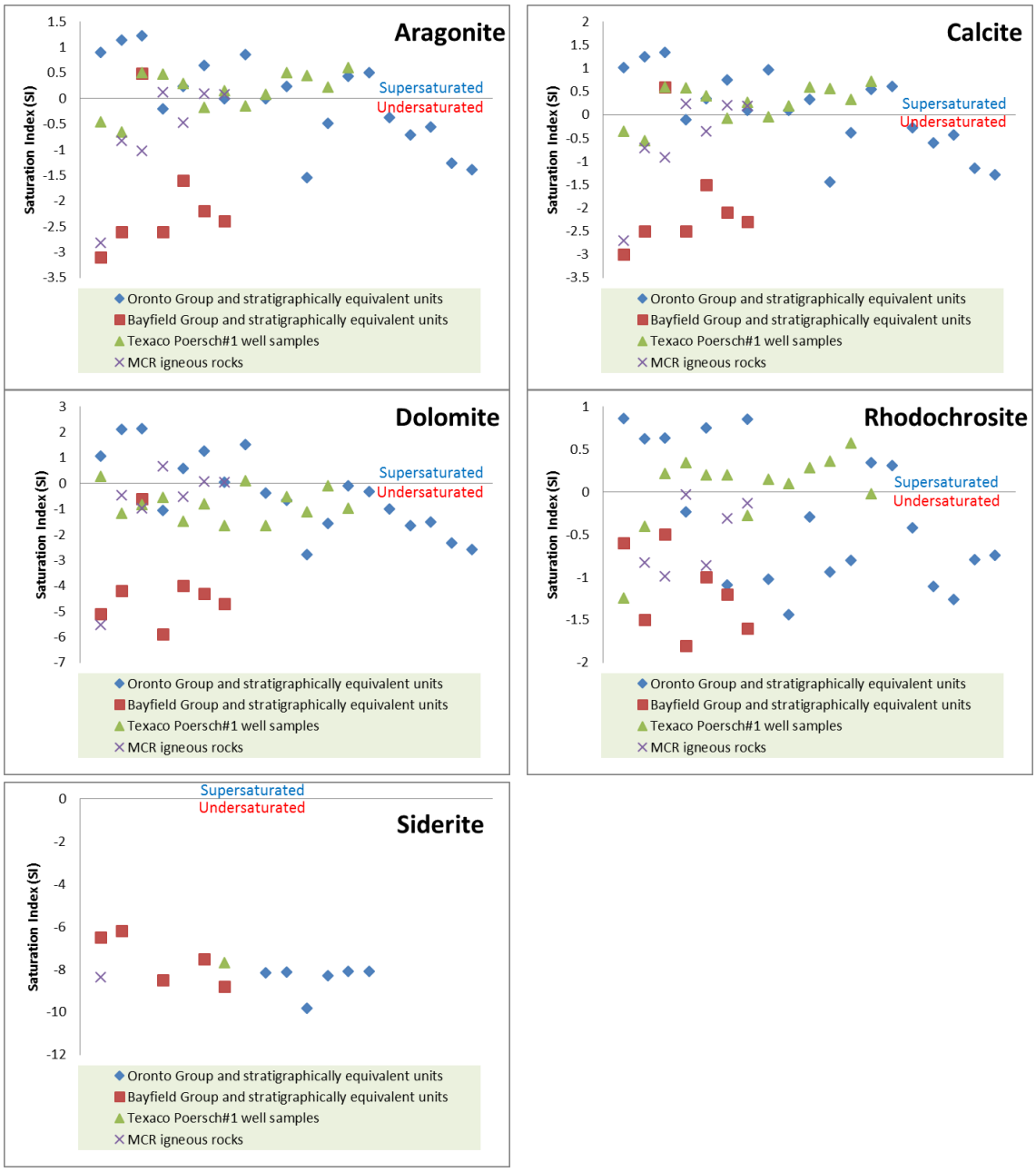

Figure 4.33 The saturation indices ($SI_{mineral}$) with respect of major carbonate minerals of the leachate solutions of MCR samples. The negative values represent the undersaturated state and the positive values represent the supersaturated state of the minerals.

Table 4.15 The saturation indices ($SI_{mineral}$) with respect of major carbonate minerals of the leachate solutions of the Oronto Group and stratigraphically equivalents units.

	Aragonite	Calcite	Dolomite	Rhodochrosite	Siderite
	($CaCO_3$)	($CaCO_3$)	[$CaMg(CO_3)_2$]	($MnCO_3$)	($FeCO_3$)
KEW1-1	0.9	1.0	1.1	0.9	
KEW4-2	1.1	1.2	2.1	0.6	
KEW5-1	1.2	1.3	2.2	0.6	
POT8-2	-0.2	-0.1	-1.1	-0.2	
CFSP4	0.2	0.4	0.6	0.8	
POT2	0.7	0.8	1.3	-1.1	
POT4	0.0	0.1	0.1	0.9	
POT5-1	0.9	1.0	1.5	-1.0	
C2-1	0.0	0.1	-0.4	-1.4	-8.2
C2-2	0.2	0.3	-0.7	-0.3	-8.1
C2-3	-1.6	-1.4	-2.8	-0.9	-9.8
C2-5	-0.5	-0.4	-1.6	-0.8	-8.3
D4-1	0.4	0.5	-0.1	0.3	-8.1
D4-2	0.5	0.6	-0.3	0.3	-8.1
SF1-1	-0.4	-0.3	-1.0	-0.4	
SF1-2	-0.7	-0.6	-1.6	-1.1	
SF3-2	-0.6	-0.4	-1.5	-1.3	
SH1	-1.3	-1.2	-2.3	-0.8	
SH2	-1.4	-1.3	-2.6	-0.7	

The samples collected from the Bayfield Group and its surface and subsurface equivalent stratigraphic horizons showed a general undersaturated condition with respect of carbonate mineralization (Figure 4.33; Table 4.16; Appendix Table D.18). The only exception was the E2-2 sample, which had saturation indices for aragonite and calcite of 0.49 and 0.60, respectively. This sample was characterized by the presence of calcite cement as an original rock constituent (Table 3.6). The quartz saturation index values were positive for the L'ANSE1, E2-2, and E2-4 samples. The only other silicate mineral with positive saturation index was anorthite in the BAY3 sample, but this is considered to be an unlikely mineral to occur during water-rock interactions as it is unknown in hydrothermal deposits. The Fe oxide and hydroxides minerals (i.e. hematite and goethite) were calculated to be supersaturated in the Bayfield Group and its equivalent stratigraphic units. Also, the Mn oxides (i.e. hausmannite and pyrolusite) were

supersaturated, generally, in the leachate solutions of the Bayfield Group and its equivalents. Phyllosilicate minerals represented by gibbsite, kaolinite, illite, Ca-montmorillonite, and muscovite were calculated to be supersaturated in the leachate solutions of the BAY3, E2-4, AG1, and AG2 samples.

Table 4.16 The saturation indices ($SI_{mineral}$) with respect of major carbonate minerals of the leachate solutions of the Bayfield Group and stratigraphically equivalents units.

	Aragonite	Calcite	Dolomite	Rhodochrosite	Siderite
	($CaCO_3$)	($CaCO_3$)	[$CaMg(CO_3)_2$]	($MnCO_3$)	($FeCO_3$)
BAY3(-Al)	-3.1	-3.0	-5.1	-0.6	-6.5
L'ANSE1	-2.6	-2.5	-4.2	-1.5	-6.2
E2-2	0.5	0.6	-0.6	-0.5	
E2-3	-2.6	-2.5	-5.9	-1.8	-8.5
E2-4	-1.6	-1.5	-4.0	-1.0	
AG-1	-2.2	-2.1	-4.3	-1.2	-7.5
AG-2	-2.4	-2.3	-4.7	-1.6	-8.8

Aragonite, calcite and, rhodochrosite were commonly determined to be supersaturated in the Texaco Poersch#1 well based on the USGS PHREEQC™ modelling code (Figure 4.33; Table 4.17). Dolomite was determined to be supersaturated in both the 5,397.3′A and B samples. Silicate minerals were represented by quartz (in 5,397.3′A and B, 8,051.1′A, and 10,514′B) and microcrystalline quartz (chalcedony in 8,051.1′A). Hausmannite and pyrolusite were calculated to be supersaturated in all leachate solutions collected from the Texaco Poersch#1 well samples. The 11,061′A sample showed a positive saturation index for both goethite and hematite minerals, exclusively. Saturation indices of the Texaco Poersch#1 well leachate solutions are illustrated in Appendix Table D.19.

Table 4.17 The saturation indices ($SI_{mineral}$) with respect of major carbonate minerals of the leachate solutions of the Texaco Poersch#1 well samples.

	Aragonite	Calcite	Dolomite	Rhodochrosite	Siderite
	($CaCO_3$)	($CaCO_3$)	[$CaMg(CO_3)_2$]	($MnCO_3$)	($FeCO_3$)
5,397.3′ A	-0.5	-0.4	0.3	-1.2	
5,404' A	-0.7	-0.6	-1.2	-0.4	
8,051.1′ A	0.5	0.6	-0.8	0.2	
8,476′-8,480′ A	0.5	0.6	-0.5	0.3	
10,514′ A	0.3	0.4	-1.5	0.2	
10,666′ A	-0.2	-0.1	-0.8	0.2	
11,061′ A	0.2	0.3	-1.7	-0.3	-7.7
5,397.3′ B	-0.2	0.0	0.1	0.2	
8,051.1′ B	0.1	0.2	-1.7	0.1	
8,476′-8,480′ B	0.5	0.6	-0.5	0.3	
10,514′ B	0.5	0.6	-1.1	0.4	
10,666′ B	0.2	0.3	-0.1	0.6	
11,061′ B	0.6	0.7	-1.0	0.0	

The leachate solutions of MCR igneous rock samples were determined by reacting representative samples from the Duluth complex (DUL), Beaver Bay complex (BEV), and North Shore Volcanic Group (GHB and GHC). These samples were, also, modeled for the mineral species using the PHREEQC^{TM} aqueous geochemical software (Figure 4.33; Table 4.18). The carbonate mineralization from the leachate solutions of BEV, DUL, and GHB samples were all determined to be undersaturated for carbonate phases with the exception of the GHB2 sample, which had a saturation index of 0.23 and 0.68 for calcite and dolomite, respectively. The clastic interflow sediment samples GHC1 and GHC2 showed positive saturation indices for calcite, aragonite, and dolomite. Quartz was determined to be supersaturated in all MCR igneous rock samples accept for BEV1, and chalcedony was supersaturated for the DUL1, DUL2, GHC1, and GHC2 samples. The Mn oxides, represented by hausmannite and pyrolusite, were supersaturated in all investigated samples except for the BEV1 sample. This latter sample was determined to be supersaturated with respect to Fe hematite and goethite.

Table 4.18 The saturation indices ($SI_{mineral}$) with respect of major carbonate minerals of the leachate solutions of the MCR igneous rocks samples.

	Aragonite	Calcite	Dolomite	Rhodochrosite	Siderite
	($CaCO_3$)	($CaCO_3$)	[$CaMg(CO_3)_2$]	($MnCO_3$)	($FeCO_3$)
BEV1	-2.8	-2.7	-5.5		-8.4
DUL-1	-0.8	-0.7	-0.5	-0.8	
DUL-2	-1.0	-0.9	-1.0	-1.0	
GHB-1	0.1	0.2	0.7	0.0	
GHB-2	-0.5	-0.4	-0.5	-0.9	
GHC-1	0.1	0.2	0.1	-0.3	
GHC-2	0.1	0.2	0.1	-0.1	

4.3.4 Conceptual Model of CO_2 Sequestration in MCR. The conceptualized box model illustrated in Figure 4.34 shows three different environmental changes affecting the reactions of repository host rocks during a hypothetical CO_2 injection process for the MCR sequence. This model would be appropriate as well for any other setting involving a combination of relatively inert siliciclastic and higher solubility carbonate minerals. The reaction box model has transient, temporal, and spatial variations. Each box is treated as a hypothetical semi-closed system allowing reactions to run to completion and then transitioning into the environment characteristic of the next reaction box once the first set of reactions have ended (e.g., calcite has been consumed). Environmental conditions of each of the three boxes may also move outwards or inwards relative to the site(s) of well injection depending on the injection rate of CO_2 into the subsurface repository and reaction rates of the rock material. This model is based on the results of the batch reactors of samples collected from the MCR and other experiments discussed earlier.

Box 1 shows the effect of CO_2 injection and carbonic acid formation on the dissolution processes affecting calcite and other minerals in the near-field to the CO_2 injection well(s). Because calcite is so much more reactive under acidic conditions relative to the silicate, oxide, and other minerals in the stratigraphic sections of the MCR, it will tend to dominate the acid neutralization reactions and inhibit the dissolution of silicates and oxides. The surface area of the exposed calcite, solution pH, and

temperature will be the most important parameters affecting calcite dissolution, which is expected to be between 5.21×10^{-4} to 4.00×10^{-5} mol/cm^2.day, or 20.1 to 1.6 mg/ cm^2.day. The average proportion of calcite cement in the CHC samples was 13% (range between 6.6 and 23.5%). Therefore, one cm^3 of Keweenawan rocks should have 0.13 cm^3 of calcite on average, which represents 352.3 mg of calcite (calcite density 2710 mg/cm^3) and 141.1 mg Ca (Ca mole% in calcite is 40.04%). The porosity increased by such dissolution was determined to be 30% in the first hours of the injection processes as seen in the core flooding of the KEW3-1 sample. The effective porosity will continue to be enhanced as one segregated pore zone is connected to another through the progressive dissolution along calcite cleavage planes as revealed in Figures 4.17 and 4.18. The pressure regime resulting from the injection processes will also enhance the rate that the fluid penetrates through the opened cleavage planes and activated fractures. Silicate and oxide dissolution is considered to be negligible in this stage as long as calcite remains in the system.

Assuming that the whole surface area of a calcite grain will be exposed directly to the acidified fluids, the calcite cement will completely dissolve in a range of 3 to 127 days from 1 cm^3 block of sample have a calcite cement between 6.6% and 23.5%. Acid neutralization processes will now be controlled by the kinetically slower reactions with silicate minerals such as feldspars and pyroxenes, once all of the local calcite has been consumed. In the Box 2 situation, carbonic acid may be present at pH <4 or may be partially neutralized. Dissolution of the silicate and oxide rock minerals will begin to occur or be accelerated following the Goldich stability of the minerals. Ca, Mg, K, Na, and Si will be released into solution from the dissolution processes affecting these phases. The continuing injection of CO_2 will replenish the carbonic acid and keep the pH in the Box 2 region at a value of about 4, and push the Box 1 region to a location outwards of Box 2. The acidity of the aquifer fluid will be the main agent to accelerate the dissolution of the silicate minerals. In addition, increasing the exposed surface area of the silicate minerals through uncovering by previous dissolution of the carbonates, and any temperature increases associated with CO_2 injection and exothermic mineral reactions may accelerate the dissolution rate of silicate and other non-carbonate mineral phases.

In the Box 3 environment, the reactions with calcite and silicate minerals has effectively neutralized all carbonic acid and allowed the pH to rise up to neutral or mildly alkaline conditions. The ions present in the original brine solution of the aquifer fluids plus the released alkali and especially alkaline earth components from dissolving mineral phases will lead to high solution activities, and may eventually cause carbonate minerals to precipitate once saturation levels have been achieved with respect to any carbonate phase(s). This scenario could be influenced by spatial variability (after the migration and neutralizing of the supercritical CO_2 phase away from the injection well site) or temporal variations (after dissolving the supercritical CO_2 phase and neutralizing the acids; Section 1.1). A 200 year interval of converting supercritical inorganic carbon into aqueous phase CO_2 species was estimated by Ennis-King and Paterson (2003) from a model that created of 100 m reservoir, one MtC/y injection rate, 40°C temperature, 10MPa pressure, 10^{-13} m^2 horizontal permeability, and 10^{-14} m^2 vertical permeability. The model determines that CO_2 will be dominantly in an aqueous phase after 200 years after CO_2 injection terminated. The Box 3 reactions would be expected to occur in the more distal locations of a repository while CO_2 injection was occurring, or collapse back inwards towards the injection wells once CO_2 injection has ceased.

Watson and Gibson-Poole (2005) suggested an "ideal" geochemical setting for CO_2 sequestration in the reservoirs. That "ideal model" is unlike the traditional CO_2 sequestration in highly permeable mature reservoir [Figure 4.35 (A)]. High permeability reservoirs by their nature have a high ability to ensure effective injection of anthropogenic gasses, but typically have a low capability to induce carbonate mineralization by water-rock-CO_2 interactions. This association often occurs because the minerals that tend to provide Ca^{2+} and Mg^{2+} ions for carbonate mineralization also tend to be altered into permeability-limiting clay minerals that fill pore spaces. For example, Bayfield Group and stratigraphically equivalent units will be geochemically inert because they are composed dominantly of quartz. Watson and Gibson-Poole suggest that the best geological juxtaposition for a repository horizon is the presence of low-permeability (< 50 mD) and immature rocks, for carbonate mineralization, that overlie a highly permeable zone (> 100 mD) as an injection layer as in Figure 4.35 (B). Also, the low-

permeability zone will decrease the diffusion velocity to ensure more water-rock-CO_2 interaction time, and allowing to more lateral migration of the CO_2 plume.

The Texaco Poersch#1 well contained a 22 ft-thick porous layer (up to 15% porosity determined by geophysical analysis; Berendsen, et al., 1988). This layer could act as an injection horizon especially if the injection horizon dimensions can be increased by horizontal drilling. More geophysical studies are also needed to define the extent and geometry of the 22 ft-thick zone, and both hydrolytic fracturing and aquifer acidification processes could be useful for a successful injection process. The potential sequestration zone in this sequence (i.e. the low permeability immature rocks that overlain the 22 ft-thick zone) have an average porosity of 2% and are enriched in Ca-bearing minerals like Ca-plagioclase [Figure 4.35 (C)]. Based on the geothermal gradient 1.05 °F/100 ft (19°C/km; Anderson, 1990) and the estimated formation pore pressure gradient 0.45 psi/ft, the minimum depth required to keep CO_2 as supercritical-phase will be located anywhere below 838 ft at the Texaco Poersch#1 well.

Horizontally layered flood basalts tend to have low effective vertical porosities, so, if the basalt is not heavy fractured or jointed they could be considered as possible seal rocks. The Carrajung basaltic floods, Gippsland Basin (Australia) is an example of a mafic rock that could act as an effective seal for oil produced from the Golden Beach Formation (Sloan and others, 1992). Other benefit of the basaltic floods are their potential self-selling properties. If there is an acidic fluid passing through the MCR basaltic rocks than carbonate minerals may precipitate within the fractures following alteration and block fluid or gas migration.

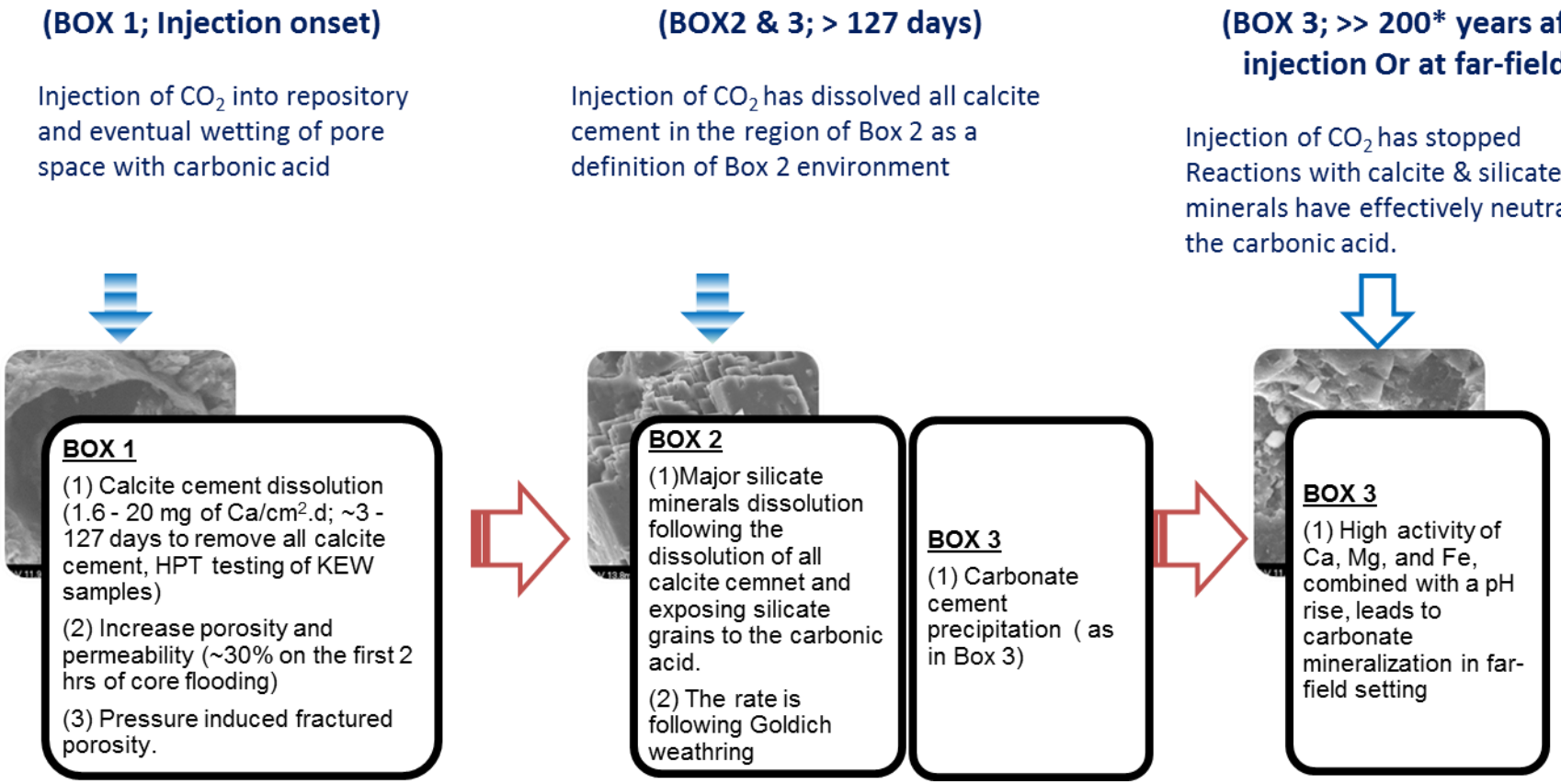

Figure 4.34 Conceptual model of the geochemical processes that follows the injection of super critical CO_2 in the MCR rocks.
* Refers to the time required to convert all injected CO_2 to dissolved phases after the termination of the injection processes are from Ennis-King and Paterson, 2003.

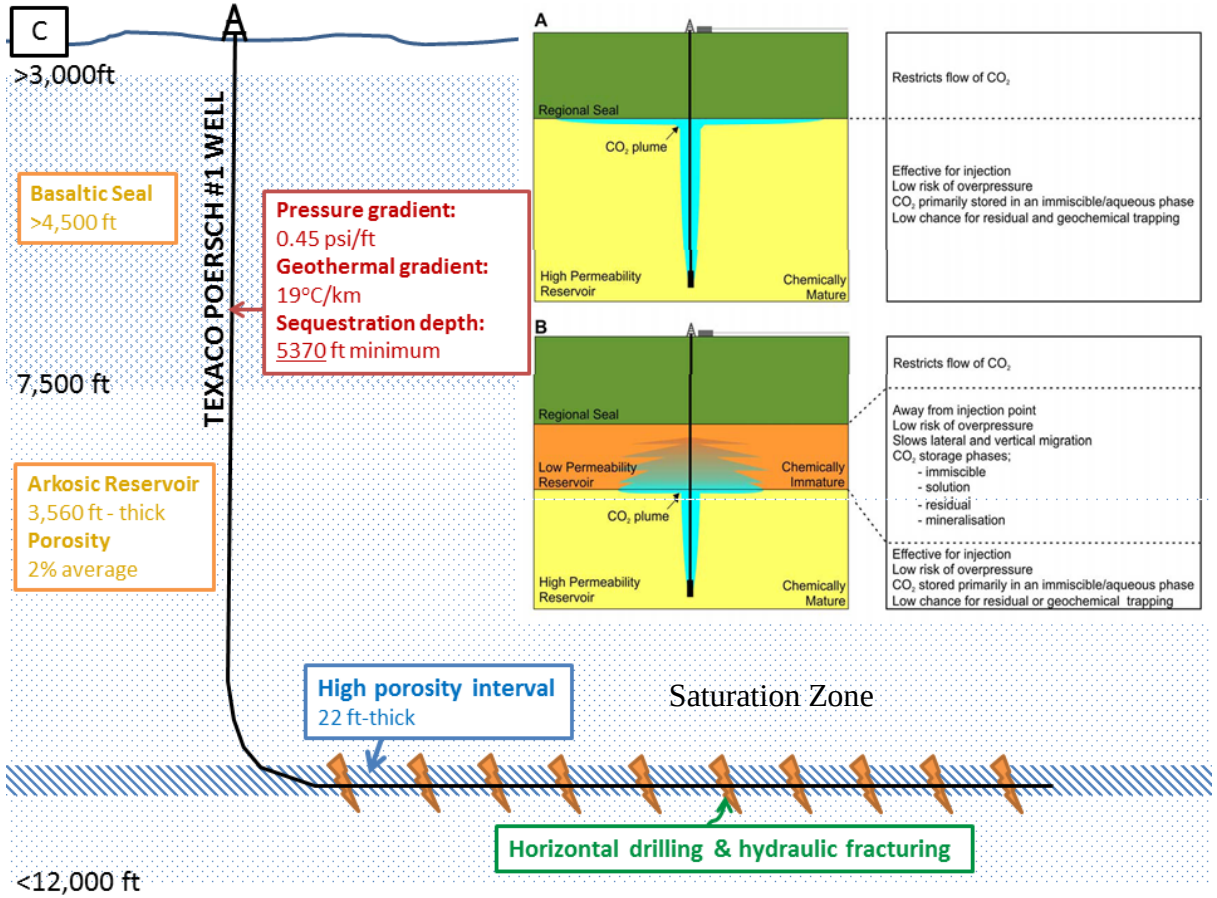

Figure 4.35 Conceptual model of deep CO_2 sequestration. The model created by Watson and Gibson-Poole (2005) for (A) the traditional CO_2 sequestration in siliciclastic reservoir and (B) the "ideal" reservoir system for mineralogical sequestration. (C) Example from the Texaco Poersch#1 well in Kansas.

5 CONCLUSIONS

Midcontinent rift clastic and volcanic rocks were investigated for their mineralogical and geochemical aspects for CO_2 sequestration, with a particular emphasis on investigating the process of mineral sequestration of CO_2 by precipitation of carbonate minerals. These aspects including the ability of the aquifer minerals to release Ca^{2+}, Mg^{2+}, and Fe^{2+} to induce the mineralization of carbonate minerals. The Oronto Group, and its stratigraphically equivalent horizons, exhibit attractive characteristics for mineral sequestration (i.e. enrichment of Ca-, Mg-, and Fe-bearing silicate and oxides). Also, the thickness, depth throughout much of the Midcontinent region, lateral continuity, presence of effective seal rocks, minimal number of intrusive drilling wells represented the favored characteristics for CO_2 sequestration in the Oronto Group (Thorleifson, 2008). However, the impermeable nature of this group has rendered it as an unlikely target for geologic carbon sequestration. Because of its permeable characteristics, the Bayfield Group and its stratigraphic equivalents represent an attractive target for effective CO_2 injection. However, a regional and effective seal rock for these group is mostly not present, as they are usually covered, unconformably, by basal Cambrian-aged permeable sandstones. The Bayfield Group sequence rocks also typically lack the Ca-, Mg-, and Fe-bearing silicate and oxides required to produce mineralizing reactions.

Detailed petrographic investigations on the Oronto Group and its stratigraphic equivalents from samples collected from both surface outcrops in the Lake Superior Region and in drill core samples recovered from buried MCR sections in Iowa and Kansas revealed the domination of lithic fragments within the Copper Harbor Conglomerate (e.g., > 75% lithics in the Oronto Group samples). The feldspathic and quartz contents increased stratigraphically upwards in both the overlying Nonesuch and Freda Formations. That trend of chemical maturation continued as the age of the rift clastics was decreased (i.e. Bayfield and Jacobsville sandstones were the most chemically and texturally mature sandstones). Accessory minerals of mica, epidote, heavy minerals, and iron oxides were identified in the Oronto Group samples. Chlorite, illite, calcite,

orthoclase, quartz, and laumontite were identified from the XRD analysis of the clay-sized matrix material in the Keweenawan Oronto Group samples. Meanwhile, samples collected from the Potato River, Copper Falls State Park, and the Eischied well in Iowa contained chlorite, illite, smectite (traces), calcite, orthoclase, quartz, and laumontite. The stratigraphically uncorrelated (as neither Oronto Group nor Bayfield Group) Texaco Poersch #1 samples showed a similar matrix and fine grained-mineralogy to that in the Oronto Group. Additionally, dolomite and zinnwaldite peaks were detected by the XRD analysis. Calcite cementation was dominant in the KEW samples (between 6.6% and 23.5%). Meanwhile, both iron oxide and calcite cement were identified in the Potato River Samples.

The porosity of the Oronto Group samples was between 0.0 and 5.3% for sandy lenses between the larger clast fragments, as determined by petrographic analysis. The CHC sample KEW3-1 (collected in Esrey Park on the Keweenawan Peninsula of Michigan) had 8.9% open porosity plus an additional 10.4% of the pore space filled with calcite cement. The sample was also collected from a sandy lens within a conglomeratic unit, so the actual rock porosity should less than half of this value as larger pebbles and cobbles with very limited porosities comprise ~50% of the observed rock outcrop at this location. A sample collected from the Poersch #1 Well in Kansas at the 11,061 ft depth was found to contain 7.9% open porosity (lab water flooding experimental porosity from this present study; Table 2.1) abundant feldspar, and only trace amounts of calcite cement. This sample was collected from a 22ft-thick zone (between 11,055 and 11,077 feet) that exhibited up to 15% porosity as determination by geophysical well logging analysis (Berendsen et al., 1988).

Chemical analyses of the Oronto Group and stratigraphically equivalent surface and subsurface samples are enriched in the alkaline earth oxides (between 4 and 12 wt. % CaO + MgO; Figure 4.2). Also, the North Shore Volcanic Group (NSVG) and Beaver Bay and Duluth complexes had a high percentage of CaO and MgO of 19 and 15 wt%, respectively (Figure 4.4). The amount of the alkali earth metal oxides suggests that these rock units would have great potential for immobilizing injected CO_2 by reacting with the groundwater fluids to precipitate carbonate minerals.

The chemical composition of the leachate fluids of the HPT testing of the samples collected from the Oronto Group revealed high Ca release concentrations (average of 349 ppm) as compared to the Bayfield Group and its equivalent stratigraphic units (average of 25.5 ±19 ppm; sample E2-2, which released Ca at a concentration of 496 ppm, was excluded from this average). The molal release rate of Ca in calcite-cemented samples of the Oronto Group sometimes reached more than 10-times the release rate of other rock components such as Mg, K, Na, and Si. Also, some calcite cemented-samples exhibited a continuous enhancement in permeability during the flooding test assessment (e.g., ~30% increase in two hours of testing for the KEW3-1 sample) as a result of calcite dissolution. The dissolution of calcite cement should normally increase the porosity-permeability of sediments close to the injection well site due to the acidification by carbonic acid and its subsequent influence on dissolving pore-blocking calcite cements. However, some samples exhibited a reduction of the permeability during the core flooding test (Texaco Poersch #1; 11,061.5′ sample; Figure 4.28). The reason for this decrease has not been determined, but may have resulted from small acid-resistant grains being dislodged from regions where calcite was dissolving. Once released, these grains can become entrained in the moving water, and then can be lodged in the narrow pore throats separating the larger diameter pore regions from each other. Another potential cause for this reduction in permeability may involve the swelling of clay minerals.

The dissolution rates for silicate minerals aremuch slower than the rate of calcite (i.e., calcite reached a pH of 8.78 in two days of calcite dissolution experiment, while the fastest silicate mineral reaction involved olivine, which reacted to produce a pH of 8.46 in one week). The fastest rates of corrosion occurred along the corners and edges of the minerals as revealed by locations of dissolution pits on altered samples. The mafic mineral' content is another factor playing a significant role in releasing Ca, Mg, and Fe required for mineral sequestration as the HPT testing of MCR samples revealed elevated concentrations of the major elements in leachate solutions. The concentration of Si indicated the mafic silicate mineral's dissolution, and the concentration of Mg were more likely sourced from the silicate minerals than the calcite cement, which was found to be a low Mg-calcite for Keweenawan samples ($Ca_{99.5}Mg_{0.5}$ mole%). The main source of Mg

was thus the dissolution of mafic minerals that were available in the mafic lithic fragments in both the MCR clastics and the basaltic floods.

The PHREEQC equilibrium saturation code was used to evaluate the saturation status of the leachate solution with respect to carbonate minerals under our testing conditions. The saturation indices (SI) were positive in 23 of 30 samples from the Oronto Group, the Eischoid#1 Units C and D, the Poersch #1, and the NSVG samples. The HPT experiment was conducted with deionized water to evaluate the potential of the MCR rocks to release Ca, Mg, and Fe and induce the precipitation of carbonate minerals in a CO_2-rich environment. In the real CO_2 injection scenario, the groundwater that originally occurred in equilibrium in subsurface conditions will be initially saline and will likely respond more rapidly to produce carbonate minerals as a result of adding Inorganic Dissolved Carbon (IDC) species ($H_2CO_{3(aq)}$, HCO_3^-, and CO_3^{2-}). That response is represented by more rapid dissolution processes at a higher $H_2CO_{3(aq)}$ activity (*near-field*) and more precipitation once the activity of HCO_3^- and CO_3^{2-} increase as a function of increasing solution pH (*far field*). Newly precipitated calcite crystals were detected on two of the reacted MCR samples from the HPT static experiments, one in as little as six days, and the second following 102 days of reaction. The experimental solutions had SI values of +0.9 and +1.1 for KEW1.1 and KEW5.1, respectively.

The Bayfield Group samples were feldspathic quartz-arenite to quartz-arenite sedimentary rocks with minor traces of both mica and heavy minerals. The matrix and clay-sized grains were dominated by kaolinite and traces of illite. The cement was composed of albite, calcite, and iron oxide in the Unit E of the Eischied #1 well; iron oxide and calcite cement in the Jacobsville sample; and iron oxide in Chequamegon Formation (i.e. the youngest stratigraphic unit of the Bayfield Group). The average porosity of the Bayfield Group samples was 13.4 ± 4.3% and the permeability of Bayfield Group BAY2 sample was > 340 mD. The percentage of the alkali earth metals in the Bayfield Group its stratigraphic equivalents were significantly lower relative to the Oronto Group (only between 0 and 2 wt%). The HPT testing of the Bayfield Group and its equivalent stratigraphic units showed lower overall concentrations and slower release rates of Ca-, Mg-, and Fe-required for mineral sequestration. Therefore, based on

characteristics of Bayfield Group, the unit may be considered a good target for physical sequestration if the required stratigraphic traps are found to exist within the overlying Paleozoic Rock sections, but the lack of the Ca, Mg, and Fe content will made less favored for the mineral sequestration.

The main concern about using the MCR Oronto Group for geologic CO_2 sequestration is related the the overall low permability of the aquifer unit that may hinder the injection of CO_2. Recent studies by Bachu and Bennion (2008) and DOE/NTEL (2008) revealed the injectability window started from 0.1 mD as a lower limit for the natural gas reservior, and the efficient porosity of CO_2 storage ranged between 3 -35%. Subsurface modeling of CO_2 injection in the Cambrian-aged Mt. Simon Formation by Barnes et al., (2009) suggests a cutoff values of 10% porosity and between 8 and 33 mD permeability. The permeability values determined from the present set of experiments, at <2 mD, will render the Oronto Group sediments as unattractive targets for CO_2 sequestration even following calcite cement dissolution. Forthermore, the fast diffusion and the low adherence of the supercritical CO_2, compared to the aqueous and gaseous CO_2 phases, will be much applicable at such permeability limit (Kim et al., 2012; Tokunaga, 2012; Hamm et al., 2013). The high porosity-permeability (13.4 ± 4.3%) Bayfield sandstone has a great capacity to sequester CO_2 physically, and to ensure an effective storage, however the unit generally lacks an effective impermeable cover rock throughout the MCR near the Lake Superior region and have limited carbonate mineralization potential. One favorable location for CO_2 injection where impermeable cap rocks have been tectonically emplaced over the high-porosity Bayfield Group sediments is at the Texaco Poercsh#1 well in Kansas. A 22 ft-thick porous zone (up to 15% porosity) has been identified geophysically by Berendsen, et al. (1988) and this zone is stratigraphically overlain by thick arkosic sandstone with a average porosity of 5%. These sedimentary zones represent a a good target for sequestration. Any CO_2 injected at this site would tend to migrate upwards where it may come in contact with tectonically juxtaposed lower MCR volcanics and sediments that could provide favorable environments for carbonate mineral precipitation reactions. Additional investigations would be needed to deleniate the extent of the high-porosity zone(s) and the extent of possible startigraphic and/or structural traps beneath the reversed faulted blocks of MCR.

APPENDIX

A. INTRODUCTION MATTER

Appendix A.1. Method for X-Ray Diffraction Scan for Clay Minerals

Modified from unpublished procedure described by George S. Austin - New Mexico Bureau of Miners & Mineral Resources, original source attributed to Walter Parham's of the Minnesota Geological Survey.

The clay minerals mounted on the slide glasses should be treated in three different ways as the following:

Scan A - Untreated

No treatment – rapid scan; ~3° to 38° 2θ at 2°2θ/minute,

No treatment – slow scan; 24° to 26° 2θ at 0.4° 2θ/minute (an optional run that may be needed to differentiate chlorite from kaolinite)

Scan B –After an overnight exposure in ethylene glycol atmosphere

Ethylene Glycol treated 2° to 15° 2θ at 2°2θ/minute

Scan C – Heat Treated ½ hour at 375°C

Heat treated - 2° to 15° 2θ at 2°2θ/minute.

The following peak heights over background should be recorded. The positions of these peaks may vary slightly from these angles.

1) No treatment rapid scan run at 12.4° 2Ø – $K_{(1)}$,
2) No treatment rapid scan run 17.8° 2θ – $I_{(2)}$,
3) No treatment rapid scan run 18.4°to 18.9° 2θ- $C_{(3)}$;
4) No treatment slow scan run at 24.9° 2θ – $K_{(2)}$
5) No treatment slow scan run at 25.1° 2θ – $C_{(4)}$;
6) Ethylene glycol treated run at 5.2° 2θ – $M_{(1)}$
7) Ethylene glycol treated run at 8.8° 2θ – $I_{(1G)}$;
8) Heated run at 8.8° 2θ – $I_{(1H)}$.

The counts of these peaks used to calculate the proportional composition of kaolinite, illite, mixed illite-smectite, smectite, and chlorite clays. The accuracy of this quantification is generally accurate to +/- 10% and the proportions of clays that have <5 to 10% concentrations may not be detected. The quantifications of the clays are following these equations:

$$\text{Illite} = \frac{I_{(1G)}}{T} \times 10$$

$$\text{Montmorillonite} = \frac{M_{(1)}}{4T} \times 10$$

$$\text{Chlorite} = \frac{C_{(3)}}{I_{(2)}} \times \frac{I_{(1G)}}{T} \times 10$$

Mixed-layer clay minerals = $\frac{I_{(1H)} - \left[I_{(1G)} + \frac{M_{(1)}}{4}\right]}{T} \times 10$

Kaolinite = $\frac{K_{(1)}}{T} \times 10$

Or,

Kaolinite = $\frac{K_{(2)}}{2C_{(4)}} \times \frac{C_{(3)}}{I_{(2)}} \times \frac{I_{(1G)}}{T} \times 10$ (if chlorite present)

Where,

T = $I_{(1H)} + K_{(1)}$

Or,

T = $I_{(1H)} + \left\{\frac{[C_{(3)}][I_{(1G)}]}{I_{(2)}}\right\} + \left\{\frac{[K_{(2)}][C_{(3)}][I_{(1G)}]}{[2C_{(4)}][I_{(2)}]}\right\}$ (if chlorite present)

$I_{(1H)}$ = counts for illite, montmorillonite, and mixed-layer clay minerals.

If your x-ray machine is not aligned correctly, you may get varying peak intensities from run to run. You can get better results by standardizing your curves by using the 12.4° 2θ peak as a standard and adjusting the counts for the other peaks, or by using the quartz peaks at 20.8 and 26.6° 2θ if quartz is present.

Appendix A.2. Cleaning Procedures for Teflon Vessels

1. Wash off fluid and solid left inside the Teflon vessels with tap water.
2. Using a non-metal brush, brush off any leftover in the vessels (top and bottom) and clean the vessels under a running tap water. If using a metal brush makes sure the metal tip does not touch the vessels.
3. Fill in the vessels with 5% nitric acid cleaning solution, close the vessel tightly using a green tightening apparatus, place and leave the vessels in the oven for three hours at 90°. Turn the vessels upside down after the first two hours.
4. After three hours, take out the vessels and let them cool down to the room temperature for approximately half an hour.
5. Flush excess acid into sink with tap water and clean the vessels by filling them twice with deionized water.
6. Fill the vessels with deionized water for the third time, close the vessels tightly and leave the vessels in the oven for four hours at 90°.

7. After four hours, take out the vessels and let them cool down to the room temperature.
8. Throw away the water in the vessels and rinse again with deionized water once, fill up the vessels for the second time with deionized water and close them tightly.
9. Leave the vessels in the oven overnight at 90°.
10. Take out the vessels the next day and take a pH reading and record the results.
11. The pH readings for each vessel should be in between pH 5.0 and pH 7.0. If the pH values are outside the range, repeat cleaning procedures three to ten.
12. Leave the vessels fully opened to dry overnight at room temperature.

Appendix A.3. Cleaning Procedures for Brand New Nalgene Bottles

1. Fill up the new bottles with 3% or 5% Nitric Acid cleaning solution, close them tightly and leave them soaked with the acid for at least overnight at room temperature.
2. After being filled up overnight, transfer the acid to new bottles for additional cleaning or return acid to stock solution.
3. Rinse the bottles two times, filled them up with deionized water, make sure the caps are slightly opened and leave the bottles in the oven for 4 hours at 90°.
4. Take the bottles out and let them cool down to room temperature.
5. Rinse the bottle once, filled it up with deionized water, leave the caps slightly opened and leave them in the oven overnight at 90°.
6. Take out the bottles the next day and let them cool down to room temperature.
7. Dispose of away the water.
8. Dry up the empty bottles in the oven for a couple of hours at 90°.
9. Cap bottles, store in clean zip-lock plastic bag until use in experimental tests.

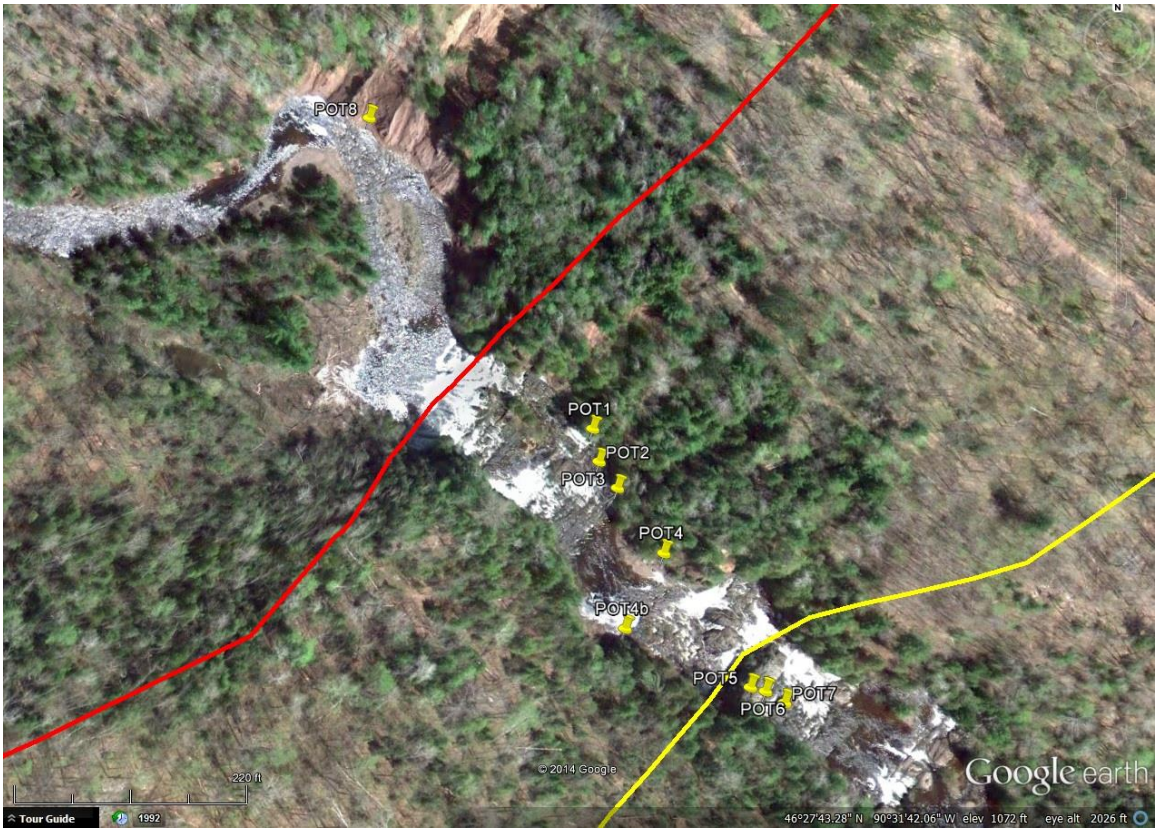

Figure A. 1 Google Earth map view is showing the sampling locations of Potato River Falls' samples (longitude and latitude are indicate to the bottom right of image). The red line represents the approximate boundary between Nonesuch shale (to right) and Freda Formation (to left), and the yellow line represents the suggested boundary between the Nonesuch shale (to left) and CHC (to right). Regional location map for location of the Potato River section is shown in Figure 1.6.

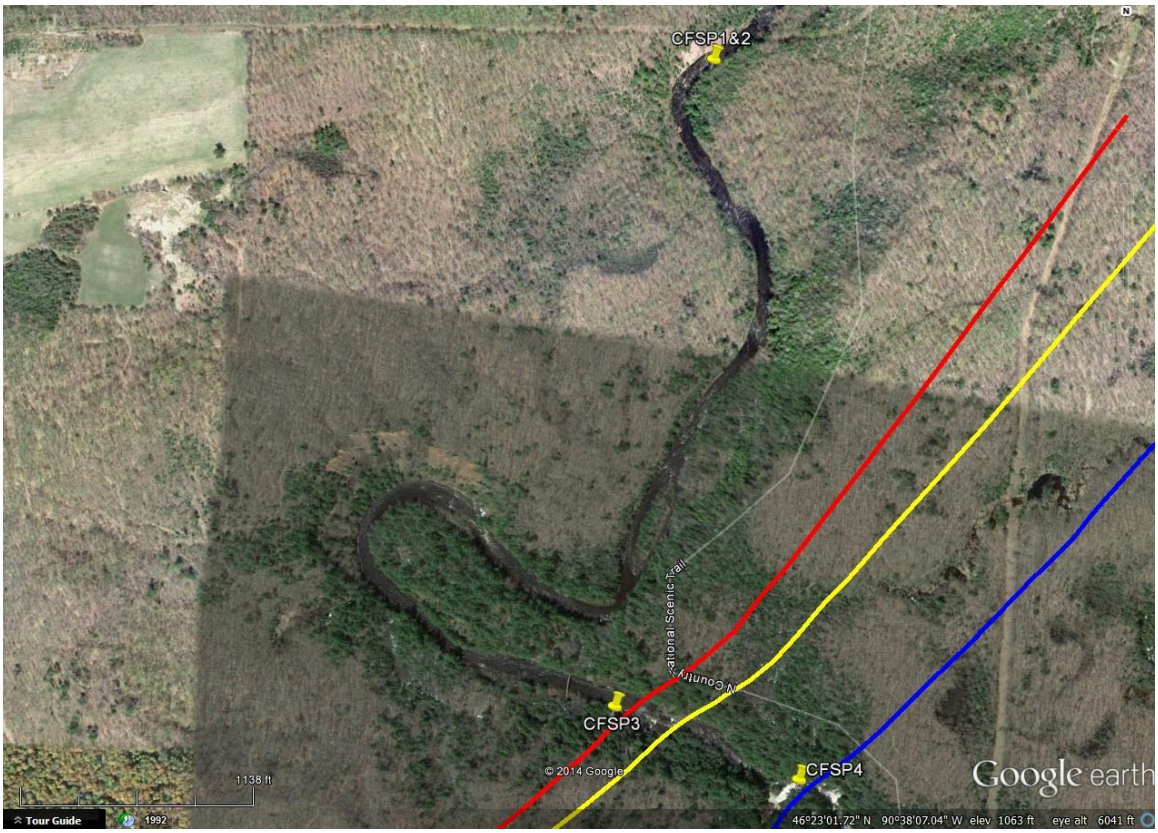

Figure A. 2 Google Earth map view is showing the sampling locations of CFSP1, 2, 3, and 4 samples. The red line represents the approximate boundary between Nonesuch shale (to right) and Freda Formation (to left), the yellow line represents the suggested boundary between the Nonesuch shale (to left) and CHC (to right), and the blue line represents the approximate boundary between the CHC (to the left) and Portage lake volcanic rocks to (the right). Regional location map for location of the Potato River section is shown in Figure 1.5.

Figure A. 3 Google Earth map view showing the sampling location of the BAY1 sample.

Appendix A.4. The chemical input data for the PHREEQC software model.

```
TITLE KEW1-1
SOLUTION 1
        pH 6.08 charge
        temp 90
        pe 0.815
        density 0.97
        units ppm
        Ca 702
        Mg 39
        Mn 7.8
        K 17
        Si 26
        Na 4.3
EQUILIBRIUM_PHASES 1
        O2(g) 1.16
        CO2(g) 0.95
END

TITLE KEW4-2
SOLUTION 1
        pH 5.87 charge
        temp 90
        pe 1.0921
        density 0.97
        units ppm
        Ca 796
        Mg 166
        Mn 3.2
        K 23
        Si 64
        Na 4.8
EQUILIBRIUM_PHASES 1
        O2(g) 1.16
        CO2(g) 0.95
END

TITLE KEW5-1
SOLUTION 1
        pH 5 charge
        temp 90
        pe 0.5053
        density 0.97
        units ppm
        Ca 915
        Mg 134
        Mn 3.1
        K 22
        Si 74
        Na 12
EQUILIBRIUM_PHASES 1
        O2(g) 1.16
        CO2(g) 0.95
END

TITLE POT2
SOLUTION 1
        pH 6.43 charge
        temp 90
        pe 0.5379
        density 0.97
        units ppm
        Ca 459
        Mg 128
        Mn 0.1
        K 32
        Si 70
        Na 4.4
EQUILIBRIUM_PHASES 1
        O2(g) 1.16
        CO2(g) 0.95
END

TITLE POT4
SOLUTION 1
        pH 6.22 charge
        temp 90
        pe 1.0921
        density 0.97
        units ppm
        Ca 230
        Mg 81
        Mn 17
        K 15
        Si 121
        Na 2.9
EQUILIBRIUM_PHASES 1
        O2(g) 1.16
        CO2(g) 0.95
END

TITLE POT5
SOLUTION 1
        pH 6.42 charge
        temp 90
        pe 1.1736
        density 0.97
```

```
        units ppm
        Ca 600
        Mg 120
        Mn 0.1
        K 19
        Si 51
        Na 7.7
EQUILIBRIUM_PHASES 1
        O2(g) 1.16
        CO2(g) 0.95
END

TITLE CFSP4
SOLUTION 1
        pH 5.78 charge
        temp 90
        pe 1.1084
        density 0.97
        units ppm
        Ca 282
        Mg 109
        Mn 10
        K 51
        Si 141
        Na 1
EQUILIBRIUM_PHASES 1
        O2(g) 1.16
        CO2(g) 0.95
END

TITLE C2-1
SOLUTION 1
        pH 6.24 charge
        temp 90
        pe 0.74491
        density 0.97
        units ppm
        Ca 267.2
        Fe 0.1
        Mg 35.3
        Mn 0.1
        K 16.3
        Si 28.3
        Na 15.9
EQUILIBRIUM_PHASES 1
        O2(g) 1.16
        CO2(g) 0.96
END

TITLE C2-2
SOLUTION 1
        pH 5.77 charge
        temp 90
        pe 0.94866
        density 0.97
        units ppm
        Ca 376.7
        Fe 0.1
        Mg 8.8
        Mn 1.2
        K 5.5
        Si 44.6
        Na 5.5
EQUILIBRIUM_PHASES 1
        O2(g) 1.16
        CO2(g) 0.96
END

TITLE C2-3
SOLUTION 1
        pH 5.65 charge
        temp 90
        pe 1.31704
        density 0.97
        units ppm
        Ca 44.6
        Fe 0.8
        Mg 27.8
        Mn 1.5
        K 9.3
        Si 44.6
        Na 14.1
EQUILIBRIUM_PHASES 1
        O2(g) 1.16
        CO2(g) 0.95
END

TITLE C2-5
SOLUTION 1
        pH 5.71 charge
        temp 90
        pe 1.3692
        density 0.97
        units ppm
        Ca 176.1
        Fe 0.1
        Mg 13.8
        Mn 0.8
        K 8.5
        Si 10.8
        Na 13.7
EQUILIBRIUM_PHASES 1
```

```
        O2(g) 1.16
        CO2(g) 0.95
END

TITLE POT8-2
SOLUTION 1
        pH 5.80 charge
        temp 90
        pe 1.2714
        density 0.97
        units ppm
        Ca 230
        Mg 16
        Mn 2.1
        K 29
        Si 164
        Na 5.4
EQUILIBRIUM_PHASES 1
        O2(g) 1.16
        CO2(g) 0.95
END

TITLE SF1-1
SOLUTION 1
        pH 5.78 charge
        temp 90
        pe 1.1084
        density 0.97
        units ppm
        Ca 223.3
        Mg 36.7
        Mn 2
        K 9
        Si 41.2
        Na 18.4
EQUILIBRIUM_PHASES 1
        O2(g) 0.99
        CO2(g) 1.167317
END

TITLE SF1-2
SOLUTION 1
        pH 6.16 charge
        temp 90
        pe 0.7661
        density 0.97
        units ppm
        Ca 159.4
        Mg 29.7
        Mn 0.6
        K 8.2
        Si 37.3
        Na 16
EQUILIBRIUM_PHASES 1
        O2(g) 0.99
        CO2(g) 1.1673171
END

TITLE SF3-1
SOLUTION 1
        pH 5.86 charge
        temp 90
        pe 1.0595
        density 0.97
        units ppm
        Ca 287.6
        Mg 37.6
        Mn 1.7
        K 6.8
        Si 41.2
        Na 15.9
EQUILIBRIUM_PHASES 1
        O2(g) 0.99
        CO2(g) 1.1673171
END

TITLE SF3-2
SOLUTION 1
        pH 5.82 charge
        temp 90
        pe 1.0921
        density 0.97
        units ppm
        Ca 167.9
        Mg 20.3
        Mn 0.3
        K 5.9
        Si 27.9
        Na 12.9
EQUILIBRIUM_PHASES 1
        O2(g) 1.167317
        CO2(g) 0.99
END

TITLE SH1
SOLUTION 1
        pH 5.38 charge
        temp 90
        pe 1.4833
        density 0.97
        units ppm
        Ca 67
```

```
        Mg 32.2
        Mn 1.7
        K 9.5
        Si 36.7
        Na 13.2
EQUILIBRIUM_PHASES 1
        O2(g) 1.167317
        CO2(g) 1
END

TITLE SH2
SOLUTION 1
        pH 5.38 charge
        temp 90
        pe 1.5159
        density 0.97
        units ppm
        Ca 58
        Mg 29
        Mn 2.2
        K 8.4
        Si 37
        Na 12.2
EQUILIBRIUM_PHASES 1
        O2(g) 1.167317
        CO2(g) 0.99
END

TITLE D4-1
SOLUTION 1
        pH 5.85 charge
        temp 90
        pe 0.8639
        density 0.97
        units ppm
        Ca 451.5
        Fe 0.1
        Mg 14.8
        Mn 4
        K 12
        Si 68.1
        Na 12.3
EQUILIBRIUM_PHASES 1
        O2(g) 1.16
        CO2(g) 0.96
END

TITLE D4-2
SOLUTION 1
        pH 6 charge
        temp 90
        pe 1.08395
        density 0.97
        units ppm
        Ca 486.2
        Fe 0.1
        Mg 7
        Mn 3.5
        K 7.6
        Si 36.3
        Na 5.6
EQUILIBRIUM_PHASES 1
        O2(g) 1.16
        CO2(g) 0.94
END

TITLE BAY3
SOLUTION 1
        pH 5.39 charge
        temp 90
        pe 1.4018
        density 0.97
        units ppm
        Al 132
        Ca 4
        Fe 17
        Mg 18
        Mn 10
        K 10
        Si 30
        Na 3.7
EQUILIBRIUM_PHASES 1
        O2(g) 1.16
        CO2(g) 0.97
END

TITLE BAY3 (Repeated without
Al)
SOLUTION 1
        pH 5.39 charge
        temp 90
        pe 1.4018
        density 0.97
        units ppm
        Ca 4
        Fe 17
        Mg 18
        Mn 10
        K 10
        Si 30
        Na 3.7
EQUILIBRIUM_PHASES 1
```

```
        O2(g) 1.16
        CO2(g) 0.97
END

TITLE L'ANSE1
SOLUTION 1
        pH 4.78 charge
        temp 90
        pe 1.4018
        density 0.97
        units ppm
        Ca 9.4
        Fe 27
        Mg 28
        Mn 1
        K 7.3
        Si 64
        Na 1
EQUILIBRIUM_PHASES 1
        O2(g) 1.16
        CO2(g) 0.98
END

TITLE E2-2
SOLUTION 1
        pH 5.9 charge
        temp 90
        pe 0.87205
        density 0.97
        units ppm
        Ca 496.9
        Mg 3.7
        Mn 0.6
        K 4.8
        Si 50.5
        Na 4.4
EQUILIBRIUM_PHASES 1
        O2(g) 1.16
        CO2(g) 0.96
END

TITLE E2-3
SOLUTION 1
        pH 4.96 charge
        temp 90
        pe 2.07825
        density 0.97
        units ppm
        Ca 26.5
        Mg 1.4
        Mn 1.1
        Fe 0.3
        K 4.5
        Si 18.6
        Na 4.5
EQUILIBRIUM_PHASES 1
        O2(g) 1.16
        CO2(g) 0.94
END

TITLE E2-4
SOLUTION 1
        pH 5.06 charge
        temp 90
        pe 1.70172
        density 0.97
        units ppm
        Ca 63.3
        Al 0.2
        Mg 3.2
        Mn 2.3
        K 7.7
        Si 48.6
        Na 7.8
EQUILIBRIUM_PHASES 1
        O2(g) 1.16
        CO2(g) 0.95
END

TITLE AG1
SOLUTION 1
        pH 5.06 charge
        temp 90
        pe 1.79137
        density 0.97
        units ppm
        Al 1.8
        Ca 27.5
        Fe 1.8
        Mg 11.4
        Mn 2.1
        K 24.4
        Si 30.4
        Na 1.6
EQUILIBRIUM_PHASES 1
        O2(g) 1.16
        CO2(g) 1
END

TITLE AG2
SOLUTION 1
        pH 5.59 charge
```

```
        temp 90
        pe 1.29259
        density 0.97
        units ppm
        Al 0.1
        Ca 22.5
        Fe 0.1
        Mg 9.7
        Mn 1.3
        K 21.2
        Si 25
        Na 1.4
EQUILIBRIUM_PHASES 1
        O2(g) 1.16
        CO2(g) 1
END

TITLE 5397.3′A
SOLUTION 1
        pH 5.94 charge
        temp 90
        pe 0.77588
        density 0.97
        units ppm
        Ca 54.2
        Mg 240.4
        Mn 0.1
        K 19.6
        Si 48.6
        Na 99.9
EQUILIBRIUM_PHASES 1
        O2(g) 1.16
        CO2(g) 1
END

TITLE 5397.3′B
SOLUTION 1
        pH 6.12 charge
        temp 90
        pe 0.84271
        density 0.97
        units ppm
        Ca 158.5
        Mg 120.2
        Mn 3.4
        K 13.1
        Si 45.8
        Na 63.6
EQUILIBRIUM_PHASES 1
        O2(g) 1.16
        CO2(g) 1
END

TITLE 5404′A
SOLUTION 1
        pH 5.73 charge
        temp 90
        pe 1.3366
        density 0.97
        units ppm
        Al 0.2
        Ca 110.3
        Mg 48.6
        Mn 1.9
        K 16.6
        Si 48.9
        Na 41.9
EQUILIBRIUM_PHASES 1
        O2(g) 1.167317
        CO2(g) 0.99
END

TITLE 8051.1′A
SOLUTION 1
        pH 5.79 charge
        temp 90
        pe 1.05787
        density 0.97
        units ppm
        Ca 513
        Mg 2.4
        Mn 3
        K 4.7
        Si 76.4
        Na 7.1
EQUILIBRIUM_PHASES 1
        O2(g) 1.16
        CO2(g) 0.99
END

TITLE 8051.1′B
SOLUTION 1
        pH 5.78 charge
        temp 90
        pe 1.22902
        density 0.97
        units ppm
        Ca 342
        Mg 1.6
        Mn 2.3
        K 2.8
        Si 11.8
```

```
        Na 2.5
EQUILIBRIUM_PHASES 1
        O2(g) 1.16
        CO2(g) 0.98
END

TITLE 8476′- 8480′A
SOLUTION 1
        pH 6.03 charge
        temp 90
        pe 1.05787
        density 0.97
        units ppm
        Ca 502.3
        Mg 4.9
        Mn 4.1
        K 2.8
        Si 37.4
        Na 4.9
EQUILIBRIUM_PHASES 1
        O2(g) 1.16
        CO2(g) 0.99
END

TITLE 8476′- 8480′B
SOLUTION 1
        pH 5.81 charge
        temp 90
        pe 1.18501
        density 0.97
        units ppm
        Ca 518.3
        Mg 4.8
        Mn 3.5
        K 2
        Si 20.9
        Na 3.5
EQUILIBRIUM_PHASES 1
        O2(g) 1.16
        CO2(g) 1
END

TITLE 10514′A
SOLUTION 1
        pH 5.87 charge
        temp 90
        pe 1.2225
        density 0.97
        units ppm
        Ca 419.4
        Mg 1.1
        Mn 3.6
        K 1.8
        Si 16.4
        Na 3
EQUILIBRIUM_PHASES 1
        O2(g) 1.16
        CO2(g) 0.98
END

TITLE 10514′B
SOLUTION 1
        pH 5.8 charge
        temp 90
        pe 0.9617
        density 0.97
        units ppm
        Ca 496.9
        Mg 1.5
        Mn 4.5
        K 2.6
        Si 51.3
        Na 4.7
EQUILIBRIUM_PHASES 1
        O2(g) 1.16
        CO2(g) 1
END

TITLE 10666′A
SOLUTION 1
        pH 5.84 charge
        temp 90
        pe 1.24369
        density 0.97
        units ppm
        Ca 242
        Mg 25.9
        Mn 5.7
        K 3.7
        Si 21.5
        Na 15.1
EQUILIBRIUM_PHASES 1
        O2(g) 1.16
        CO2(g) 1
END

TITLE 10666′B
SOLUTION 1
        pH 5.9 charge
        temp 90
        pe 1.1736
        density 0.97
```

```
        units ppm
        Ca 360.7
        Mg 32.6
        Mn 8.6
        K 3.5
        Si 25.4
        Na 15.1
EQUILIBRIUM_PHASES 1
        O2(g) 1.16
        CO2(g) 1
END

TITLE 11061′A
SOLUTION 1
        pH 5.85 charge
        temp 90
        pe 1.21924
        density 0.97
        units ppm
        Ca 363.3
        Fe 0.3
        Mg 1.2
        Mn 1.4
        K 3.2
        Si 9.2
        Na 4.3
EQUILIBRIUM_PHASES 1
        O2(g) 1.16
        CO2(g) 0.97
END

TITLE 11061′B
SOLUTION 1
        pH 5.77 charge
        temp 90
        pe 0.99267
        density 0.97
        units ppm
        Ca 566.4
        Mg 1.1
        Mn 1.5
        K 3.5
        Si 39.5
        Na 7.8
EQUILIBRIUM_PHASES 1
        O2(g) 1.16
        CO2(g) 0.97
END

TITLE BEV1
SOLUTION 1
        pH 5 charge
        temp 90
        pe 2.02772
        density 0.97
        units ppm
        Ca 17.3
        Fe 0.4
        Mg 7
        K 1.9
        Si 27.1
        Na 3.8
EQUILIBRIUM_PHASES 1
        O2(g) 1.16
        CO2(g) 0.93
END

TITLE DUL1
SOLUTION 1
        pH 5.92 charge
        temp 90
        pe 0.99267
        density 0.97
        units ppm
        Ca 39.4
        Mg 192.1
        Mn 0.4
        K 3.9
        Si 90.2
        Na 7.2
EQUILIBRIUM_PHASES 1
        O2(g) 1.16
        CO2(g) 0.97
END

TITLE DUL2
SOLUTION 1
        pH 5.84 charge
        temp 90
        pe 1.05461
        density 0.97
        units ppm
        Ca 38.2
        Mg 134.6
        Mn 0.4
        K 4.7
        Si 74.8
        Na 6.7
EQUILIBRIUM_PHASES 1
        O2(g) 1.16
        CO2(g) 0.96
END
```

```
TITLE GHB1
SOLUTION 1
        pH 6.12 charge
        temp 90
        pe 0.79381
        density 0.97
        units ppm
        Ca 224.5
        Mg 183.6
        Mn 1.8
        K 1.4
        Si 52.6
        Na 24
EQUILIBRIUM_PHASES 1
        O2(g) 1.16
        CO2(g) 1.03
END

TITLE GHB2
SOLUTION 1
        pH 5.87 charge
        temp 90
        pe 1.0432
        density 0.97
        units ppm
        Ca 123.6
        Mg 101.3
        Mn 0.5
        K 1.1
        Si 44.2
        Na 19.6
EQUILIBRIUM_PHASES 1
        O2(g) 1.16
        CO2(g) 1.01
END

TITLE GHC1
SOLUTION 1
        pH 5.93 charge
        temp 90
        pe 0.98452
        density 0.97
        units ppm
        Ca 288.6
        Mg 66.7
        Mn 1.2
        K 0.7
        Si 124.1
        Na 19.5
EQUILIBRIUM_PHASES 1
        O2(g) 1.16
        CO2(g) 1
END

TITLE GHC2
SOLUTION 1
        pH 6.22 charge
        temp 90
        pe 0.71883
        density 0.97
        units ppm
        Ca 278.9
        Mg 67
        Mn 1.8
        K 0.5
        Si 125
        Na 14.4
EQUILIBRIUM_PHASES 1
        O2(g) 1.16
        CO2(g) 0.98
END
```

APPENDIX

B. PETROLOGY OF THE MCR CLASTICS

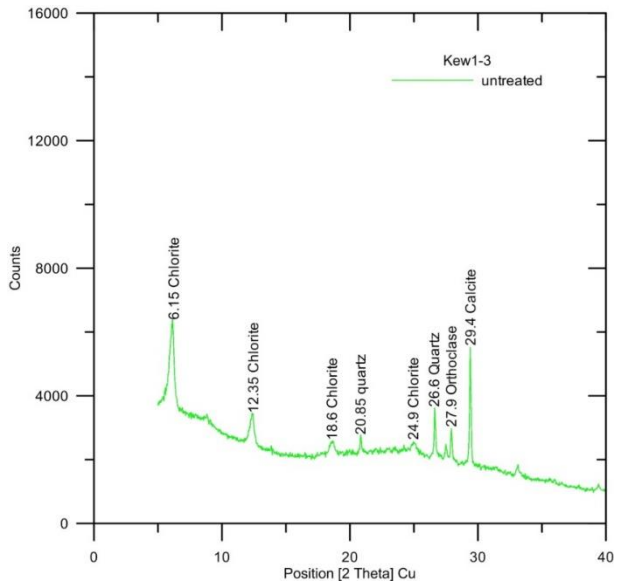

Figure B.1 X-Ray Diffraction spectrum of Eagle River sample (KEW1-3) showing the composition of the clay-size matrix fraction.

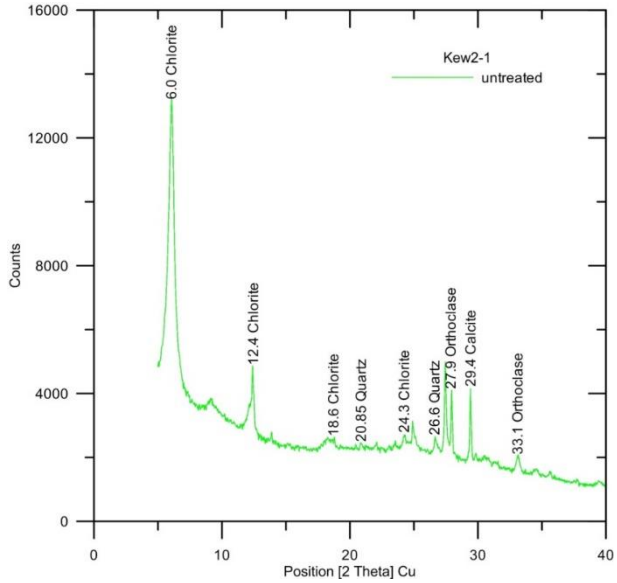

Figure B.2 X-Ray Diffraction spectrum of Baily Creek Falls samples (KEW2-1) showing the composition of the clay-size matrix fraction.

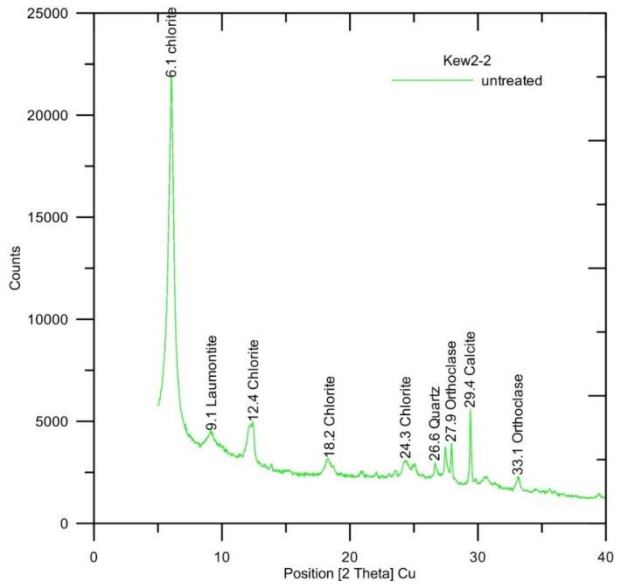

Figure B. 3 X-Ray Diffraction spectrum of Baily Creek Falls samples (KEW2-2) showing the composition of the clay-size matrix fraction.

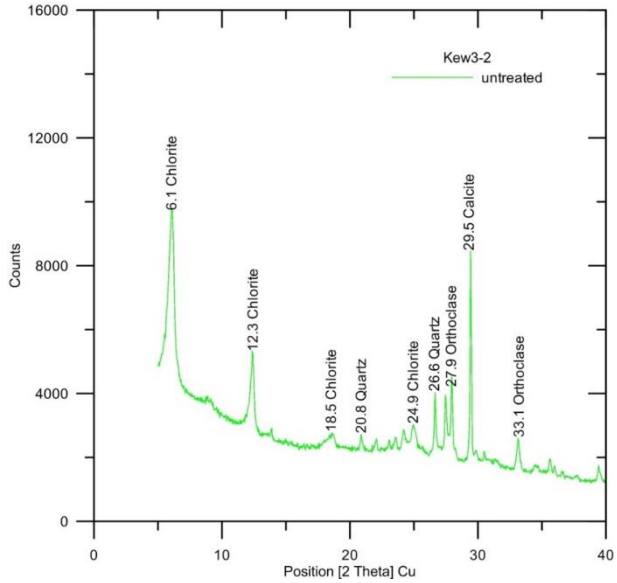

Figure B. 4 X-Ray Diffraction spectrum of Esrey Park sample (KEW3-2) showing the composition of the clay-size matrix fraction.

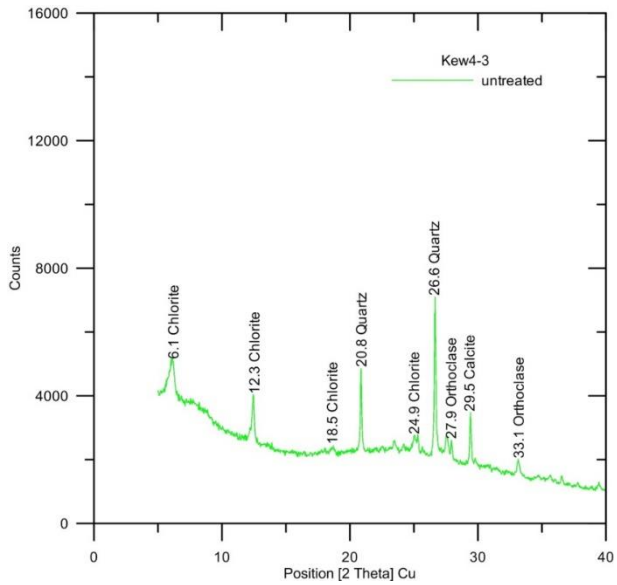

Figure B. 5 X-Ray Diffraction spectrum of Dan Point sample (KEW4-3) showing the composition of the clay-size matrix fraction.

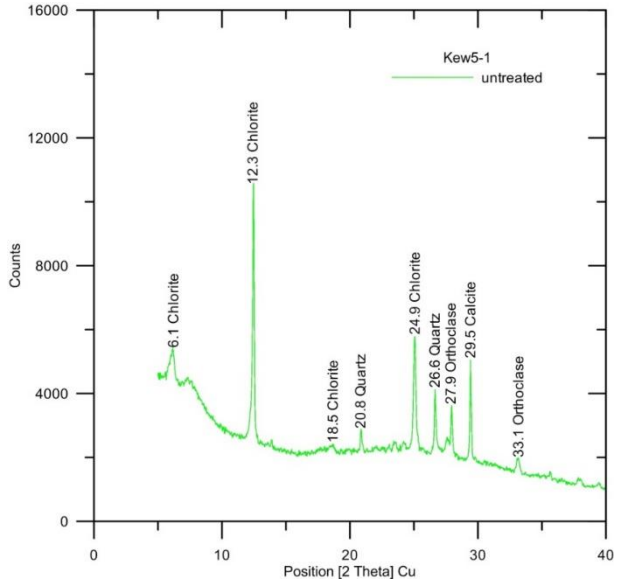

Figure B. 6 X-Ray Diffraction spectrum of Hobard State Park sample (KEW5-1) showing the composition of the clay-size matrix fraction.

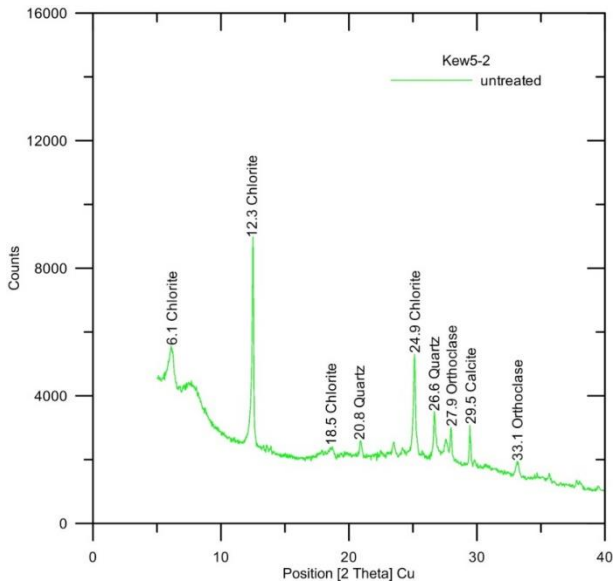

Figure B. 7 X-Ray Diffraction spectrum of Hobard State Park sample (KEW5-2) showing the composition of the clay-size matrix fraction.

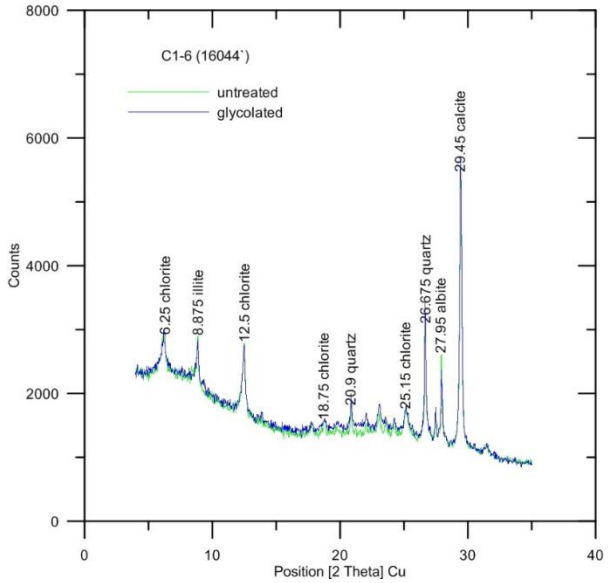

Figure B. 8 X-Ray Diffraction spectra of Amoco M. G. Eischeid #1 well samples, Iowa (C1-6) showing the composition of the clay-size matrix fraction.

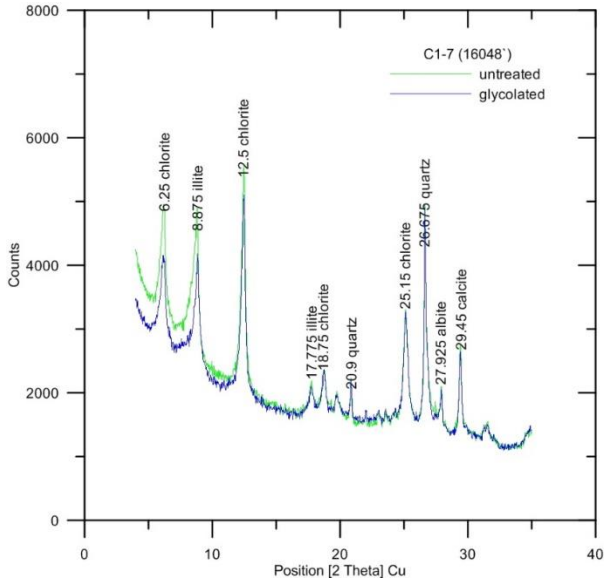

Figure B. 9 X-Ray Diffraction spectra of Amoco M. G. Eischeid #1 well sample, Iowa (C1-7) showing the composition of the clay-size matrix fraction.

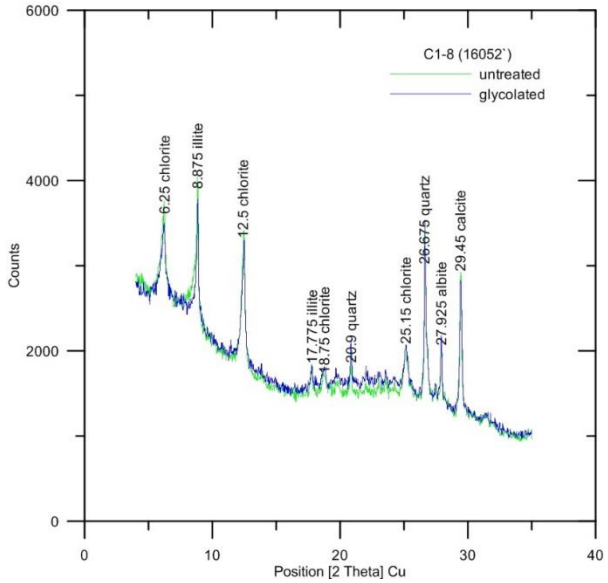

Figure B. 10 X-Ray Diffraction spectra of Amoco M. G. Eischeid #1 well sample, Iowa (C1-8) showing the composition of the clay-size matrix fraction.

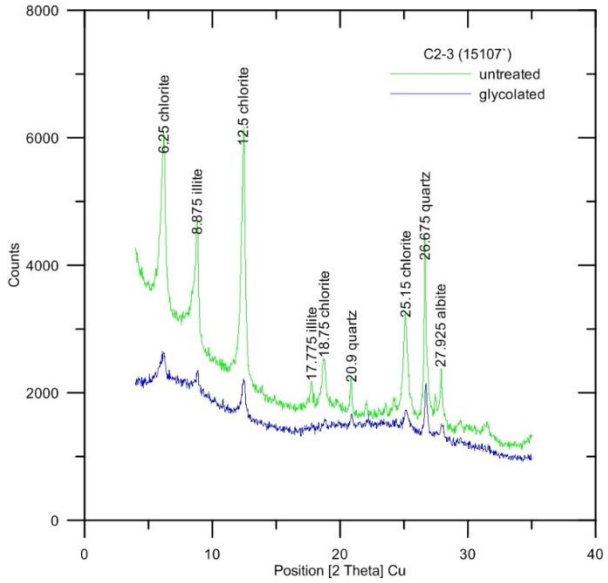

Figure B. 11 X-Ray Diffraction spectra of Amoco M. G. Eischeid #1 well sample, Iowa (C2-3) showing the composition of the clay-size matrix fraction.

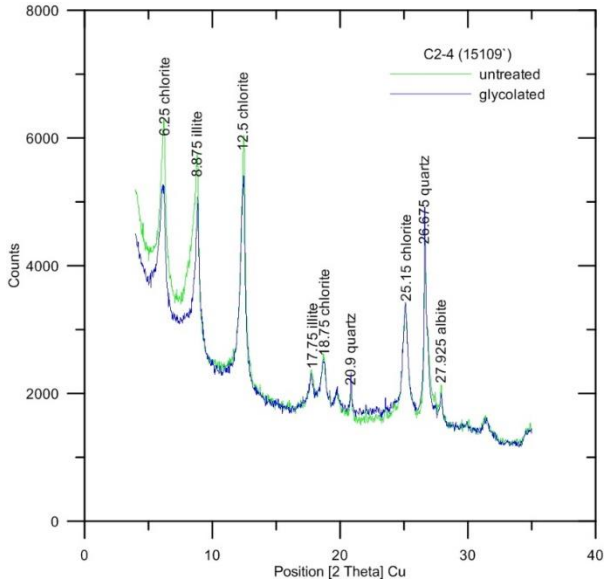

Figure B. 12 X-Ray Diffraction spectra of Amoco M. G. Eischeid #1 well sample, Iowa (C2-4) showing the composition of the clay-size matrix fraction.

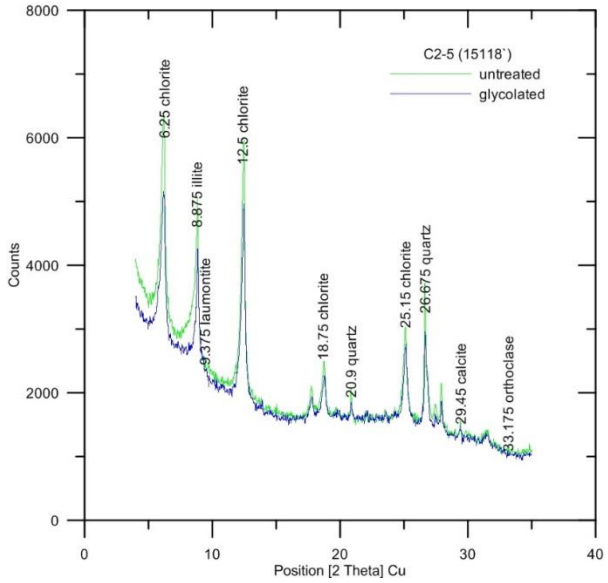

Figure B. 13 X-Ray Diffraction spectra of Amoco M. G. Eischeid #1 well sample, Iowa (C2-5) showing the composition of the clay-size matrix fraction.

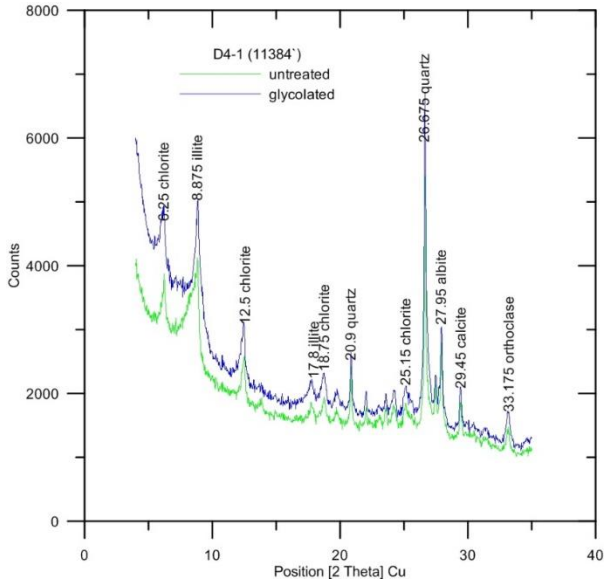

Figure B. 14 X-Ray Diffraction spectra of Amoco M. G. Eischeid #1 well sample, Iowa (D4-1) showing the composition of the clay-size matrix fraction.

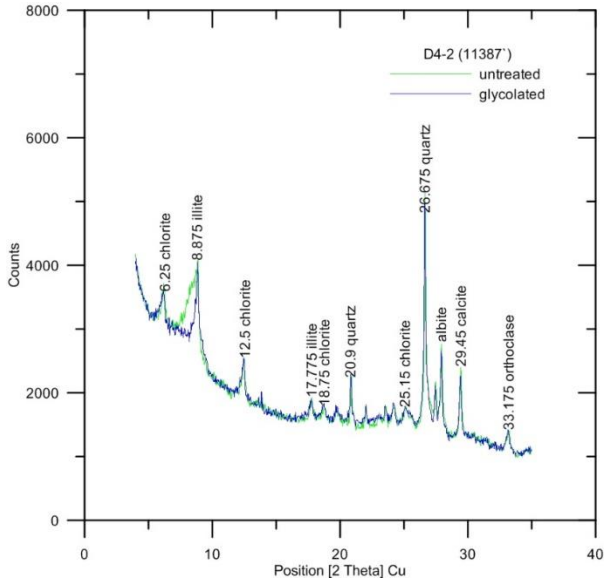

Figure B. 15 X-Ray Diffraction spectra of Amoco M. G. Eischeid #1 well sample, Iowa (D4-2) showing the composition of the clay-size matrix fraction.

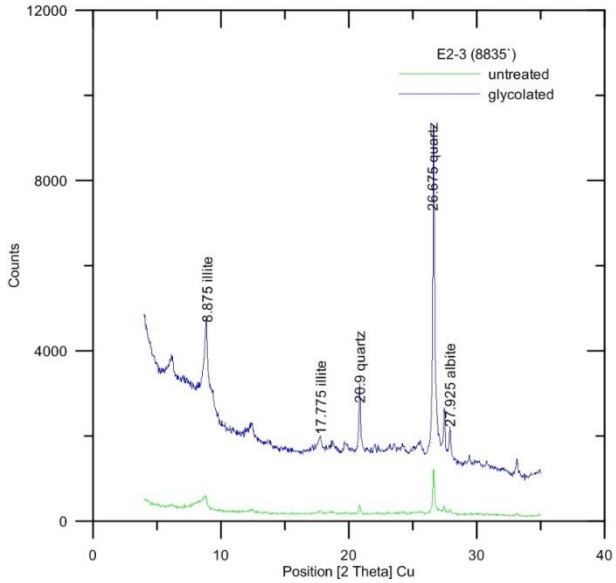

Figure B. 16 X-Ray Diffraction spectra of Amoco M. G. Eischeid #1 well sample, Iowa (E2-3) showing the composition of the clay-size matrix fraction.

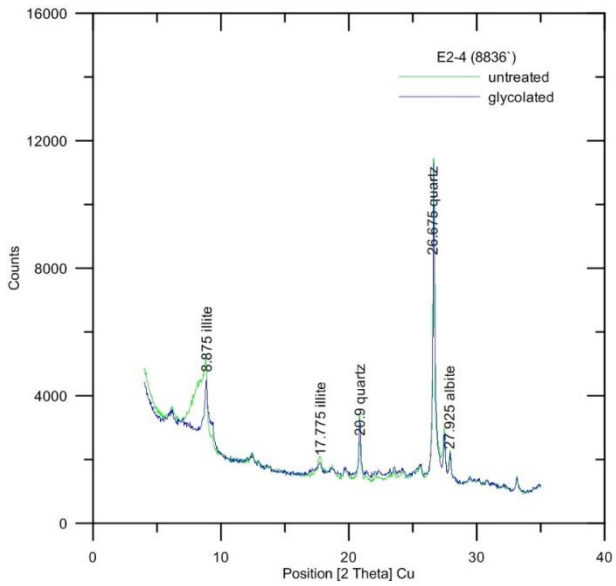

Figure B. 17 X-Ray Diffraction spectra of Amoco M. G. Eischeid #1 well sample, Iowa (E2-4) showing the composition of the clay-size matrix fraction.

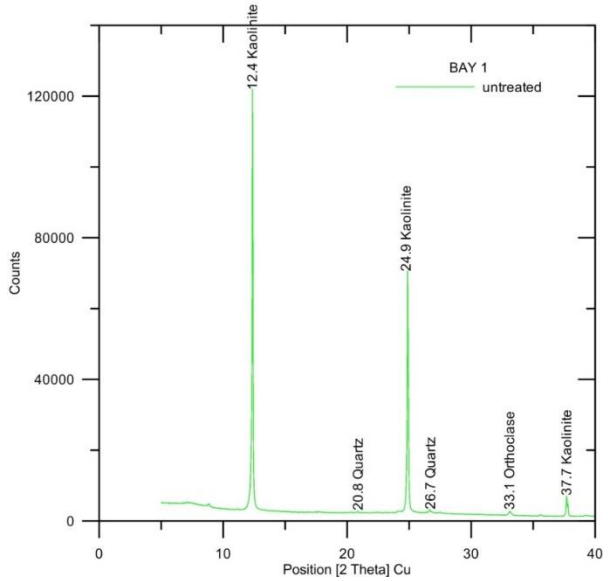

Figure B. 18 X-Ray Diffraction spectrum of Bayfield formation sample (BAY1) showing the composition of the clay-size matrix fraction.

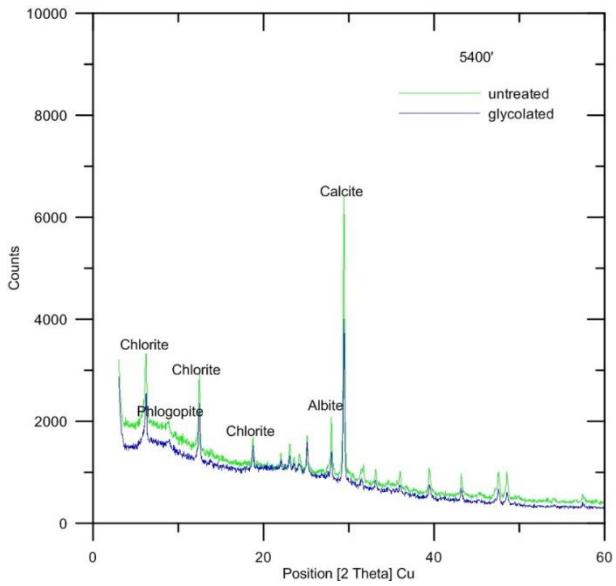

Figure B. 19 X-Ray Diffraction spectra of Kansas Texaco Poersch #1 well sample (5400′) showing the composition of the clay-size matrix fraction.

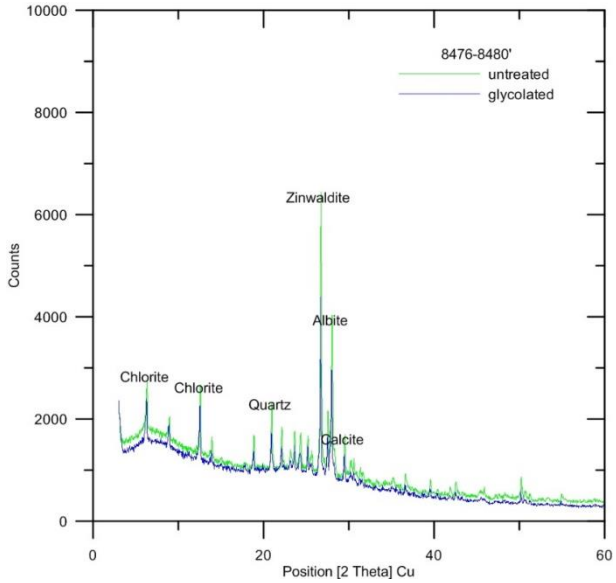

Figure B. 20 X-Ray Diffraction spectra of Kansas Texaco Poersch #1 well sample (8,476-8,480′) showing the composition of the clay-size matrix fraction.

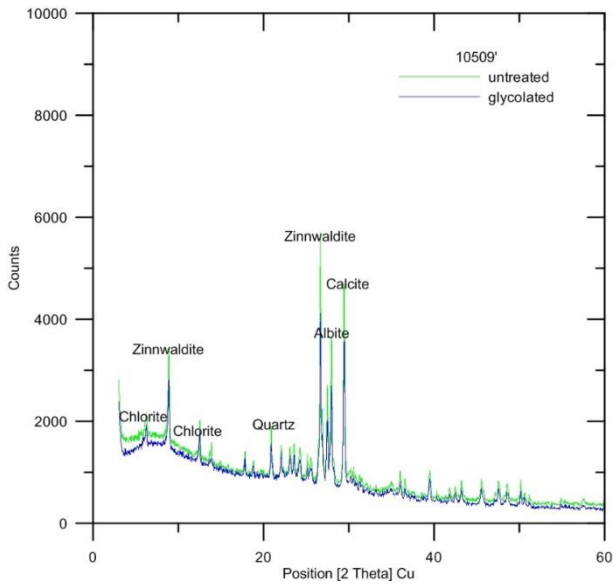

Figure B. 21 X-Ray Diffraction spectra of Kansas Texaco Poersch #1 well sample (10,509′) showing the composition of the clay-size matrix fraction.

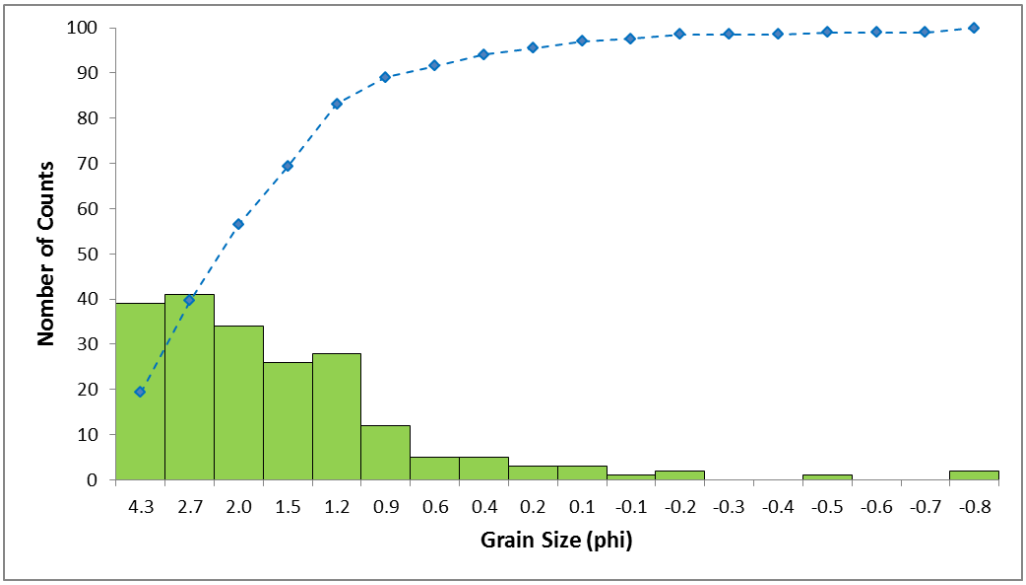

Figure B. 22 Grain size distribution of Eagle River Falls samples, showing arenaceous grain size distribution for sample KEW1-1. The dashed line represents cumulative grain size for the sample.

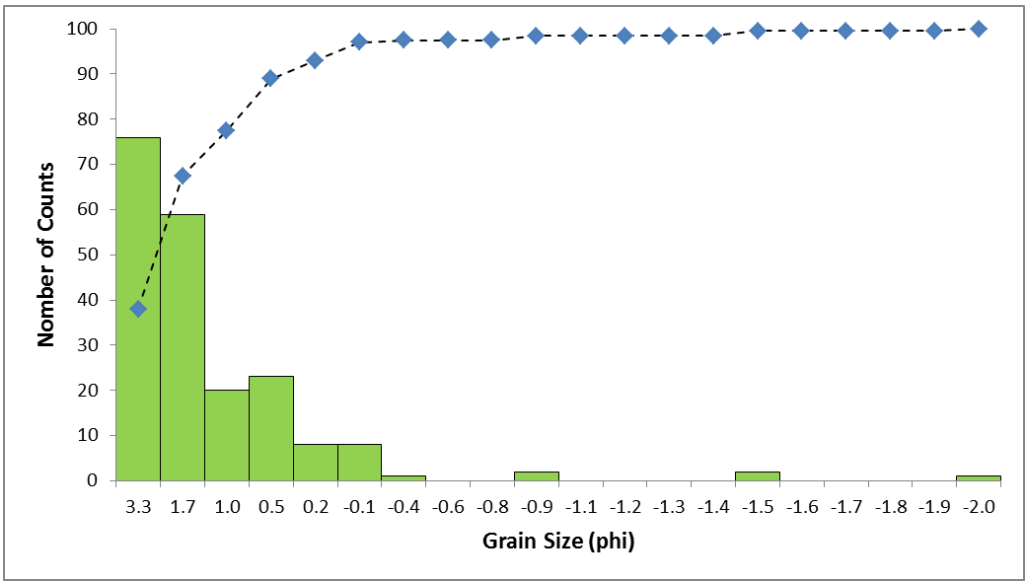

Figure B. 23 Grain size distribution of Baily Creek Falls samples, showing arenaceous grain size KEW2-1. The dashed line represents cumulative grain size for the sample.

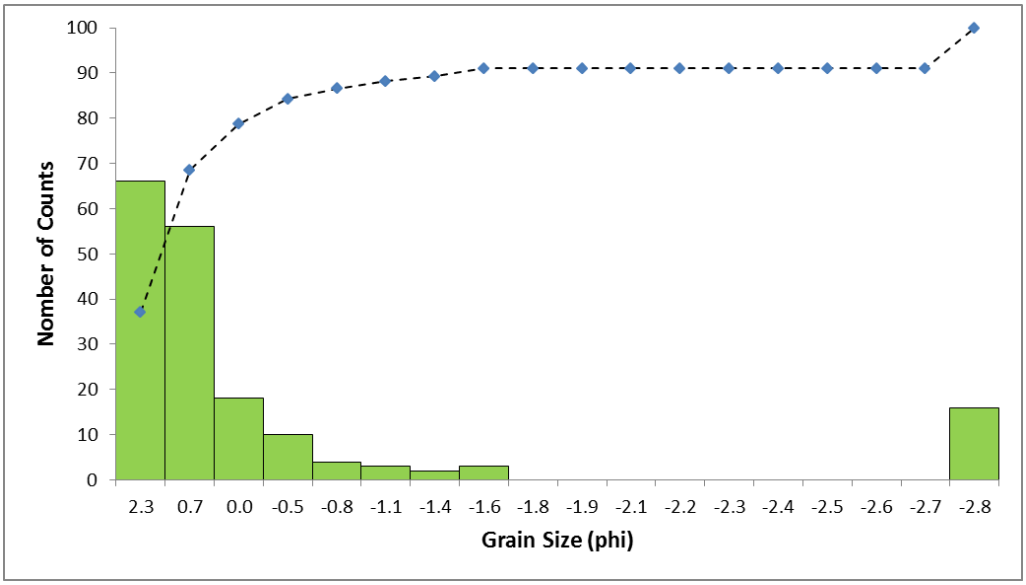

Figure B. 24 Grain size distribution of Esrey Park samples, showing arenaceous grain size KEW3-1. The dashed line represents cumulative grain size for the sample.

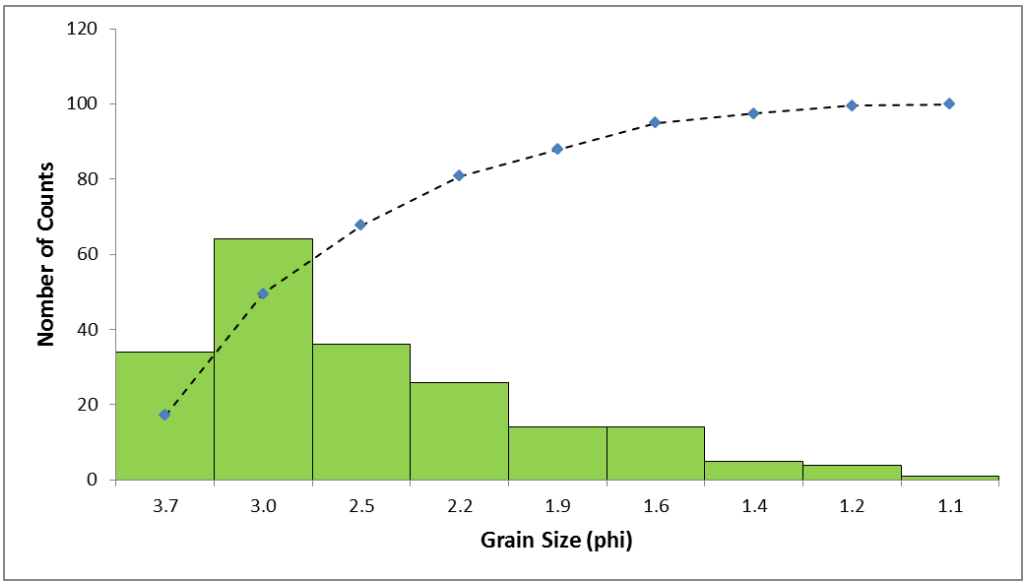

Figure B. 25 Grain size distribution of Dan point samples, showing arenaceous grain size KEW4-1. The dashed line represents cumulative grain size for the sample.

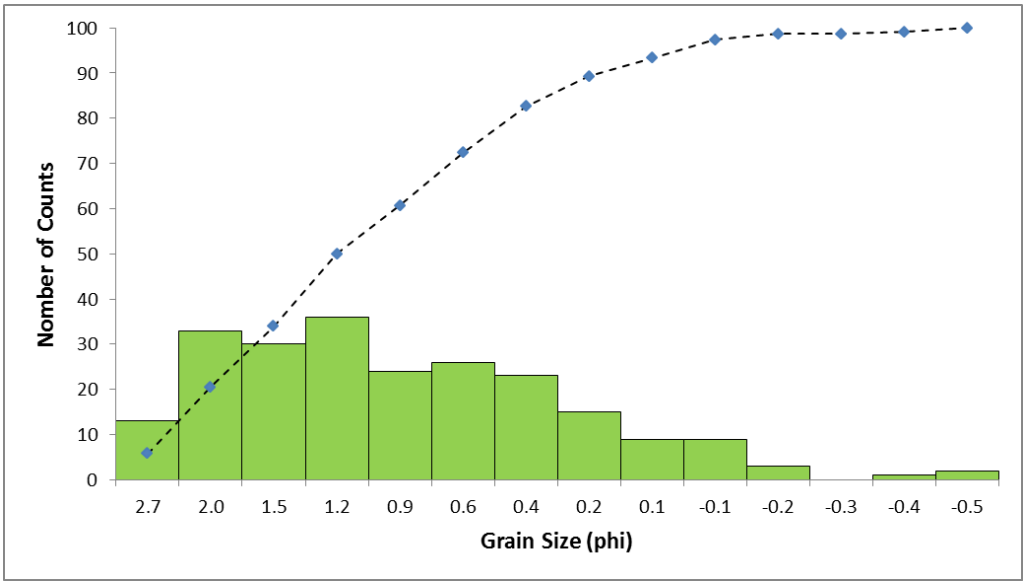

Figure B. 26 Grain size distribution of Hobard State Park samples, showing arenaceous grain size KEW5-1. The dashed line represents cumulative grain size for the sample.

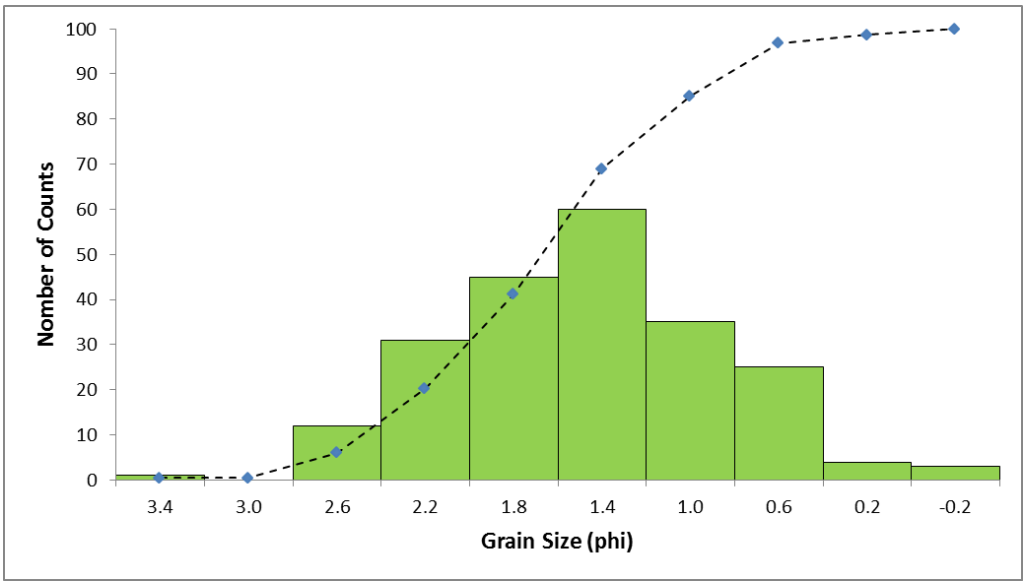

Figure B. 27 Grain size distribution and cumulative frequency % curve of POT8-1 sample. The dashed line represents cumulative grain size for the sample.

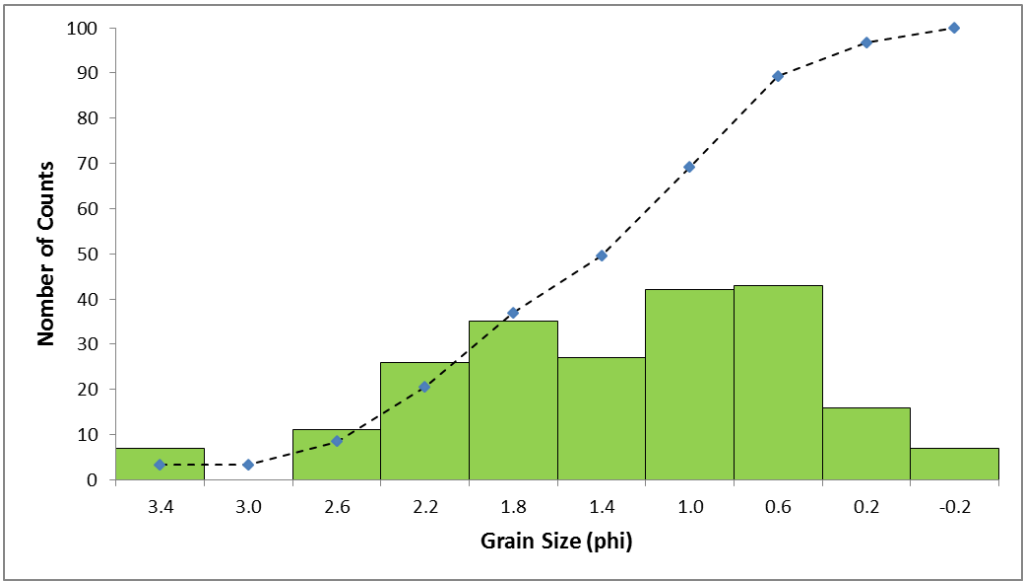

Figure B. 28 Grain size distribution and cumulative frequency % curve of POT4 sample. The dashed line represents cumulative grain size for the sample.

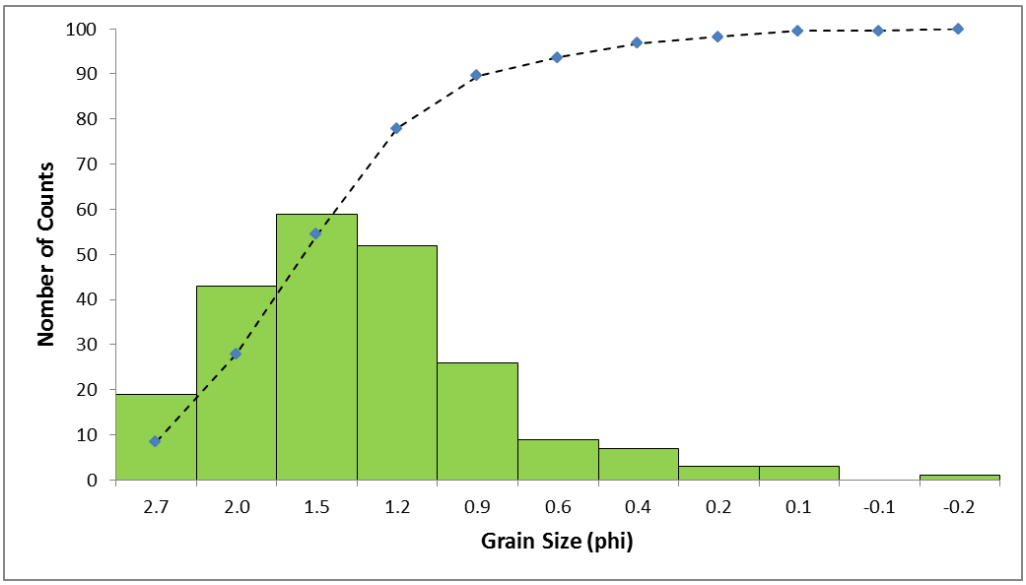

Figure B. 29 Grain size distribution of Dardemple Park (BAY1) sample showing grain size of medium to course grained arenite. The dashed line represents cumulative grain size for the sample.

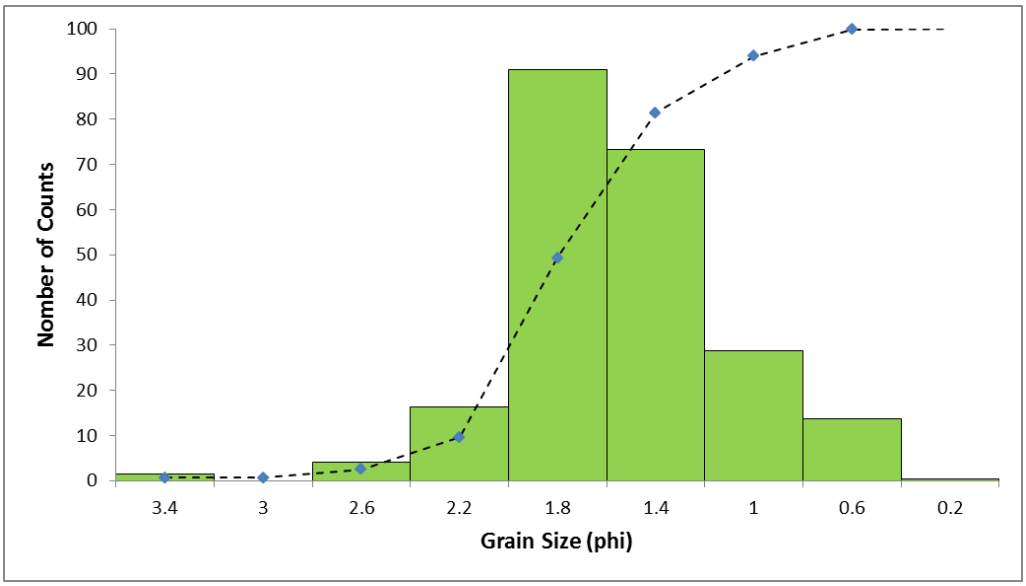

Figure B. 30 Histogram of grain size distribution and cumulative frequency % curve of L'ANSE1 sample. The dashed line represents cumulative grain size for the sample.

APPENDIX

C.THE CHEMICAL COMPOSITION OF THE MCR CLASTIC AND VOLCANIC ROCKS

Table C. 1 The accuracy data for XRF chemical analysis during runs with the MCR samples. LOI is Loss on Ignition.

Kansas well, SH, SF, and AG samples	SiO_2	Al_2O_3	Fe_2O_3	CaO	MgO	Na_2O	K_2O	MnO	TiO_2	P_2O_5	LOI	SUM
Analysis of Standard	50.1	20.78	6.19	8.01	0.54	7.21	1.61	0.11	0.28	0.13	4.65	99.84
Expected Std.	49.9	20.69	6.21	8.05	0.54	7.1	1.66	0.108	0.287	0.131	4.65	
Accuracy Error %	-0.40	-0.43	0.32	0.50	0.00	-1.53	3.11	-1.82	2.50	0.77	0.00	

Iowa well samples	SiO_2	Al_2O_3	Fe_2O_3	CaO	MgO	Na_2O	K_2O	MnO	TiO_2	P_2O_5	LOI	SUM
Analysis of Standard	49.9	20.69	6.21	8	0.54	7.25	1.59	0.11	0.28	0.12	4.56	99.25
Expected Std.	49.9	20.69	6.21	8.05	0.54	7.1	1.66	0.108	0.287	0.131	4.56	
Accuracy Error%	0.00	0.00	0.00	0.63	0.00	-2.07	4.40	-1.82	2.50	9.17	0.00	

KEW, POT, CFSP, and BAY samples	SiO_2	Al_2O_3	Fe_2O_3	CaO	MgO	Na_2O	K_2O	MnO	TiO_2	P_2O_5	LOI	SUM
Standard	49.7	20.58	6.29	8.04	0.52	7.13	1.62	0.11	0.27	0.12	4.56	99.04
Standard	49.8	20.61	6.3	8.05	0.52	7.17	1.62	0.11	0.27	0.12	4.56	99.17
STD. dev.	0.071	0.021	0.007	0.007	0.000	0.028	0.000	0.000	0.000	0.000	0.000	0.092
Average Std.	49.75	20.595	6.295	8.05	0.52	7.15	1.62	0.11	0.27	0.12	4.56	99.105
Expected Std.	49.9	20.69	6.21	8.05	0.54	7.1	1.66	0.108	0.287	0.13	4.56	
Accuracy Error%	0.30	0.46	-1.35	0.06	3.85	-0.70	2.47	-1.82	6.30	8.33	0.00	
Precision %	0.14	0.10	0.11	0.09	0.00	0.40	0.00	0.00	0.00	0.00	0.00	

Table C. 2 XRF results of the Oronto Group CHC samples collected from Keweenawan Peninsula, MI. The values in wt%; LOI is Loss on Ignition.

	SiO_2	Al_2O_3	Fe_2O_3	CaO	MgO	Na_2O	K_2O	MnO	TiO_2	P_2O_5	LOI
KEW1-1	55.70	12.68	8.49	6.14	1.89	3.59	3.83	0.09	1.42	0.14	6.11
KEW1-2	58.10	10.85	6.53	7.81	1.62	3.10	3.67	0.11	1.07	0.11	7.05
KEW1-3	51.80	9.19	4.15	14.70	1.36	2.43	3.28	0.09	0.49	0.07	12.34
KEW2-2	48.50	12.18	8.99	9.56	3.56	3.74	2.46	0.12	1.80	0.18	8.63
KEW3-S	50.20	12.62	14.56	4.30	3.49	3.35	2.18	0.14	4.72	0.26	3.61
KEW3-1	45.30	10.57	9.45	13.33	3.23	3.02	1.79	0.12	1.61	0.18	11.41
KEW4C	58.10	12.04	12.59	0.52	4.57	1.86	4.57	0.13	1.83	0.22	3.65
KEW4S	57.00	10.95	9.60	3.02	4.67	0.49	5.89	0.15	1.67	0.24	6.04
KEW4-1	62.70	9.86	5.24	5.97	2.44	1.46	3.91	0.06	1.00	0.14	6.74
KEW4-2	56.60	12.13	12.22	0.87	5.00	1.70	4.64	0.15	1.95	0.40	3.88
KEW4-3	50.20	7.88	8.70	11.85	3.77	0.88	3.11	0.11	1.80	0.17	11.57
KEW5-1	53.50	12.99	5.80	7.94	2.64	3.67	3.87	0.08	1.08	0.21	8.19
KEW5-2	50.9	14.51	7.08	5.75	4.52	2.46	4.8	0.08	1.15	0.19	8.3
Average	**53.7**	**11.42**	**8.72**	**7.06**	**3.29**	**2.44**	**3.69**	**0.11**	**1.66**	**0.19**	**7.50**
Stdev.	**4.6**	**1.70**	**2.93**	**4.27**	**1.17**	**1.05**	**1.10**	**0.03**	**0.97**	**0.08**	**2.85**

Table C. 3 XRF results of the Oronto Group samples collected from Potato River Falls (POT), Superior Falls (SF), Saxon Harbor (SH), and Copper Falls State Park, WI. The values in wt%; LOI is Loss on Ignition.

	Unit	SiO_2	Al_2O_3	Fe_2O_3	CaO	MgO	Na_2O	K_2O	MnO	TiO_2	P_2O_5	LOI
POT6	CHC	52.2	13.01	14.98	1.95	4.53	1.87	3.71	0.13	2.19	0.21	3.97
POT7	CHC	59.3	11.65	11.38	1.62	4.59	2.03	3.17	0.13	1.31	0.17	3.56
CFSP4	CHC	55.9	10.96	11.12	6.86	3.28	1.30	1.59	0.14	1.53	0.19	7.01
Average		**55.8**	**11.87**	**12.49**	**3.48**	**4.13**	**1.73**	**2.82**	**0.13**	**1.68**	**0.19**	**4.85**
Stdev.		**2.9**	**0.85**	**1.76**	**2.40**	**0.60**	**0.31**	**0.90**	**0.00**	**0.37**	**0.02**	**1.54**
POT1	Nonesuch	53.1	16.10	12.12	2.19	4.39	1.65	2.67	0.19	1.27	0.19	5.95
POT2	Nonesuch	49.3	13.04	12.38	7.49	4.12	2.08	1.23	0.20	1.82	0.21	7.69
POT3	Nonesuch	54.3	14.35	12.83	2.69	4.62	1.88	1.87	0.19	1.64	0.20	5.04
POT4	Nonesuch	54.0	12.68	13.77	4.06	4.23	2.04	1.39	0.16	1.77	0.21	4.78
POT4b	Nonesuch	55.0	14.81	11.74	2.01	5.03	1.95	3.31	0.17	1.46	0.22	4.49
POT5	Nonesuch	55.8	12.30	13.85	2.19	4.41	1.81	3.67	0.12	1.87	0.21	3.42
POT5b	Nonesuch	53.5	13.39	13.00	1.60	6.35	2.01	3.48	0.18	1.57	0.18	4.59
CFSP3	Nonesuch	57.9	10.64	9.92	6.43	1.58	2.82	2.71	0.10	0.96	0.14	6.20
Average		**54.1**	**13.41**	**12.45**	**3.58**	**4.34**	**2.03**	**2.54**	**0.16**	**1.55**	**0.20**	**5.27**
Stdev.		**2.3**	**1.57**	**1.18**	**2.08**	**1.24**	**0.33**	**0.89**	**0.03**	**0.29**	**0.02**	**1.22**
POT8-1	Freda	54.5	12.16	12.40	5.93	3.31	0.16	1.10	0.15	2.13	0.19	7.46
POT8-2	Freda	70.2	9.29	6.74	4.57	1.42	0.11	0.77	0.06	1.02	0.15	5.24
CFSP1	Freda	55.5	16.63	10.50	1.47	3.31	0.45	3.61	0.20	1.42	0.11	6.79
CFSP2	Freda	76.1	8.97	3.72	2.44	1.07	0.78	1.54	0.09	0.85	0.05	3.72
SF1	Freda	75.5	11.20	2.02	0.89	1.06	2.33	3.51	0.03	0.60	0.13	2.01
SF2	Freda	74.7	9.58	1.65	3.42	0.94	2.03	2.16	0.07	0.70	0.12	3.88
SF3	Freda	79.0	9.37	1.66	1.34	0.95	1.78	2.42	0.05	0.67	0.12	2.33
SF4	Freda	70.6	12.25	4.12	1.01	1.79	2.13	3.57	0.06	0.82	0.16	3.10
SH	Freda	72.9	10.22	5.31	0.37	1.53	1.63	3.67	0.06	0.92	0.15	2.32
Average		**69.9**	**11.07**	**5.35**	**2.38**	**1.71**	**1.27**	**2.48**	**0.09**	**1.01**	**0.13**	**4.09**
Stdev.		**8.4**	**2.28**	**3.66**	**1.78**	**0.90**	**0.84**	**1.09**	**0.05**	**0.46**	**0.04**	**1.88**

Table C. 4 XRF results of clastic sedimentary samples collected from Eischeid #1well, IA. The values in wt%; LOI is Loss on Ignition.

	SiO_2	Al_2O_3	Fe_2O_3	CaO	MgO	Na_2O	K_2O	MnO	TiO_2	P_2O_5	LOI
C2-1	48.1	5.76	0.99	22.92	0.55	0.94	2.57	0.10	0.17	0.13	18.11
C2-2	72.1	11.00	3.13	2.77	1.70	2.50	2.22	0.04	0.90	0.31	2.79
C2-3	62.6	14.15	6.62	1.83	3.95	2.28	2.68	0.07	1.27	0.23	3.87
C2-4	58.5	16.49	7.67	0.97	4.87	1.82	3.57	0.07	0.94	0.19	4.92
C2-5	61.1	15.26	6.47	1.80	4.66	2.09	2.96	0.07	0.96	0.20	4.56
C1-6	39.3	8.42	3.56	22.95	1.85	1.75	1.79	0.09	0.57	0.13	19.25
C1-7	53.7	14.91	6.93	6.14	3.94	1.84	3.22	0.07	0.81	0.16	8.32
C1-8	47.0	11.67	4.90	14.19	2.77	1.87	2.57	0.08	0.74	0.16	13.44
Aver.	55.3	12.21	5.03	9.20	3.04	1.89	2.70	0.07	0.80	0.19	9.41
Stdev.	9.7	3.47	2.16	8.87	1.46	0.43	0.52	0.02	0.30	0.06	6.21
D4-1	71.3	10.65	5.04	2.63	1.12	2.62	2.41	0.07	1.59	0.26	2.23
D4-2	69.5	10.84	4.14	3.83	1.18	2.60	2.75	0.08	0.95	0.20	3.67
D4-3	65.7	13.16	5.06	2.73	1.88	2.91	2.98	0.08	0.95	0.19	3.50
Aver.	68.8	11.55	4.75	3.06	1.39	2.71	2.71	0.08	1.16	0.22	3.13
Stdev.	2.3	1.14	0.43	0.54	0.34	0.14	0.23	0.00	0.30	0.03	0.64
E2-2	82.8	6.99	2.11	1.57	0.44	0.82	2.58	0.04	0.34	0.07	1.87
E2-3	77.9	9.37	3.35	0.76	0.84	1.04	3.59	0.05	0.31	0.10	1.92
E2-4	80.9	8.41	2.92	0.70	0.65	0.91	3.51	0.04	0.22	0.08	1.64
Aver.	**80.5**	**8.26**	**2.79**	**1.01**	**0.64**	**0.92**	**3.23**	**0.04**	**0.29**	**0.08**	**1.81**
Stdev.	**2.0**	**0.98**	**0.51**	**0.40**	**0.16**	**0.09**	**0.46**	**0.00**	**0.05**	**0.01**	**0.12**

Table C. 5 XRF results of Bayfield and Jacobsville sandstones. The values in wt%; LOI is Loss on Ignition.

	Unit	SiO_2	Al_2O_3	Fe_2O_3	CaO	MgO	Na_2O	K_2O	MnO	TiO_2	P_2O_5	LOI
BAY-1	Bayfield	92.2	3.37	1.45	0.03	0.13	0.07	1.77	0.02	0.12	0.02	0.96
BAY-2b	Bayfield	92.5	3.47	1.18	0.02	0.04	0.11	2.03	0.05	0.16	0.03	0.77
BAY-3	Bayfield	92.2	2.98	1.26	0.01	0.05	0.07	1.91	0.01	0.28	0.02	0.79
BAY-2a	Bayfield	93.4	2.98	0.90	0.02	0.05	0.09	1.76	0.01	0.25	0.01	0.48
AF	Jacobsville	91.6	2.74	1.01	0.05	0.09	0.04	2.06	<0.01	0.20	0.03	0.65
L'ANSE1	Jacobsville	76.9	9.34	3.50	0.33	1.59	0.14	4.03	0.04	0.46	0.09	3.00
L'ANSE2	Jacobsville	76.8	9.26	3.60	0.30	1.58	0.14	4.04	0.03	0.48	0.10	2.98
Average		**87.9**	**4.88**	**1.84**	**0.11**	**0.50**	**0.09**	**2.51**	**0.03**	**0.28**	**0.04**	**1.38**
Stdev.		**7.0**	**2.81**	**1.09**	**0.13**	**0.68**	**0.03**	**0.97**	**0.01**	**0.13**	**0.03**	**1.03**

Table C. 6 XRF results of clastic dominated samples collected from Kansas Texaco Poersch #1well. The values in wt%; LOI is Loss on Ignition.

Depth (ft.)	SiO_2	Al_2O_3	Fe_2O_3	CaO	MgO	Na_2O	K_2O	MnO	TiO_2	P_2O_5	LOI
5396′	49.7	15.30	7.89	4.08	9.04	2.90	2.90	0.17	1.73	0.26	5.71
5400′	22.2	7.41	17.15	26.17	2.38	2.73	0.49	0.11	1.57	0.21	20.18
8052.5′	71.6	12.55	2.17	2.91	0.51	3.43	4.15	0.04	0.27	0.07	2.41
8476-8480′	72.5	11.48	2.68	3.24	1.10	4.26	2.39	0.06	0.37	0.1	2.36
10,666′	48.9	15.41	13.21	3.36	6.34	6.47	0.46	0.33	1.27	0.24	3.83
10,509.5′	66.2	10.54	2.25	7.37	0.34	3.25	3.53	0.09	0.44	0.10	5.68
11,061.5′	62.3	18.13	2.64	1.50	0.17	4.46	9.34	0.01	0.16	0.06	1.35
Aver.	**56.20**	**12.97**	**6.86**	**6.95**	**2.84**	**3.93**	**3.32**	**0.12**	**0.83**	**0.15**	**5.93**
Stdev.	**16.44**	**3.32**	**5.68**	**8.02**	**3.22**	**1.20**	**2.78**	**0.10**	**0.62**	**0.08**	**6.02**

Table C. 7 XRF results of mafic volcanic and intrusive rock samples collected from Kansas Texaco Poersch #1well (Berendsen et al., 1988).

Depth (ft)	Lithology	SiO_2	Al_2O_3	Fe_2O_3	MnO	TiO_2	CaO	MgO	Na_2O	K_2O	LOI	Total
2860-2870	Gabbro	43.11	16.27	11.57	0.21	1.35	10.21	8.93	1.53	3.16	3.99	100.33
3720-3730	Basalt	42.45	14.68	13.09	0.2	1.05	7.95	14.92	1.12	1.31	3.2	99.97
4760-4770	Basalt	46.51	15.15	13.68	0.21	2.63	8.12	5.53	2.99	2.61	3.19	100.62
6130-6140	Basalt	46.44	14.89	12.68	0.21	2.09	8.21	6.61	2.28	4.26	2.92	100.59
7180-7190	Basalt	42.94	14.02	16.93	0.24	2.97	7.14	5.84	2.5	4.99	3.18	100.75
8330-8340	Arkose	58.88	13.07	3.13	0.05	0.58	7.98	9.17	2.68	3.55	0.83	99.92
8730-8740	Gabbro	42.24	14.48	16.33	0.29	2.77	8	6.12	1.79	4.93	3.34	100.29
6780-6790	Basalt	44.8	16.1	13.58	0.21	1.62	8.91	8.14	2.04	1.98	2.09	99.47
9590-9600	Arkose	66.02	12.68	1.89	0.21	0.32	1.9	0.46	2.3	12.76	1.97	100.51
10730-10740	Basalt	49.56	15.12	11.54	0.27	1.55	5.37	6.3	3.74	4.84	2.4	100.69

Table C. 8 XRF results of clastic sedimentary samples collected from the NSVG interflow clastics (GH-C); Silver Bay Anorthosite (BEV); from the NSVG basalt (GH-B); Lax Lake Gabbro (LLG; Miller and Chandler, 1997); Blesner lake Gabbro (BLG; Miller and Chandler, 1997); Victor Head Diabase (VHD; Miller and Chandler, 1997); Beaver River Diabase (BBD; Miller and Chandler, 1997)Silver Bay Gabbro (SBG; Miller and Chandler, 1997); Upper Manitou Gabbro (UMG; Miller and Chandler, 1997). The values in wt%; LOI is Loss on Ignition.

	SiO_2	Al_2O_3	Fe_2O_3	CaO	MgO	Na_2O	K_2O	MnO	TiO_2	P_2O_5	LOI	SUM
GH-C	52.2	17.06	4.18	9.17	2.32	2.42	0.58	0.06	0.98	0.09	9.51	98.56
GH-B	46.5	15.65	10.15	10.15	8.84	2.24	0.27	0.17	1.12	0.11	4.69	99.94
LLG	47.7	16.2	12.5	9.7	4.8	2.74	0.78	0.19	2.27	0.24	1.17	98.29
BLG	49.5	18.6	9.4	10.21	3.63	3.8	0.7	0.14	1.7	0.14	2.85	100.67
VHD	49.7	15.9	11.2	9.5	5.3	2.57	0.68	0.15	1.71	0.25	1.39	98.35
BBD	48	16.7	10.5	10.4	7.8	2.3	0.35	0.17	1.31	0.14	1.71	99.38
SBG	49.5	12.4	15.4	7.8	3.6	2.85	1.17	0.23	3.25	0.47	1.42	98.09
UMG	48.3	16.3	11.6	10.2	5.7	2.58	0.56	0.18	1.64	0.14	0.99	98.19
BEV1	50.2	29.52	1.14	13.16	0.6	3.59	0.19	0.01	0.12	0.01	0.8	99.39
BEV2	50	30.44	0.78	13.63	0.35	3.34	0.19	0.01	0.11	<0.01	0.63	99.46
BEV3	50.8	28.77	1.2	12.47	0.63	3.82	0.22	0.02	0.14	<0.01	0.75	98.87

APPENDIX

D. HIGH TEMPERATURE - PRESSURE TEST DATA

Table D. 1 The accuracy and precision data for pH analyses.

pH	4.00 Standard	7.00 Standard	pH (Continued)	4.00 Standard	7.00 Standard
1	3.94	6.97	12	4.05	7.03
2	3.97	6.97	13	4.05	7.03
3	4.00	6.98	14	4.05	7.03
4	4.01	7.01	15	4.01	6.95
5	4.00	7.01	16	4.01	6.95
6	4.02	7.03	17	4.01	6.95
7	3.95	6.94	20	4.03	6.92
8	4.00	7.01	21	4.03	6.92
9	4.00	6.99	22	4.03	6.92
10	3.95	6.94	23	4.03	6.92
11	3.95	6.94	24	4.03	6.92
12	3.99	7.00	25	4.03	6.92
13	4.15	7.11	26	4.03	6.92
14	4.02	7.03	27	4.03	6.92
15	3.99	7.00	28	4.00	6.87
16	4.00	7.01	29	3.99	6.85
17	4.01	7.00	30	3.99	6.85
18	4.05	7.05	31	4.02	7.09
19	3.99	7.00	32	4.04	7.10
20	3.95	6.94	**STDEV.**	**0.04**	**0.06**
22	4.06	7.03	**AVE.**	**4.02**	**6.99**
1	3.99	6.99	**Accuracy %**	**1.56**	**2.18**
2	3.99	6.99	**Precision %**	**0.91**	**0.80**
3	4.02	7.00			
4	4.02	7.00			
5	4.02	7.01			
6	4.04	7.02			
7	4.04	7.02			
8	4.04	7.02			
9	4.05	7.03			
10	4.05	7.03			
11	4.05	7.03			

Table D. 2 The accuracy data for ICP-OES analyses during runs with the KEW1-1, KEW2-1, KEW5-1, KEW3-2, KEW4-2, POT2, POT5-1, POT6, POT8-2, POT4, CFSP4, BAY3, and L'ANSE1 samples. Data are results for QA/QC analyses checks on 1 ppm and 10 ppm standards. Before, after, and during representing the measuring of the standred before, during and after the analysis.

0.1 ppm Standard								
	Si	Fe	Ca	Mg	K	Na	Mn	Al
DURING	0.16	0.08	0.06	0.10	0.07	0.10	0.09	0.08
1 ppm Standard								
	Si	Fe	Ca	Mg	K	Na	Mn	Al
BEFORE	1.06	1.01	0.98	1.04	1.04	1.00	1.03	1.08
DURING	1.02	0.98	0.95	1.02	1.00	0.95	0.98	0.97
AFTER	0.99	0.96	0.94	1.00	1.00	0.97	0.97	0.96
Average	1.02	0.98	0.96	1.02	1.01	0.97	0.99	1.00
STDEV.S	0.04	0.03	0.02	0.02	0.02	0.03	0.03	0.07
Accuracy %	-2.28	1.69	4.53	-1.96	-1.32	2.74	0.67	-0.33
CV precision %	3.43	2.56	2.18	1.96	2.28	2.59	3.24	6.64
10ppm Standard								
	Si	Fe	Ca	Mg	K	Na	Mn	Al
BEFORE								
DURING	9.93	9.94	9.79	10.3	10.1	9.89	10	9.96
AFTER	9.76	9.9	9.63	10.3	10	9.79	9.94	9.9
Average	9.85	9.92	9.71	10.3	10.05	9.84	9.97	9.93
STDEV.S	0.12	0.03	0.11	0.00	0.07	0.07	0.04	0.04
Accuracy %	1.57	0.81	2.99	-2.91	-0.50	1.63	0.30	0.70
CV precision %	1.22	0.29	1.17	0.00	0.70	0.72	0.43	0.43

Table D. 3 The accuracy data for ICP-OES analyses during runs with the Texaco Poersch #1 well samples, Kansas, Eischeid #1 well samples, Iowa, and BEV samples on 1 ppm and 10 ppm standards.

1 ppm Standard								
	Si	Fe	Ca	Mg	K	Na	Mn	Al
BEFORE								
DURING	1.05	1.09	1.07	1.12	1.02	1.04	1.10	1.08
DURING	1.05	1.11	1.06	1.12	0.89	1.01	1.09	1.08
AFTER	1.05	1.10	1.07	1.13	0.82	0.99	1.10	1.09
Average	1.05	9.92	9.71	10.30	10.05	9.84	9.97	9.93
STDEV.S	0.00	0.01	0.01	0.01	0.10	0.03	0.01	0.01
Accuracy %	-4.76	0.81	2.99	-2.91	-0.50	1.63	0.30	0.70
CV precision %	0.00	0.10	0.06	0.06	1.01	0.26	0.06	0.06
10 ppm Standard								
	Si	Fe	Ca	Mg	K	Na	Mn	Al
BEFORE								
DURING	10.20	10.60	10.50	10.80	10.20	10.40	10.60	10.50
DURING	10.20	10.60	10.40	10.80	10.50	10.30	10.40	10.50
AFTER	10.20	10.70	10.50	10.80	10.30	10.30	10.60	10.40
Average	10.20	10.63	10.47	10.80	10.33	10.33	10.53	10.47
STDEV.S	0.00	0.06	0.06	0.00	0.15	0.06	0.12	0.06
Accuracy %	-1.96	-5.96	-4.46	-7.41	-3.23	-3.23	-5.06	-4.46
CV precision %	0.00	0.54	0.55	0.00	1.48	0.56	1.10	0.55

Table D. 4 The accuracy data for ICP-OES analyses during runs with the core flooding experiments for KEW and BAY samples on 1 ppm and 10 ppm standards.

1 ppm Standard								
	Si	Fe	Ca	Mg	K	Na	Mn	Al
BEFORE	1.02	0.96	0.97	0.95	1.02	0.99	1.01	1.03
DURING	0.94	0.85	0.88	0.87	0.87	0.89	0.93	0.95
AFTER								
Average	0.98	0.91	0.93	0.91	0.95	0.94	0.97	0.99
STDEV.S	0.06	0.08	0.06	0.06	0.11	0.07	0.06	0.06
Accuracy %	2.04	10.50	8.11	9.89	5.82	6.38	3.09	1.01
CV precision %	5.77	8.59	6.88	6.22	11.22	7.52	5.83	5.71
10 ppm Standard								
	Si	Fe	Ca	Mg	K	Na	Mn	Al
BEFORE								
DURING	9.39	9.52	9.37	9.74	9.56	9.34	9.32	9.25
AFTER								
Average	9.39	9.52	9.37	9.74	9.56	9.34	9.32	9.25
STDEV.S	N/A	N/A	N/A	N/A	N/A	N/A	N/A	N/A
Accuracy %	6.50	5.04	6.72	2.67	4.60	7.07	7.30	8.11
CV precision %	N/A	N/A	N/A	N/A	N/A	N/A	N/A	N/A

Table D. 5 The accuracy data for ICP-OES analyses during runs with the core flooding of 11,061.5′ sample, SF, SH, AG, DUL, GHB, and GHC samples on 1 ppm and 10 ppm standards.

1 Standard								
	Si	Fe	Ca	Mg	K	Na	Mn	Al
BEFORE	1.01	1.10	1.04	1.06	1.05	1.00	1.04	1.04
DURING	1.02	1.09	1.06	1.08	1.06	1.04	1.06	1.04
DURING	1.04	1.10	1.07	1.09	1.07	1.03	1.05	1.07
AFTER	1.02	1.10	1.06	1.09	1.06	1.01	1.06	1.06
Average	1.03	1.10	1.06	1.09	1.06	1.03	1.06	1.06
STDEV.S	0.01	0.01	0.01	0.01	0.01	0.02	0.01	0.02
Accuracy %	-2.60	-8.81	-5.96	-7.98	-5.96	-2.60	-5.36	-5.36
CV precision %	1.12	0.53	0.54	0.53	0.54	1.49	0.55	1.45
10 ppm Standard								
	Si	Fe	Ca	Mg	K	Na	Mn	Al
BEFORE	10.40	10.70	10.50	10.70	10.50	10.30	10.30	10.40
DURING	10.40	11.00	10.60	10.90	10.60	10.40	10.50	10.60
DURING	10.40	11.00	10.60	11.00	10.60	10.30	10.40	10.60
AFTER	10.30	10.70	10.70	10.70	10.60	10.20	10.40	10.50
Average	10.37	10.90	10.63	10.87	10.60	10.30	10.43	10.57
STDEV.S	0.06	0.17	0.06	0.15	0.00	0.10	0.06	0.06
Accuracy %	-3.54	-8.26	-5.96	-7.98	-5.66	-2.91	-4.15	-5.36
CV precision %	0.56	1.59	0.54	1.41	0.00	0.97	0.55	0.55

Table D. 6 The accuracy data for T1, T2, T3, T4, T5, T6, T7, T8, T9, T10, T11, T12, T13, T10, T11, T12, T13, T14, T15, T16, MO, CR, and 50°C samples based on 1 ppm and 10 ppm standards.

1 ppm Standard								
	Si	Fe	Ca	Mg	K	Na	Mn	Al
BEFORE	0.81	0.83	0.81	0.84	0.87	0.79	0.81	0.79
DURING	1.01	1.06	1.01	1.05	0.42	0.70	1.02	1.01
DURING	1.01	1.07	1.02	1.06	0.45	0.71	1.01	1.02
DURING	1.00	1.05	1.03	1.06	1.02	0.96	1.03	1.01
DURING	0.99	1.03	1.03	1.06	1.03	0.96	1.03	1.00
AFTER	0.99	1.04	1.04	1.07	1.03	0.95	1.04	1.01
Average	0.99	1.04	1.03	1.06	1.03	0.96	1.03	1.01
STDEV.S	0.01	0.01	0.01	0.01	0.01	0.01	0.01	0.01
Accuracy %	0.70	-3.85	-3.23	-5.96	-2.60	4.49	-3.23	-0.66
CV precision %	0.61	0.96	0.56	0.54	0.56	0.64	0.56	0.57
10 ppm Standard								
	Si	Fe	Ca	Mg	K	Na	Mn	Al
DURING	10.10	10.50	10.40	10.80	10.20	10.30	10.50	10.20
AFTER	10.00	10.40	10.30	10.60	10.40	10.20	10.40	10.00
Average	10.05	10.45	10.35	10.70	10.30	10.25	10.45	10.10
STDEV.S	0.07	0.07	0.07	0.14	0.14	0.07	0.07	0.14
Accuracy %	-0.50	-4.31	-3.38	-6.54	-2.91	-2.44	-4.31	-0.99
CV precision %	0.70	0.68	0.68	1.32	1.37	0.69	0.68	1.40

Table D. 7 Summary of accuracy and CV precision % for Appendices Tables D.2 to Table D.6.

Accuracy 1 %	**Si**	**Fe**	**Ca**	**Mg**	**K**	**Na**	**Mn**	**Al**
Table D.2	2.28	1.69	4.53	1.96	1.32	2.74	0.67	0.33
Table D.3	4.76	0.81	2.99	2.91	0.50	1.63	0.30	0.70
Table D.4	2.04	10.50	8.11	9.89	5.82	6.38	3.09	1.01
Table D.5	2.60	8.81	5.96	7.98	5.96	2.60	5.36	5.36
Table D.6	0.70	3.85	3.23	5.96	2.60	4.49	3.23	0.66
Accuracy 10 %	**Si**	**Fe**	**Ca**	**Mg**	**K**	**Na**	**Mn**	**Al**
Table D.2	1.57	0.81	2.99	2.91	0.50	1.63	0.30	0.70
Table D.3	1.96	5.96	4.46	7.41	3.23	3.23	5.06	4.46
Table D.4	6.50	5.04	6.72	2.67	4.60	7.07	7.30	8.11
Table D.5	3.54	8.26	5.96	7.98	5.66	2.91	4.15	5.36
Table D.6	0.50	4.31	3.38	6.54	2.91	2.44	4.31	0.99
CV precision 1 %	**Si**	**Fe**	**Ca**	**Mg**	**K**	**Na**	**Mn**	**Al**
Table D.2	3.43	2.56	2.18	1.96	2.28	2.59	3.24	6.64
Table D.3	0.00	0.10	0.06	0.06	1.01	0.26	0.06	0.06
Table D.4	5.77	8.59	6.88	6.22	11.22	7.52	5.83	5.71
Table D.5	1.12	0.53	0.54	0.53	0.54	1.49	0.55	1.45
Table D.6	0.61	0.96	0.56	0.54	0.56	0.64	0.56	0.57
CV precision 10%	**Si**	**Fe**	**Ca**	**Mg**	**K**	**Na**	**Mn**	**Al**
Table D.2	1.22	0.29	1.17	0.00	0.70	0.72	0.43	0.43
Table D.3	0.00	0.54	0.55	0.00	1.48	0.56	1.10	0.55
Table D.4	N/A	N/A	N/A	N/A	N/A	N/A	N/A	N/A
Table D.5	0.56	1.59	0.54	1.41	0.00	0.97	0.55	0.55
Table D.6	0.70	0.68	0.68	1.32	1.37	0.69	0.68	1.40

Table D. 8 The molal concentration (mole/kg.) of leachate solutions collected after Oronto Group samples after HTP testing.

Molal	Si	Al	Fe	Ca	Mg	Na	K	Mn
KEW1-1	9.26E-04	<3.71E-06	<1.79E-06	1.75E-02	1.60E-03	1.10E-04	7.39E-04	1.42E-04
KEW4-2	2.28E-03	<3.71E-06	<1.79E-06	1.99E-02	6.83E-03	1.23E-04	1.00E-03	5.82E-05
KEW5-1	2.63E-03	<3.71E-06	<1.79E-06	2.28E-02	5.51E-03	3.07E-04	9.57E-04	5.64E-05
POT8-2	5.84E-03	<3.71E-06	<1.79E-06	5.74E-03	6.58E-04	1.38E-04	1.26E-03	3.82E-05
POT2	2.49E-03	<3.71E-06	<1.79E-06	3.19E-03	1.81E-04	8.18E-04	4.35E-06	1.82E-06
POT4	4.31E-03	<3.71E-06	<1.79E-06	2.02E-03	1.19E-04	3.84E-04	7.39E-04	3.09E-04
POT5-1	1.82E-03	<3.71E-06	<1.79E-06	2.99E-03	3.17E-04	4.86E-04	4.35E-06	1.82E-06
CFSP4	5.02E-03	<3.71E-06	<1.79E-06	2.72E-03	4.11E-05	1.30E-03	4.35E-04	1.82E-04
C2-1	1.01E-03	<3.71E-06	1.79E-06	6.67E-03	1.45E-03	4.07E-04	7.09E-04	1.82E-06
C2-2	1.59E-03	<3.71E-06	1.79E-06	9.40E-03	3.62E-04	1.41E-04	2.39E-04	2.18E-05
C2-3	1.59E-03	1.11E-05	1.43E-05	1.11E-03	1.14E-03	3.61E-04	4.05E-04	2.73E-05
C2-5	3.85E-04	<3.71E-06	1.79E-06	4.39E-03	5.68E-04	3.50E-04	3.70E-04	1.46E-05
D4-1	2.42E-03	<3.71E-06	1.79E-06	1.13E-02	6.09E-04	3.15E-04	5.22E-04	7.28E-05
D4-2	1.29E-03	<3.71E-06	1.79E-06	1.21E-02	2.88E-04	1.43E-04	3.31E-04	6.37E-05
SF1-1	1.47E-03	<3.71E-06	<1.79E-06	5.57E-03	1.51E-03	4.71E-04	3.91E-04	3.64E-05
SF1-2	1.33E-03	<3.71E-06	<1.79E-06	3.98E-03	1.22E-03	4.09E-04	3.57E-04	1.09E-05
SF1 ave	1.40E-03	<3.71E-06	<1.79E-06	4.77E-03	1.37E-03	4.40E-04	3.74E-04	2.37E-05
SF3-1	1.47E-03	<3.71E-06	<1.79E-06	7.18E-03	1.55E-03	4.07E-04	2.96E-04	3.09E-05
SF3-2	9.93E-04	<3.71E-06	<1.79E-06	4.19E-03	8.35E-04	3.30E-04	2.57E-04	5.46E-06
SF3 ave	1.23E-03	<3.71E-06	<1.79E-06	5.68E-03	1.19E-03	3.68E-04	2.76E-04	1.82E-05
SH-1	1.31E-03	<3.71E-06	<1.79E-06	1.67E-03	1.32E-03	3.38E-04	4.13E-04	3.09E-05
SH-2	1.32E-03	<3.71E-06	<1.79E-06	1.45E-03	1.19E-03	3.12E-04	3.65E-04	4.00E-05
SH ave	1.31E-03	<3.71E-06	<1.79E-06	1.56E-03	1.26E-03	3.25E-04	3.89E-04	3.55E-05

Table D. 9 Surface area normalized release results from solutions collected from Oronto Group sample high-pressure-temperature corrosion test vessels. Values in mol/cm2.d.

Mol/cm^2.d	Si	Al	Fe	Ca	Mg	Na	K	Mn
KEW1-1	2.76E-05	<1.10E-07	<5.33E-08	5.21E-04	4.78E-05	3.27E-06	2.20E-05	4.23E-06
KEW4-2	5.41E-06	<8.79E-09	<4.25E-09	4.71E-05	1.62E-05	2.91E-07	2.37E-06	1.38E-07
KEW5-1	4.62E-06	<6.49E-09	<3.14E-09	4.00E-05	9.66E-06	5.38E-07	1.68E-06	9.89E-08
POT8-2	4.87E-05	<3.09E-08	<1.49E-08	4.78E-05	5.49E-06	1.15E-06	1.05E-05	3.19E-07
POT2	1.16E-05	<1.72E-08	<8.33E-09	1.49E-05	8.42E-07	3.81E-06	2.02E-08	8.47E-09
POT4	4.01E-05	<3.45E-08	<1.67E-08	1.88E-05	1.11E-06	3.57E-06	6.88E-06	2.88E-06
POT5-1	8.90E-06	<1.82E-08	<8.78E-09	1.47E-05	1.55E-06	2.38E-06	2.13E-08	8.92E-09
CFSP4	2.06E-05	<1.52E-08	<7.34E-09	1.11E-05	1.69E-07	5.35E-06	1.78E-06	7.46E-07
C2-1	6.04E-06	<2.22E-08	1.07E-08	3.99E-05	8.70E-06	2.44E-06	4.25E-06	1.09E-08
C2-2	5.96E-06	<1.39E-08	6.72E-09	3.53E-05	1.36E-06	5.28E-07	8.97E-07	8.19E-08
C2-3	8.56E-06	5.99E-08	7.72E-08	6.00E-06	6.17E-06	1.94E-06	2.18E-06	1.47E-07
C2-5	6.10E-06	<5.88E-08	2.84E-08	6.97E-05	9.01E-06	5.56E-06	5.87E-06	2.31E-07
D4-1	7.83E-06	<1.20E-08	5.78E-09	3.64E-05	1.97E-06	1.02E-06	1.69E-06	2.35E-07
D4-2	1.89E-05	<5.42E-08	2.62E-08	1.77E-04	4.21E-06	2.09E-06	4.83E-06	9.31E-07
SF1-1	3.33E-07	<8.43E-10	<4.07E-10	1.27E-06	3.43E-07	1.07E-07	8.9E-08	8.28E-09
SF1-2	2.54E-07	<7.09E-10	<3.43E-10	7.61E-07	2.34E-07	7.83E-08	6.82E-08	2.09E-09
SF1 ave.	2.94E-07	<7.76E-10	<3.75E-10	1.01E-06	2.89E-07	9.26E-08	7.86E-08	5.18E-09
SF3-1	2.34E-07	<5.92E-10	<2.86E-10	1.15E-06	2.47E-07	6.49E-08	4.72E-08	4.94E-09
SF3-2	1.55E-07	<5.78E-10	<2.79E-10	6.53E-07	1.3E-07	5.14E-08	4E-08	8.51E-10
SF3 ave.	1.95E-07	<5.85E-10	<2.82E-10	8.99E-07	1.89E-07	5.82E-08	4.36E-08	2.9E-09
SH-1	2.14E-07	<6.07E-10	<2.93E-10	2.74E-07	2.17E-07	5.53E-08	6.77E-08	5.07E-09
SH-2	2.18E-07	<6.12E-10	<2.96E-10	2.39E-07	1.97E-07	5.15E-08	6.03E-08	6.61E-09
SH ave.	2.16E-07	<6.09E-10	<2.94E-10	2.56E-07	2.07E-07	5.34E-08	6.4E-08	5.84E-09

Table D. 10 The molal concentration (mole/kg.) of leachate solutions collected after Bayfield Group samples HTP corrosion testing.

Molal	Si	Al	Fe	Ca	Mg	Na	K	Mn
BAY3	1.07E-03	3.71E-04	2.36E-03	4.17E-04	1.65E-04	4.35E-04	4.60E-04	6.73E-05
L'NAS1	2.28E-03	<3.71E-05	1.79E-06	6.62E-04	3.87E-04	3.18E-04	7.16E-04	1.82E-05
E2-2	1.80E-03	<3.71E-06	<1.79E-06	1.22E-02	1.52E-04	1.91E-04	1.23E-04	1.09E-05
E2-3	6.62E-04	<3.71E-06	5.37E-06	6.50E-04	5.76E-05	1.96E-04	1.15E-04	2.00E-05
E2-4	1.73E-03	7.41E-06	<1.79E-06	1.55E-03	1.32E-04	3.39E-04	1.97E-04	4.19E-05
AG-1	1.08E-03	6.67E-05	3.22E-05	6.74E-04	4.69E-04	6.96E-05	6.24E-04	3.82E-05
AG-2	8.90E-04	<3.71E-06	<1.79E-06	5.52E-04	3.99E-04	6.09E-05	5.42E-04	2.37E-05

Table D. 11 Surface area normalized release results from solutions collected from Bayfield Group after high-pressure-temperature corrosion testing. Values in mol/cm2.d.

Mol/cm^2.d	Si	Al	Fe	Ca	Mg	K	Na	Mn
BAY3	8.17E-06	2.84E-06	1.81E-05	3.19E-06	1.26E-06	3.33E-06	3.52E-06	5.15E-07
L'NASE1	6.03E-06	<9.80E-08	4.74E-09	1.75E-06	1.02E-06	8.40E-07	1.89E-06	4.82E-08
E2-2	7.93E-06	<1.63E-08	<7.90E-09	5.37E-05	6.71E-07	8.44E-07	5.41E-07	4.82E-08
E2-3	2.46E-05	<1.38E-07	2.00E-07	2.42E-05	2.14E-06	7.28E-06	4.28E-06	7.45E-07
E2-4	7.32E-06	3.13E-08	<7.57E-09	6.56E-06	5.57E-07	1.43E-06	8.33E-07	1.77E-07
AG-1	1.56E-06	9.60E-08	4.64E-08	9.71E-07	6.75E-07	1.00E-07	8.98E-07	5.50E-08
AG-2	1.18E-06	<4.91E-09	<2.37E-09	7.31E-07	5.29E-07	8.07E-08	7.18E-07	3.14E-08

Table D. 12 The molal concentration (mole/kg.) of leachate solutions collected after Kansas Texaco Poersch #1 well samples HTP corrosion testing.

Molal	Si	Al	Fe	Ca	Mg	K	Na	Mn
5,397.3′A	1.73E-03	<3.71E-06	<1.79E-06	1.35E-03	9.89E-03	5.01E-04	4.35E-03	1.82E-06
5,397.3′B	1.63E-03	,3.71E-06	<1.79E-06	3.95E-03	4.95E-03	3.35E-04	2.77E-03	6.19E-05
5,404′A	1.74E-03	7.41E-06	<1.79E-06	2.75E-03	2.00E-03	4.25E-04	1.82E-03	3.46E-05
8,051.1′A	2.72E-03	<3.71E-06	<1.79E-06	1.28E-02	9.87E-05	1.20E-04	3.09E-04	5.46E-05
8,051.1′B	4.20E-04	<3.71E-06	<1.79E-06	8.53E-03	6.58E-05	7.16E-05	1.09E-04	4.19E-05
8,476-8,470′A	1.33E-03	<3.71E-06	<1.79E-06	1.25E-02	2.02E-04	7.16E-05	2.13E-04	7.46E-05
8,476-8,480′B	7.44E-04	<3.71E-06	<1.79E-06	1.29E-02	1.97E-04	5.12E-05	1.52E-04	6.37E-05
10,514′A	5.84E-04	<3.71E-06	<1.79E-06	1.05E-02	4.53E-05	4.60E-05	1.30E-04	6.55E-05
10,514′B	1.83E-03	<3.71E-06	<1.79E-06	1.24E-02	6.17E-05	6.65E-05	3.22E-04	8.19E-05
10,666′A	7.66E-04	<3.71E-06	<1.79E-06	6.04E-03	1.07E-03	9.46E-05	6.57E-04	1.04E-04
10,666′B	9.04E-04	<3.71E-06	<1.79E-06	9.00E-03	1.34E-03	8.95E-05	6.57E-04	1.57E-04
11,061′A	3.28E-04	<3.71E-06	5.37E-06	9.06E-03	4.94E-05	5.88E-05	1.87E-04	2.55E-05
11,061′B	1.41E-03	<3.71E-06	<1.79E-06	1.41E-02	4.53E-05	8.95E-05	3.39E-04	2.73E-05

Table D. 13 Surface area normalized release results from solutions collected from Kansas Texaco Poersch #1 well samples after high-pressure-temperature corrosion testing. Values in mol/cm^2.d.

Mol/m^2.sec	Si	Al	Fe	Ca	Mg	K	Na	Mn
5,397.3′A	4.7E-07	<1.01E-09	<4.87E-10	3.68E-07	2.69E-06	1.36E-07	1.18E-06	4.95E-10
5,397.3′B	7.12E-07	<1.62E-09	<7.82E-10	1.73E-06	2.16E-06	1.46E-07	1.21E-06	2.7E-08
5397.3′ ave.	5.11E-06	<1.13E-08	<5.48E-09	9.05E-06	2.09E-05	1.22E-06	1.03E-05	1.19E-07
5404.0′	8.33E-06	3.55E-08	<8.57E-09	1.32E-05	9.57E-06	2.03E-06	8.72E-06	1.65E-07
8,051.1′A	4.25E-07	<5.79E-10	<2.8E-10	2E-06	1.54E-08	1.88E-08	4.82E-08	8.53E-09
8,051.1′B	2.28E-06	<2.01E-08	<9.73E-09	4.64E-05	3.58E-07	3.89E-07	5.91E-07	2.27E-07
8051.1′ ave.	1.17E-05	<8.95E-08	<4.32E-08	2.09E-04	1.61E-06	1.76E-06	2.76E-06	1.02E-06
8,476-8,470′A	9.62E-07	<2.68E-09	<1.29E-09	9.05E-06	1.46E-07	5.17E-08	1.54E-07	5.39E-08
8,476-8,480′B	1.67E-06	<8.31E-09	<4.02E-09	2.9E-05	4.43E-07	1.15E-07	3.41E-07	1.43E-07
8476-8480′ ave.	1.14E-05	<4.75E-08	<2.29E-08	1.64E-04	2.54E-06	7.19E-07	2.14E-06	8.50E-07
10,514′A	6.19E-07	<3.93E-09	<1.9E-09	1.11E-05	4.8E-08	4.88E-08	1.38E-07	6.95E-08
10,514′B	2.39E-07	<4.86E-10	<2.35E-10	1.62E-06	8.08E-09	8.71E-09	4.22E-08	1.07E-08
10514.0′ ave.	3.71E-06	<1.91E-08	<9.21E-09	5.49E-05	2.42E-07	2.48E-07	7.80E-07	3.46E-07
10,666′A	3.73E-07	<1.81E-09	<8.72E-10	2.94E-06	5.19E-07	4.61E-08	3.2E-07	5.05E-08
10,666′B	7.79E-07	<3.19E-09	<1.54E-09	7.75E-06	1.16E-06	7.71E-08	5.66E-07	1.35E-07
10666.0′ ave.	4.98E-06	<2.16E-08	<1.04E-08	4.62E-05	7.23E-06	5.32E-07	3.83E-06	8.01E-07
11,061′A	1.81E-06	<2.04E-08	2.96E-08	5E-05	2.72E-07	3.24E-07	1.03E-06	1.4E-07
11,061′B	3.23E-07	<8.51E-10	<4.11E-10	3.24E-06	1.04E-08	2.06E-08	7.79E-08	6.27E-09
11061.0′ ave.	9.19E-06	<9.19E-08	<1.30E-07	2.30E-04	1.22E-06	1.49E-06	4.79E-06	6.34E-07

Table D. 14 The molal concentration (mole/kg.) of leachate solutions collected from MCR igneous rocks samples after HTP corrosion testing.

Molal	Si	Al	Fe	Ca	Mg	K	Na	Mn
GHB-1	1.87E-03	<3.71E-06	<1.79E-06	5.60E-03	7.55E-03	3.58E-05	1.04E-03	3.28E-05
GHC-1	4.42E-03	<3.71E-06	<1.79E-06	7.20E-03	2.74E-03	1.79E-05	8.48E-04	2.18E-05
GHB-2	1.57E-03	<3.71E-06	<1.79E-06	3.08E-03	4.17E-03	2.81E-05	8.53E-04	9.10E-06
GHC-2	4.45E-03	<3.71E-06	<1.79E-06	6.96E-03	2.76E-03	1.28E-05	6.26E-04	3.28E-05
DUL-1	3.21E-03	<3.71E-06	<1.79E-06	9.83E-04	7.90E-03	9.97E-05	3.13E-04	7.28E-06
DUL-2	2.66E-03	<3.71E-06	<1.79E-06	9.53E-04	5.54E-03	1.20E-04	2.91E-04	7.28E-06

Table D. 15 Surface area normalized release results from solutions collected from MCR igneous rocks samples after opining the HPT vessels. Values in mol/cm2.d.

$Mol/m^2.s$	Si	Al	Fe	Ca	Mg	K	Na	Mn
GHB-1	2.13E-07	<4.21E-10	<2.04E-10	6.37E-07	8.59E-07	4.07E-09	1.19E-07	3.72E-09
GHC-1	9.08E-07	<7.62E-10	<3.68E-10	1.48E-06	5.64E-07	3.68E-09	1.74E-07	4.49E-09
GHB-2	1.78E-07	<4.19E-10	<2.02E-10	3.48E-07	4.71E-07	3.18E-09	9.63E-08	1.03E-09
GHC-2	9.77E-07	<8.14E-10	<3.93E-10	1.53E-06	6.05E-07	2.81E-09	1.38E-07	7.19E-09
DUL-1	1.09E-06	<1.26E-09	<6.07E-10	3.33E-07	2.68E-06	3.38E-08	1.06E-07	2.47E-09
DUL-2	9.19E-07	<1.28E-09	<6.18E-10	3.29E-07	1.91E-06	4.15E-08	1.01E-07	2.51E-09

Table D. 16 ICP-OES results from solution collected after opining the HPT vessels for (POT4). Values are in ppm (mg/kg.). The accuracy range is between 0.91 ppm and 1.12 for a 1 ppm concentration standard.

Sample ID	Time (hours)	Si	Fe	Ca	Mg	K	Na	Mn	Al
T1	48	21.16	<0.1	166.22	30.36	6.97	0.63	1.24	<0.1
T2	48	24.24	<0.1	71.79	17.33	7.60	0.71	1.90	<0.1
T3	48	17.97	<0.1	177.57	27.07	7.09	0.61	1.18	<0.1
T4	194	37.85	<0.1	188.67	37.55	6.04	<0.1	2.69	<0.1
T5	288	33.25	<0.1	151.67	42.35	8.56	0.18	<0.1	<0.1
T6	336	38.43	<0.1	111.70	49.24	9.61	1.41	0.15	<0.1
T7	336	39.04	<0.1	101.50	52.85	8.47	0.78	<0.1	<0.1
T8	336	29.87	<0.1	87.66	43.53	7.99	0.75	<0.1	<0.1
T9	432	35.46	<0.1	202.52	50.78	9.40	1.03	<0.1	<0.1
T10	432	35.46	<0.1	217.25	53.79	10.49	1.11	<0.1	<0.1
T11	488	44.75	<0.1	139.36	50.46	9.07	0.95	1.08	<0.1
T12	675	26.22	<0.1	162.79	35.44	7.30	0.95	<0.1	<0.1
T13	819	45.96	<0.1	129.16	70.89	6.31	1.14	<0.1	<0.1
T14	1175	53.46	<0.1	93.10	74.78	8.05	0.98	0.10	<0.1
T15	1367	42.06	<0.1	154.42	70.60	9.76	1.69	<0.1	<0.1
T16	5913	46.25	<0.1	357.41	138.76	11.95	3.63	4.05	<0.1
Blank1	95	<0.1	<0.1	<0.1	<0.1	<0.1	<0.1	<0.1	<0.1
Blank2	627	0.22	<0.1	<0.1	<0.1	<0.1	<0.1	<0.1	<0.1
Blank3	915	0.11	<0.1	<0.1	<0.1	<0.1	<0.1	<0.1	<0.1
Crushed	2112	58.02	<0.1	201.41	128.96	8.03	2.65	4.63	<0.1
Mounted	4343	40.32	<0.1	347.52	237.55	32.92	5.46	2.62	<0.1
At 50°C	69	7.45	0.14	35.15	9.85	3.79	0.84	1.12	<0.1
At 50°C	236	18.40	<0.1	109.11	22.90	3.00	1.03	2.76	<0.1
At 50°C	833	30.34	<0.1	145.41	30.04	3.00	1.00	3.61	<0.1

Table D. 17 The saturation indices ($SI_{mineral}$) of the leachate solutions of Oronto Group samples collected from the Keweenawan Peninsula (KEW), Potato River (POT), Copper Falls State Park (CFSP), and the Units C and D of the Eischied#1 well. The negative values represent the undersaturation state of the mineral and the positive values represent the supersaturation state of the mineral.

	Aragonite ($CaCO_3$)	Calcite ($CaCO_3$)	Dolomite [$CaMg(CO_3)_2$]	Rhodochrosite ($MnCO_3$)	Siderite ($FeCO_3$)	Quartz (SiO_2)	Chalcedony (SiO_2)	Chrysotile ($Mg_3Si_2O_5(OH)_4$)	Sepiolite ($Mg_2Si3O_{7.5}OH:3H_2O$)	Talc ($Mg_3Si_4O_{10}(OH)_2$)	Hausmannite (Mn_3O_4)	Manganite (MnOOH)	Pyrochroite ($Mn(OH)_2$)	Pyrolusite ($MnO2:H_2O$)	Hematite (Fe_2O_3)	Goethite (FeOOH)
KEW1-1	0.9	1.0	1.1	0.9	-	-0.2	-0.4	-7.2	-7.7	-3.7	6.5	-1.7	-8.2	7.4	-	-
KEW4-2	1.1	1.2	2.1	0.6	-	0.2	0.0	-4.0	-4.9	0.3	5.8	-1.9	-8.4	7.2	-	-
KEW5-1	1.2	1.3	2.2	0.6	-	0.3	0.0	-4.0	-4.8	0.4	5.9	-1.9	-8.4	7.2	-	-
POT8-2	-0.2	-0.1	-1.1	-0.2	-	0.6	0.4	-8.6	-7.4	-3.5	3.3	-2.8	-9.3	6.3	-	-
CFSP4	0.2	0.4	0.6	0.8	-	0.5	0.3	-5.2	-5.2	-0.2	6.2	-1.8	-8.3	7.3	-	-
POT2	0.7	0.8	1.3	-1.1	-	0.2	0.0	-5.0	-5.5	-0.6	0.7	-3.6	-10.1	5.5	-	-
POT4	0.0	0.1	0.1	0.9	-	0.5	0.2	-6.2	-5.9	-1.3	6.5	-1.7	-8.2	7.4	-	-
POT5-1	0.9	1.0	1.5	-1.0	-	0.1	-0.1	-5.1	-5.8	-1.0	0.9	-3.6	-10.0	5.6	-	-
C2-1	0.0	0.1	-0.4	-1.4	-8.2	-0.2	-0.4	-8.8	-8.7	-5.2	-0.4	-4.0	-10.5	5.1	14.0	5.9
C2-2	0.2	0.3	-0.7	-0.3	-8.1	0.0	-0.2	-9.9	-9.2	-5.9	3.1	-2.9	-9.3	6.3	14.1	5.9
C2-3	-1.6	-1.4	-2.8	-0.9	-9.8	0.0	-0.2	-10.9	-9.8	-7.0	1.1	-3.5	-10.0	5.6	15.1	6.4
C2-5	-0.5	-0.4	-1.6	-0.8	-8.3	-0.6	-0.8	-11.7	-11.4	-8.9	1.6	-3.3	-9.8	5.8	13.8	5.8
SF1-1	-0.4	-0.3	-1.0	-0.4	-	0.0	-0.2	-9.9	-9.2	-6.0	2.0	-3.2	-9.7	5.9	-	-
SF1-2	-0.7	-0.6	-1.6	-1.1	-	-0.1	-0.3	-10.8	-9.9	-7.0	-0.1	-3.9	-10.3	5.2	-	-
SF3-2	-0.6	-0.4	-1.5	-1.3	-	-0.2	-0.4	-10.6	-9.9	-7.0	0.1	-3.8	-10.3	5.3	-	-
SH1	-1.3	-1.2	-2.3	-0.8	-	-0.1	-0.3	-10.7	-9.8	-6.9	1.4	-3.4	-9.9	5.7	-	-
SH2	-1.4	-1.3	-2.6	-0.7	-	-0.1	-0.3	-11.0	-10.0	-7.2	1.6	-3.3	-9.8	0.8	-	-
D4-1	0.4	0.5	-0.1	0.3	-8.1	0.2	0.0	-8.5	-7.9	-4.1	5.0	-2.2	-8.7	6.9	14.2	6.0
D4-2	0.5	0.6	-0.3	0.3	-8.1	-0.1	-0.3	-9.8	-9.2	-6.0	4.9	-2.2	-8.7	6.9	14.2	6.0

Table D. 18 The saturation indices (SImineral) of the leachate solutions of Bayfield Group samples collected from the Bayfield Peninsula (BAY), L'Anse area (L'ANSE), Agate Falls (AG), and the Unit E of the Eischied#1 well. The negative values represent the undersaturation state of the mineral and the positive values represent the supersaturation state of the mineral.

	Aragonite ($CaCO_3$)	Calcite ($CaCO_3$)	Dolomite [$CaMg(CO_3)_2$]	Rhodochrosite ($MnCO_3$)	Siderite ($FeCO_3$)	Quartz (SiO_2)	K-feldspar ($KAlSi_3O_8$)	Albite ($NaAlSi_3O_8$)	Anorthite ($CaAl_2Si_2O_8$)	Chalcedony (SiO_2)	Chrysotile ($Mg_3Si_2O_5(OH)_4$)	Sepiolite ($Mg_2Si_3O_{7.5}OH{\cdot}3H_2O$)	Talc ($Mg_3Si_4O_{10}(OH)_2$)	Hausmannite (Mn_3O_4)	Manganite (MnOOH)	Pyrochroite ($Mn(OH)_2$)	Pyrolusite ($MnO_2{\cdot}H_2O$)	Hematite (Fe_2O_3)	Goethite (FeOOH)
BAY3(-Al)	-3.1	-3.0	-5.1	-0.6	-6.5	-0.2	-	-	-	-0.4	-13	-12	-9.8	2.1	-3.2	-9.6	5.95	17.3	7.5
L'ANSE1	-2.6	-2.5	-4.2	-1.5	-6.2	0.2	-	-	-	-0	-12	-10	-7.5	-0.5	-4	-10	5.1	17.8	7.8
E2-2	0.5	0.6	-0.6	-0.5	-	0.1	-	-	-	-0.1	-10	-9.4	-6.4	2.5	-3	-9.5	6.1	-	-
E2-3	-2.6	-2.5	-5.9	-1.8	-8.5	-0.4	-	-	-	-0.6	-18	-15	-15	-1.5	-4.4	-11	4.7	13.5	5.6
E2-4	-1.6	-1.5	-4.0	-1.0	-	0.1	-2.4	-4.1	-2.8	-0.2	-14	-12	-10	1.1	-3.5	-10	5.6	-	-
AG-1	-2.2	-2.1	-4.3	-1.2	-7.5	-0.1	-1.8	-4.7	-2.2	-0.4	-14	-12	-10	0.2	-3.8	-10	5.3	15.4	6.5
AG-2	-2.4	-2.3	-4.7	-1.6	-8.8	-0.2	-3.5	-6.4	-5.2	-0.5	-15	-13	-11	-0.9	-4.2	-11	4.9	12.7	5.2

Table D. 18 The saturation indices (SImineral) of the leachate solutions of Bayfield Group samples collected from the Bayfield Peninsula (BAY), L'Anse area (L'ANSE), Agate Falls (AG), and the Unit E of the Eischied#1 well. The negative values represent the undersaturation state of the mineral and the positive values represent the supersaturation state of the mineral. (Cont.)

	Chlorite(14A) ($Mg_5Al_2Si_3O_{10}(OH)_8$)	Ca-Montmorillonite [$Ca_{0.16}Al_{2.3}Si_{3.6}O_{10}(OH)_2$]	Gibbsite ($Al(OH)_3$)	Illite $K_{0.6}Mg_{0.2}Al_{2.3}Si_{3.5}O_{10}(OH)_2$	Kaolinite ($Al_2Si_2O_5(OH)_4$)	K-mica ($KAl_3Si_3O_{10}(OH)_2$)
BAY3(-Al)	-	-	-	-	-	-
L'ANSE1	-	-	-	-	-	-
E2-2	-	-	-	-	-	-
E2-3	-	-	-	-	-	-
E2-4	-16	1.0	1.2	-0.6	3.74	6.1
AG-1	-14	3.0	2.1	1.0	5.06	8.4
AG-2	-18	-0.4	0.8	-2.5	2.26	4.1

Table D. 19 The saturation indices ($SI_{mineral}$) of the leachate solutions of samples collected from the Texaco Poersch #1 well. The negative values represent the undersaturation state of the mineral and the positive values represent the supersaturation state of the mineral.

.	Aragonite ($CaCO_3$)	Calcite ($CaCO_3$)	Dolomite [$CaMg(CO_3)_2$]	Rhodochrosite ($MnCO_3$)	Siderite ($FeCO_3$)	Quartz (SiO_2)	Chalcedony (SiO_2)	K-feldspar ($KAlSi_3O_8$)	Albite ($NaAlSi_3O_8$)	Anorthite ($CaAl_2Si_2O_8$)	Chrysotile ($Mg_3Si_2O_5(OH)_4$)	Sepiolite ($Mg_2Si3O_{7.5}OH:3H_2O$)	Talc ($Mg_3Si_4O_{10}(OH)_2$)	Hausmannite (Mn_3O_4)	Manganite (MnOOH)
5,397.3′ A	-0.5	-0.4	0.3	-1.2	-	0.1	-0.2	-	-	-	-5.2	-5.9	-1.1	0.1	-3.8
5,404' A	-0.7	-0.6	-1.2	-0.4	-	0.1	-0.2	-1.7	-3.0	-1.8	-8.8	-8.3	-4.7	2.6	-3.0
8,051.1′ A	0.5	0.6	-0.8	0.2	-	0.3	0.0	-	-	-	-10.8	-9.4	-6.4	4.5	-2.4
8,476′-8,480′ A	0.5	0.6	-0.5	0.3	-	-0.1	-0.3	-	-	-	-10.5	-9.7	-6.7	4.9	-2.2
10,514′ A	0.3	0.4	-1.5	0.2	-	-0.4	-0.6	-	-	-	-13.5	-12.3	-10.4	4.5	-2.4
10,666′ A	-0.2	-0.1	-0.8	0.2	-	-0.3	-0.5	-	-	-	-9.9	-9.7	-6.6	4.4	-2.4
11,061′ A	0.2	0.3	-1.7	-0.3	-7.7	-0.7	-0.9	-	-	-	-14.1	-13.1	-11.5	3.1	-2.8
5,397.3′ B	-0.2	0.0	0.1	0.2	-	0.0	-0.2	-	-	-	-6.6	-6.9	-2.6	4.3	-2.4
8,051.1′ B	0.1	0.2	-1.7	0.1	-	-0.6	-0.8	-	-	-	-13.6	-12.6	-10.8	3.6	-2.7
8,476′-8,480′ B	0.5	0.6	-0.5	0.3	-	-0.3	-0.5	-	-	-	-11.1	-10.4	-7.8	4.6	-2.3
10,514′ B	0.5	0.6	-1.1	0.4	-	0.1	-0.1	-	-	-	-11.9	-10.4	-7.8	4.9	-2.2
10,666′ B	0.2	0.3	-0.1	0.6	-	-0.2	-0.4	-	-	-	-8.8	-8.8	-5.3	5.5	-2.0
11,061′ B	0.6	0.7	-1.0	0.0	-	0.0	-0.2	-	-	-	-12.1	-10.7	-8.2	3.8	-2.6

Table D. 19 The saturation indices (SImineral) of the leachate solutions of samples collected from the Texaco Poersch #1 well. The negative values represent the undersaturation state of the mineral and the positive values represent the supersaturation state of the mineral (cont.)

.	Pyrochroite ($Mn(OH)_2$)	Pyrolusite ($MnO2:H_2O$)	Hematite (Fe_2O_3)	Goethite ($FeOOH$)	Chlorite(14A) ($Mg_5Al_2Si_3O_{10}(OH)_8$)	Ca-Montmorillonite $[Ca_{0.16}Al_{2.3}Si_{3.6}O_{10}(OH)_2]$	Gibbsite ($Al(OH)_3$)	Illite $K_{0.6}Mg_{0.2}Al_{2.3}Si_{3.5}O_{10}(OH$	Kaolinite ($Al_2Si_2O_5(OH)_4$)	K-mica ($KAl_3Si_3O_{10}(OH)_2$)
5,397.3′ A	-10.3	5.3	-	-	-	-	-	-	-	-
5,404' A	-9.5	6.1	-	-	-6.7	2.1	1.3	0.5	3.9	6.9
8,051.1′ A	-8.8	6.8	-	-	-	-	-	-	-	-
8,476′-8,480′ A	-8.7	6.9	-	-	-	-	-	-	-	-
10,514′ A	-8.9	6.7	-	-	-	-	-	-	-	-
10,666′ A	-8.9	6.7	-	-	-	-	-	-	-	-
11,061′ A	-9.3	6.3	14.9	6.4	-	-	-	-	-	-
5,397.3′ B	-8.9	6.7	-	-	-	-	-	-	-	-
8,051.1′ B	-9.2	6.4	-	-	-	-	-	-	-	-
8,476′-8,480′ B	-8.8	6.8	-	-	-	-	-	-	-	-
10,514′ B	-8.7	6.9	-	-	-	-	-	-	-	-
10,666′ B	-8.5	7.1	-	-	-	-	-	-	-	-
11,061′ B	-9.1	6.5	-	-	-	-	-	-	-	-

Table D. 20 The saturation indices ($SI_{mineral}$) of the leachate solutions of of MCR igneous rocks samples collected from Silver Bay (Beaver Bay Complex; BEV), Ely city area (Duluth complex; DUL), and Good Harbor Bay (North Shore Volcanic Group; GHB and GHC). The negative values represent the undersaturation state of the mineral and the positive values represent the supersaturation state of the mineral.

	Aragonite ($CaCO_3$)	Calcite ($CaCO_3$)	Dolomite [$CaMg(CO_3)_2$]	Rhodochrosite ($MnCO_3$)	Siderite ($FeCO_3$)	Quartz (SiO_2)	Chalcedony (SiO_2)	Chrysotile ($Mg_3Si_2O_5(OH)_4$)	Sepiolite ($Mg_2Si3O_{7.5}OH:3H_2O$)	Talc ($Mg_3Si_4O_{10}(OH)_2$)	Hausmannite (Mn_3O_4)	Manganite (MnOOH)	Pyrochroite ($Mn(OH)_2$)	Pyrolusite ($MnO2:H_2O$)	Hematite (Fe_2O_3)	Goethite (FeOOH)
BEV1	-2.8	-2.7	-5.5	-	-8.4	-0.2	-0.4	-15.6	-13.4	-12.1	-	-	-	-	13.7	5.7
DUL-1	-0.8	-0.7	-0.5	-0.8	-	0.3	0.1	-5.5	-5.7	-0.9	1.4	-3.4	-9.9	5.7	-	-
DUL-2	-1.0	-0.9	-1.0	-1.0	-	0.3	0.0	-6.7	-6.6	-2.3	1.0	-3.5	-10.0	5.6	-	-
GHB-1	0.1	0.2	0.7	0.0	-	0.1	-0.1	-5.7	-6.2	-1.5	3.6	-2.7	-9.1	6.5	-	-
GHB-2	-0.5	-0.4	-0.5	-0.9	-	0.0	-0.2	-7.5	-7.6	-3.6	1.2	-3.5	-9.9	5.7	-	-
GHC-1	0.1	0.2	0.1	-0.3	-	0.5	0.3	-6.5	-6.2	-1.7	2.9	-2.9	-9.4	6.2	-	-
GHC-2	0.1	0.2	0.1	-0.1	-	0.5	0.3	-6.5	-6.1	-1.6	3.5	-2.7	-9.2	6.4	-	-

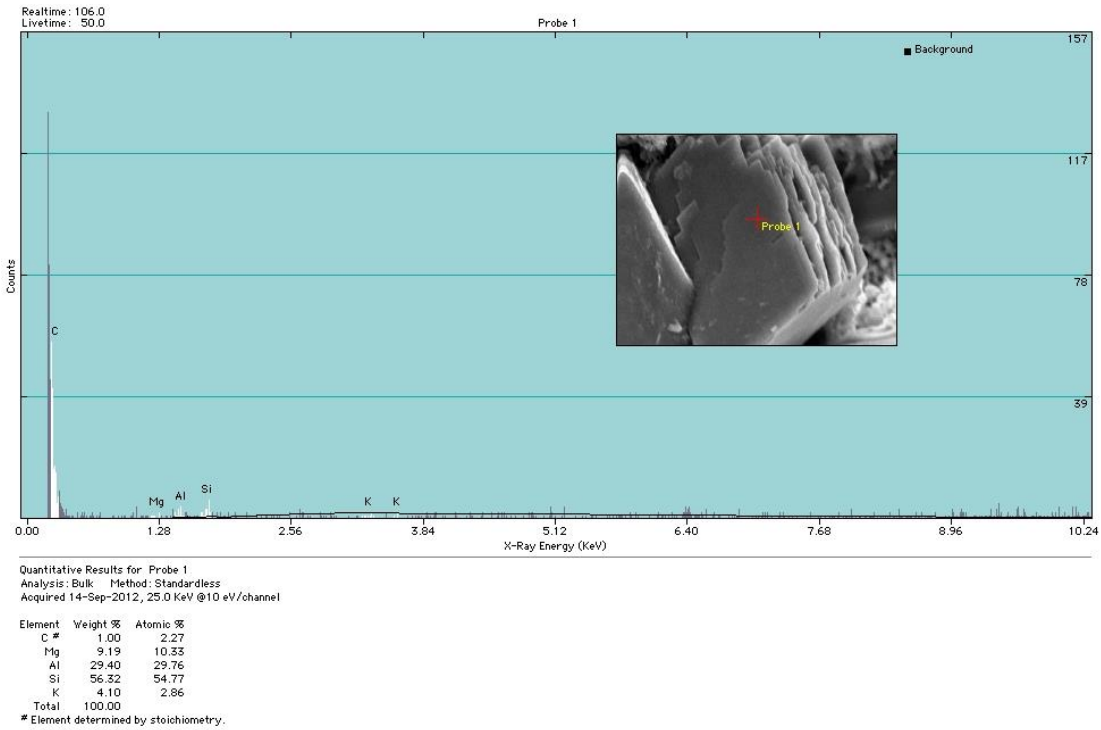

Figure D. 1 Energy dispersive spectra (EDS) of Nonesuch POT4 sample. The red cross indicates position of the focused electron beam during generation of the EDS specrum.

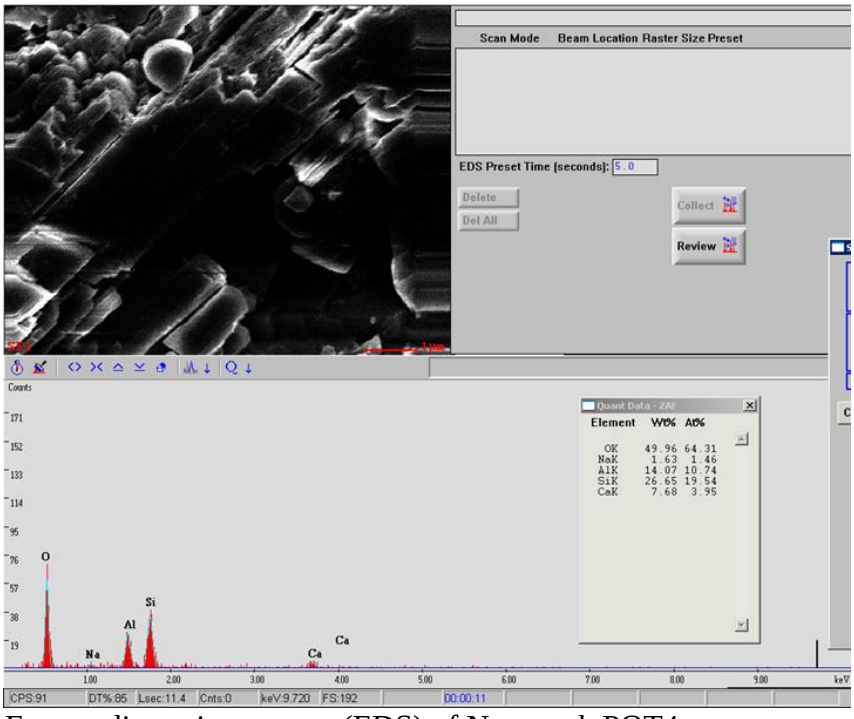

Figure D. 2 Energy dispersive spectra (EDS) of Nonesuch POT4.

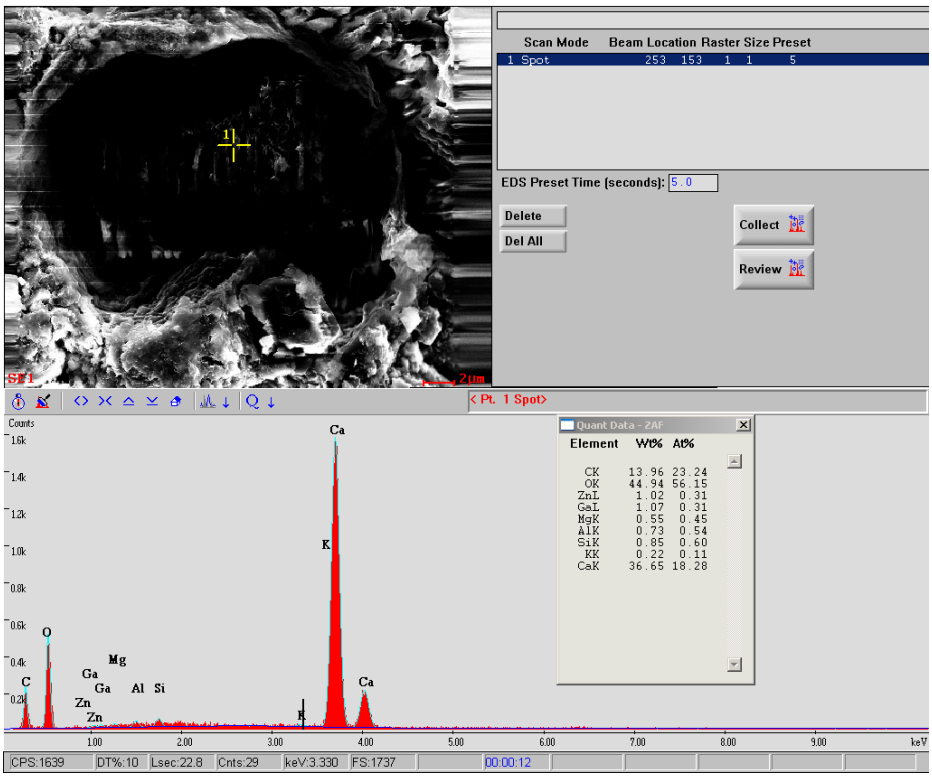

Figure D. 3 Energy dispersive spectra (EDS) of CHC (KEW1-1) sample.

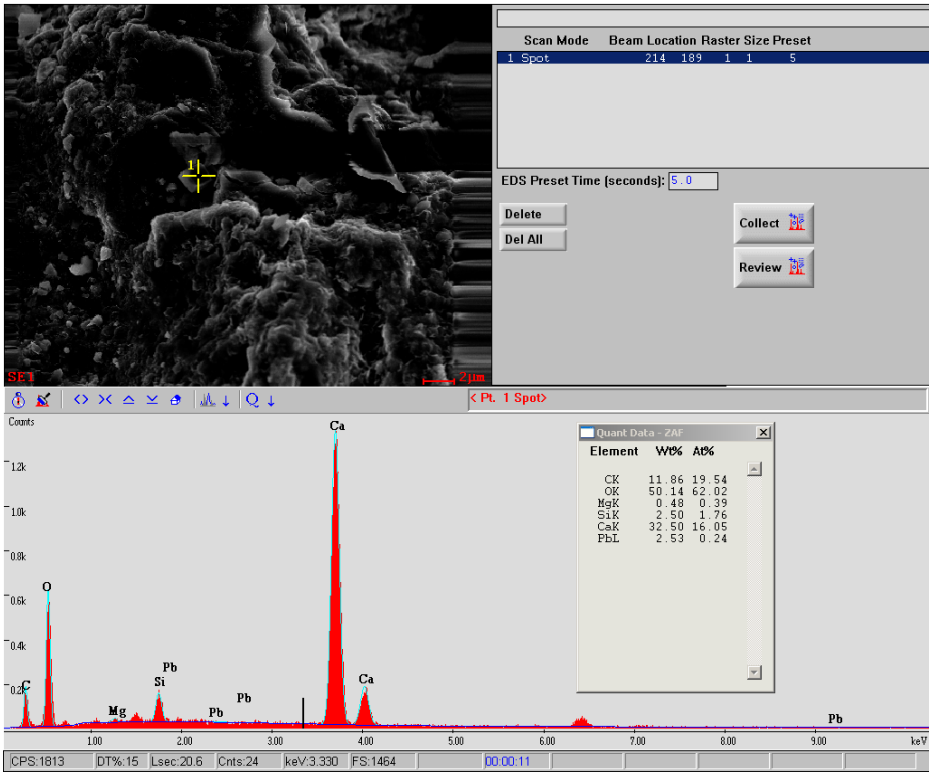

Figure D. 4 Energy dispersive spectra (EDS) of Nonesuch (KEW5-1) sample

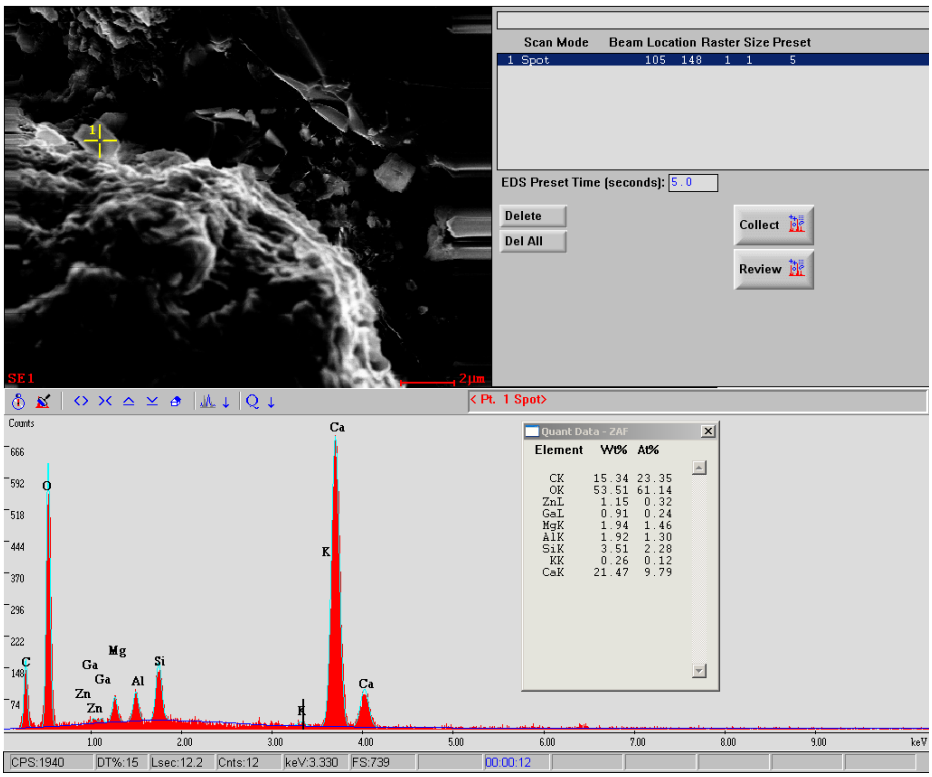

Figure D. 5 Energy dispersive spectra (EDS) of Nonesuch (KEW5-1) sample

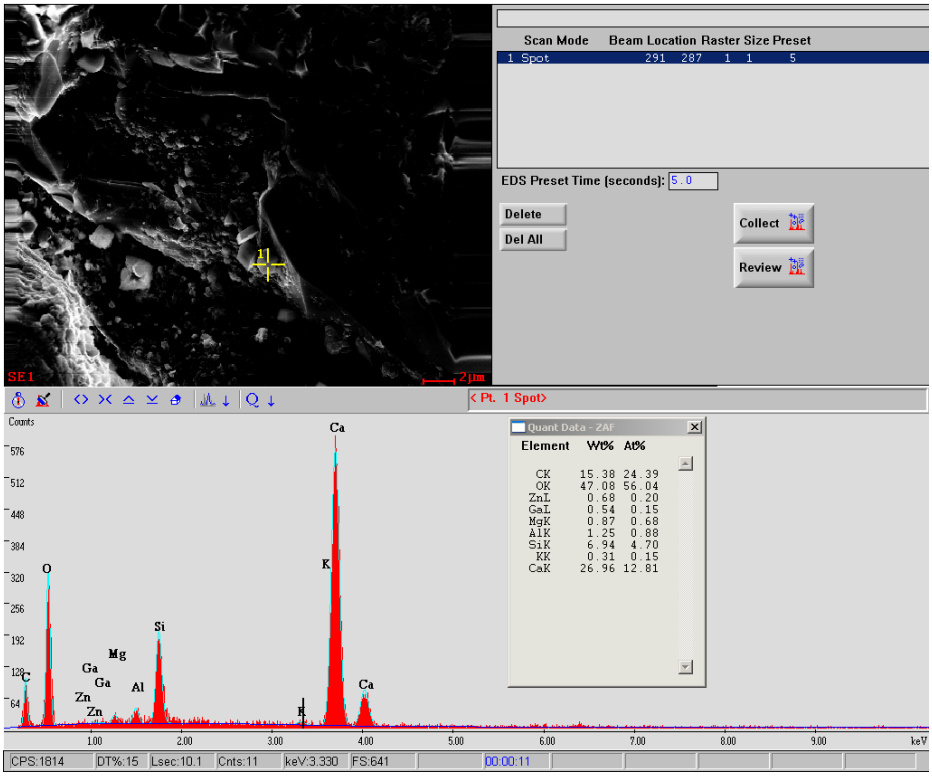

Figure D. 6 Energy dispersive spectra (EDS) of Nonesuch (KEW5-1) sample

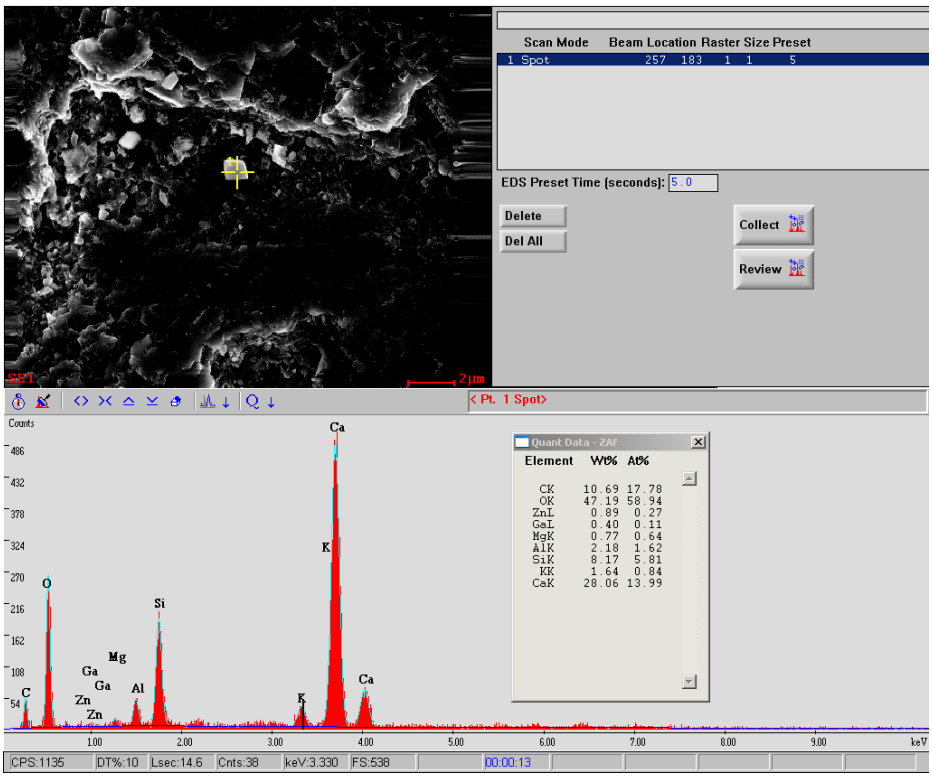

Figure D. 7 Energy dispersive spectra (EDS) of Nonesuch (KEW1-1) sample

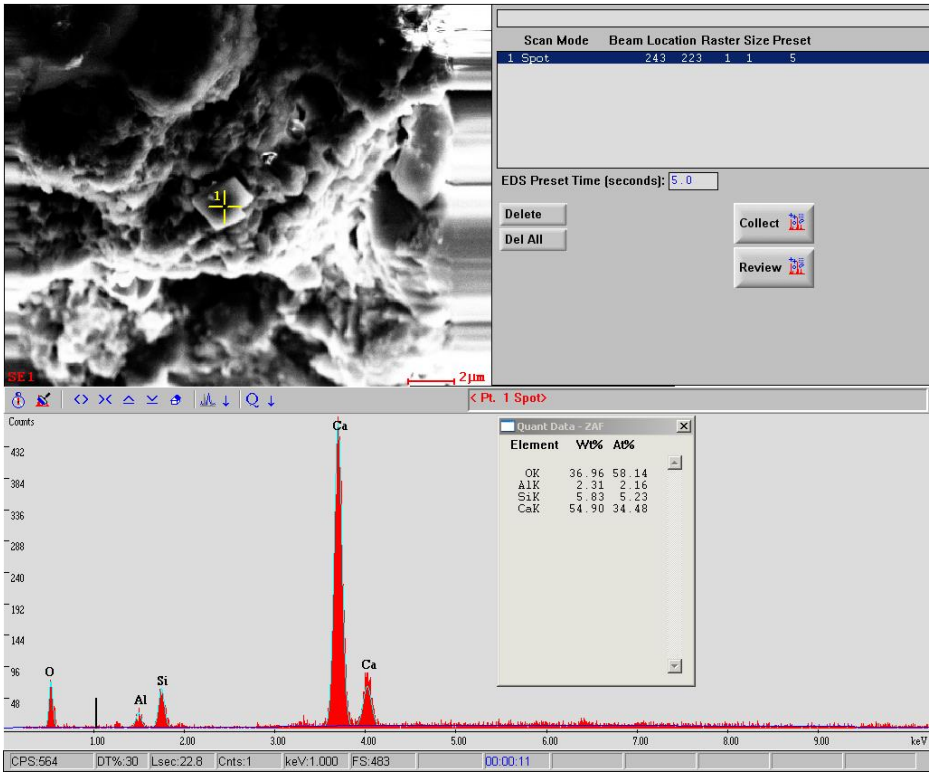

Figure D. 8 Energy dispersive spectra (EDS) of Nonesuch (KEW1-1) sample

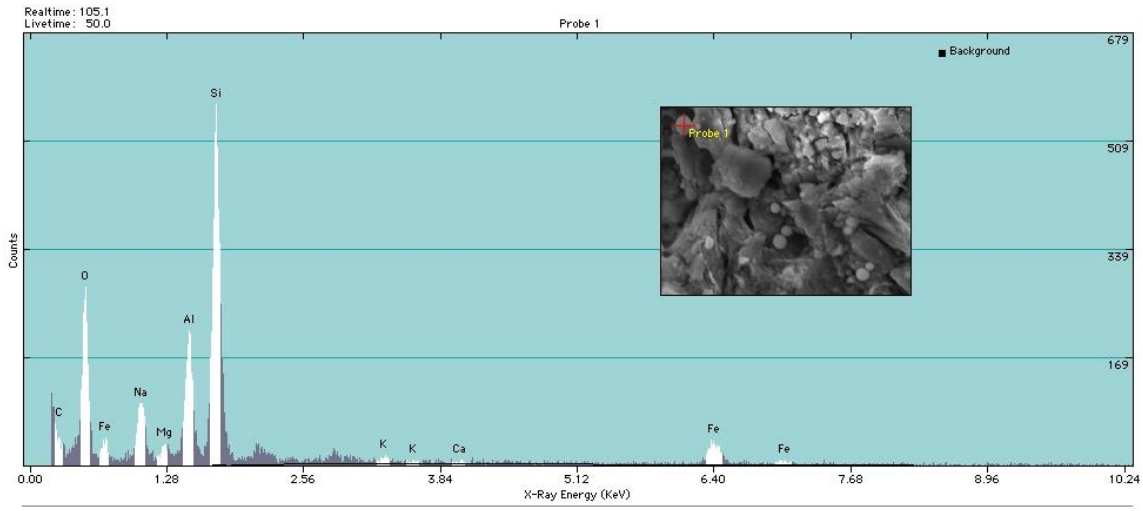

Quantitative Results for Probe 1
Analysis: Bulk Method: Standardless
Acquired 14-Sep-2012, 25.0 KeV @10 eV/channel

Element	Weight %	Atomic %
B	10.93	19.62
C #	1.00	1.62
O	33.62	40.79
Na	8.82	7.45
Mg	1.27	1.01
Al	10.92	7.86
Si	28.96	20.02
K	0.53	0.27
Ca	0.01	0.01
Fe	3.93	1.37
Total	100.00	

Element determined by stoichiometry.

Figure D. 9 Energy dispersive spectra (EDS) of Nonesuch (POT4) sample

BIBLIOGRAPHY

Anderson, R.R., 1990, Review of the Precambrian geology history of the central United States and the Midcontinent Rift system: *in* The Amoco M.G. Eischeid #1 deep petroleum test Carroll County, Iowa, Preliminary Investigations, Special Report Series #2, R.R. Anderson (ed.), Iowa Department of Natural Resources, p. 1-25.

Anderson, R. R., 1992, *The Midcontinent Rift of Iowa: University of Iowa*, Ph.D. dissertation, 324 pp.

Anderson, R. R., 1997, Keweenawan Supergroup clastic rocks in the Midcontinent Rift of Iowa: *in* Middle Proterozoic to Cambrian Rifting, Central North America, Ojakangas, R.W., Dickas, A.B., Green, J.C. (Eds.), Geological Socciaty of America Special Papers., v. 312, p. 211 –230.

Arnorsson, S.N.A. and Stefansson, A.S., 1999, Assessment of feldspar solubility constants in water in the range 0 to 350°C at vapor saturation pressures: *American Journal of Science*, v. 299, p. 173-209.

Bachu, S., 2000, Sequestration of CO_2 in geological media: criteria and approach for site selection in response to climate change: *Energy Conversion and Management*, v. 41, no. 9, p. 953-970.

Bachu, 2002, Sequestration of CO_2 in geological media in response to climate change: road map for site selection using the transform of the geological space into the CO_2 phase space: *Energy Conversion and Management*, v. 43, no. 1, p. 87-102.

Bachu, S., & Bennion, B., 2008, Effects of in-situ conditions on relative permeability characteristics of CO_2-brine systems. *Environmental Geology*, *54*(8), 1707-1722.

Bachu, S., Gunter, W., and Perkins, E., 1994, Aquifer disposal of CO_2: Hydrodynamic and mineral trapping: *Energy Conversion and Management*, v. 35, no. 4, p. 269-279.

Barnes, D. A., Bacon, D. H., & Kelley, S. R., 2009, Geological sequestration of carbon dioxide in the Cambrian Mount Simon Sandstone: Regional storage capacity, site characterization, and large-scale injection feasibility, Michigan Basin. *Environmental Geosciences*, *16*(3), 163-183.

Behrend, J., Green, A., Cannon, W., Hutchinson, D., Lee, M., Milkereit, B., Agena, W., and Spencer, C., 1988, Crustal structure of the Midcontinent rift system: Results from GLIMPCE deep seismic reflection profiles: *Geology*, v. 16, no. 1, p. 81-85.

Bénézeth, P., Palmer, D. A., Anovitz, L. M., and Horita, J., 2007, Dawsonite synthesis and reevaluation of its thermodynamic properties from solubility measurements: Implications for mineral trapping of CO_2: *Geochimica et Cosmochimica Acta*, v. 71, no. 18, p. 4438-4455.

Bennett, P. C., 1991, Quartz dissolution in organic-rich aqueous systems: *Geochimica et Cosmochimica Acta*, v. 55, no. 7, p. 1781-1797.

Berendsen, P., M. Borcherding, R. M., Doveton, J., Gerhard, L., Newell, K. D., Steeples, D., and Watney, W. L., 1988, Texaco Poersch #1, Washington County, Kansas-Preliminary geologic report of the pre-Phanerozoic rocks: Kansas Geological Survey, Open-file Report 88-22.

Berman, R. G., 1988, Internally-consistent thermodynamic data for minerals in the system Na_2O-K_2O-CaO-MgO-FeO-Fe_2O_3-Al_2O_3-SiO_2-TiO_2-H_2O-CO_2: *Journal of Petrology*, v. 29, no. 2, p. 445-522.

Berner, R., 1975, The role of magnesium in the crystal growth of calcite and aragonite from sea water: *Geochimica et Cosmochimica Acta*, v. 39, no. 4, p. 489-504.

Berner, R. A., 2003, The long-term carbon cycle, fossil fuels and atmospheric composition: *Nature*, v. 426, no. 6964, p. 323-326.

Berner, R. A., and Lasaga, A. C., 1983, The carbonate-silicate geochemical cycle and its effect on atmospheric carbon dioxide over the past 100 million years: *American Journal of Science*, v. 283, no. 7, p. 641-683.

Berner, R. A., and Morse, J. W., 1974, Dissolution kinetics of calcium carbonate in sea water; IV, Theory of calcite dissolution: *American Journal of Science*, v. 274, no. 2, p. 108-134.

Boggild, O. B., 1930, The shell structure of the mollusks: Det Kongelige Danske Videnskabernes Selskabs Skrifter: *Natruvidenskabelig og Mathematisk*, Afdeling, Ser. 9, v. 2, p. 231-326.

Bornhorst, T. J., 1997, Tectonic context of native copper deposits of the North American Midcontinent Rift System: *in* Middle Proterozoic to Cambrian Rifting, Central North America, Ojakangas, R.W., Dickas, A.B., Green, J.C. (Eds.), Geological Sociaty of America Special Papers., v. 312, p. 127-136.

Bornhorst, T. J., Paces, J. B., Grant, N. K., Obradovich, J. D., and Huber, N. K., 1988, Age of native copper mineralization, Keweenaw Peninsula, Michigan: *Economic Geology*, v. 83, no. 3, p. 619-625.

Brannon, J. C., 1984, *Geochemistry of successive lava flows of the Keweenawan North Shore Volcanic Group*: Washington University St Louis, MO, Ph.D. Dissertation, 312 pp.

Buchanan, R., and McCauley, J., 1987, *Roadside Kansas: A Traveller's Guide to Its Geology and Landmarks*: Kansas Geological Survey, 376 pp.

Bush, P., 1973, Some aspects of the diagenetic history of the sabkha in Abu Dhabi: *in* The Persian Gulf, Holocene Carbonate Sedimentation and Diagenesis in a Shallow Epicontinental Sea, Bruce H. Purser (ed.), Springer, p. 395-407.

Cannon, W., Peterman, Z., and Sims, P., 1993, Crustal-scale thrusting and origin of the Montreal River monocline-A 35-km-thick cross section of the midcontinent rift in northern Michigan and Wisconsin: *Tectonics*, v. 12, no. 3, p. 728-744.

Cannon, W. F., 1994, Closing of the Midcontinent rift-A far—field effect of Grenvillian compression: *Geology*, v. 22, no. 2, p. 155-158.

Cannon, W. F., and Hinze, W. J., 1992, Speculations on the origin of the North American Midcontinent rift: *Tectonophysics*, v. 213, no. 1, p. 49-55.

Cannon, W. F., and Nicholson, S. W., 1992, *Revisions of stratigraphic nomenclature within the Keweenawan Supergroup of northern Michigan*: U.S. Geological Survey, Bulletin 1970A, 21 pp.

Craddock, C., 1972, Late Precambrian regional geologic setting: Geology of Minnesota: a centennial volume: Minnesota Geological Survey, p. 281-291.

Crane, W. R., 1929, Mining methods and practice in the Michigan copper mines: *US Bureau of Mines bulletin*, v. 306, p.3.

Daniels, P. A., 1982, 7C: Upper Precambrian sedimentary rocks: Oronto Group, Michigan- Wisconsin: Geological Society of America Memoirs, v. 156, p. 107-134.

Dickas, A.B. and Mudrey, M.G., 1997, Segmented structure of the middle Proterozoic Midcontinent Rift System, North America, *in* Middle Proterozoic to Cambrian Rifting, Central North America, Ojakangas, R.W., Dickas, A.B., Green, J.C. (Eds.), Geological Socciaty of America Special Papers., v. 312, p. 37-46.

Dickinson, W., 1985, Interpreting Provenance Relations from Detrital Modes of Sandstones: *in* Provenance of Arenites, Zuffa, G. G., (ed.), Volume 148, Springer Netherlands, p. 333-361.

Dickinson, W. R., 1970, Interpreting detrital modes of graywacke and arkose: *Journal of Sedimentary Research,* v. 40, no. 2.

DOE/NETL (U.S. Department of Energy/National Energy Technology Laboratory), 2008, Carbon sequestration atlas of the United States and Canada (Atlas II), online ed.:Morgantown, West Virginia, National Energy Technology Laboratory: http://www.netl.doe.gov/technologies/carbon_seq/refshelf/atlasII/atlasII.pdf(accessed July 16, 2009).

Doughty, C., and Pruess, K., 2004, Modeling Supercritical Carbon Dioxide Injection in Heterogeneous Porous Media: *Vadose Zone Journal*, v. 3, no. 3, p. 837-847.

Dove, P. M., 1999, The dissolution kinetics of quartz in aqueous mixed cation solutions: *Geochimica et Cosmochimica Acta*, v. 63, no. 22, p. 3715-3727.

Dove, P. M., and Crerar, D. A., 1990, Kinetics of quartz dissolution in electrolyte solutions using a hydrothermal mixed flow reactor: *Geochimica et Cosmochimica Acta*, v. 54, no. 4, p. 955-969.

Duan, Z., and Sun, R., 2003, An improved model calculating CO_2 solubility in pure water and aqueous NaCl solutions from 273 to 533 K and from 0 to 2000 bar: *Chemical geology*, v. 193, no. 3, p. 257-271.

Elmore, E., R, J, G., W, S., and H, M., 1989, The Precambrian Nonesuch Formation of the North American Mid-Continent Rift, sedimentology and organic geochemical aspects of lacustrine deposition: *Precambrian Research*, v. 43, no. 3, p. 191-213.

Elmore, R. D., 1984, The Copper Harbor Conglomerate: A late Precambrian fining-upward alluvial fan sequence in northern Michigan: *Geological Society of America Bulletin*, v. 95, no. 5, p. 610-617.

Ennis-King, J. and L. Paterson, 2001, Reservoir engineering issues in the geological disposal of carbon dioxide, *in* Proceedings of the 5th International Conference on Greenhouse Gas Control Technologies (GHGT-5), D. Williams, D. Durie, P. McMullan, C. Paulson and A. Smith (EDS.), 13–16 August 2000, Cairns, Australia, CSIRO Publishing, Collingwood, Victoria, Australia, pp. 290–295.

Ennis-King, J, C.M. Gibson-Poole, S.C. Lang and L. Paterson, 2003: Long term numerical simulation of geological storage of CO_2 in the Petrel sub-basin, North West Australia. *in* Proceedings of the 6th International Conference on Greenhouse Gas Control Technologies (GHGT-6), J. Gale and Y. Kaya (EDS.), 1–4 October2002, Kyoto, Japan, Pergamon, v.I, 507–511.

Ferrante, M. J., Stuve, J., and Richardson, D. W., 1976, Thermodynamic data for synthetic dawsonite: Report of Investigations, v. 8129, 13 pp.

Folk, R. L., Andrews, P. B., & Lewis, D.,1970, Detrital sedimentary rock classification and nomenclature for use in New Zealand: *New Zealand Journal of Geology and Geophysics*, *13*(4), 937-968.

Garrels, R. M., & Mackenzie, F. T.,1967, Origin of the chemical compositions of some springs and lakes, *Equilibrium concepts in natural water systems*, v. 67, p. 222-242.

Giammar, D. E., Bruant Jr, R. G., and Peters, C. A., 2005, Forsterite dissolution and magnesite precipitation at conditions relevant for deep saline aquifer storage and sequestration of carbon dioxide: *Chemical Geology*, v. 217, no. 3, p. 257-276.

Goldich, S. S., 1938, A study in rock-weathering: *The Journal of Geology*, p. 17-58.

Golubev, S. V., and Pokrovsky, O. S., 2006, Experimental study of the effect of organic ligands on diopside dissolution kinetics: *Chemical Geology*, v. 235, no. 3–4, p. 377-389.

Green, J. C., 1982a, 5: Geology of Keweenaw an extrusive rocks: Geological Society of America Memoirs, v. 156, p. 47-56.

Green, J. C., 1982b, Geology of Keweenawan extrusive rocks: Geology and tectonics of the Lake Superior Basin: Geological Society of America Memoir, v. 156, p. 47-55.

Green, J. C., 1983, Geologic and geochemical evidence for the nature and development of the Middle Proterozoic (Keweenawan) Midcontinent Rift of North America: *Tectonophysics*, v. 94, no. 1, p. 413-437.

Gunter, W. D., Perkins, E. H., and McCann, T. J., 1993, Aquifer disposal of CO_2-rich gases: Reaction design for added capacity: *Energy Conversion and Management*, v. 34, no. 9, p. 941-948.

Hamblin, W., 1965, Basement control of Keweenawan and Cambrian sedimentation in Lake Superior region: *AAPG Bulletin*, v. 49, no. 7, p. 950-958.

Hamblin, W. K., and Horner, W. J., 1961, Sources of the Keweenawan conglomerates of northern Michigan: *The Journal of Geology*, p. 204-211.

Hamm, L. M., Bourg, I. C., Wallace, A. F., and Rotenberg, B., 2013, Molecular simulation of CO_2-and CO_3-brine-mineral systems: *Reviews in Mineralogy and Geochemistry*, v. 77, no. 1, p. 189-228.

Hey, M. H., 1963, Appendix to the second edition of an index of mineral species and varieties arranged chemically, Trustees of the British Museum (Natural History).

Hoffman, P. F., 1989, Precambrian geology and tectonic history of North America: *The Geology of North America*, p. 447-512.

Holland, H. D., 1984, The chemical evolution of the atmosphere and oceans, Princeton University Press, 587 pp.

Huijgen, W. J. J., Witkamp, G.-J., and Comans, R. N. J., 2006, Mechanisms of aqueous wollastonite carbonation as a possible CO_2 sequestration process: *Chemical Engineering Science*, v. 61, no. 13, p. 4242-4251.

Kaszuba, J. P., Janecky, D. R., and Snow, M. G., 2005, Experimental evaluation of mixed fluid reactions between supercritical carbon dioxide and NaCl brine: Relevance to the integrity of a geologic carbon repository: *Chemical Geology*, v. 217, no. 3, p. 277-293.

Katz, D. A., Eberli, G. P., Swart, P. K., and Smith, L. B., 2006, Tectonic-hydrothermal brecciation associated with calcite precipitation and permeability destruction in Mississippian carbonate reservoirs, Montana and Wyoming: *AAPG Bulletin*, v. 90, no. 11, p. 1803-1841.

Kim, T. W., Tokunaga, T. K., Shuman, D. B., Sutton, S. R., Newville, M., and Lanzirotti, A., 2012, Thickness measurements of nanoscale brine films on silica surfaces under geologic CO_2 sequestration conditions using synchrotron X-ray fluorescence: *Water Resources Research*, v. 48, no. 9.

King, E. R., and Zietz, I., 1971, Aeromagnetic study of the midcontinent gravity high of central United States: *Geological Society of America Bulletin*, v. 82, no. 8, p. 2187-2208.

Kirste, D. M., Watson, M. N., & Tingate, P. R., 2004, Geochemical modelling of CO_2-water-rock interaction in the Pretty Hill formation, Otway Basin: *in* Eastern Australasian basins symposium II. Special publication, p. 19-22.

Klewin, K. W., 1987, The Petrology and Geochemistry of the Keweenawan Potato River Intrusion, Northern Wisconsin. Northern Illinois University, Ph.D. Dissertation, 376 pp.

Klewin, K. W., and Berg, J. H., 1991, Petrology of the Keweenawan Mamainse Point lavas, Ontario: Petrogenesis and continental rift evolution: *Journal of Geophysical Research*: Solid Earth, v. 96, no. B1, p. 457-474.

Klewin, K. W., and Shirey, S. B., 1992, The igneous petrology and magmatic evolution of the Midcontinent rift system: *Tectonophysics*, v. 213, no. 1, p. 33-40.

Knauss, K. G., Johnson, J. W., and Steefel, C. I., 2005, Evaluation of the impact of CO_2, co-contaminant gas, aqueous fluid and reservoir rock interactions on the geologic sequestration of CO_2: *Chemical geology*, v. 217, no. 3, p. 339-350.

Langmuir, D., 1997, *Aqueous Environmental Geochemistry*: Prentice Hall, New Jersey, 602 pp.

Lasaga, A.C., Soler, J.M., Ganor, J., Burch, T.E., and Nagy, K.L., 1994, Chemical weathering rate laws and global geochemical cycles, *Geochimica et Cosmochimica Acta*, v. 58, p. 2361-2386.

Lemmon, E., McLinden, M., and Friend, D., 2005, Thermophysical properties of fluid systems: *in* NIST Chemistry WebBook, NIST Standard Reference Database Number, P.J. Linstrom and W.G. Mallard, (Eds.), National Institute of Standards and Technology, Gaithersburg MD, v. 69. http://webbook.nist.gov, (retrieved September 2, 2014).

Lively, R., Jameson, R., Alexander, E., and Morey, G., 1992, Radium in the Mt. Simon-Hinckley aquifer, east-central and southeastern Minnesota: Minnesota Department of Natural Resources, Division of Waters, Information Circular 36, 58 p.

Livnat, A., 1983, *Metamorphism and copper mineralization of the Portage Lake Lava Series, northern Michigan*: University of Michigan, Ph.D. dissertation, **292** pp.

Ludvigson, G., McKay, R., and Anderson, R., 1990, Petrology of Keweenawan sedimentary rocks in the MG Eisched# 1 drillhole: *in* The Amoco M.G. Eischeid #1 deep petroleum test Carroll County, Iowa, Preliminary Investigations, Special Report Series #2, R.R. Anderson (ed.), Iowa Department of Natural Resources, p. 77-112.

Machel, H. G., and Mountjoy, E. W., 1986, Chemistry and environments of dolomitization—a reappraisal: *Earth-Science Reviews*, v. 23, no. 3, p. 175-222.

Martell, A. E., Smith, R. M., and Motekaitis R. J., 1997, Critically Selected Stability Constants of Metal Complexes Database. Version 3.0 Texas A & M University, College Station.

Metz, B., Davidson, O., De Coninck, H., Loos, M., & Meyer, L., 2005, *IPCC Special Report on Carbon Dioxide Capture and Storage*, Cambridge University Press. 431 pp.

Meybeck, M., 1987, Global chemical weathering of surficial rocks estimated from river dissolved loads: *American Journal of Science*, v. 287, no. 5, p. 401-428.

Meyer, H., 1984, The influence of impurities on the growth rate of calcite: *Journal of Crystal Growth*, v. 66, no. 3, p. 639-646.

Miller, J.D., 2007, The Midcontinent Rift in the Lake Superior Region: A 1.1 Ga Large Igneous Province Large Igneous Provinces Commission, accessed November, 2013, http://www.largeigneousprovinces.org/07nov

Miller, J. D., and Chandler, V. W., 1997, Geology, petrology, and tectonic significance of the Beaver Bay Complex, northeastern Minnesota: *in* Middle Proterozoic to Cambrian Rifting, Central North America, Ojakangas, R.W., Dickas, A.B., Green, J.C. (Eds.), Geological Socciaty of America Special Papers., v. 312, p. 73-96.

Morse, J. W., 2003, Formation and Diagenesis of Carbonate Sediments: *in* Holland, H. D., and Turekian, K. K., eds., Treatise on Geochemistry: Oxford, Pergamon, p. 67-85.

Morse, J. W., and Mackenzie, F. T., 1990, *Geochemistry of sedimentary carbonates*: Elsevier, 706 pp.

Murphy, R., Lammers, K., Smirnov, A., Schoonen, M. A. A., and Strongin, D. R., 2011, Hematite reactivity with supercritical CO_2 and aqueous sulfide: *Chemical Geology*, v. 283, no. 3–4, p. 210-217.

Nicholson, S. W., Dicken, C. L., Foose, M. P., Mueller, J., 2004, *Integrated geologic map databases for the United States; the upper midwest states: Minnesota, Wisconsin, Michigan, Illinois, and Indiana*: US Geological Survey Open-File Report, 1355 pp.

Oelkers, E. H., Gislason, S. R., and Matter, J., 2008, Mineral carbonation of CO_2: *Elements*, v. 4, no. 5, p. 333-337.

Ojakangas, R., 1986, Reservoir characteristics of the Keweenawan Supergroup, Lake Superior region: Precambrian petroleum potential, Wisconsin and Michigan: *Geoscience Wisconsin*, v. 11, p. 25-31.

Ojakangas, R., Morey, G., and Green, J., 2001, The Mesoproterozoic midcontinent rift system, Lake Superior region, USA: *Sedimentary Geology*, v. 141, p. 421-442.

Ojakangas, R. W., and Morey, G., 1982, Keweenawan sedimentary rocks of the Lake Superior region: a summary: Geology and tectonics of the Lake Superior basin: Geological Society of America Memoir, v. 156, p. 157-164.

Olanders, B., and Steenari, B.-M., 1995, Characterization of ashes from wood and straw: *Biomass and Bioenergy*, v. 8, no. 2, p. 105-115.

Pacala, S., and Socolow, R., 2004, Stabilization wedges: solving the climate problem for the next 50 years with current technologies: *science*, v. 305, no. 5686, p. 968-972.

Paces, J. B., and Miller, J. D., 1993, Precise U-Pb ages of Duluth Complex and related mafic intrusions, northeastern Minnesota: Geochronological insights to physical, petrogenetic, paleomagnetic, and tectonomagmatic processes associated with the 1.1 Ga Midcontinent Rift System: *Journal of Geophysical Research*: Solid Earth (1978–2012), v. 98, no. B8, p. 13997-14013.

Palandri, J. L., and Kharaka, Y. K., 2005, Ferric iron-bearing sediments as a mineral trap for CO_2 sequestration: Iron reduction using sulfur-bearing waste gas: *Chemical Geology*, v. 217, no. 3–4, p. 351-364.

PHREEQ software program (United States Geological Survey, version 3.1.2.8538; Parkhurst, D.L. and Appelo, C.A.J. (3/3/2014).

Plumber, L., and Busenberg, E., 1982, The solubilities of calcite, aragonite and vaterite in CO_2–H_2O solutions between 0 and 90°C, and an evaluation of the aqueous model for the system $CaCO_3$–CO_2–H_2O: *Geochim. et Cosmochim. Acta*, v. 46, p. 1011-1040.

Power, I. M., Harrison, A. L., Dipple, G. M., Wilson, S. A., Kelemen, P. B., Hitch, M., and Southam, G., 2013, Carbon mineralization: from natural analogues to engineered systems: *Reviews in Mineralogy and Geochemistry*, v. 77, no. 1, p. 305-360.

Pratt, L. M., Summons, R. E., and Hieshima, G. B., 1991, Sterane and triterpane biomarkers in the Precambrian Nonesuch Formation, North American Midcontinent Rift: *Geochimica et Cosmochimica* Acta, v. 55, no. 3, p. 911-916.

Pytkowicz, R. M., 1965, Rates of inorganic calcium carbonate nucleation: *The Journal of Geology*, v. 73, p. 196-199.

Radha, A., and Navrotsky, A., 2013, Thermodynamics of carbonates: *Reviews in Mineralogy and Geochemistry*, v. 77, no. 1, p. 73-121.

Railsback, L. B. (1999). Patterns in the compositions, properties, and geochemistry of carbonate minerals: *Carbonates and Evaporites*, v. 14, no. 1, p. 1-20.

Railsback, L.B., 2011, Surface features on a growing or dissolving crystal: *in* Some fundamentals of mineralogy and geochemistry. http://www.gly.uga.edu/railsback/FundamentalsIndex.html

Rsson, S. N. A., and Nsson, A. S., 1999, Assessment of feldspar solubility constants in water in the range 0 to 350°C at vapor saturation pressures: *American Journal of Science*, v. 299, p. 173–209.

Ryan, P., 2014, *Environmental and Low Temperature Geochemistry*, John Wiley & Sons, 416 pp.

Sheps, K. M., Max, M. D., Osegovic, J. P., Tatro, S. R., and Brazel, L. A., 2009, A case for deep-ocean CO_2 sequestration: *Energy Procedia*, v. 1, no. 1, p. 4961-4968.

Shock, E. L., and Helgeson, H. C., 1988, Calculation of the thermodynamic and transport properties of aqueous species at high pressures and temperatures: Correlation algorithms for ionic species and equation of state predictions to 5 kb and 1000 C: *Geochimica et Cosmochimica Acta*, v. 52, no. 8, p. 2009-2036.

Shock, E. L., Helgeson, H. C., and Sverjensky, D. A., 1989, Calculation of the thermodynamic and transport properties of aqueous species at high pressures and temperatures: Standard partial molal properties of inorganic neutral species: *Geochimica et Cosmochimica Acta*, v. 53, no. 9, p. 2157-2183.

Sloan, M. W., Moore, P. S., and McCutcheon, A., 1992, Kipper-a unique oil and gas discovery, Gippsland Basin, Australia, *APPEA*, 32, 1010-1010.

Smith, J. W., and Milton, C., 1966, Dawsonite in the Green River formation of Colorado: *Economic geology*, v. 61, no. 6, p. 1029-1042.

Southwick, D. L., Morey, G. B., and McSwiggen, P. L., 1988, Geologic Map (Scale 1: 250,000) of the Penokean Orogen, Central and Eastern Minnesota, and Accompanying Text. Minnesota Geological Survey, RI 37.

Stein, S., van der Lee, S., Jurdy, D., Stein, C., Wiens, D., Wysession, M., Revenaugh, J., Frederiksen, A., Darbyshire, F., and Bollmann, T., 2011, Learning from failure: The SPREE Mid-Continent Rift Experiment: *GSA Today*, v. 21, no. 9, p. 5-7.

Suszek, T., 1997, Petrography and sedimentation of the middle Proterozoic (Keweenawan) Nonesuch Formation, western Lake Superior region: *in* Middle Proterozoic to Cambrian Rifting, Central North America, Ojakangas, R.W., Dickas, A.B., Green, J.C. (Eds.), Geological Socciaty of America Special Papers., v. 312, p. 195-210.

Thiel, E., 1956, Correlation of gravity anomalies with the Keweenawan geology of Wisconsin and Minnesota: *Geological Society of America Bulletin*, v. 67, no. 8, p. 1079-1100.

Thorleifson, L. H., 2008, *Potential Capacity for Geologic Carbon Sequestration in the Midcontinent Rift System in Minnesota*: Minnesota Geological Survey, University of Minnesota, 138 pp.

Tokunaga, T. K., 2012, DLVO-based estimates of adsorbed water film thicknesses in geologic CO_2 reservoirs: *Langmuir*, v. 28, no. 21, p. 8001-8009.

Tryhorn, A., and Ojakangas, R., 1972, Sedimentation and petrology of the upper Precambrian Hinckley Sandstone of east-central Minnesota: Geology of Minnesota: a centennial volume: Minnesota Geological Survey, p. 431-435.

Ueda, A., Kato, K., Ohsumi, T., Yajima, T., Ito, H., Kaieda, H., Metcalfe, R., and Takase, H., 2005, Experimental studies of CO_2-rock interaction at elevated temperatures under hydrothermal conditions: *Geochemical Journal*, v. 39, no. 5, p. 417-425.

Walter, L.M., 1986. Relative efficiency of carbonate dissolution and precipitation during diagenesis: a progress report on the role of solution chemistry, Roles of organic matter: *in* mineral diagenesis, Gautier, D.L. (Ed.), Society for Sedimentary Geology, Special Publication 38, pp. 1–12.

Watson M. N, Gibson-Poole C. M., 2005, Reservoir selection for optimised geological injection and storage of carbon dioxide: a combined geochemical and stratigraphic perspective: *in* The fourth annual conference on carbon capture and storage. National Energy Technology Laboratory, US Department of Energy, Alexandria, 2‑5 May 2005.

Weege, R., and Pollack, J., 1971, Recent developments in the native-copper district of Michigan, Society of Economic Geologists Guidebook for Field Conference: Michigan Copper District, p. 18-43.

Weiblen, P. W., and Morey, G., 1980, A summary of the stratigraphy, petrology, and structure of the Duluth Complex: *American Journal of Science*, v. 280-A, p. 88-133.

Wellman, T.P, Grigg, R.B., McPherson, B.J., Svec, R.K., and Lichtner, P.C., 2003, Evaluation of CO_2-Brine-Reservoir Rock Interaction with Laboratory Flow Tests and Reactive Transport Modeling, SPE International Symposium on Oilfield Chemistry, paper 80228.

White, W. M., 2013, Geochemistry, John Wiley & Sons. 672 pp.

White, W. S., 1968, The native-copper deposits of northern Michigan, in Ore Deposits of the United States, 1933-1967: *American Institute of Mining Engineers*, v. 1, p. 303-325.

White, W. S., 1972, The base of the upper Keweenawan, Michigan and Wisconsin: *U.S. Geological Survey Bulletin*: 1354-F, p. F1-F23.

White, S. P., Allis, R. G., Moore, J., Chidsey, T., Morgan, C., Gwynn, W., & Adams, M., 2005, Simulation of reactive transport of injected CO_2 on the Colorado Plateau, Utah, USA. *Chemical geology*, v. 217(3), 387-405.

Witzke, B., 1990, General stratigraphy of the Phanerozoic and Keweenawan sequence: *in* The Amoco M.G. Eischeid #1 deep petroleum test Carroll County, Iowa, Preliminary Investigations, Special Report Series #2, R.R. Anderson (ed.), Iowa Department of Natural Resources, p. 39-57.

Woelk, T. S., and Hinze, W. J., 1991, Model of the midcontinent rift system in northeastern Kansas: *Geology*, v. 19, no. 3, p. 277-280.

Woollard, G. P., 1943, Transcontinental gravitational and magnetic profile of North America and its relation to geologic structure: *Geological Society of America Bulletin*, v. 54, no. 6, p. 747-789.

Xu, T., Apps, J. A., and Pruess, K., 2005, Mineral sequestration of carbon dioxide in a sandstone–shale system: *Chemical Geology*, v. 217, no. 3–4, p. 295-318.

Xu, X., Chen, S., and Zhang, D., 2006, Convective stability analysis of the long-term storage of carbon dioxide in deep saline aquifers: *Advances in Water Resources*, v. 29, no. 3, p. 397-407.

Zerai, B., Saylor, B. Z., and Matisoff, G., 2006, Computer simulation of CO_2 trapped through mineral precipitation in the Rose Run Sandstone, Ohio: *Applied Geochemistry*, v. 21, no. 2, p. 223-240.

ELECTRONIC RESOURCES:

Web-Phreeq, 2014, http://www.ndsu.nodak.edu/web phreeq/

Peace Software, 2014, http://www.peacesoftware.de/einigewerte/einigewerte_e.html

Chemical Portal, 2014, http://www.webqc.org/balance.php

Gas Solubility, 2014, http://calc.kl-edi.ac.cn/Pages/Solubility.aspx

VITA

Alsedik Mohamed Ali Abousif was born and raised in a small village south-western Libya called Qwirat. He was educated in the schools of the same village for the primary school stages and completed his high school stage in a nearby town called Ghurayfah in June 1993. In the same year, he attended Sebha University (Sebha, Libya), in which he got a bachelor's degree in geology in 1999. In 2001, Mr. Abousif started to lecture as a TA in the Department of Geology of the Sabha University, which granted him a scholarship for MSc degree in geology. In August 2004, he pursued a Masters in stratigraphy and sedimentology from the Academy of Graduate Studies, Tripoli, Libya. After his graduation in 2007, he returned to teach at Geology Department of Sebha University. In 2009, he joined Missouri University of Science and Technology (Rolla, MO) pursuing his Ph.D. in geochemistry.